



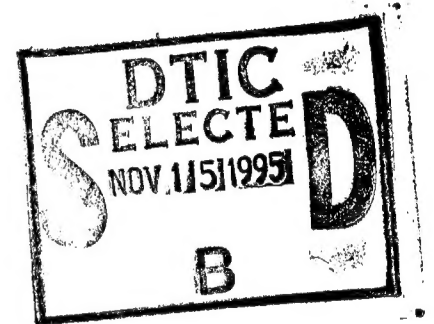
**Defense Nuclear Agency  
Alexandria, VA 22310-3398**



**DNA-TR-94-133**

## **Equation of State Investigations of Geologic Materials**

**Frank W. Davies  
Eric A. Smith  
Ktech  
901 Pennsylvania Avenue, NE  
Albuquerque, NM 87110-7491**



**October 1995**

**19951114 053**

**Technical Report**

**CONTRACT No. DNA 001-92-C-0057**

**Approved for public release;  
distribution is unlimited.**

**DTIC QUALITY INSPECTED 8**

Destroy this report when it is no longer needed. Do not return to sender.

PLEASE NOTIFY THE DEFENSE NUCLEAR AGENCY,  
ATTN: CSTI, 6801 TELEGRAPH ROAD, ALEXANDRIA, VA  
22310-3398, IF YOUR ADDRESS IS INCORRECT, IF YOU  
WISH IT DELETED FROM THE DISTRIBUTION LIST, OR  
IF THE ADDRESSEE IS NO LONGER EMPLOYED BY YOUR  
ORGANIZATION.



## DISTRIBUTION LIST UPDATE

This mailer is provided to enable DNA to maintain current distribution lists for reports. (We would appreciate your providing the requested information.)

- ☐ Add the individual listed to your distribution list.
- ☐ Delete the cited organization/individual.
- ☐ Change of address.

### NOTE:

Please return the mailing label from the document so that any additions, changes, corrections or deletions can be made easily. For distribution cancellation or more information call DNA/IMAS (703) 325-1036.

NAME: \_\_\_\_\_

ORGANIZATION: \_\_\_\_\_

### OLD ADDRESS

### CURRENT ADDRESS

---

---

---

---

---

---

TELEPHONE NUMBER: (    ) \_\_\_\_\_

### DNA PUBLICATION NUMBER/TITLE

### CHANGES/DELETIONS/ADDITIONS, etc.)

(Attach Sheet if more Space is Required)

---

---

---

---

---

---

DNA OR OTHER GOVERNMENT CONTRACT NUMBER: \_\_\_\_\_

CERTIFICATION OF NEED-TO-KNOW BY GOVERNMENT SPONSOR (if other than DNA): \_\_\_\_\_

SPONSORING ORGANIZATION: \_\_\_\_\_

CONTRACTING OFFICER OR REPRESENTATIVE: \_\_\_\_\_

SIGNATURE: \_\_\_\_\_

CUT HERE AND RETURN



DEFENSE NUCLEAR AGENCY  
ATTN: IMAS  
6801 TELEGRAPH ROAD  
ALEXANDRIA, VA 22310-3398

DEFENSE NUCLEAR AGENCY  
ATTN: IMAS  
6801 TELEGRAPH ROAD  
ALEXANDRIA, VA 22310-3398

REPORT DOCUMENTATION PAGE			Form Approved OMB No. 0704-0188	
Public reporting burden for this collection of information is estimated to average 1 hour per response including the time for reviewing instructions, searching existing data sources, gathering and maintaining the data needed, and completing and reviewing the collection of information. Send comments regarding this burden estimate or any other aspect of this collection of information, including suggestions for reducing this burden, to Washington Headquarters Services, Directorate for Information Operations and Reports, 1215 Jefferson Davis Highway, Suite 1204, Arlington, VA 22202-4302, and to the Office of Management and Budget, Paperwork Reduction Project (0704-0188), Washington, DC 20503				
1. AGENCY USE ONLY (Leave blank)		2. REPORT DATE 951001		3. REPORT TYPE AND DATES COVERED Technical 930401 - 940131
4. TITLE AND SUBTITLE Equation of State Investigations of Geologic Materials			5. FUNDING NUMBERS C - DNA 001-92-C-0057 PE - 62715H PR - AF TA - AR WU - DH920057	
6. AUTHOR(S) Frank W. Davies and Eric A. Smith				
7. PERFORMING ORGANIZATION NAME(S) AND ADDRESS(ES) Ktech 901 Pennsylvania Avenue, NE Albuquerque, NM 87110-7491			8. PERFORMING ORGANIZATION REPORT NUMBER TR 94-02	
9. SPONSORING/MONITORING AGENCY NAME(S) AND ADDRESS(ES) Defense Nuclear Agency 6801 Telegraph Road Alexandria, VA 22310-3398 FCTTS/Seemann			10. SPONSORING/MONITORING AGENCY REPORT NUMBER DNA-TR-94-133	
11. SUPPLEMENTARY NOTES This work was sponsored by the Defense Nuclear Agency under RDT&E RMC Code B4662D AF AR 00018 4200 25904D.				
12a. DISTRIBUTION/AVAILABILITY STATEMENT Approved for public release; distribution is unlimited.			12b. DISTRIBUTION CODE	
13. ABSTRACT (Maximum 200 words)  This report documents the results of dynamic material response tests of 5 rock and 2 grouts that were performed in support of DNA's HYDROPLUS yield verification program. Pennsylvania slate, Maine slate, thawed permafrost phyllite, SHIST granite, Sierra White granite, HSG-14 grout and a granite grout were characterized in the stress range of 0.5 to 15 GPa by the derivation of Hugoniot data and by loading and release paths calculated from La-grangian analyses of in situ stress gauge measurements. The anisotropic response of the Pennsylvania and Maine Slates was quantified. An inflection in the Hugoniot of thawed permafrost Phyllite was detected at a stress of 14.8 GPa and particle velocity of 0.95 km/s. The HSG-4 and granite grouts each show dispersive wave propagation characteristics at low stresses (<2 GPa). Transmitted wave profile measurements in SHIST and Sierra White granites also showed a dispersive ramp loading at low stresses. Evidence of a yield or phase transition beginning at 6 GPa and stiffening at about 10 GPa was observed in SHIST granite. A two wave structure was seen at 13.4 GPa. The Sierra White granite high stress data are consistent with the inflection in the SHIST granite Hugoniot at 10 GPa.				
14. SUBJECT TERMS Granite Hugoniot HYDROPLUS Granite Grout Equation Of State Permafrost Phyllite Slate HSF-14 Grout			15. NUMBER OF PAGES 148	
			16. PRICE CODE	
17. SECURITY CLASSIFICATION OF REPORT UNCLASSIFIED		18. SECURITY CLASSIFICATION OF THIS PAGE UNCLASSIFIED		19. SECURITY CLASSIFICATION OF ABSTRACT UNCLASSIFIED
				20. LIMITATION OF ABSTRACT SAR

**UNCLASSIFIED**

**SECURITY CLASSIFICATION OF THIS PAGE**

**CLASSIFIED BY:**

**N/A since Unclassified.**

**DECLASSIFY ON:**

**N/A since Unclassified.**

**SECURITY CLASSIFICATION OF THIS PAGE**

**UNCLASSIFIED**

## SUMMARY

This report documents 44 gas gun tests conducted on 7 materials in support of DNA's HYDROPLUS yield verification program. All rock and grout samples were obtained from cores provided by DNA. These samples were prepared by Ktech, Terra Tek, and United States Army Corp. of Engineers/Waterways Experimental Station (USACE/WES). Table S-1 describes the source of these cores. Table S-2 defines the 41 tests performed. It lists the materials tested, material test conditions, stress ranges examined, the number of shots, and the sections of this document where the results and discussions are presented. Experiments were conducted to characterize 5 rocks, and 2 grouts. Hugoniot data were obtained for Pennsylvania slate, Maine slate, thawed permafrost phyllite, SHIST granite, Sierra White granite, HSG-14 grout, and a granite grout. The Hugoniot data for each material supplemented with loading and release paths were derived from Lagrangian analyses of in situ stress gauge measurements. All rock and grout were maintained and tested in their "as-received" (but unknown) water content condition.

Table S-1. Material core sample summary.

Core	Source Location	Hole Number	Interval (m)
Pennsylvania Slate	Penn Big Bed Slate, Co Allentown, PA	Blocks S3 and S4	—
Maine Slate	Mowson Slate Co. Quarry, Bangor, ME	Block M4	—
Phyllite	Lupin Mine, Northwest Territories, Canada	LU-2 and LU-2A	3.85 to 8.30
HSG-14 Grout	Waterways Experiment Station	4" Diam. Canisters	—
Granite Grout	Waterways Experiment Station	4" Dia. Canisters	—
SHIST Granite	SHIST Test Site	Hole #1	47.7 to 51.8
Sierra White Granite	Sierra White Quarry, Raymond, CA	—	—

Justification	
By _____	
Distribution/ _____	
Availability Codes	
Dist <b>A-1</b>	Avail and/or Special

Table S-2. Shot summary.

Results Section	Material	Material Condition	Nominal Stress Range (GPa)	No. of shots (Ambient Temp.)
3	Pennsylvania Slate	"as-received"	0.5 - 8.0	3
4	Maine Slate	"as-received"	0.5 - 10	8
5	Phyllite	"as-received"	11 - 17	2
6	HSG-14 Grout	"as-received"	0.8 - 10	7
7	Granite Grout	"as-received"	0.5 - 10	8
8	SHIST Granite	"as-received"	0.5 - 15	9
9	Sierra White Granite	"as-received"	0.5 - 10	7

Pennsylvania Slate: Three ambient temperature experiments were conducted on Pennsylvania Slate to examine the effect of cleavage plane orientation to the shock front. Samples were cut such that their impact surfaces were either parallel to (Y orientation) or normal to (Z orientation) the slate cleavage plane. Previously reported tests (Davies 1994) used Y orientation samples. These tests used Z orientation samples.

Comparison of time resolved transmitted wave profiles at different impact stresses indicates that there is little or no difference in the Z and Y direction shock response above about 2 GPa. However, below about 1 GPa samples shocked in the Z direction have higher shock velocities and shock impedances than those samples shocked in the Y direction. Ultrasonic longitudinal velocities are also higher in the Z direction ( $C_{LZ} = 5.73$  km/s and  $C_{LY} = 4.08$  km/s).

The leading edge of a propagating stress wave in the Z oriented material has more structure than the Y oriented material with the suggestion of a dispersive precursor. Additionally, the Z oriented material loading path shows more curvature than the similar path for the X oriented material. While Pennsylvania Slate is clearly anisotropic the small directional differences in the stress wave propagation characteristics are not significant to HYDROPLUS analyses.

Maine Slate: Five Lagrangian stress gauge and two VISAR measurements were conducted on Maine Slate from the Devonian age Carrabassett formation in the stress range from 0.5 to 11 GPa.



The test samples were cut such that propagating shock fronts were parallel to the cleavage plane of the slate. The Hugoniot data in the shock velocity-particle velocity plane can be represented by:

$$U_s = 4.86 (0.09) + 0.79 u_p (0.23)$$

where  $U_s$  and  $u_p$  are in km/s and the numbers in parenthesis are the standard errors of the constants of the fits. Maine Slate has a slightly higher impedance than Pennsylvania Slate, but there is relatively little difference between the two materials. There is evidence in the Maine Slate data of an inflection in the Hugoniot at 0.1 km/s particle velocity, whereas an inflection was identified in Pennsylvania Slate (Davies 1994) at about 0.3 km/s particle velocity.

Phyllite: Two tests were conducted on thawed permafrost phyllite at stresses of 11 and 17 GPa to extend to high stresses the phyllite data reported by Davies (1994).

The Hugoniot data can be represented by:

$$U_s = 5.087 + 0.540 u_p \text{ for } 0 < \sigma < 14.9 \text{ GPa}$$

$$\text{and } U_s = 4.939 + 0.696 u_p \text{ for } 14.9 < \sigma < 50 \text{ GPa}$$

were the shock velocity  $U_s$  and the particle velocity  $u_p$  are in km/s. SNL data at 14, 35, and 50 GPa (Furnish 1993) were included to extend the fits to 50 GPa.

The measured transmitted particle velocity profiles show no evidence of a precursor in the range of 10 to 15 GPa (0.7 to 1.0 km/s particle velocity). However, an inflection was detected in the Hugoniot at 14.8 GPa and 0.95 km/s.

HSG-14 Grout: Five Lagrangian stress gauge and three VISAR experiments were conducted to characterize a limestone matching grout, HSG-14 grout. This high density silicate grout which had particle diameters of up to 4 mm was prepared by Waterways Experiment Station.

The measured transmitted stress wave profiles show that the leading edge of the wave is dispersive and that the peak stress is attenuating with distance. All the transmitted profiles above 0.85 GPa show an inflection in the leading edge of the wave. At high impact stresses, the stress wave

steepens above this inflection. These attributes are consistent with the Hugoniot changing from downward concave at low stresses to upward concave at higher stresses. The Hugoniot data can be represented in the shock velocity-particle velocity plane by:

$$U_s = 4.42 (0.37) - 2.96 (1.60) \text{ for } 0 < \sigma < 3.5 \text{ GPa}$$

$$\text{and } U_s = 2.75 (0.16) + 1.52 (0.30) \text{ for } 3.5 < \sigma < 11 \text{ GPa}$$

where the shock velocity  $U_s$  and the particle velocity  $u_p$  are given in km/s and the numbers in parenthesis are the standard errors of the constants.

Granite Grout: Five Lagrangian stress gauge and three VISAR experiments were conducted to characterize a Granite grout. Like the HSG-14 grout, the measured transmitted stress wave profiles show that the leading edge to the wave is dispersive and that the peak stress is attenuating with distance. The dispersive precursor amplitude is 0.1 GPa and the leading toe propagates at 3.3 km/s.

The Hugoniot changes from downward concave to upward concave at 0.85 GPa. Above this point, the propagating wave is a shock which overtakes the dispersive precursor. The shock completely overruns the precursor somewhere between 5 and 10 GPa. The Hugoniot data can be represented in the shock velocity-particle velocity plane by:

$$U_s = 1.69 (0.070) - 0.667 (0.63)u_p \text{ for } 0 < \sigma < 0.85 \text{ GPa}$$

$$\text{and } U_s = 0.97 (0.266) + 2.42 (0.30)u_p \text{ for } 0.85 < \sigma < 11 \text{ GPa}$$

where the shock velocity  $U_s$ , and the particle velocity  $u_p$  are given in km/s and the numbers in parenthesis are the standard errors of the constants. The granite and HSG-14 grouts show a class of behavior that is very similar to that observed for HJC-7 concrete, an 3/8" aggregate concrete. Each material can be described as a high impedance aggregate in a low impedance matrix and geometric dispersion of a propagating stress wave should be expected in each case. The small aggregate size of the grouts allows valid laboratory scale experiments to be conducted. Additional experimental data particularly in the low stress regime when combined with the development of a geometric dispersion hydrocode model will provide significant insight into the dynamic behavior of this class of material.

SHIST Granite: Five Lagrangian stress gauge and four VISAR measurements were conducted between 0.4 and 13.4 GPa on SHIST Granite from WSMR. Longitudinal sound-speed measurements show that sonic velocity is a function of sample thickness. Velocities ranged from 6.3 km/s at 5 mm to 5.3 km/s at 51 mm. The measured transmitted wave profiles show a dispersive ramped loading wave whose rise time increases with increasing stress and the top of the pulse is rounded off. At 13.4 GPa, the transmitted wave was separated into a two wave structure.

The Hugoniot data showed a yield or phase transition beginning at 6 GPa and stiffening at about 10 GPa. The Hugoniot data is represented by three fits to the data in the  $U_s - u_p$  plane.

$$U_s = 4.950 (0.0402) + 1.135 (0.2829)u_p \text{ for } (0 < \sigma < 4 \text{ GPa})$$

$$U_s = 5.927 (0.2396) - 1.357 (0.3967)u_p \text{ for } (6 < \sigma < 9.5 \text{ GPa})$$

$$U_s = 3.273 (0.1178) + 1.474 (0.1107)u_p \text{ for } (9.5 < \sigma < 18 \text{ GPa})$$

where  $U_s$  and  $u_p$  are in km/s and numbers in parenthesis are standard errors for the constants.

Sierra White Granite: Six Lagrangian stress gauge experiments and three VISAR experiments were conducted on Sierra White Granite. As with the SHIST Granite, longitudinal sound-speed measurements show that sonic velocity is a function of sample thickness. Measured sonic velocities ranged from 5.61 km/s at 5 mm to 3.97 km/s at 19-mm depth.

The transmitted wave profile measurements show the same dispersive ramp loading and rounding of the top of the pulse as was seen in the SHIST Granite. The rise time of the ramped loading wave increased with increasing propagation distance. The Hugoniot data can be represented by two linear  $U_s - u_p$  fits:

$$U_s = 4.566 (0.074) + 4.820(0.680)u_p \text{ for } 0 < \sigma < 2 \text{ GPa}$$

$$U_s = 5.240 (0.054) + 0.161 (0.218)u_p \text{ for } 2 < \sigma < 6 \text{ GPa}$$

where  $U_s$  and  $u_p$  are in km/s and the numbers in parenthesis are stand errors of the constants. The high stress data point at 10 GPa is consistent with the inflection in the SHIST Granite Hugoniot.

## PREFACE

Ktech Corporation was tasked under Contract DNA001-92-C-0057, Subtask 01-26 to measure the dynamic response of materials relevant to the Defense Nuclear Agency (DNA HYDROPLUS yield verification program. This work was conducted at the DNA Materials Response Impact Facility at Kirtland Air Force Base. Mr. Douglas Seemann, DNA/FCTP, was the Contracting Officer Representative. The work was directed by Ms. Audrey Martinez, DNA/FCTP. Russell Hallett, Sherri Heyborne, John Liwski, and Tom Thornhill of Ktech provided valuable assistance in the fabrication test and analysis of the experiments.

## CONVERSION TABLE

Conversion factors for U.S. customary to metric (SI) units of measurement.

MULTIPLY ----- > BY ----- > TO GET  
TO GET < ----- BY < ----- DIVIDE

angstrom	1.000 000 X E -10	meters (m)
atmosphere (normal)	1.013 25 X E +2	kilo pascal (kPa)
bar	1.000 000 X E +2	kilo pascal (kPa)
barn	1.000 000 X E -28	meter <sup>2</sup> (m <sup>2</sup> )
British thermal unit (thermochemical)	1.054 350 X E +3	joule (J)
calorie (thermochemical)	4.184 000	joule (J)
cal (thermochemical/cm <sup>2</sup> )	4.184 000 X E -2	mega joule/m <sup>2</sup> (MJ/m <sup>2</sup> )
curie	3.700 000 X E +1	* giga becquerel (GBa)
degree (angle)	1.745 329 X E -2	radian (rad)
degree Fahrenheit	$t_k = (t_f + 459.67)/1.8$	degree kelvin (K)
electron volt	1.602 19 X E -19	joule (J)
erg	1.000 000 X E -7	joule (J)
erg/second	1.000 000 X E -7	watt (W)
foot	3.048 000 X E -1	meter (m)
foot/pound-force	1.355 818	joule (J)
gallon (U.S. liquid)	3.785 412 X E -3	meter <sup>3</sup> (m <sup>3</sup> )
inch	2.540 000 X E -2	meter (m)
jerk	1.000 000 X E +9	joule (J)
joule/kilogram (J/kg) radiation dose absorbed	1.000 000	Gray (Gy)
kilotons	4.183	terajoules
kip (1000 lbf)	4.448 222 X E +3	newton (N)
kip/inch <sup>2</sup> (ksl)	6.894 757 X E +3	kilo pascal (kPa)
ktap	1.000 000 X E +2	newton-second/m <sup>2</sup> (N-s/m <sup>2</sup> )
micron	1.000 000 X E -6	meter (m)
mil	2.540 000 X E -5	meter (m)
mile (international)	1.609 344 X E +3	meter (m)
ounce	2.834 952 X E -2	kilogram (kg)
pound-force (lbs avoirdupois)	4.448 222	newton (N)
pound-force inch	1.129 848 X E -1	newton-meter (N/m)
pound-force/inch	1.751 268 X E +2	newton/meter (N/m)
pound-force/foot <sup>2</sup>	4.788 026 X E -2	kilo pascal (kPa)
pound-force/inch <sup>2</sup> (psi)	6.894 757	kilo pascal (kPa)
pound-mass (lbm avoirdupois)	4.535 924 X E -1	kilogram (kg)
pound-mass-foot <sup>2</sup> (moment of inertia)	4.214 011 X E -2	kilogram-meter <sup>2</sup> (kg/m <sup>2</sup> )
pound-mass/foot <sup>3</sup>	1.601 846 X E +1	kilogram/meter <sup>3</sup> (kg/m <sup>3</sup> )
rad (radiation dose absorbed)	1.000 000 X E -2	** Gray (Gy)
roentgen	2.579 760 X E -4	coulomb/kilogram (C/kg)
shake	1.000 000 X E -8	second (s)
slug	1.459 390 X E +1	kilogram (kg)
torr (mm Hg, 0° C)	1.333 22 X E -1	kilo pascal (kPa)

\* The becquerel (Bq) is the SI unit of radioactivity; 1 Bq = 1 event/s.

\*\* The Gray (Gy) is the SI unit of absorbed radiation.

## TABLE OF CONTENTS

Section	Page
SUMMARY .....	iii
PREFACE .....	viii
CONVERSION TABLE .....	ix
FIGURES .....	xii
TABLES .....	xv
<b>1 INTRODUCTION .....</b>	<b>1</b>
1.1 BACKGROUND .....	1
1.2 DOCUMENT ROADMAP .....	2
<b>2 EXPERIMENTAL AND ANALYTICAL TECHNIQUES .....</b>	<b>3</b>
2.1 SAMPLE CHARACTERIZATION .....	3
2.2 GAS GUN TECHNIQUES .....	4
2.2.1 Lagrangian Stress Measurements .....	5
2.2.2 VISAR Measurements .....	6
2.3 ANALYSIS TECHNIQUE .....	7
2.3.1 Steady State Analysis of Lagrangian Stress Gauge Data .....	8
2.3.2 Steady State Analysis of VISAR Particle Velocity Measurements .....	20
2.3.3 Lagrangian Analysis .....	22
<b>3 PENNSYLVANIA SLATE .....</b>	<b>27</b>
3.1 MATERIAL DESCRIPTION .....	27
3.2 TEST RESULTS .....	29
3.3 DISCUSSION .....	33
<b>4 MAINE SLATE .....</b>	<b>38</b>
4.1 MATERIAL DESCRIPTION .....	38
4.2 TEST RESULTS .....	40
4.3 DISCUSSION .....	44
<b>5 PHYLLITE RESULTS .....</b>	<b>49</b>
5.1 MATERIAL DESCRIPTION .....	49
5.2 TEST RESULTS .....	51
5.3 DISCUSSION .....	53
<b>6 HSG-14 GROUT .....</b>	<b>58</b>
6.1 MATERIAL DESCRIPTION .....	58

## TABLE OF CONTENTS (Continued)

Section	Page
6.2 TEST RESULTS .....	60
6.3 DISCUSSION .....	64
7 GRANITE GROUT .....	67
7.1 MATERIAL DESCRIPTION .....	67
7.2 TEST RESULTS .....	68
7.3 DISCUSSION .....	73
8 SHIST GRANITE .....	78
8.1 MATERIAL DESCRIPTION .....	78
8.2 TEST RESULTS .....	82
8.3 DISCUSSION .....	87
9 SIERRA WHITE GRANITE .....	90
9.1 MATERIAL DESCRIPTION .....	90
9.2 TEST RESULTS .....	92
9.3 DISCUSSION .....	96
10 REFERENCES .....	101
APPENDIX	
STRESS AND PARTICLE VELOCITY WAVEFORMS .....	104

## FIGURES

Figure	Page
2-1 Rock equation of state experimental arrangement with Lagrangian stress gauges (Configuration used to maintain water saturation) . . . . .	6
2-2 Equation of state experimental arrangement for VISAR particle velocity measurement . . .	8
2-3 The derivation of a Hugoniot point from in-situ stress gauges using steady state assumptions . . . . .	10
2-4 The Lagrangian stress configuration allows for four estimates of a Hugoniot point . . . .	11
2-5 Stress wave reverberation in gauge packages . . . . .	13
2-6 Comparison of an analytic approximation and an impedance match solution of an in-situ gauge response . . . . .	15
2-7 Comparison of an analytic approximation and an impedance mismatch calculation of the stress profile transmitted through a gauge package . . . . .	16
2-8 Comparison of an analytic approximation and an impedance mismatch solution for a second gauge package . . . . .	16
2-9 Example of interpretation of stress gauge data . . . . .	18
2-10 Equation of state experimental arrangement for VISAR particle velocity measurement . . .	21
2-11 The generation of path lines in the loading process for the Lagrangian analysis . . . . .	24
3-1 Orientation of cleavage plane in Pennsylvania slate gas gun samples . . . . .	28
3-2 Lagrangian stress-time profiles in Z oriented Pennsylvania slate . . . . .	30
3-3 VISAR particle velocity-time profiles for Z oriented Pennsylvania slate . . . . .	31
3-4 Loading and unloading paths for Z oriented Pennsylvania slate (shot 3668) . . . . .	32
3-5 Loading and unloading paths for Z oriented Pennsylvania slate (shot 3647) . . . . .	32
3-6 Comparison of stress profiles measured in Y and Z oriented Pennsylvania slate at 0.5 GPa . . . . .	34
3-7 Comparison of stress profiles measured in Y and Z oriented Pennsylvania slate at 3.5 GPa . . . . .	34
3-8 Comparison of particle velocity profiles measured in Y and Z oriented Pennsylvania slate at 8 GPa . . . . .	35
3-9 Comparison of loading and unloading paths for Y and Z oriented Pennsylvania slate at 3.5 GPa . . . . .	35
3-10 Hugoniot data for Y and Z oriented Pennsylvania slate in stress-particle velocity plane . .	36
3-11 Hugoniot data for Y and Z oriented Pennsylvania slate in stress-relative density plane . . .	36
3-12 Hugoniot data for Y and Z oriented Pennsylvania slate in shock velocity-particle velocity plane . . . . .	37
4-1 Orientation of cleavage plane in sample . . . . .	38
4-2 Lagrangian stress gauge test configuration showing test sample mounted in target holder without an aluminum buffer . . . . .	41
4-3 Visar target configuration showing test sample mounted in target holder without an aluminum buffer . . . . .	42



## FIGURES (Continued)

Figure	Page
4-4 Comparison of measured stress profiles in Pennsylvania slate using aluminum buffered, and bufferless test configurations . . . . .	42
4-5 Maine slate Hugoniot data, stress-particle velocity plane . . . . .	45
4-6 Maine slate Hugoniot data, stress-relative density ( $\rho/\rho_0$ ) plane . . . . .	45
4-7 Maine slate Hugoniot data, shock velocity-particle velocity plane . . . . .	46
4-8 Measured stress profiles in Maine slate . . . . .	46
4-9 Measured particle velocity profiles in Maine slate . . . . .	47
4-10 Comparison of Maine and Pennsylvania slate Hugoniots in the shock velocity-particle velocity plane . . . . .	47
4-11 Comparison of Maine and Pennsylvania slate Hugoniots in the stress-particle velocity plane . . . . .	48
4-12 Comparison of Maine and Pennsylvania slate Hugoniots in the stress-relative density ( $\rho/\rho_0$ ) plane . . . . .	48
5-1 Shot 3654 measured particle velocity profile . . . . .	51
5-2 Shot 3666 measured particle velocity profile . . . . .	52
5-3 Thawed phyllite Hugoniot data in the stress-particle velocity plane . . . . .	55
5-4 Thawed phyllite Hugoniot data in the stress-relative density ( $\rho/\rho_0$ ) plane . . . . .	55
5-5 Thawed phyllite Hugoniot data in the shock velocity-particle velocity plane . . . . .	56
5-6 Comparison of linear fits to thawed phyllite data in the shock velocity-particle velocity plane . . . . .	56
5-7 Comparison of experimental data in the stress-particle velocity plane to the $U_s - u_p$ fits . .	57
5-8 Comparison of experimental data in the stress relative density ( $\rho/\rho_0$ ) plane to the $U_s - u_p$ fits . . . . .	57
6-1 HSG-14 grout samples contained particles up to 4-mm diameter . . . . .	59
6-2 HSG14 Hugoniot data, stress-particle velocity plane . . . . .	61
6-3 HSG14 grout Hugoniot data, stress-relative density ( $\rho/\rho_0$ ) plane . . . . .	61
6-4 HSG14 grout Hugoniot data, shock velocity-particle velocity plane . . . . .	62
6-5 Measured stress profiles in HSG-14 grout . . . . .	62
6-6 Measured particle velocity profiles in HSG-14 grout . . . . .	63
6-7 Comparison of fitted Hugoniot to experimental data in the shock velocity-particle velocity plane . . . . .	65
6-8 Comparison of measured HSG-14 grout data to fitted Hugoniot in the stress-particle velocity plane . . . . .	65
6-9 Comparison of fitted Hugoniot to experimental data in the stress-relative density plane . .	66
7-1 Granite grout Hugoniot data, stress-particle velocity plane . . . . .	70
7-2 Granite grout Hugoniot data, stress-relative density ( $\rho/\rho_0$ ) plane . . . . .	71
7-3 Granite grout Hugoniot data, shock velocity-particle velocity plane . . . . .	71
7-4 Lagrangian gauge stress-time profiles in granite grout, (a) with aluminum buffer, (b) without aluminum buffer . . . . .	72
7-5 VISAR particle velocity-time profiles for granite grout . . . . .	73
7-6 The attenuation of peak stress as a function of impact stress for propagation distances of 5 and 10 mm . . . . .	75

# FIGURES (Continued)

Figure		Page
7-7	Comparison of fitted Hugoniot to experimental data in the shock velocity-particle velocity plane . . . . .	76
7-8	Comparison of the fitted Hugoniot to experimental data in the stress-particle velocity plane . . . . .	76
7-9	Comparison of the fitted Hugoniot to experimental data in the stress-relative density ( $\rho/\rho_0$ ) plane . . . . .	77
8-1	The dependence of longitudinal wavespeed upon SHIST granite sample thickness . . . . .	81
8-2	SHIST granite $\sigma - u_p$ Hugoniot data . . . . .	84
8-3	SHIST granite $\sigma - \rho/\rho_0$ Hugoniot data . . . . .	84
8-4	SHIST granite $U_s - u_p$ Hugoniot data . . . . .	85
8-5	Lagrangian stress-time profiles for SHIST granite . . . . .	85
8-6	Particle velocity-time profiles for SHIST granite . . . . .	86
9-1	The variation of longitudinal wavespeed with sample thickness . . . . .	92
9-2	Sierra white granite $\sigma - u_p$ Hugoniot data . . . . .	93
9-3	Sierra white granite $\sigma - \rho/\rho_0$ Hugoniot data . . . . .	94
9-4	Sierra white granite $U_s - u_p$ Hugoniot data . . . . .	94
9-5	Comparison of measured stress profiles in sierra white granite . . . . .	95
9-6	Comparison of measured particle velocity profiles in sierra white granite . . . . .	95
9-7	Comparison of SHIST granite, sierra white granite and westerly granite $\sigma - u_p$ Hugoniot data . . . . .	98
9-8	Comparison of SHIST granite, sierra white granite, and westerly granite $\sigma - \rho/\rho_0$ Hugoniot data . . . . .	99
9-9	Comparison of SHIST granite, sierra white granite, and westerly granite $U_s - u_p$ Hugoniot data . . . . .	100

## TABLES

Table	Page
S-1	Material core sample summary . . . . . iii
S-2	Shot summary . . . . . iv
2-1	Impactor and buffer materials (Hugoniot) . . . . . 5
2-2	Four estimates of the Hugoniot point are derivable from the Lagrangian stress gauge measurements . . . . . 12
3-1	XRD Mineralogy of slates M-3 and S-3 - mineralogy, approximate weight percent . . . 27
3-2	Material properties data for Z oriented Pennsylvania Slate . . . . . 28
3-3	Pennsylvania slate ultrasonic velocity measurements in y and z directions . . . . . 29
3-4	Pennsylvania slate (z oriented) shot configuration data . . . . . 30
3-5	Pennsylvania slate (Z direction) Hugoniot data . . . . . 31
4-1	Slate sample dimensions acquired from Manson Quarry, Maine . . . . . 39
4-2	XRD mineralogy of main slate (block M3) . . . . . 39
4-3	Material properties for Maine slate . . . . . 40
4-4	Maine slate shot configuration data . . . . . 41
4-5	Maine slate Hugoniot data . . . . . 43
5-1	Lithologic descriptions performed at the drill site by DNA . . . . . 50
5-2	X-ray diffraction mineralogy of phyllite . . . . . 50
5-3	Material properties for phyllite . . . . . 50
5-4	Phyllite shot configuration data . . . . . 52
5-5	Thawed phyllite Hugoniot data obtained from VISAR measurements . . . . . 53
6-1	Ingredients and mixture proportions for HSG-14 grout . . . . . 58
6-2	Material properties for HSG-14 grout . . . . . 59
6-3	HSG-14 grout . . . . . 60
6-4	HSG-14 grout hugoniot data . . . . . 63
7-1	Ingredients and mixture proportions for granite grout SHI mix #2 . . . . . 67
7-2	Material properties for granite grout . . . . . 68
7-3	Shot configuration data . . . . . 69
7-4	Granite grout hugoniot data . . . . . 70
8-1	XRD semi-quantitative mineralogy of selected samples from the SHIST site . . . . . 79
8-2	Summary of physical properties for SHIST test plugs as measured by Terra Tek . . . . 79
8-3	Summary of ultrasonic velocities and calculated dynamic properties for the SHIST test plugs as defined by Terra Tek . . . . . 80
8-4	Summary of static mechanical properties determined from unconfined compression tests for the SHIST test plugs by Terra Tek . . . . . 80
8-5	Ktech measured SHIST granite material properties . . . . . 82
8-6	SHIST granite shot configuration data . . . . . 83
8-7	SHIST granite Hugoniot data . . . . . 87
9-1	Typical composition of Sierra White Granite . . . . . 92
9-2	Sierra White granite material properties . . . . . 91
9-3	SHIST granite shot configuration data . . . . . 93

**TABLES (Continued)**

Table	Page
9-4 Sierra white granite Hugoniot data . . . . .	96

## **SECTION 1**

### **INTRODUCTION**

The Defense Nuclear Agency (DNA) has developed a method of verifying the yield of non-standard underground nuclear tests using peak radial stress and velocity at several ranges from the working point in conjunction with hydrocode calculations. This method which is known as "HYDROPLUS" requires measurements of the dynamic material properties of the geologic materials between the working point and the measurement locations as input to the hydrocode calculations. In support of this effort, the dynamic shock response for different rock types and man-made grouts was determined from plate impact experiments at the DNA Impact Facility at Kirtland AFB, New Mexico. This report describes the experimental techniques used and details the experimental results and analysis.

#### **1.1 BACKGROUND.**

The verification of the Threshold Test Ban Treaty (TTBT) protocol has been based on the use of on-site verification techniques. The HYDROPLUS method uses stress and velocity gauges to measure the peak stress and particle velocity at known ranges. Experience at the Nevada Test Site (NTS) and calculations have shown that the rate of decay of peak values vs. range is dependent on the unloading behavior from the peak state. Therefore, successful application of the HYDROPLUS method requires knowledge of the response of rocks and grouts to dynamic loading and also to the subsequent release.

Slate and phyllite were characterized as part of the data/modeling compilation for HYDROPLUS. Slates, which were obtained from the Ordovician age Martinsburg formation in Pennsylvania (Pennsylvania Slate), and from the Devonian age Carrabassett formation in Maine (Maine Slate) were tested in an "as-received" condition. The Pennsylvania Slate data reported herein examined samples which were oriented so that the cleavage planes were normal to the propagating shock front. The phyllite was received as preserved frozen, thawed, and refrozen samples and was tested in "as-received" frozen and thawed conditions to further elucidate the effects of moisture content and temperature on the observed, dynamic response of material germane to HYDROPLUS. The majority of the phyllite study was reported by Davies (1994), this report presents additional data on thawed samples at higher stresses.

A high explosive test series in granite was planned to evaluate codes and gauge emplacement techniques for HYDROPLUS. Consequently, two granites, a SHIST granite, and Sierra White Granite and granite grout were characterized.

## **1.2 DOCUMENT ROADMAP.**

This document is divided into nine major sections. The experimental configurations and the analysis techniques are presented in Section 2 for the experiments performed in this study. The experimental data are detailed in Sections 3 through 9. Within these sections a detailed description of each geological material and its derived material properties (Hugoniot points and loading and release curves) data are presented. A discussion of each individual set of results is also given in these sections. All recorded waveforms are presented in Appendix A by material type.

## **SECTION 2**

### **EXPERIMENTAL AND ANALYTICAL TECHNIQUES**

This section presents descriptions of the experimental techniques used to measure the material properties of the rocks and grouts evaluated in this program and details the analytic techniques used to interpret the measured data. The nondestructive evaluation (NDE) techniques of the test samples are detailed in Section 2.1. Gas gun techniques used to measure the Hugoniot are presented in Section 2.2 which specifies the basic experimental configurations, the material properties of the impactors and buffers, and the instrumentation techniques used in these tests. Two basic instrumentation techniques, in-situ stress gauges and interferometry, were used. The measurement techniques and their associated steady state analysis techniques are presented. Section 2.3 describes the analysis techniques used to analyze the wave profiles measured by the in-situ stress gauges and the interferometer. When non-standard experimental configurations are used they are detailed in the specific results section.

#### **2.1 SAMPLE CHARACTERIZATION.**

Nondestructive evaluation (NDE) of samples prior to testing was limited to bulk density measurements and ultrasonic longitudinal velocity measurements. All of these measurements were taken at ambient temperature. Sample water content was maintained during handling and measurements. Tabulations of sample thickness, density, and longitudinal velocity for each material are contained in the individual material sections. Average and standard deviation (std. dev.) values for density and longitudinal velocity are also given for each material. The individual sample thicknesses listed are an average of five measurements taken on each as-received sample. This "average" thickness differs from the "center" thickness listed in the "shot configuration data" tables in the individual material "test results" sections. The "center" thickness may also differ from the "average" thickness because some samples were lapped to achieve the required flatness after the initial measurements were made.

Prepared samples were nominally 5- or 10-mm thick and 48- or 64-mm in diameter. The dimensions of each sample were determined by multiple micrometer measurements. The accuracy of the sample thickness measurements is one percent.

Bulk densities were determined from sample weight and volume measurements. Two techniques for measuring sample volume were used: geometric and immersion. The geometric method was based on sample thickness and diameter measurements. The immersion method employed Archimedes principle of buoyancy where the samples were immersed in water and the buoyant force ( $F_b$ ) was measured. Since the volume of the sample is equal to the volume of the water displaced, the volume can be determined from the buoyant force and density of water ( $\rho_w$ ) by:

$$\text{Sample volume} = \frac{F_b}{\rho_w} \quad (2.1)$$

For dry samples, the geometric method was used for density measurement. The immersion method was used on saturated samples which were not perfect cylinders (e.g., chipped or pitted edges). Pits or voids in the edges of samples would yield a low density measurement if the geometric method was used. The accuracy of these density measurements is  $\pm 1$  percent.

Ultrasonic velocity measurements were made to check sample integrity and to estimate shock impedances for experiment design. Sample longitudinal ultrasonic velocity measurements were taken in the through-the-thickness direction by measuring the transit time through the sample of a pulse generated by a 19.1-mm diameter 10-MHz quartz crystal transducer clamped to one face of a disk and detected by a similar transducer on the opposite face. The coupling medium between the transducers and sample was water. The accuracy of the ultrasonic measurements is  $\pm 5$  percent.

## 2.2 GAS GUN TECHNIQUES.

Plane shock wave experiments were conducted on the 105-mm diameter, single stage, light gas gun at the DNA Material Response Impact Facility at Kirtland AFB, New Mexico. Stress wave propagation characteristics in geologic materials were measured using plate impact techniques (Lee, 1989). These transmitted wave experiments provided wave propagation and Hugoniot data for the materials. At lower stresses, in-material gauge techniques were used while an interferometric technique provided Hugoniot data above 6 GPa. The materials were examined in "as-received" water content states at ambient temperatures.

The samples were mounted at the end of the gas gun in a sealed target holder. Sample and impactor were carefully aligned prior to each shot to provide planar impact. Tilt between impactor and



sample, as determined by tilt pins, was generally less than 1.0 marad. Precisely spaced shorting pins were placed near the muzzle of the gun to measure projectile velocity to an accuracy of  $\pm 0.5$  percent. Signals were generated when the pins were shorted by projectile contact. These data signals, and the data signals generated by the in-situ stress gauges and interferometry, were recorded on Tektronix 7612D and LeCroy 9450 digitizers. The target chamber and barrel of the gun were evacuated to below 0.1 mtorr prior to each shot to eliminate air cushion effects. Thin plate impactors of either tungsten carbide (WC) (Karnes, Private Communication), 4340 steel (Butcher 1964), or 6061-T6 aluminum (Christman 1971, and Marsh 1979) were used to generate well defined stress waves in the test samples. The Hugoniot for these materials are listed in Table 2-1.

Table 2-1. Impactor and buffer materials (Hugoniot).

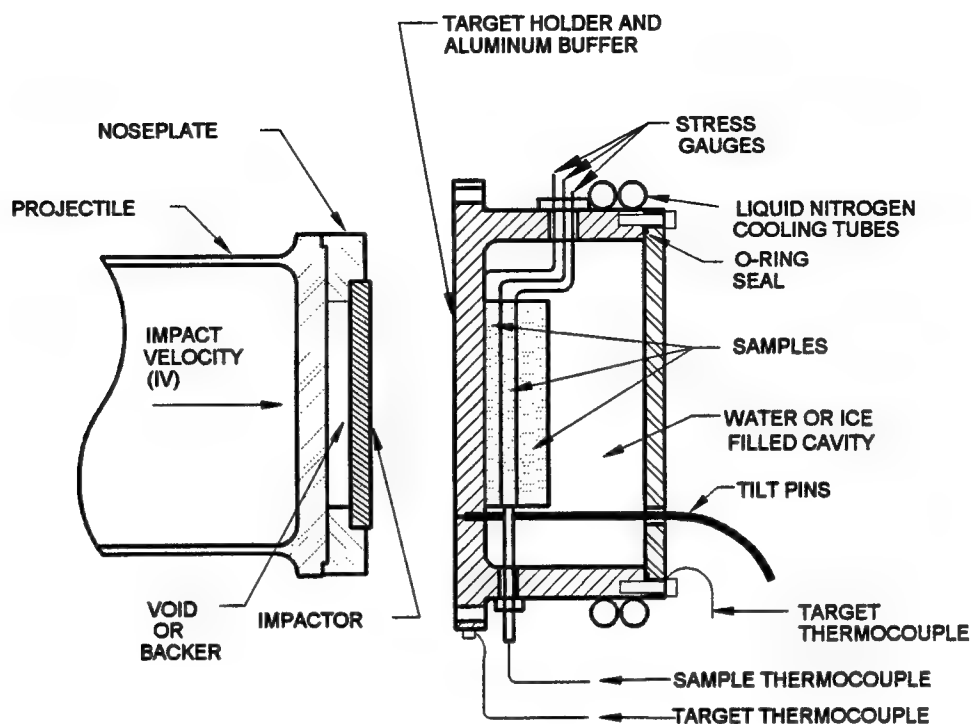
Hugoniot Coefficients*					
A	B	C	D	Initial Density (g/cm <sup>3</sup> ) $\pm 1\%$	Range (GPa)
6061-T6 Al (Christman, 1971 and Marsh, 1979)					
0	17.21	0	0	2.703	0.0 - 0.6
0.1	14.04	3.77	0	2.703	0.6 - 16.0
0	14.46	3.62	0	2.703	7.0 - 107.8
Tungsten Carbide (WC)(Karnes, Private Communication)					
0	102.5	0	0	14.85	0.0 - 3.0
-0.21	106.22	-95.69	124.7	14.85	3.0 - 27.5
4340 Steel, Rc54 Hardness (Butcher, 1964)					
0	455	0	0	7.85	0.0 - 2.7
2.56	415.84	0	0	7.85	2.7 - 6.2
*Stress ( GPa ) = A + Bu <sub>p</sub> + Cu <sub>p</sub> <sup>2</sup> + Du <sub>p</sub> <sup>3</sup>					

### 2.2.1 Lagrangian Stress Measurements.

The experimental configuration is shown in Figure 2-1. The impactor was contained in an aluminum nose plate and mounted on the front of the projectile. When necessary, low density (0.27 g/cm<sup>3</sup>) carbon foam or PMMA backed the impactor to keep it from bowing as it accelerated down the barrel.

The target holders in which the geological samples were mounted consisted of a vacuum tight aluminum housing sealed to prevent the water from evaporating or subliming in the vacuum, (Figure 2.1). In some instances the front face of the aluminum housing was bored out so that the

projectile impacted the geological sample directly. The four tilt pins were equally spaced around the perimeter of the front surface of the target holder.



Configuration used to maintain water saturation.

Figure 2-1. Rock equation of state experimental arrangement with Lagrangian stress gauges.

Dynasen model C300-50--EKRT carbon gauges (Lee 1981) were used to make Lagrangian stress measurements at three depths in the rock as shown in Figure 2-1. The carbon gauge packages consisted of a 0.064 mm thick carbon gauge bonded between two 0.013-mm thick sheets of teflon with Hysol 2038 epoxy. This resulted in a total gauge package thickness that ranged from 0.10 to 0.11 mm and a gauge package diameter equal to that of the sample. Gauge packages were bonded to samples and aluminum buffer with super glue. Super glue was used because it adheres well to wet and frozen materials. Material thicknesses were measured before and after each assembly step. A press was used in each of these processes to ensure thin glue bonds. Bonds were generally less than 0.01-mm thick. Target holders were then filled with water to maintain sample saturation as required.

### 2.2.2 VISAR Measurements.

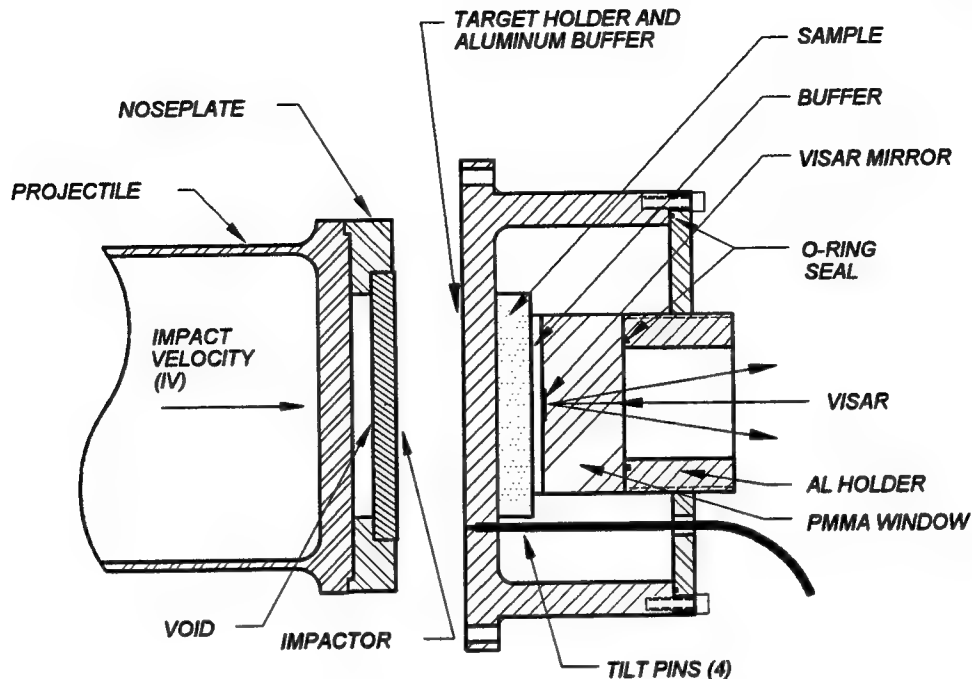
Particle velocity measurements were made on the high pressure EOS experiments (above 6.0 GPa) using a Velocity Interferometer System for Any Reflector (VISAR)(Barker 1972, and Smith 1989).

The particle velocity histories were recorded to determine the material EOS and to support shock response modeling efforts. The VISAR system (Smith 1989) had a double delay leg that enabled acquisition of two independent velocity measurements (identified as Leg 1 and Leg 2 throughout this report).

The target configuration for VISAR experiments is shown in Figure 2-2. The target holders in which the geological samples were mounted consisted of a vacuum tight aluminum housing sealed to prevent water from evaporating or subliming in the vacuum (Figure 2-2). In some instances when water content was not an issue the front face of the aluminum housing was bored out so that the projectile impacted the geological sample directly. A diffuse mirror was applied directly to the surface of a window of either PMMA (Barker 1970) or lithium fluoride (LiF)(Wise 1986). The LiF windows were bonded directly to the sample. When PMMA was used, a thin (0.75 mm) buffer of PMMA was located between the sample and window. The PMMA window assemblies were used for the lower impedance materials such as the tuffs and grouts, whereas LiF was used for the higher impedance rocks. The PMMA buffer served to smooth out stress waves from heterogeneous materials. The VISAR measured the change in particle velocity induced by the stress wave propagation across the sample-LiF window interface or in the PMMA window. The sample-window assembly was placed into the target as shown in Figure 2-2 and the sample bonded directly to the aluminum buffer. A press was used in the bonding process to achieve a thin glue bond which was typically less than 0.01-mm thick. Thickness measurements were made before and after each gluing step to determine sample and bond thickness.

### **2.3 ANALYSIS TECHNIQUE.**

This section provides a description of the analysis techniques that are used to translate the measured stress and particle velocity time profiles and shock velocities into equation of state and constitutive relationship parameters.



Configuration used to maintain water saturation.

Figure 2-2. Equation of state experimental arrangement for VISAR particle velocity measurement.

### 2.3.1 Steady State Analysis of Lagrangian Stress Gauge Data.

Figure 2-3 illustrates the Lagrangian stress gauge experiments performed for the HYDROPLUS program. It shows a distance-time plot of the propagation of the stress wave generated in the impactor and target on impact, the stress wave time histories that would be measured by in-situ gauges at three locations in the sample, and identifies the buffer/sample interface conditions in the stress-particle velocity plane. This illustration has assumed that:

- (a) the impactor and buffer are the same material,
- (b) The impact generates a two wave system in both the impactor and buffer (i.e., there is an elastic precursor propagating in the impactor/buffer material), and
- (c) the sample Hugoniot has an inflection (i.e., there is a precursor propagating in the sample material due to either yielding or a phase change).

In this case, three wave fronts propagate in the sample as illustrated in Figure 2-3 and would be measured by the in-situ carbon gauges.

Since the raw data are in terms of stress vs. time at fixed Lagrangian positions, two flow parameters, stress ( $\sigma$ ) and shock velocity ( $U_s$ ), are derived directly from the data. Other Hugoniot parameters such as particle velocity ( $u$ ), relative density ( $\rho/\rho_0$ ), or energy ( $E$ ) can be derived from steady waves using the Rankine-Hugoniot relationships for conservation of momentum, mass, and energy:

$$\sigma - \sigma_0 = \rho_0 (U_s - u_0) (u - u_0) \quad (2.2)$$

$$\rho/\rho_0 = (U_s - u_0) / (U_s - u) \quad (2.3)$$

$$E - E_0 = \Delta E = \frac{1}{2} (\sigma + \sigma_0) \left( \frac{1}{\rho_0} - \frac{1}{\rho} \right) \quad (2.4)$$

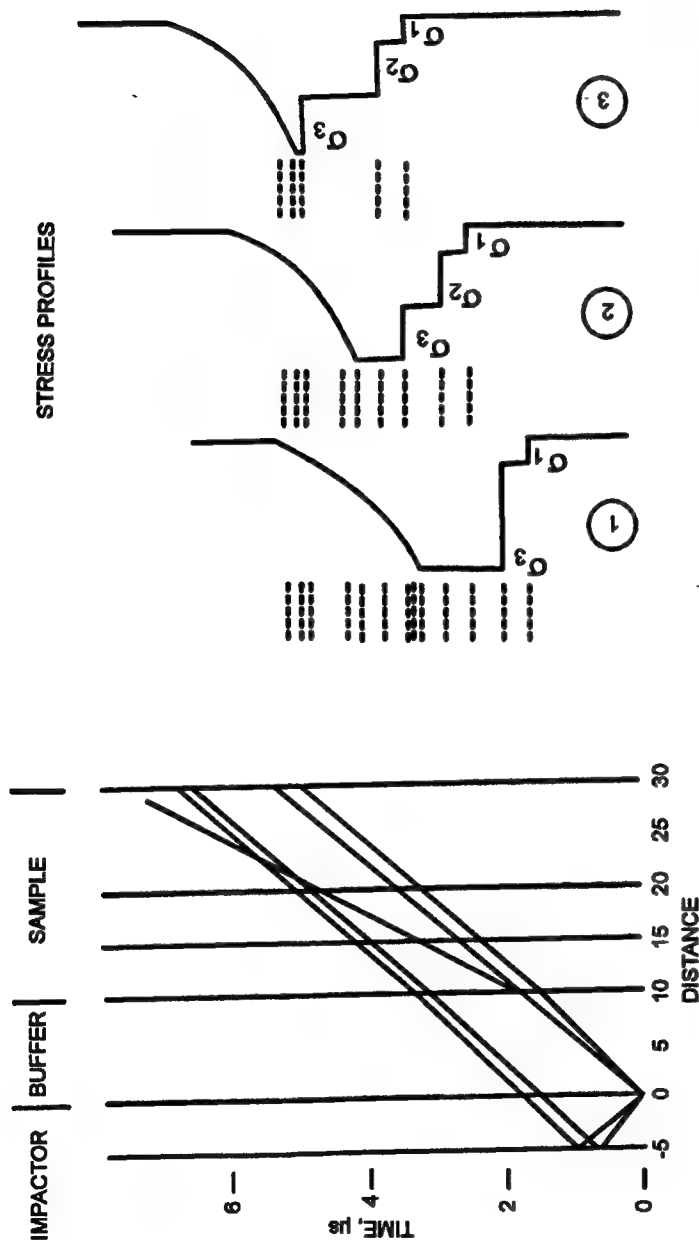
where subscript 0 denotes the state ahead of the shockwave.

For a single shock traveling into undisturbed material with an initial density ( $\rho_0$ ), these equations reduce to:

$$\Delta \sigma = \rho_0 U_s u, \quad \rho/\rho_0 = \frac{U_s}{U_s - u}, \quad \Delta E = \frac{1}{2} u^2 \quad (2.5)$$

The measured stress profiles also provide significant information on the unloading of the sample. In the illustration of Figure 2-3, the stress profiles show the duration of the peak stress decreasing with increasing propagation distance. Measuring the onset of unloading defines the velocity of the leading edge of the rarefaction fan. Only this leading edge is shown in the ray traces of the distance-time plot in Figure 2-3. The shape of the unloading portion of the stress profiles is a function of the unloading characteristics of both the buffer and the sample. The Lagrangian analysis described in Section 2.3.3 defines the sample unloading path.

When a complete, ideal set of data is recorded, the data over-define a point on the Hugoniot. Four estimates of the Hugoniot conditions can be determined from the measurements as illustrated graphically in Figure 2-4 and summarized in Table 2-2. Cases 1 and 3 assume a steady wave (i.e., the amplitude of the initial shock front is invariant with propagation distance). Case 2 only requires measurement of the stress at the buffer/sample interface. Case 4 uses a Lagrangian analysis which is described in detail in Section 2.3.3.



LEGEND	
$\sigma_1$	= TRANSMITTED BUFFER PRECURSOR ( $P_b$ )
$\sigma_2$	= SAMPLE PRECURSOR ( $P_s$ )
$\sigma_3$	= SAMPLE HUGONIOT DATA POINT
(A)	= RAYLEIGH LINE DEFINED BY $P_b$ SHOCK VELOCITY
(B)	= RAYLEIGH LINE DEFINED BY $P_s$ SHOCK VELOCITY
(C)	= RAYLEIGH LINE DEFINED BY MAIN SHOCK VELOCITY

Figure 2-3. The derivation of a Hugoniot point from in-situ stress gauges using steady state assumptions.

DAVIES21.CDR-C

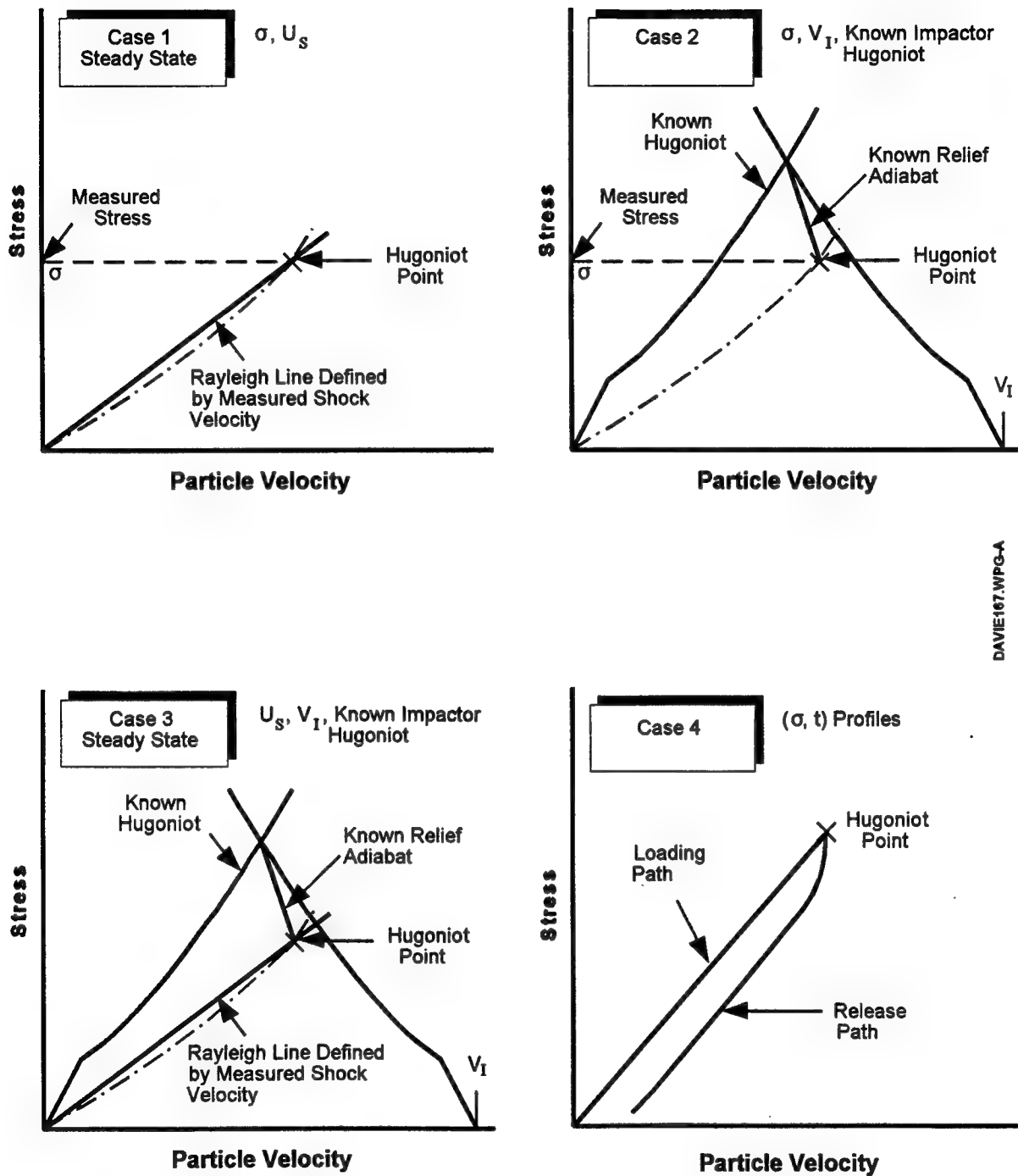


Figure 2-4. The Lagrangian stress configuration allows for four estimates of a Hugoniot point.

Table 2-2. Four estimates of the Hugoniot point are derivable from the Lagrangian stress gauge measurements.

Case No.	Data	Estimated Accuracy	Comments
Case 1	$\sigma, U_s$	$\sigma = \pm 5.0\%$ $u_p = \pm 7.5\%$ $U_s = \pm 2.5\%$	Primary technique if wave is steady.
Case 2	$\sigma, V_1$	$\sigma = \pm 5.0\%$ $u_p = \pm 10.0\%$	Does not require a steady wave.
Case 3	$U_s, V_1$	$\sigma = \pm 10.0\%$ $u_p = \pm 10.0\%$ $U_s = \pm 2.5\%$	Least accurate.
Case 4	$(\sigma, \tau)$ profiles	$\sigma = \pm 2.5\%$ $u_p = \pm 5.0\%$ $\rho/\rho_0 = \pm 7.5\%$	Equivalent to Case 1 for steady waves.

In general, several of these estimates are derived for each shot. The variations in material response define which combination of the techniques is used. The specific analyses used are defined in each results section. The best estimate of the Hugoniot conditions is obtained by averaging these several estimates in the  $U_s - u_p$  plane and then calculating the other flow variables using the Rankine-Hugoniot relationships.

**Case 1: Measurement of Stress and Shock Velocity.** Measurement of the stress amplitude and shock velocity of a shock transition is adequate to define a point on the Hugoniot. No other knowledge is required. Typically, the accuracy of the stress gauge measurements is  $\pm 5.0$  percent and the shock velocity  $\pm 2.5$  percent. (The accuracy of the carbon gauge is amplitude dependent.)

Thus, the accuracy of the Hugoniot point is  $\pm 5.0$  percent in stress and  $\pm 7.5$  percent in particle velocity. (Note that it is not valid to define the uncertainty limits of a Hugoniot point by a box. The actual uncertainty bands lie along a diagonal of the box and the limit points still lie close to the actual Hugoniot.) In practice, the measured waveforms are not ideal square waves and their interpretation depends upon judgements based upon a knowledge of the experiment, the gauge response, and signatures typical of various classes of material (e.g., rate dependent or porous). The actual waveforms are not an ideal step function for several reasons:



1. the imbedded gauge package has a different impedance than its host,
2. tilt,
3. the impactor impacts an aluminum buffer, not the test sample, and
4. the test material may exhibit time dependent properties.

Gauge response: The imbedded gauge package will ring-up to the incident stress wave amplitude as shown in Figure 2-5. The measured gauge stress history, (2), shows a rounded rise which is more pronounced the larger the mismatch in impedance between the gauge and the host material.

The rise time of the transmitted wave profile, (3), is also degraded by the gauge package, however not as severely as the measured stress profile, (2). The second gauge package modifies the transmitted wave profile, (4), in a similar manner, thus further increasing the distortion.

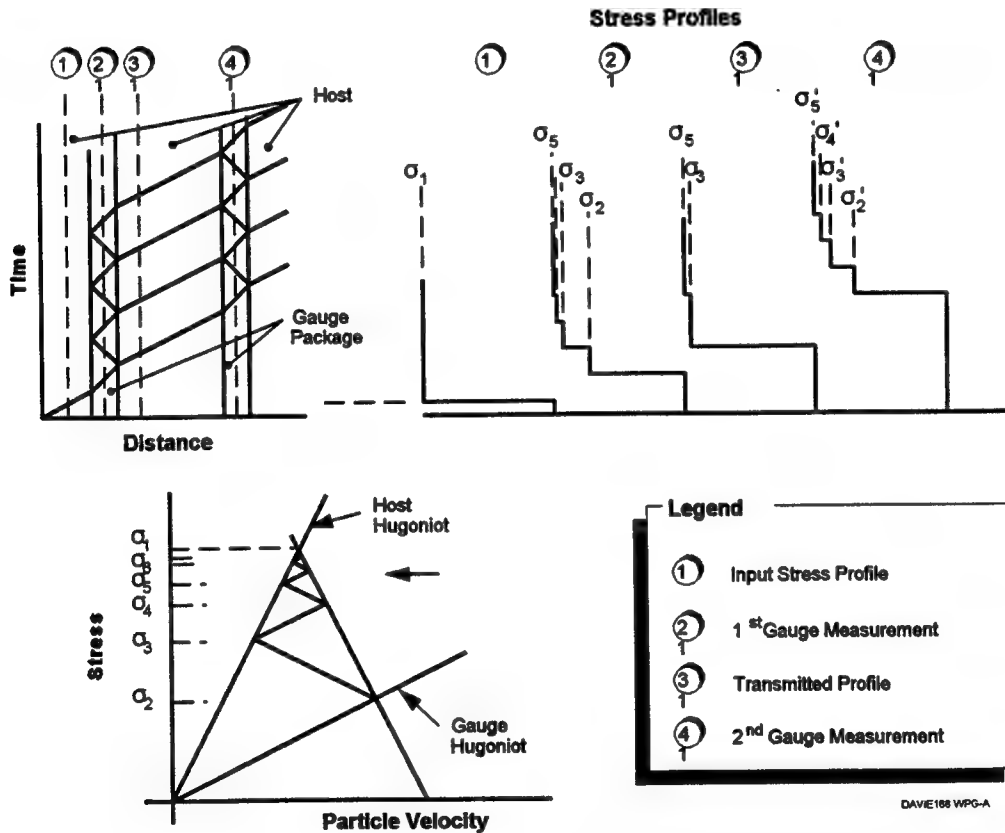


Figure 2-5. Stress wave reverberation in gauge packages.

The first gauge profile,  $\sigma_{G1}$ , can be approximated by:

$$\sigma_{G1} = \sigma_1 e^{c^n \cdot \ln A} \quad (2.6)$$

where:

- $\sigma$  = the incident stress
- $A$  =  $2G(R+G)^{-1}$
- $C$  =  $(R-G)(R+G)^{-1}$
- $R$  = shock impedance of host material
- $G$  = shock impedance of the gauge package
- $n$  =  $t/t_G$

and  $t_G$  = the characteristic transit time of the gauge package.

Figure 2-6 compares this approximation to the impedance mismatch calculation performed using realistic linear impedances for the gauge package and a hardrock host material. This approximation is less accurate as the impedance mismatch increases.

The stress profile transmitted into the host material is approximated by:

$$\sigma_{T1} = \sigma_1 \cdot e^{c^n \cdot \ln B} \quad (2.7)$$

where

$$B = 2R(R+G)^{-1} \quad (2.8)$$

Figure 2-7 compares this approximation to the impedance mismatch calculations. Finally, the second gauge profile is approximated by:

$$\sigma_{G2} = \sigma_{T1} \cdot \sigma_{G1} \quad (2.9)$$

Figure 2-8 compares this approximation to the more rigorous impedance mismatch calculations.

To summarize, the impedance mismatch between the gauge package and the host material results in a distortion of the propagating stress wave profile (increased rise time and rounding of the pulse).

Analytic corrections can be applied to the measured wave profile to correct for this distortion

(accurate to about 1 percent). The gauge rings up to the incident stress value in less than four transit times ( $4\tau$ ) of the gauge package. Thus, the best estimate of the Hugoniot stress amplitude is obtained by measuring the gauge output at least four transit times ( $4\tau$ ) after shock arrival. Such an estimate does not require a gauge correction.

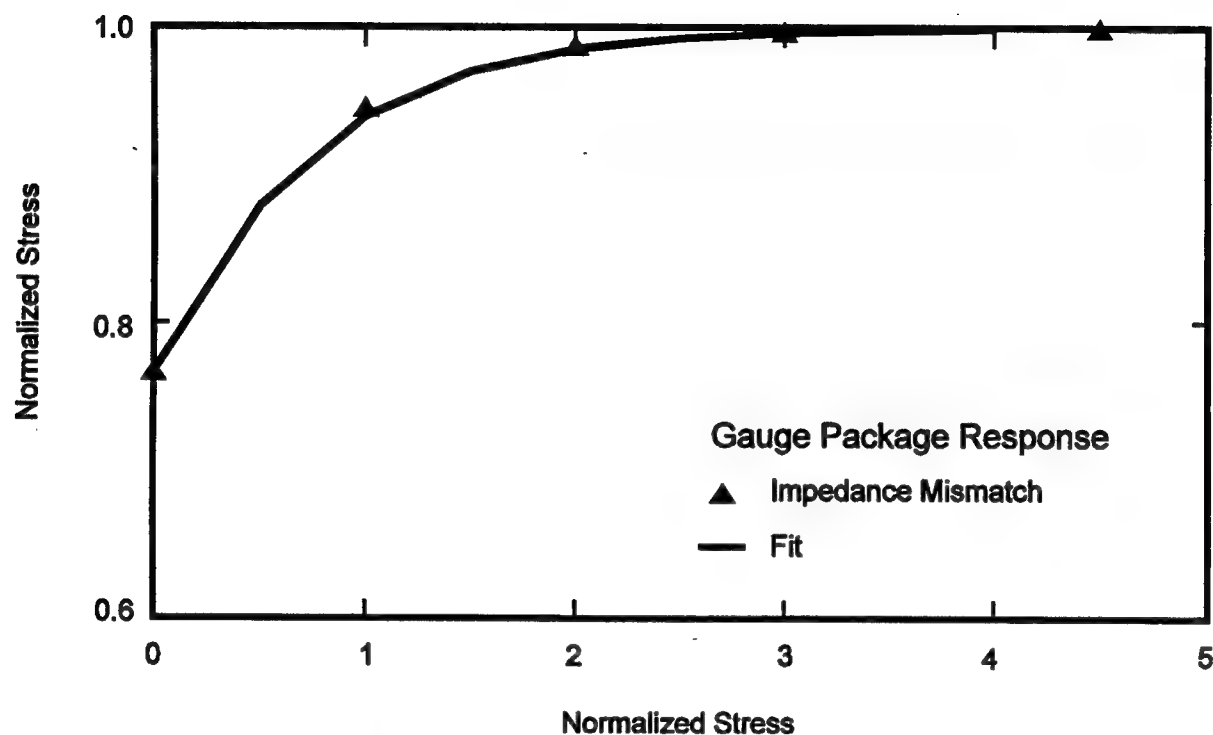


Figure 2-6. Comparison of an analytic approximation and an impedance match solution of an in-situ gauge response.

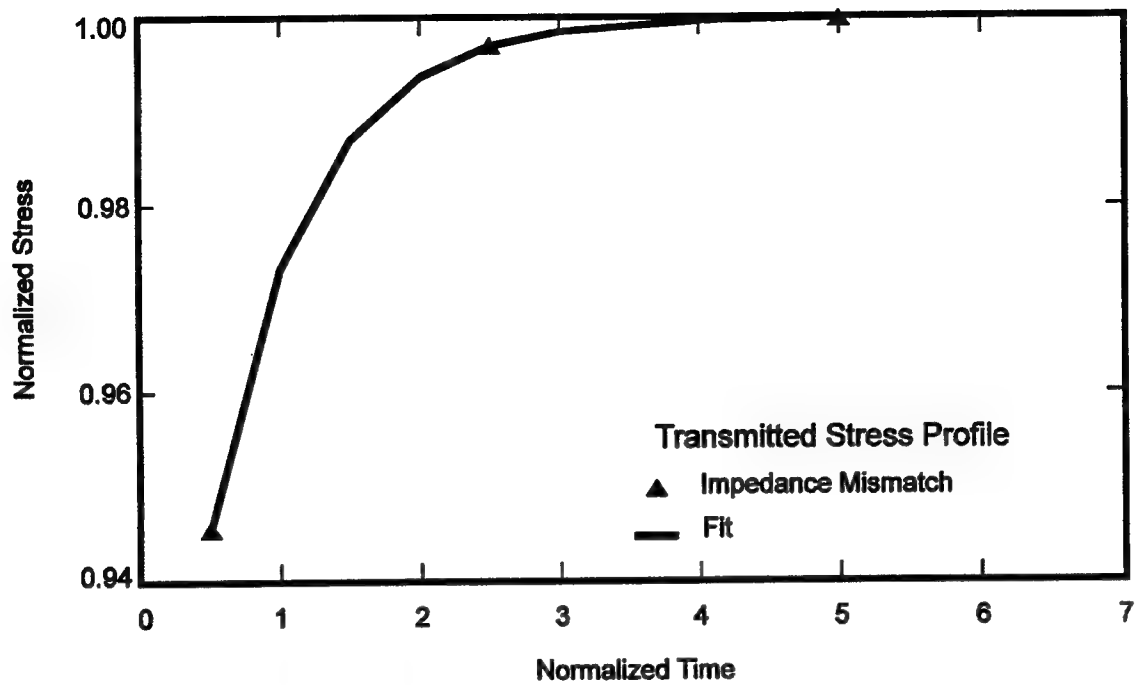


Figure 2-7. Comparison of an analytic approximation and an impedance mismatch calculation of the stress profile transmitted through a gauge package.

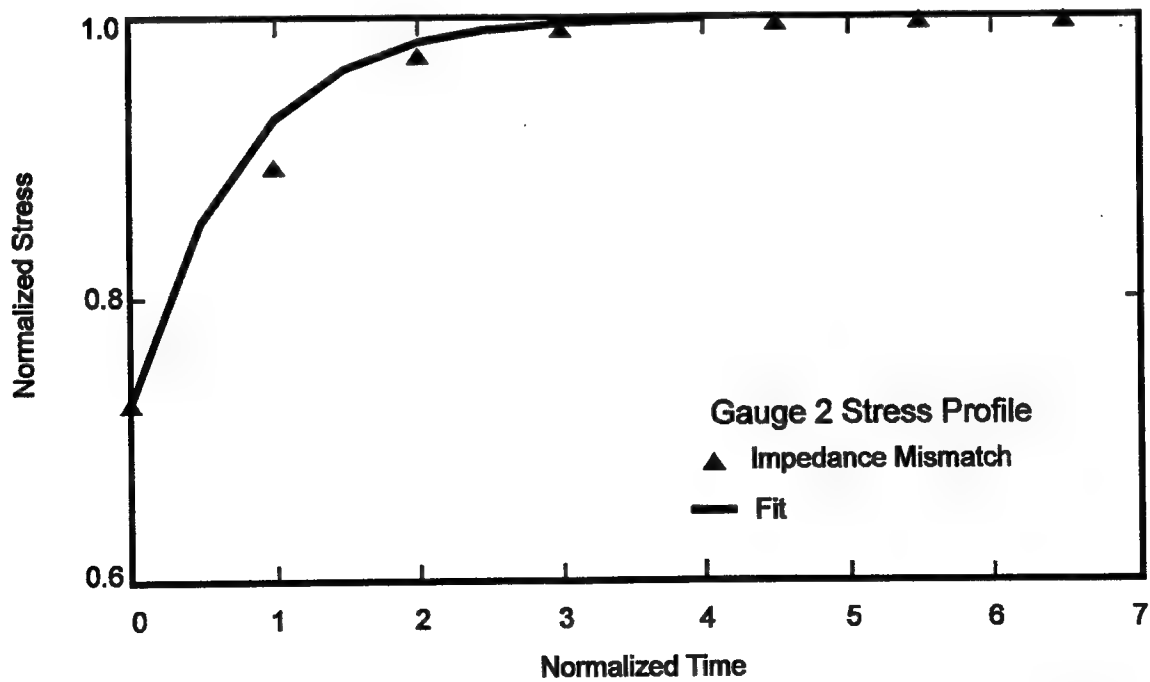


Figure 2-8. Comparison of an analytic approximation and an impedance mismatch solution for a second gauge package.

Tilt: These experiments are design to minimize tilt between the impactor and target at impact. In general, the tilt is less than  $10^{-3}$  radians. This translates into a gauge rise time of  $0.1 \mu\text{sec}$  at an impact velocity of  $0.10 \text{ km/s}$ . Tilt is measured on each shot. If the loading is a ramp rather than a shock (a discontinuity), the loading is isentropic and the final state achieved does not lie on the Hugoniot (the Hugoniot differs from an isentrope in the third order). A general rule-of-thumb is to discard the data if the incident rise time is greater than  $0.25 \mu\text{s}$ .

Aluminum buffer: An aluminum buffer, which is an integral part of the sample container, fronts the test samples. The sample container is necessary to maintain the in-situ water content of the HYDROPLUS test samples in the vacuum environment of the gas gun. For impacts that generate stresses greater than  $0.6 \text{ GPa}$  and less than  $11.5 \text{ GPa}$ , a two-wave structure is generated in the aluminum. Consequently, the test samples are not loaded by a single shock and the "Hugoniot conditions" derived from these experiments actually lie on a Hugoniot centered on the precursor conditions. The difference between the Hugoniot centered at ambient conditions and the Hugoniot centered at the precursor conditions is thought to be small, but has not been quantified. The precursor conditions in the aluminum are estimated as  $\sigma = \text{HEL}$ ,  $0.57 \text{ GPa}$ ,  $U_s = 6.368 \text{ km/s}$ ,  $u_p = 0.033 \text{ km/s}$ ,  $\rho/\rho = 1.005$ . Aluminum is usually of higher impedance than the test material. In the stress-relative density plane Hugoniots centered at different density are usually just displaced from each other by the density difference. Thus, the errors in using the measured recentered Hugoniot as the ambient Hugoniot are small, particularly at high stresses (greater than  $4 \text{ GPa}$ ). The two-wave structure generated in the aluminum which is smeared by the gauge response adds to the apparent rise time of the in-situ stress gauges. The measured stress release profiles are dominated by the unloading characteristics of the aluminum flyer and buffer.

Time dependent material properties: The measured stress wave profile will differ from ideal if the material properties are time dependent. For example, the measured input profile of a strain rate dependent material may exhibit an initial peak and a decay to an equilibrium value. For profiles measured within the material strain rate dependence will result in a steady shock followed by a gradual rise to equilibrium conditions. For the HYDROPLUS experiments an attempt has been made to define the "equilibrium state" from each measured wave profile. This is usually compatible with measuring the stress wave amplitude at a time of greater than  $\sim 4\tau$  (gauge package response).

Determination of stress amplitude and shock velocity. Figure 2-9 shows a typical set of measured waveforms and indicates the procedure for determining the stress amplitude and shock velocity. The gauge packages are 0.11-mm thick; thus, a single transit time through the gauge is 36 ns and  $4\tau$  is 0.15  $\mu$ s. The stress amplitude at a time greater than  $4\tau$  is measured on gauges 1 and 2. The actual "Hugoniot stress" is a judgement that is based upon experience but can, in general, be defined as the first plateau. Consistency in the interpretation of the gauge records from shot to shot is important. The best estimate of the Hugoniot stress is the average of the two gauge readings if the stress pulses are flat topped. The shock velocity is determined by the measurement of the transit time between the two gauges. This transit time is measured at half the Hugoniot stress amplitude on each stress profile.

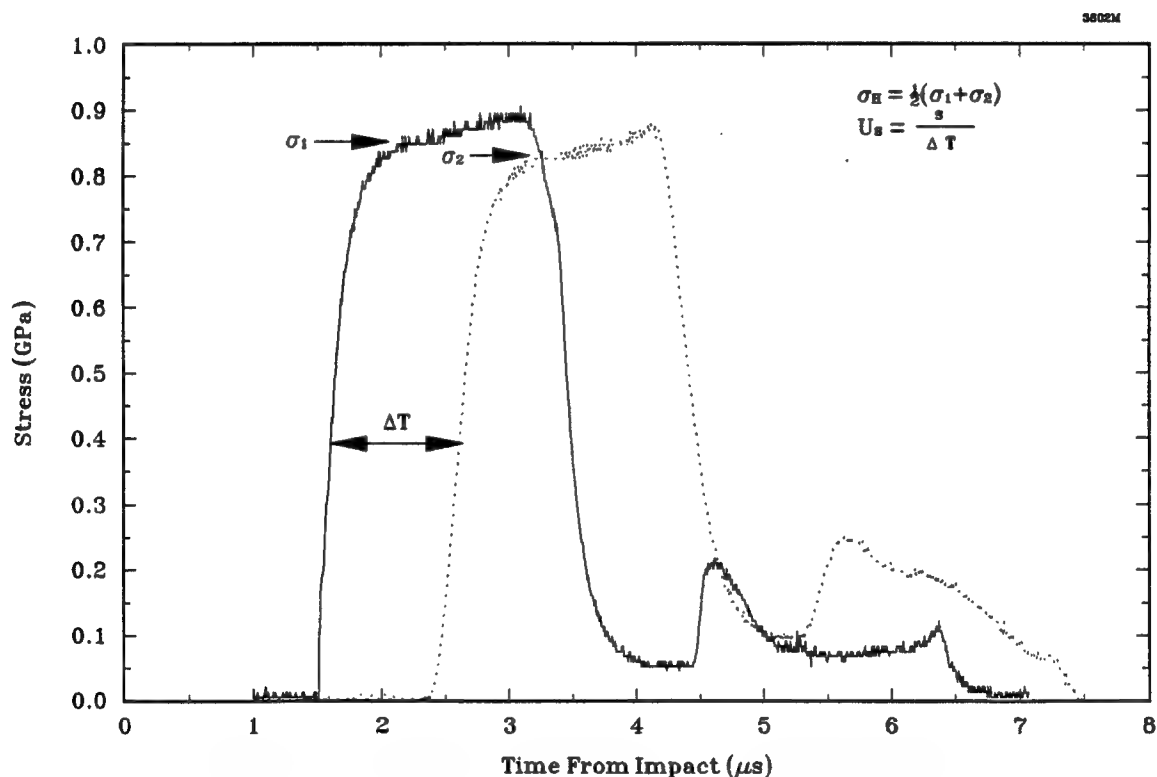


Figure 2-9. Example of interpretation of stress gauge data.

Case 2: Measurement of Impact Velocity and Stress at Buffer/Sample Interface. In Case 2, a point on the Hugoniot is defined by measurement of the amplitude of the stress wave at the buffer/sample interface, the impact velocity ( $V_I$ ), and knowledge of the Hugoniot and relief adiabat of the impactor and buffer. Figure 2-4 illustrates the case where the impactor and buffer are the same material. This measurement technique only requires gauge 1 data and, thus, does not require a steady wave assumption. Unless there is a gauge failure, this estimate of the Hugoniot can always be obtained. The discussion in Section 2.3.1 of the factors controlling the shape of the measured stress profile are equally applicable here. The accuracy of the derived Hugoniot data are also dependent upon the accuracy of the impact velocity ( $\pm 0.5$  percent), the impactor Hugoniot, and the impactor relief adiabat. The accuracy of the stress amplitude is typically  $\pm 5.0$  percent while the location of the impactor Hugoniot and relief adiabat is known, at best, to  $\pm 5$  percent. Thus, the accuracy of the Hugoniot data points are  $\pm 5.0$  percent in stress and  $\pm 10$  percent in particle velocity.

Case 3: Measurement of Sample Shock Velocity and Impact Velocity. In Case 3, a point on the Hugoniot is derived from the measurement of shock velocity in the sample, impact velocity, and the known Hugoniot of the impactor and buffer. The technique invokes the steady wave assumption. Again, Figure 2-4 shows the case where the impactor and buffer are the same material.

As discussed in Section 2.3.1, Case 1, the shock velocity is determined by measuring the transit time of the propagated waves at half amplitude. If the material under consideration generates a multiwave structure (either an elastic precursor or a phase change) then the propagation velocity of each wave front must be measured. Note that if a two-wave structure is generated in the test material, gauge-1 measures conditions on the Hugoniot centered at ambient conditions and gauge-2 measures conditions on a Hugoniot that is recentered on the precursor conditions.

The location of the impactor Hugoniot and relief adiabat is known, at best, to  $\pm 5$  percent and the slope of the Rayleigh line is measured to  $\pm 2.5$  percent. This is the least accurate of the Hugoniot estimates. The uncertainties in the impact Hugoniot and measured shock velocity compound to about  $\pm 10$  percent in both stress and particle velocity.

Case 4: Lagrangian Analysis: The stress histories measured by the in-situ stress gauges are used to calculate histories of particle velocities, specific volume and other related variables in a one-dimensional flow using the Lagrangian analysis method of Seaman. This analysis technique is

discussed in detail in Section 2.3.3. These histories are generated by a stepwise integration of the conservation laws of mass, momentum, and energy. Thus, for a steep fronted stress wave (a shock) the loading path is the Rayleigh line. When the profile has a large rise time (i.e., a ramp) then the loading is the isentrope and the end point is off the Hugoniot. However, the difference between the Hugoniot and the isentrope centered at the same conditions is of the third order (i.e., if Hugoniot

$$\sigma - \sigma_0 = \sum_{n=1}^3 A_n (\nu_0 - \nu^n) \quad (2.10)$$

and adiabat

$$\sigma - \sigma_0 = \sum_{n=1}^3 B_n (\nu_0 - \nu^n) \quad (2.11)$$

then

$$A_1 = B_1, \quad A_2 = B_2 \text{ but } A_3 \neq B_3, \text{ etc.} \quad (2-12)$$

so the error is small in assuming that the end point represents the Hugoniot) particularly at the modest stresses associated with the HYDROPLUS Lagrangian stress measurements.

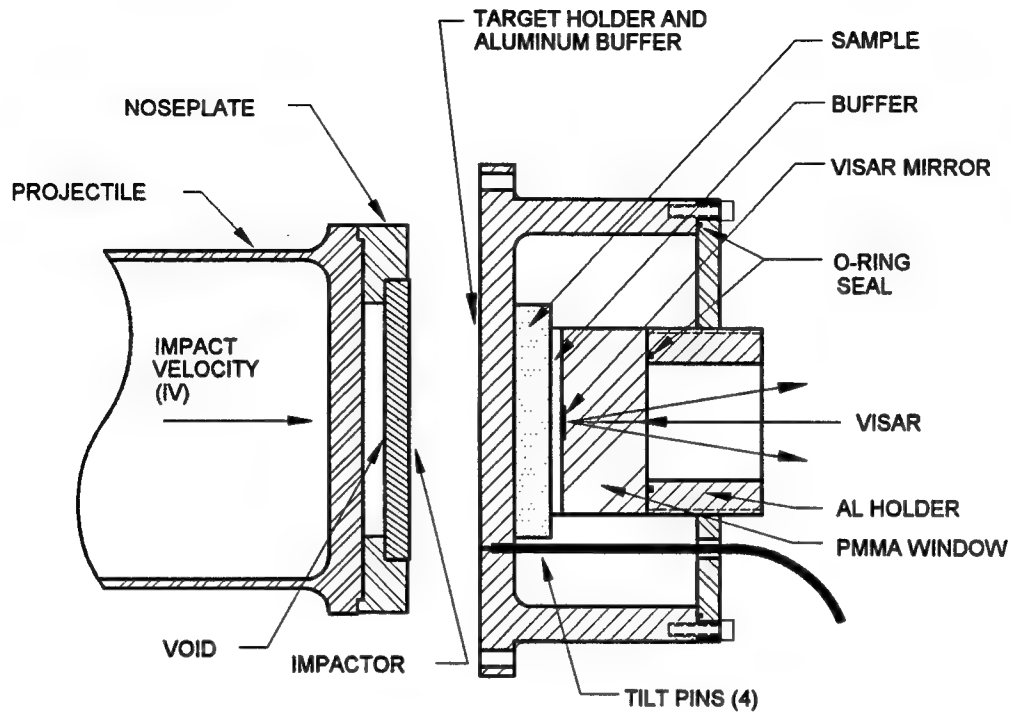
Evaluation of the calculated loading path can identify precursors and the validity of assuming that the end point lies on the Hugoniot. Loading paths that are not reasonable approximations to a straight line(s) are not used to define Hugoniot states. Particle velocity and specific volumes derived from the stress profiles have an estimated accuracy of  $\pm 5$  percent and  $\pm 10$  percent, respectively. These uncertainties are discussed in more detail in Section 2.3.3.

### 2.3.2 Steady State Analysis of VISAR Particle Velocity Measurements.

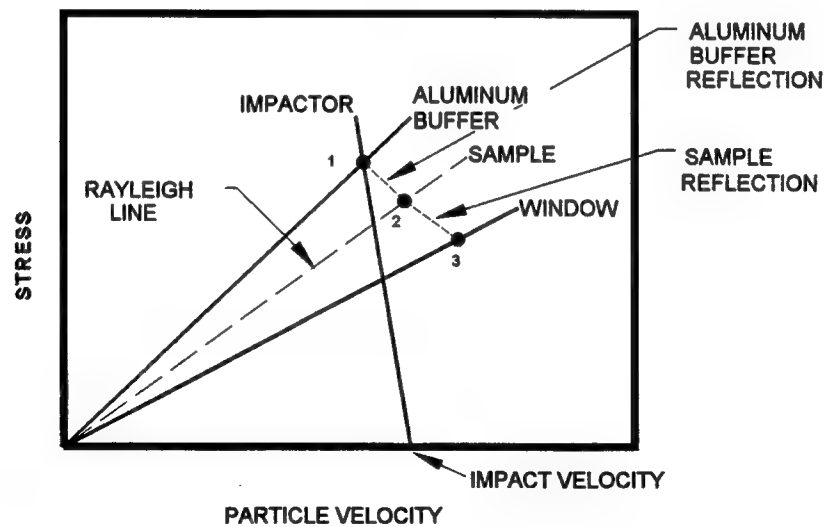
The target configuration for VISAR experiments is shown in Figure 2-10(a). The VISAR measures the change in particle velocity induced by the stress wave propagation across the sample-LiF window interface or in the PMMA window.

For VISAR experiments, shock velocities are derived from the measurements of shock transit time through the sample. The transit time is derived from tilt pin data which defines impact time and the arrival time of the half amplitude of the stress wave at the VISAR mirror. Hugoniot data are derived





(a) Experimental configuration.



(b) Shock response diagram.

Figure 2-10. Equation of state experimental arrangement for VISAR particle velocity measurement.

from the measured shock velocity and sample density using standard impedance match techniques and the Hugoniot relationships. The shock response diagram in Figure 2-10(b) shows the stress and particle velocity states in the materials for a given impact velocity. The Hugoniots have been approximated by linear shock impedances of the respective materials. A reflection of the 6061-T6 aluminum Hugoniot was used for unloading of aluminum into the sample. The equilibrium impact stress in the aluminum target-holder buffer is represented by Point 1, and the stress and particle velocity states transmitted into the sample are represented by Point 2. The slope of the Rayleigh Line is determined by the measured shock velocity and a Hugoniot point is defined as the intersection between the sample Rayleigh line and the unloading path of the 6061-T6 aluminum buffer. The states transmitted into the window and measured with the VISAR interferometer are represented by Point 3. The VISAR particle velocity profile can be compared to hydrocode calculated stress and particle velocity profiles at Point 3 to check validity of data.

### 2.3.3 Lagrangian Analysis.

The stress histories measured by the in-situ stress gauges are used to calculate histories of particle velocities, specific volume, and other relatable variables in a one-dimensional flow using the nonsteady Lagrangian analysis method of Seaman (Seaman 1987). The computed stress-particle velocity and stress-specific volume paths can be extremely useful in developing equations of state or constitutive relations. The loading portions generally follow Rayleigh lines and may reveal precursors and rate dependence. The unloading paths can usually be taken as adiabats and therefore as curves on the equation of state surface after the presence of the deviator stress has been accounted for. Seaman's Lagrangian analysis method is derived from earlier work by Fowles and Williams (Fowles 1970) and Grady (Grady 1973). The basic equations upon which the Lagrangian analysis techniques rest are the conservation laws of mass, momentum, and energy. In Lagrangian coordinates, these relations are:

$$\left( \frac{\partial v}{\partial t} \right)_h - \frac{1}{\rho_0} \left( \frac{\partial u}{\partial h} \right)_t = 0 \quad \text{Mass} \quad (2.13)$$

$$\left( \frac{\partial u}{\partial t} \right)_h + \frac{1}{\rho_0} \left( \frac{\partial \sigma}{\partial h} \right)_t = 0 \quad \text{Momentum} \quad (2.14)$$

$$\left( \frac{\partial E}{\partial t} \right)_h + \frac{\sigma}{\rho_0} \left( \frac{\partial u}{\partial h} \right)_t = 0 \quad \text{Energy} \quad (2.15)$$

where  $\rho_0$  is the initial density,  $u$  is the particle velocity,  $v$  is the specific volume,  $\sigma$  is the stress in the direction of propagation,  $t$  is time,  $h$  is the initial or Lagrangian position, and  $E$  is the internal energy.

To determine the stress, velocity, volume, and energy histories at each gauge plane, the preceding equations are integrated along lines of constant  $h$  (the gauge path). The integrated forms of the above equations are:

$$v_2 = v_1 + \frac{1}{\rho_0} \int_{t_1}^{t_2} \left( \frac{\partial u}{\partial h} \right)_t dt \quad (2.16)$$

$$u_2 = u_1 - \frac{1}{\rho_0} \int_{t_1}^{t_2} \left( \frac{\partial \sigma}{\partial h} \right)_t dt \quad (2.17)$$

$$E_2 = E_1 - \frac{1}{\rho_0} \int_{t_1}^{t_2} \sigma \left( \frac{\partial u}{\partial h} \right)_t dt \quad (2.18)$$

For each of these integrals, the terms under the internal sign are evaluated numerically from the gauge records. Thus, volume histories are determined from velocity records, velocity histories from stress records, and energy histories from stress and velocity data. If only stress data are obtained, the velocities are computed from the stress data and then the volume histories are derived.

The integration of equations 2.16, 2.17, and 2.18 requires the smoothing and digitization of the measured stress profiles into discrete time intervals and the numerical evaluation of the partial derivatives. The approach is illustrated in Figure 2-11 which shows a series of stress histories obtained from in-situ Lagrangian gauges. A series of smooth curves are imagined to connect the records in such a way that the lines are approximately in the directions of wave propagation. These lines, termed path lines, are generally located with equal increments of stress and connect similar flow features in each stress profile (e.g., precursors and inflections). Figure 2-11 shows the path lines for the loading segment of the profiles. At each intersection of a path line with a gauge line the

time  $T_{jk}$  associated with the stress  $\sigma_{jk}$  is calculated from a smoothed fit through nearby stress, time points defined in the digitization process.

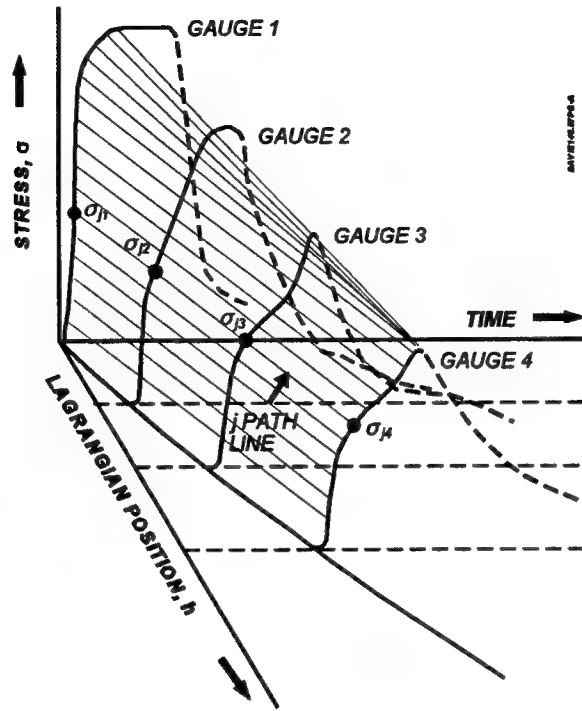


Figure 2-11. The generation of path lines in the loading process for the Lagrangian analysis.

The partial derivative  $u_2 = u_1 - \frac{1}{\rho_0} \int_{h_1}^{h_2} \left( \frac{\partial \sigma}{\partial h} \right)_t$  can now be obtained using the identity

$$\left( \frac{\partial \sigma}{\partial h} \right)_t = \frac{d\sigma}{dh} - \left( \frac{\partial \sigma}{\partial t} \right)_h \frac{\partial t}{\partial h} \quad (2.19)$$

The derivatives on the right side of equation 2.19 are derived by fitting the stress and time data to functions of  $h$  on each path line and by fitting the stress data to a function of  $t$  on each gauge line.

The numerical approximation:

$$u_{j+1,k} - u_{j,k} \approx -\frac{1}{2\rho_0} \left[ \left( \frac{d\bar{\sigma}_{jk}}{dh} + \frac{d\bar{\sigma}_{j+1,k}}{dh} \right) (T_{j+1,k} - T_{jk}) - (\sigma_{j+1,k} - \sigma_{jk}) \left( \frac{d\bar{t}_{jk}}{dh} + \frac{d\bar{t}_{j+1,k}}{dh} \right) \right] \quad (2.20)$$

is used to evaluate equation 2.17 and obtain the velocity histories where  $\sigma_{j,k}$  is the fitted value on the  $j$ th path line. Seaman's code GUINSY3 (Seaman, 1987) is used with linear fits for both stress-position and position-time, and fits up to fifth order for stress-time.

It is important to pass path lines through similar points in the flow on each gauge line and extreme care must be exercised in "fitting" the measured data.

The Lagrangian analysis performs a stepwise integration of the conservation relations to obtain stress, particle velocity, specific volume, and energy. Thus, if the stress waves approximate a discontinuity the loading path will be the Rayleigh line and the termination of the Rayleigh line will be a point on the Hugoniot. Seaman suggests that if the loading path is to a good approximation linear (or bilinear) this is sufficient justification to assume that a point on the Hugoniot is defined. In many instances in the experiments performed on this program, only one of the  $\sigma - t$  record is flat topped. Under these circumstances, the loading path frequently shows a linear rise followed by a constant or slowly varying stress segment before the release begins. The physical interpretations of these features are in question. The waveforms may be explained by rate dependent material properties. The end point of the linear portion of the loading curve can be interpreted as lying on the instantaneous Hugoniot. Clearly, the point where each release begins does not lie on the instantaneous Hugoniot. It may lie on the "equilibrium" Hugoniot. Comparison of the Hugoniot data derived from the "steady state" analyses discussed in Section 2.3.1 with that derived by the Lagrangian analysis show good agreement when the Hugonot point is defined as the termination of the Rayleigh line.

When the loading path ( $\sigma - u_p$  or  $\sigma - \rho$ ) terminates in a flat or near flat segment the applicability of the measured release path to the Hugoniot conditions has been questioned. The measured relief paths are adiabats (assuming no dissipative mechanisms and are therefore curves on the equation of state surface (after the presence of any deviator stress is accounted for). In general, the equation of state surfaces are smooth continuous surfaces, thus the measured adiabats are considered to be good approximations to the adiabat from the Hugoniot point.

The Lagrangian analysis technique makes no assumptions about the equation of state of the material. It only applies the conservation equations to the data. This is in direct contrast to the use of hydrocodes to infer a release adiabat. The hydrocodes must assume an equation of state (e.g., Mie Gruneisen) to calculate states away from the reference Hugoniot. The codes do not provide a unique definition of the release paths and, in general, relatively large variations in the code input parameters all produce stress or velocity profiles that are close to the measured profiles (i.e., the code method of deriving release adiabat material properties is insensitive). The Lagrangian analysis provides a direct measure of the unloading path without any assumptions about the equation of state of the material. It

is considered the superior method.

The accuracy of the Lagrangian code has been assessed by Seaman by exercising the code on sets of gauge records created analytically. The correct stress, particle velocity, and specific volume were known so an assessment of the accuracy of the program could be made. His results are shown below:

	STRESS ANALYSIS	
	PEAK	FINAL
Particle Velocity	3.8%	4.4%
Stress	---	---
Specific Volume	7.6%	6.8%

These data are the maximum levels of accuracy that can be expected. There are no measurement errors and thus the inaccuracies are all associated with fitting the record surface and the numerical integration of the conservation equations.

### SECTION 3

#### PENNSYLVANIA SLATE

Experimental results are presented in this section for the tests which examined the response characteristics of Pennsylvania slate. Nine tests were reported previously (Davies 1994). This report covers an additional three shots which examined the effect of cleavage plane orientation. Two of the additional experiments were conducted using the Lagrangian stress gauges, and one with the VISAR test configuration. In this section, Hugoniot data, release paths, and a shot configuration table showing details of impactor and buffer material thicknesses, sample number, density, and thickness are presented. All recorded waveforms are illustrated in Appendix A. SNLA (Furnish, letter of April 20, 1993) has also performed tests on this material.

#### 3.1 MATERIAL DESCRIPTION.

Blocks of Pennsylvania slate were provided by DNA for gas gun testing. This slate was obtained from the Penn Big Bed Slate Co. in Slatedale, PA. The slate in this quarry is from the Ordovician Age Martinsburg Formation (S. Myers, 1992 memo to A. Martinez). The blocks were roughly 125 x 125 x 65 mm in size. Blocks labeled S-3, S-4, and S-5 were all cut from the same larger block of slate. Gas gun samples were prepared from blocks S-3 and S-4. Samples were nominally 63-mm in diameter and 5- or 10-mm thick. Samples were cut from the blocks such that the impact surfaces were either parallel to or normal to the slate cleavage plane as shown in Figure 3-1. These two configurations are designated in this report Y and Z orientation, respectively. The samples for the previously reported tests used Y orientation samples. The tests reported in this document used Z orientation samples.

Material from block S-3 was sent to Terra Tek for x-ray diffraction (XRD) mineralogical analysis. The results are shown in Table 3-1 (Martin, 1993). The Pennsylvania slate S-3 was found to contain carbonate phases (calcite and iron rich dolomite).

Table 3-1. XRD Mineralogy of slates M-3 and S-3 - mineralogy, approximate weight percent.

Sample ID	Mineralogy, Approximate Weight Percent							
	Quartz	Plagioclase	Calcite	Ferroan Dolomite	Pyrite	Chlorite	Illite ± Mica	Amorphous
S-3	37	12	12	7	3	8	16	5

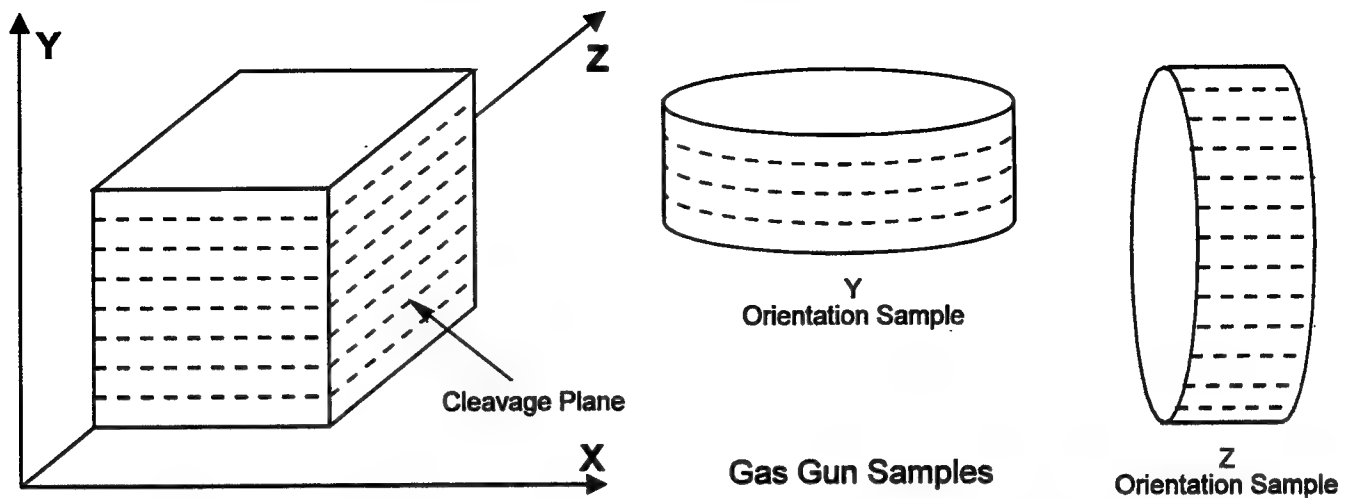


Figure 3-1. Orientation of cleavage plane in Pennsylvania slate gas gun samples.

Sample characterization data for normal oriented (z) samples are presented in Table 3-2. The accuracy of each measurement is indicated at the top of each column. The sample thicknesses listed in Table 3-2 are as-received sample thicknesses. The average sample density was  $2.736 \text{ g/cm}^3$  (std. dev. = 0.002) and the average ultrasonic longitudinal velocity was  $5.75 \text{ km/s}$  (std. dev. = 0.04).

Table 3-2. Material properties data for Z oriented Pennsylvania Slate.

Measurement Accuracy	± 1%	± 1%	± 5%	± 5%	
Sample No.	Average Thickness (mm)	Density (gm/cc)	Longitudinal Velocity (km/sec)	Shear Velocity	
				X Direction (km/sec)	Y Direction (km/sec)
S4T-1	4.879	2.736	5.813	2.596	3.264
S4T-2	5.040	2.736	5.702	2.698	3.393
S4T-3	9.994	2.738	5.718	2.557	3.295
S4T-4	5.043	2.739	5.734	2.557	3.295
S4T-5	5.033	2.737	5.694	2.614	3.332
S4T-6	5.031	2.7333	5.7497		
S4T-7	5.032	2.7336	5.7803		
S4T-8	5.034	2.7380	5.7826		
S4T-9	5.037	2.7353			
S4T-10	9.007	2.7376	5.7480		
S4T-11	9.004	2.7350	5.7461		
Average		2.736	5.747	2.616	3.321
Std Deviation		0.0019	0.035	0.0514	0.0478



Table 3-3 summarizes the ultrasonic measurements performed on these Pennsylvania slate samples as a function of orientation with the cleavage plane. The longitudinal wavespeed is higher when the cleavage planes are normal to the sample and sensor surfaces (Z orientation) (5.75 compared to 4.08 km/s). This difference suggests that the cleavage planes are loosely coupled or may be filled with a lower shock impedance material.

Table 3-3. Pennsylvania slate ultrasonic velocity measurements in y and z directions.

Pennsylvania Slate Ultrasonic Velocity Measurements			
Measurement Direction	Shear Wave Direction	Average Ultrasonic Velocity	
		Longitudinal (km/s)	Shear (km/s)
Longitudinal			
y	N/A	4.08 (std. 0.06)	
z	N/A	5.73 (std. 0.04)	
Shear			
z	x		2.62 (std. 0.05)
z	y		3.32 (std. 0.02)
y	x or z		2.19 (std. 0.02)

Cleavage Plane Orientation



DAVE394.CDR-B

### 3.2 TEST RESULTS.

Two ambient temperature experiments at 0.5 and 3.5 GPa were conducted on Z oriented Pennsylvania slate samples using the Lagrangian stress gauge experimental configuration described in Section 2.2. One high-stress experiment (8.0 GPa) used the VISAR configuration which is detailed in Section 2.2. These stress levels were selected to evaluate cleavage orientation over the complete range of stresses previously investigated.

Table 3-4 contains shot configuration information for each of these three experiments. Impactor and buffer material thicknesses, and thicknesses and densities of individual samples in each target are listed. Sample thicknesses are as-built center thicknesses. Table 3-4 also lists the impact velocity for each shot. Stress or velocity-time profile plots for each experiment are presented in Figures 3-2 and 3-3.

Table 3-4. Pennsylvania slate (z oriented) shot configuration data.

	Thickness (mm) and Density (g/cm <sup>3</sup> )											
			Sample 1			Sample 2			Sample 3			
Shot #	Impact Thk	6061-T6 Buffer Thk	No.	Ctr. Thk.	$\rho_o$	No	Ctr. Thk.	$\rho_o$	No	Ctr. Thk.	$\rho_o$	Impact Vel (km/s)
3668	6.24	9.47	S4T-6	5.03	2.73	S4T-7	5.03	2.73	S4T-11	9.00	2.74	0.068
3647	6.21	9.35	S4T-2	5.04	2.74	S4T-5	5.04	2.74	S4T-3	9.97	2.74	0.487
3646	6.13	9.54	S4T-4	5.04	2.74	LiF	25.40	2.65				1.067

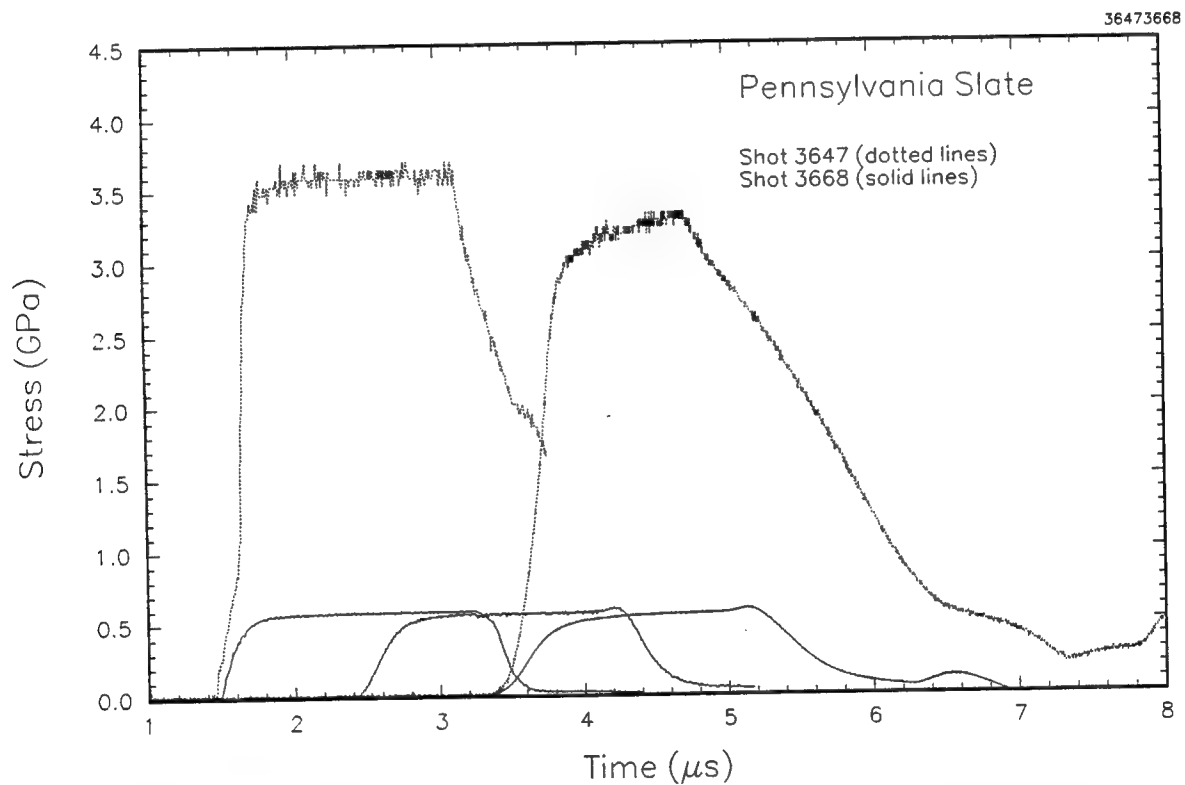


Figure 3-2. Lagrangian stress-time profiles in Z oriented Pennsylvania slate.

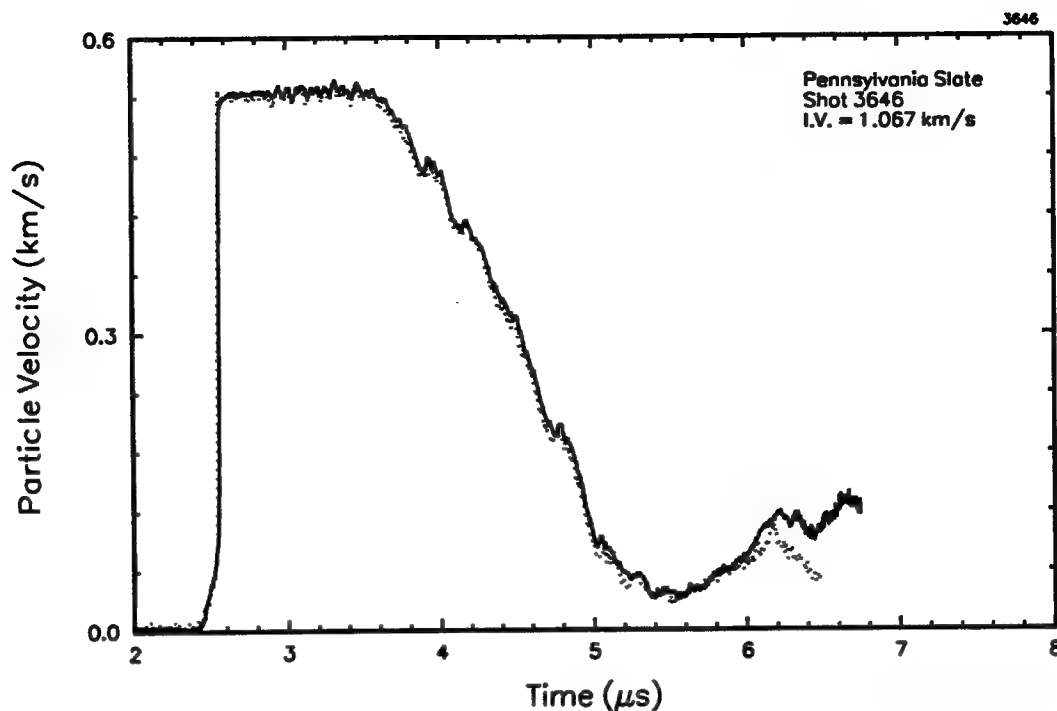


Figure 3-3. VISAR particle velocity-time profiles for Z oriented Pennsylvania slate.

The Hugoniot data listed in Table 3-5 for shots 3668 and 3647 data were by "Lagrangian analysis" of the stress profile data. The initial sample density used in all the Lagrangian analysis was the average density of all samples. The shock velocity listed in this data set is  $dh/dt$  as calculated by the Lagrangian analysis at the half amplitude stress measured by gauge-1. The loading and unloading paths derived by the Lagrangian analysis technique are shown in Figures 3-4 and 3-5 in the stress-density plane. The Hugoniot data from the VISAR shot (shot 3646) was derived by steady state analysis from measured shock velocity, sample density and the impact velocity.

Table 3-5. Pennsylvania slate (Z direction) Hugoniot data.

Shot #	Impact Velocity (km/s)	Initial Density (g/cm <sup>3</sup> )	Conf	Hugoniot			
				Stress (GPa)	$U_s$ 1/2 amp (km/s)	$u_p$ (km/s)	$\rho/\rho_0$
3668	0.068	2.74	a	0.56	4.96	0.042	1.007
3647	0.487	2.74	b	3.47	4.91	0.258	1.056
3646	1.067	2.74	b	8.16	5.34	0.558	1.117
Configuration: (a) 6061-T6 → 6061-T6/CG/S4T/CG/S4T/CG/S4T							
(b) 6061-T6 → 6061-T6/S4T/VISAR/LiF							

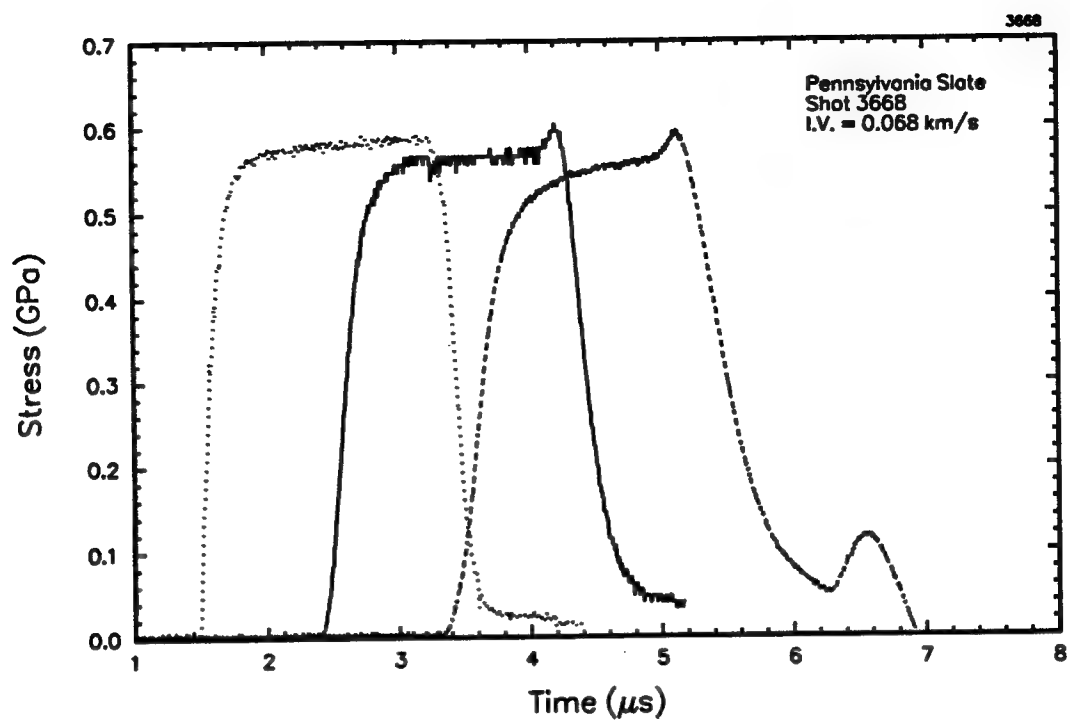


Figure 3-4. Loading and unloading paths for Z oriented Pennsylvania slate (shot 3668).

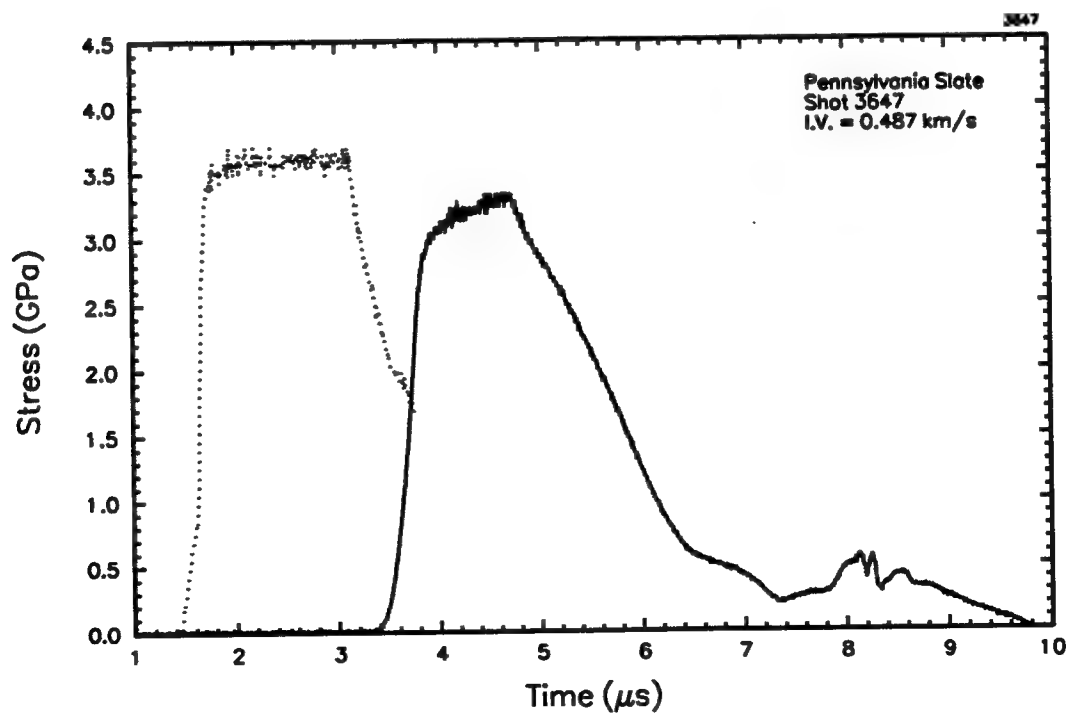


Figure 3-5. Loading and unloading paths for Z oriented Pennsylvania slate (shot 3647).

### 3.3 DISCUSSION.

The time resolved transmitted wave profiles are compared to previous tests conducted at the same impact velocities, but shocked in the Y direction in Figures 3-6, 3-7, and 3-8. These comparisons show there is little or no difference in the Z and Y direction shock response above about 2 GPa. However, the experiments on samples shocked in the Z direction show higher wave velocities below about 1 GPa than samples shocked in the Y direction. The break away precursor velocity (i.e., the toe velocity of the leading edge of the stress wave) for shots 3647 and 3668 are 5.30 and 5.52 km/s, respectively and are in good agreement with the Z direction longitudinal ultrasonic velocity of 5.75 km/s. The Y direction longitudinal ultrasonic velocity is considerably slower at 4.08 km/s, and break away shock velocities of 4.53 and 4.32 km/s were measured in the Y direction on shots 3618 and 3621, respectively.

The leading edge of the propagating stress wave in the Z oriented material has more structure than the Y oriented material with the suggestion of a dispersive precursor being present even at the highest stress shot (8.16 GPa).

Similarly, when the loading, unloading paths are compared (Figure 3-9) the Z oriented material loading path shows more curvature. The Z oriented material Hugoniot data points are compared with the Y oriented material data in Figures 3-10, 3-11, and 3-12. No significant differences between the two sets of data are noted above about 1 GPa. At 0.5 GPa, the Z oriented sample has a higher impedance than the Y oriented sample (refer to Figure 3-6).

While Pennsylvania slate is clearly anisotropic and small differences in the stress wave propagation characteristics have been detected by these measurements, the differences are not significant to HYDROPLUS analyses.

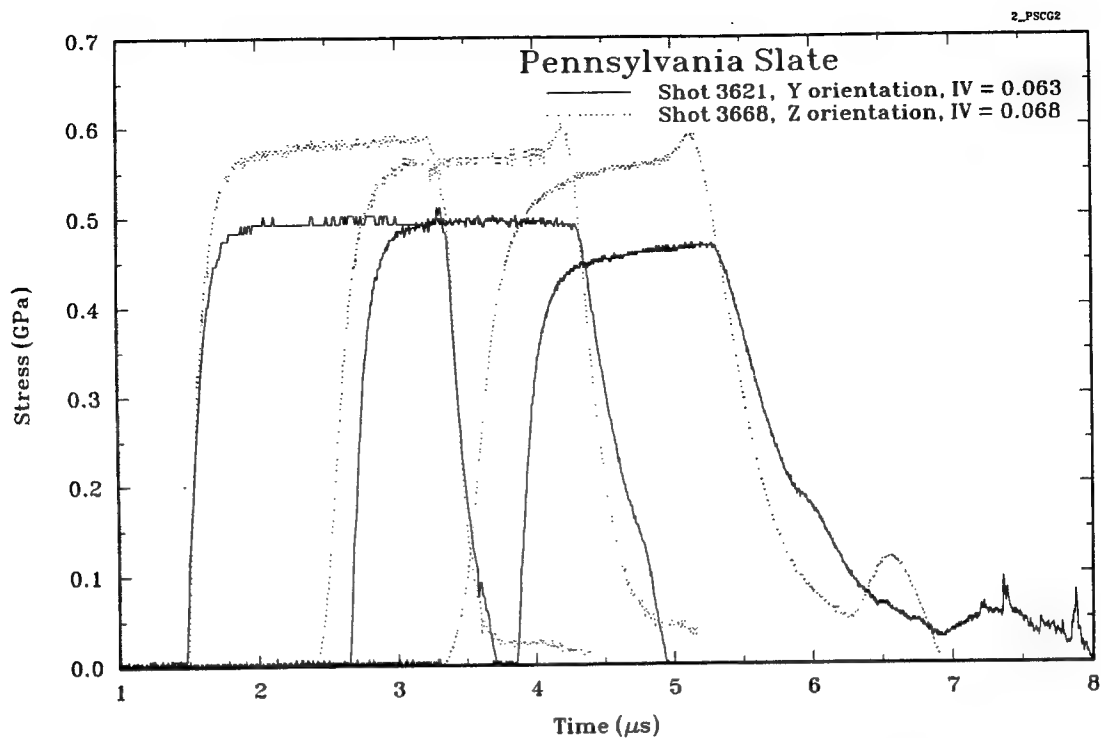


Figure 3-6. Comparison of stress profiles measured in Y and Z oriented Pennsylvania slate at 0.5 GPa.

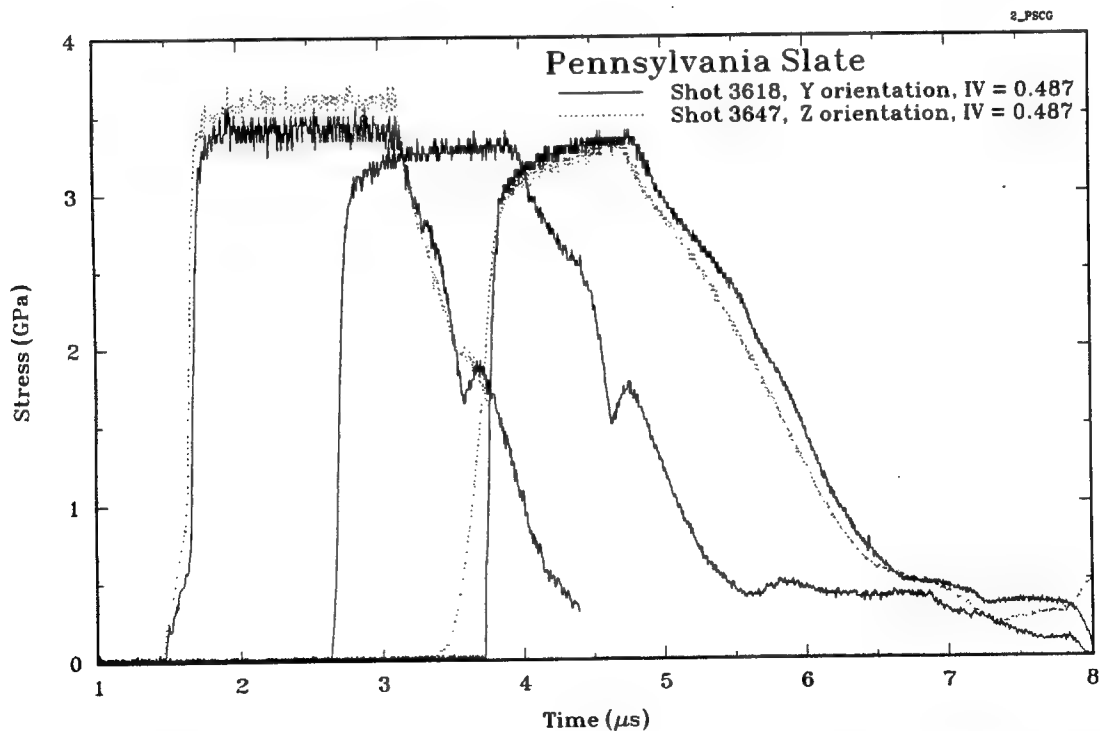


Figure 3-7. Comparison of stress profiles measured in Y and Z oriented Pennsylvania slate at 3.5 GPa.

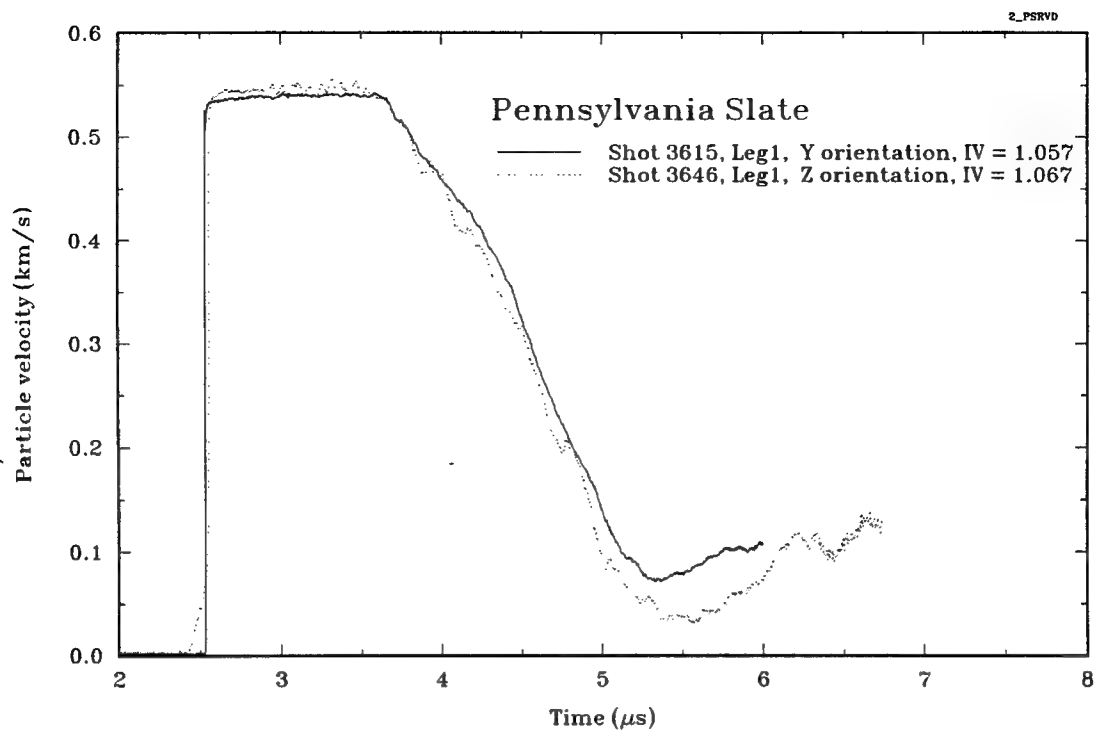


Figure 3-8. Comparison of particle velocity profiles measured in Y and Z oriented Pennsylvania slate at 8 GPa.

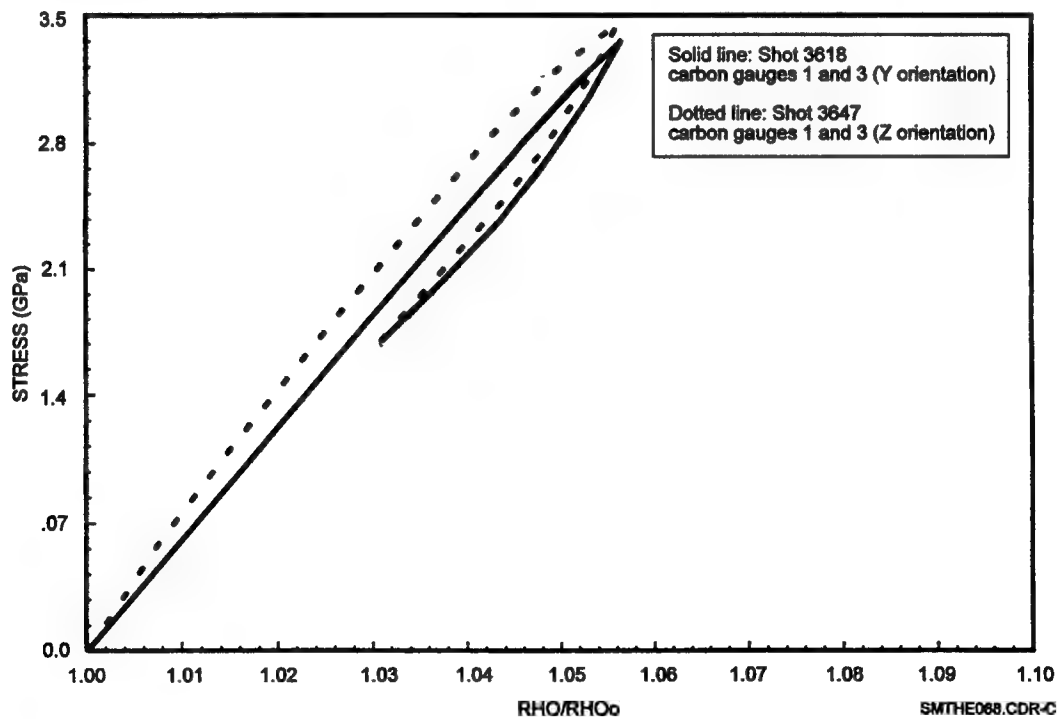


Figure 3-9. Comparison of loading and unloading paths for Y and Z oriented Pennsylvania slate at 3.5 GPa.

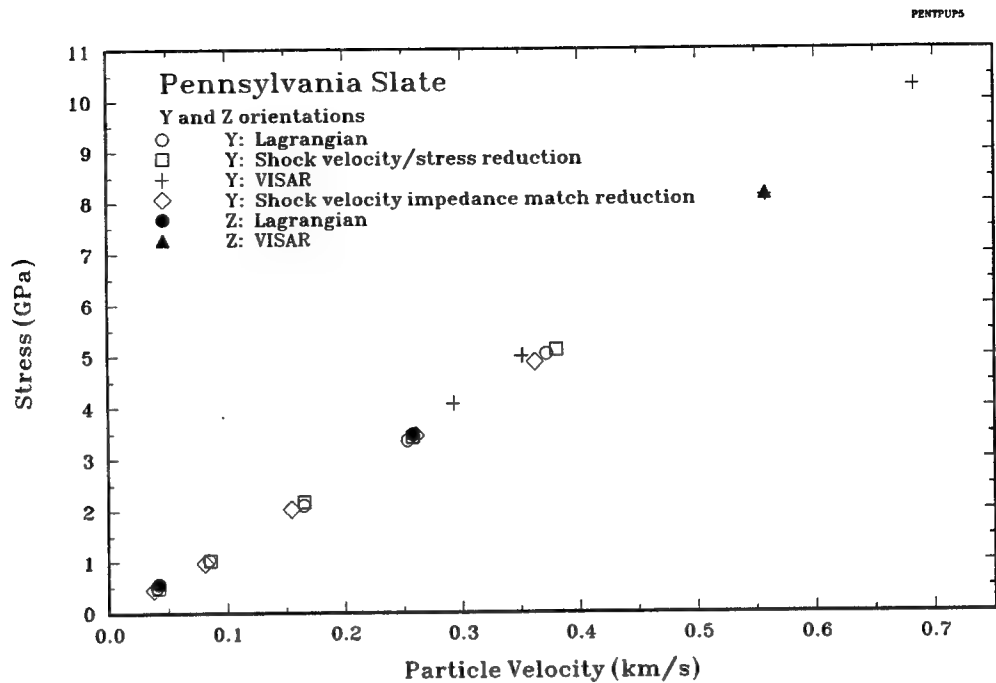


Figure 3-10. Hugoniot data for Y and Z oriented Pennsylvania slate in stress-particle velocity plane.

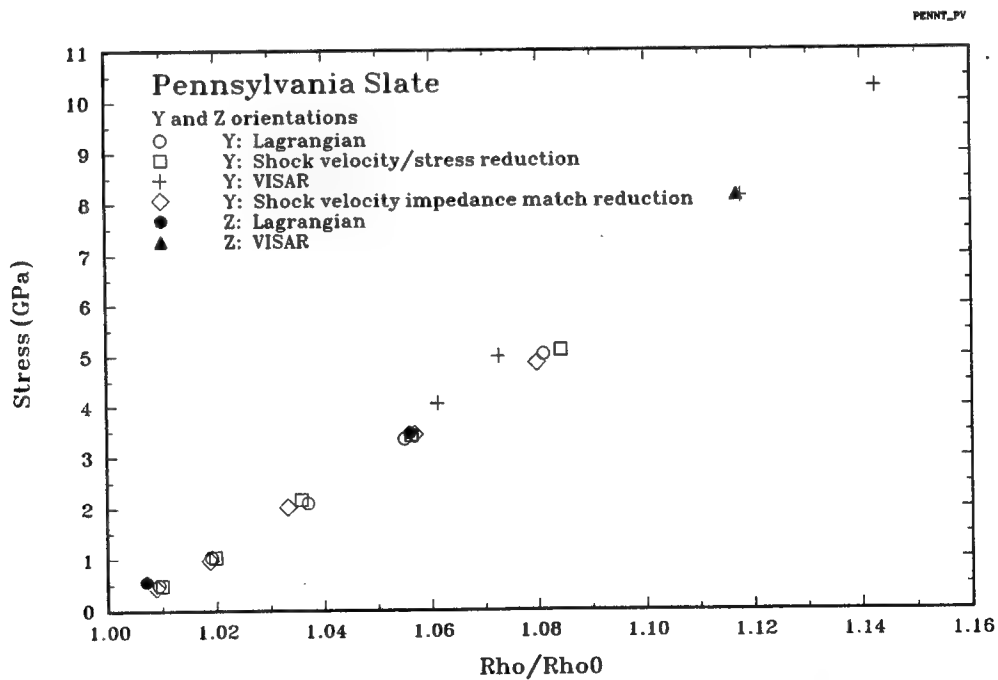


Figure 3-11. Hugoniot data for Y and Z oriented Pennsylvania slate in stress-relative density plane.



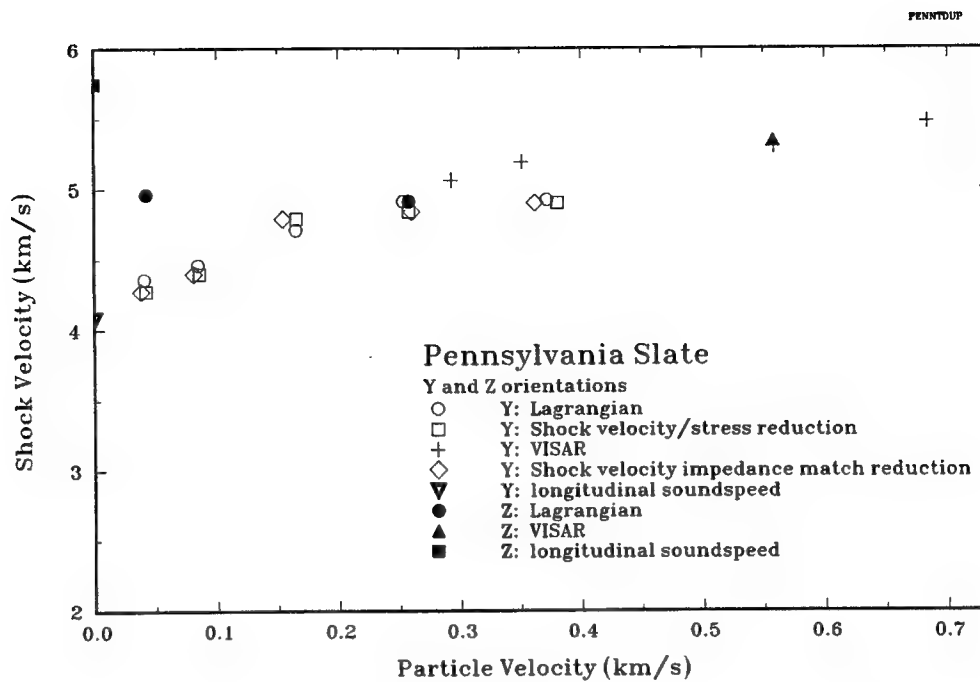


Figure 3-12. Hugoniot data for Y and Z oriented Pennsylvania slate in shock velocity-particle velocity plane.

## SECTION 4

### MAINE SLATE

Experimental results are presented in this section for the tests which examined the response characteristics of Maine Slate. Five experiments were conducted using the Lagrangian stress gauge and two with the VISAR configuration. In this section, Hugoniot data and a shot configuration table showing details of impactor and buffer material thicknesses, sample number, density and thickness are presented. All recorded waveforms are illustrated in Appendix A.

#### 4.1 MATERIAL DESCRIPTION.

Blocks of Maine Slate were provided by DNA for gas gun testing. This slate was obtained from the Monson Slate Company quarry which is located 70 miles west of Bangor, Maine. The slate in this quarry is from the Devonian Age Carrabassett Formation (S. Myers, 1992). DNA acquired six samples of apparently uniform Maine Slate. Each sample had two cleavage surfaces and rock sawed surfaces as defined in Table 4-1. Gas gun samples were prepared from Block M4. Samples were nominally 63-mm in diameter and 5- or 10-mm thick. The samples were cut from the blocks such that the impact surfaces were parallel to the slate cleavage plane as shown in Figure 4-1.

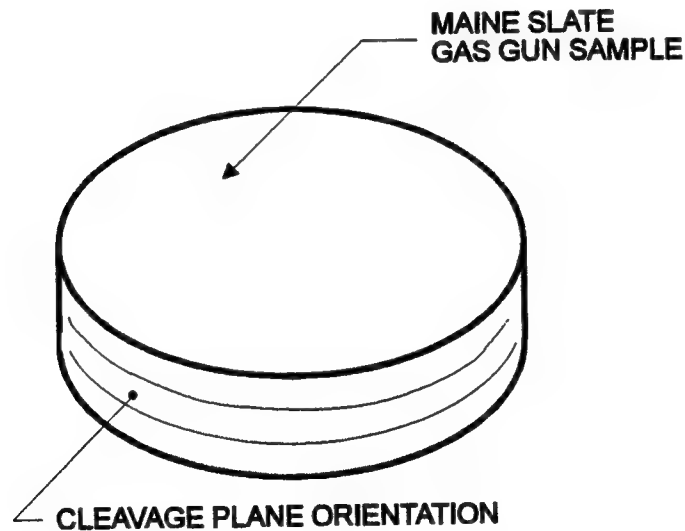


Figure 4-1. Orientation of cleavage plane in sample.

Table 4-1. Slate sample dimensions acquired from Manson Quarry, Maine.

Sample Dimensions (inches)			
Sample #	Perpendicular to Cleavage	Parallel to Cleavage	Parallel to Cleavage
M-1	1 7/8	3 1/4	7 1/4
M-2	2 7/8	3 1/2	5
M-3	3 1/8	3 1/2	4 1/8
M-4	3	3 1/2	8 3/4
M-5	2 3/4	3 1/4	6 5/8
M-6	2 7/8	3	6 1/2

The Maine Slate blocks were highly uniform, hard, gray and noncalcareous. Material from Block M3 was sent to Terra Tek for x-ray diffraction (XRD) mineralogical analysis. The results are shown in Table 4-2 (Martin, 1993). The Maine slate does not contain the carbonate phase (calcite and iron rich dolomite) that was found in the Pennsylvania Slate. Other differences between the two slates include more clay (chlante and illite) and no amorphous material or pyrite. Illite and mica were not differentiated since they have overlapping XRD peaks. The average sample density was 2.772 g/cm<sup>3</sup> (std = 0.011) and the average ultrasonic longitudinal velocity was 5.16 km/s (std = 0.18). Sample characterization data are presented in Table 4-3. The accuracy of each measurement is indicated at the top of each column. The sample thicknesses listed in Table 4-4 are as-received sample thicknesses.

Table 4-2. XRD mineralogy of main slate (block M3).

Mineralogy, Approximate Weight Percent								
Sample ID	Quartz	Plagioclase	Calcite	Ferroan Dolomite	Pyrite	Chlorite	Illite ± Mica	Amorphous
M-3	31	31	—	—	—	18	38	—

Table 4-3. Material properties for Maine slate.

Sample No.	Avg Thk. $\pm 1\%$ (mm)	Density* $\pm 1\%$ (gm/cc)	Longitudinal Velocity* (km/sec)	Shear Wave Velocity* (km/sec)
M4-1	5.037	2.76	5.08	
M4-2	5.046	2.76	5.05	
M4-3	5.039	2.77	4.87	
M4-4	5.041	2.76	5.04	
M4-5	5.034	2.79	5.17	
M4-6	5.034	2.77	4.90	
M4-7	5.036	2.78	5.32	
M4-8	5.029	2.76	5.34	
M4-9	5.028	2.78	5.24	
M4-10	5.037	2.77	5.32	
M4-11	5.035	2.77	4.93	
M4-12	5.030	2.76	5.47	
M4-13	5.031	2.76	5.37	
M4-14	5.032	2.77	4.94	
M4-15	5.036	2.77	4.88	
M4-16	9.000	2.77	5.31	
M4-17	8.997	2.77	5.33	
M4-18	9.001	2.78	5.23	3.03
M4-19**	9.003	2.77		
M4-20	9.001	2.77	5.31	3.12
M4-21	8.999	2.81	5.09	2.94
Average		2.772	5.160	3.030
Standard Deviation		0.011	0.184	0.075
*Measurements have been rounded to two significant figures, however the average and standard deviations were calculated using unrounded numbers.				
**Sample damaged.				

## 4.2 TEST RESULTS.

Five ambient temperature experiments below 5.5 GPa were conducted on the Maine Slate using a Lagrangian stress gauge experimental configuration and two high-stress experiments using a VISAR configuration. The tests configuration which were described in detail in Section 2.2 were modified for this test series. In these tests the impact face aluminum buffer was eliminated and the sample was impacted directly as shown in Figures 4-2 and 4-3.

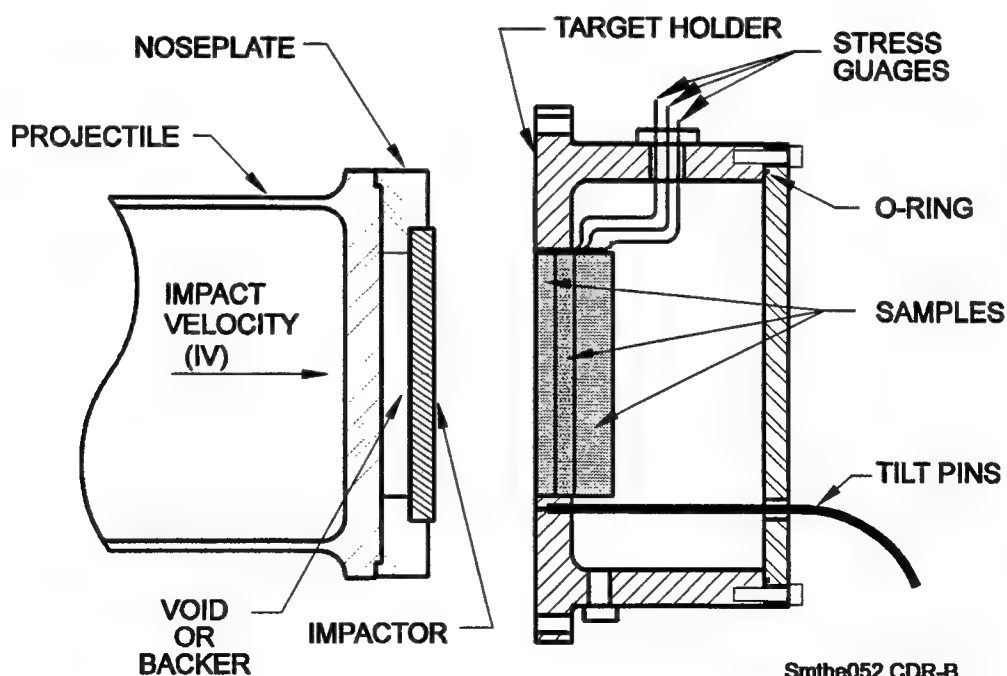
Table 4-4 contains shot configuration information for each of these experiments. Impactor thickness and thicknesses and densities of individual samples in each target are listed. Sample thicknesses are as-built center thicknesses. Stress-time and particle velocity-time profile plots for the experiments are presented in Appendix A. The aluminum buffer was eliminated from this test series because a sample cup which maintained the as-received water content was unnecessary (the water content of the samples was negligible) and the aluminum buffer complicates the data analysis. Prior to making this

configuration change test shots were fired to evaluate the use of a carbon gauge mounted on the impact face of the test sample. Figure 4-4 shows a comparison of two shots on Pennsylvania slate samples: one with a buffer and one without (The former was time shifted for this comparison plot.). Apart from the lack of an aluminum precursor on the bufferless shot and the earlier arrival of the reliefwave (the flyer is effectively thinner) the stress profiles are very similar. There may be a small overshoot on the impact face mounted carbon gauge; however, these data were considered sufficiently good to warrant conducting the Maine Slate test series using the bufferless configuration.

Table 4-4. Maine slate shot configuration data.

Shot #	Aluminum Impact Thk	Thickness (mm) and Density (g/cm <sup>3</sup> )								
		Sample 1			Sample 2			Sample 3		
		No.	Ctr Thk	$\rho_a$	No.	Ctr Thk	$\rho_a$	No.	Ctr Thk	$\rho_a$
3682	6.31	M4-3	5.04	2.77	M4-6	5.03	2.77	M4-18	9.00	2.78
3681	6.35	M4-1	5.04	2.76	M4-2	5.05	2.76	M4-17	9.00	2.77
3680	6.30	M4-7	5.04	2.78	M4-14	5.03	2.77	M4-16	9.00	2.77
3679	6.34	M4-5	5.03	2.79	M4-9	5.03	2.78	M4-21	9.00	2.77
3678	6.33	M4-10	5.04	2.77	M4-11	5.03	2.77	M4-20	9.00	2.81
3683	6.32	M4-4	5.04	2.76	LiF	25.40	2.65			2.77
3685	6.35*	M4-8	5.03	2.76	LiF	25.45	2.65			

\*Tungsten carbide impactor.



Smthe052.CDR-B

Figure 4-2. Lagrangian stress gauge test configuration showing test sample mounted in target holder without an aluminum buffer.

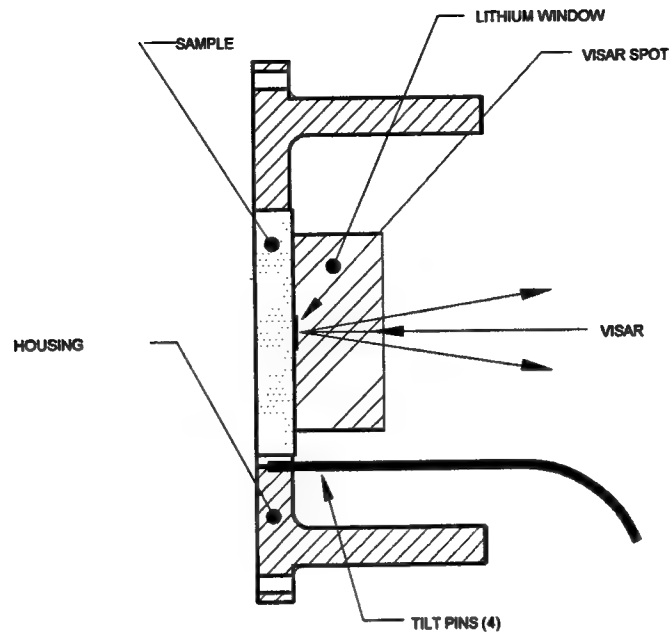


Figure 4-3. Visar target configuration showing test sample mounted in target holder without an aluminum buffer.

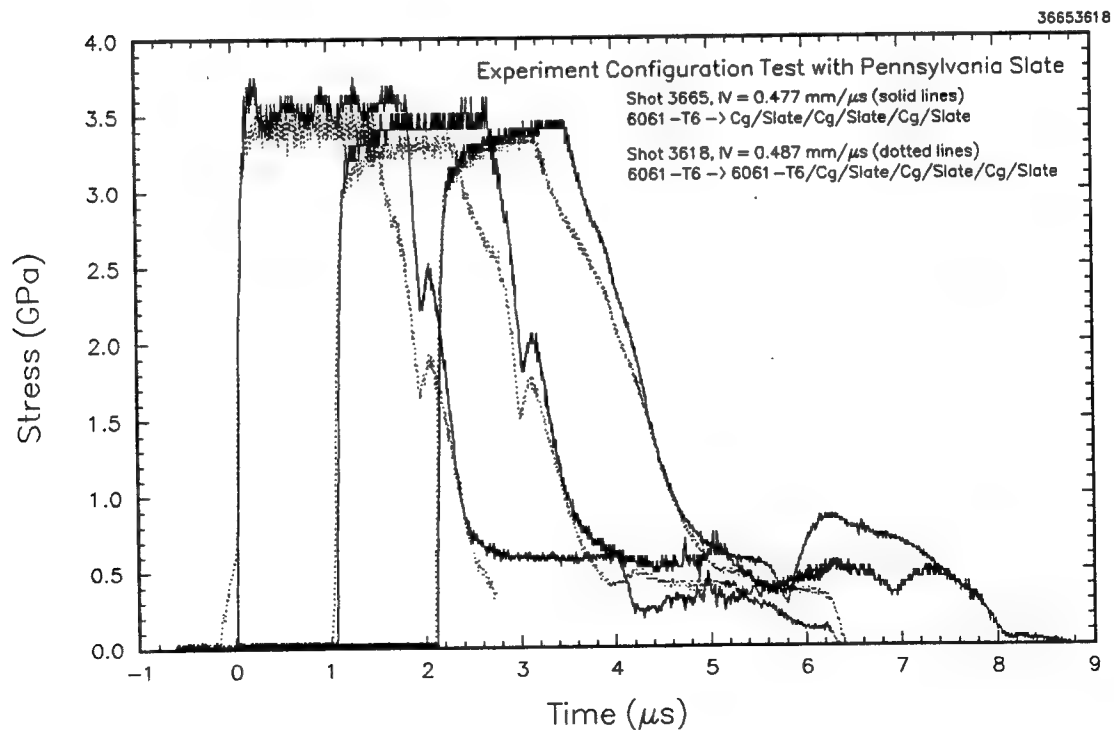


Figure 4-4. Comparison of measured stress profiles in Pennsylvania slate using aluminum buffered, and bufferless test configurations.

Hugoniot data are presented in Table 4-5. Hugoniot data for all shots were derived from measured shock velocity, sample density, and the known Hugoniot for aluminum using standard steady state impedance matching techniques. Shock velocity measurements were based on shock transit through the sample at half amplitude stress. These data sets are listed as "shock velocity impedance reduction" in Table 4-5.

Table 4-5. Maine slate Hugoniot data.

				Hugoniot			
Shot #	Impact Vel (km/s)	Initial Density (g/cm <sup>3</sup> )	Conf.	Stress (Gpa)	U <sub>s</sub> ½ amp (km/s)	u <sub>p</sub> (km/s)	ρ/ρ <sub>o</sub>
Shock Velocity Impedance Match Reduction							
3678	0.692	2.77	a	5.22	5.27	0.357	1.073
3679	0.491	2.79	a	3.62	5.09	0.255	1.053
3680	0.313	2.78	a	2.29	5.05	0.163	1.033
3681	0.152	2.76	a	1.11	4.97	0.081	1.017
3682	0.070	2.77	a	0.52	4.72	0.040	1.009
3685	0.820	2.76	c	10.77	5.50	0.709	1.148
3683	1.141	2.76	b	8.64	5.13	0.609	1.135
Gauge 1 Stress, Shock Velocity							
3678	0.692	2.77	a	5.32	5.27	0.364	1.074
3679	0.491	2.79	a	3.63	5.09	0.256	1.053
3680	0.313	2.78	a	2.43	5.05	0.173	1.035
3681	0.152	2.76	a	1.24	4.97	0.090	1.019
3682	0.070	2.77	a	0.59	4.72	0.045	1.010
Lagrangian Analysis							
3678	0.692	2.77	a	5.26	5.24	0.354	1.070
3679	0.491	2.77	a	3.62	5.11	0.254	1.058
3680	0.313	2.77	a	2.42	4.98	0.172	1.038
3681	0.152	2.77	a	1.23	4.91	0.090	1.016
3682	0.070	2.77	a	0.597	4.66	0.046	1.011
Configuration: (a) 6061 T6 ~ CG/Slate/CG/Slate/CG Slate (b) 6061 T6 ~ Slate/VISAR/LiF (c) WC ~ Slate/VISAR/LiF							

The Lagrangian stress data were also analyzed in two other ways for comparison. The Hugoniot data set listed as "stress shock velocity reduction" was determined from the measured impact stress and shock velocity using the initial density and Hugoniot relations. The measured shock velocity was derived from shock transit times through the sample at half amplitude stress.

The last data set listed in Table 4-5 was obtained by "Lagrangian analysis." The initial sample density used in all the Lagrangian analysis was the average density of all samples. The shock velocity listed in this data set is  $dh/dt$  as calculated by the Lagrangian analysis at the half amplitude stress measured by gauge-1.

Comparison of the differences in the three data sets is an indication of uncertainty between the different methods of data analysis. Typically the stress, shock velocity, particle velocity, and density standard errors of the means are 2.5, 1.3, and 0.1 percent, respectively. Figure 4-5, 4-6, and 4-7 present the Hugoniot data in stress-particle velocity, stress-relative density, and shock velocity-particle velocity planes, respectively. Stress-time profiles for the Lagrangian shots are presented in Figure 4-8. Particle velocity-time profiles for the VISAR shots are shown in Figure 4-9.

### 4.3 DISCUSSION.

An examination of the Hugoniot data in the shock velocity-particle plane suggests that the data can be represented by a single straight line fit.

$$U_s = 4.86 (0.09) + 0.79 u_p (0.23)$$

where  $U_s$  and  $u_p$  are in km/s and the numbers in parenthesis are the standard errors of the constants of the fits. This fit was to the "shock velocity impedance match" data only. The measured data are compared to the calculated fits in the shock velocity-particle velocity, stress-particle velocity, and stress-relative density planes in Figures 4-10, 4-11, and 4-12, respectively. The measured data for Pennsylvania Slate (Davies 1994) in the same range are also shown in these plots. The Maine Slate is slightly higher impedance than the Pennsylvania Slate. There is evidence in the Maine Slate data set of an inflection in the Hugoniot at about 0.1 km/s particle velocity (Figure 4-10). More data would be needed below 0.5 GPa to confirm this. A similar inflection is seen in the Pennsylvania Slate data at about 0.3 km/s (4 GPa) particle velocity.



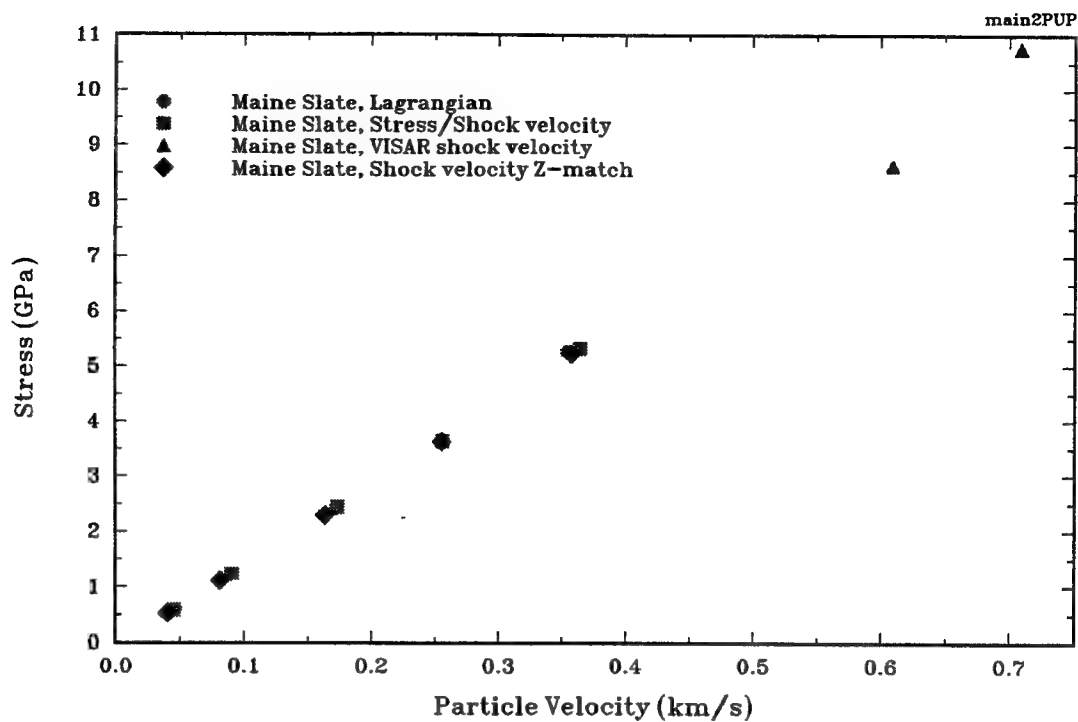


Figure 4-5. Maine slate Hugoniot data, stress-particle velocity plane.

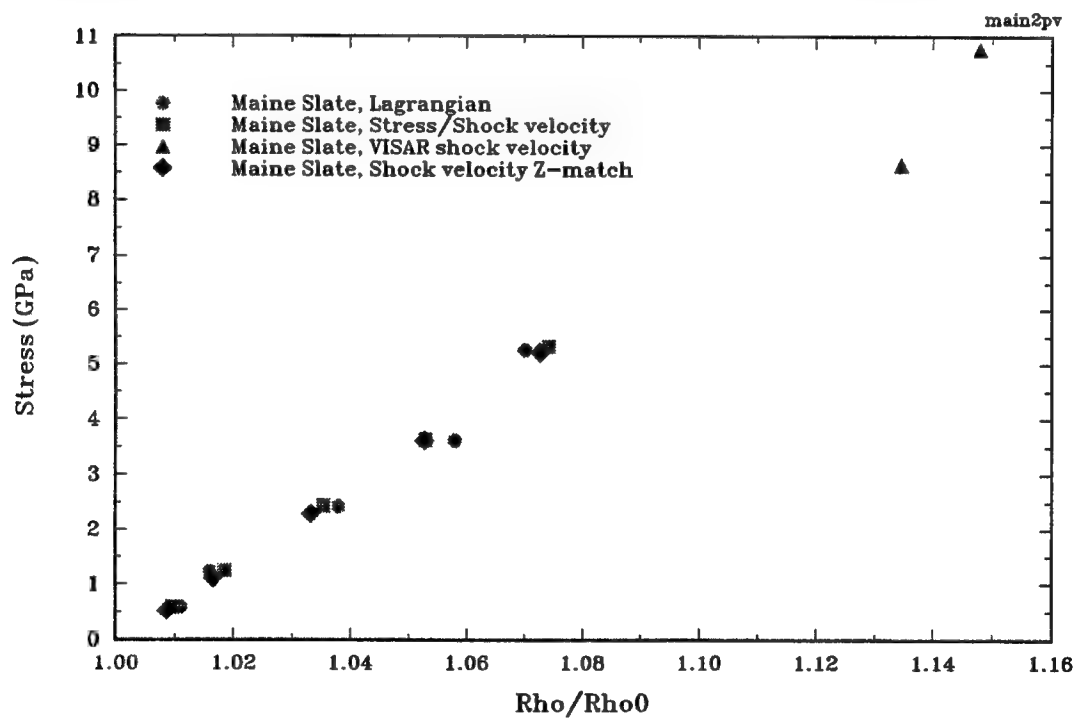


Figure 4-6. Maine slate Hugoniot data, stress-relative density ( $\rho/\rho_0$ ) plane.

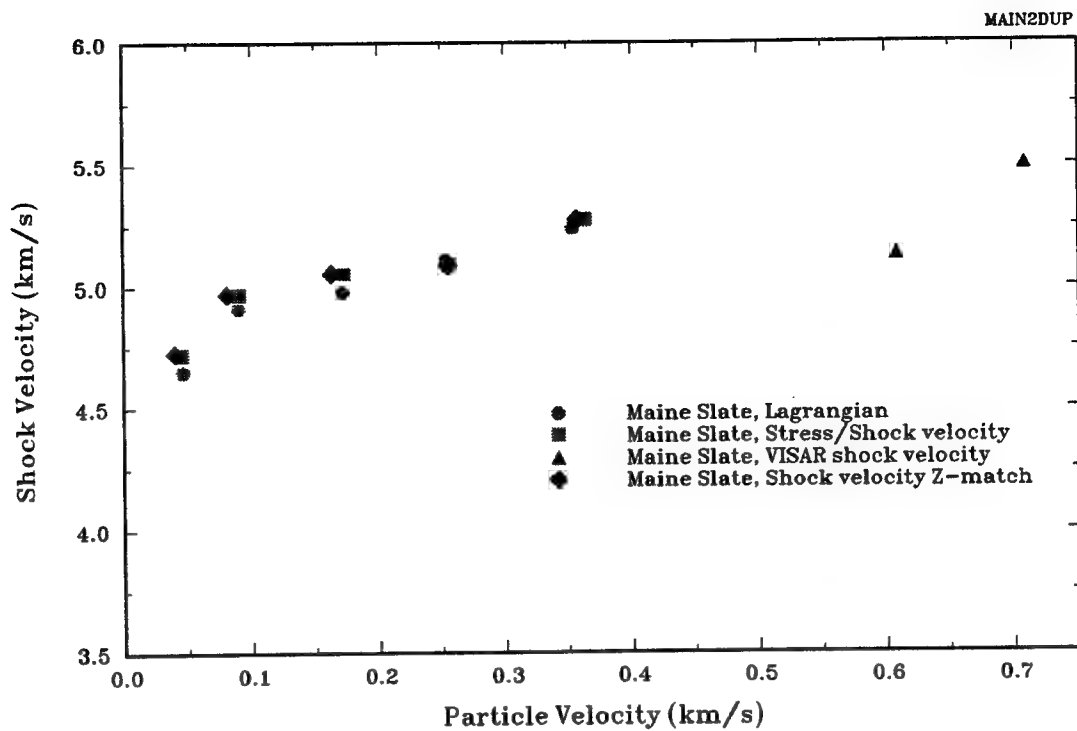


Figure 4-7. Maine slate Hugoniot data, shock velocity-particle velocity plane.

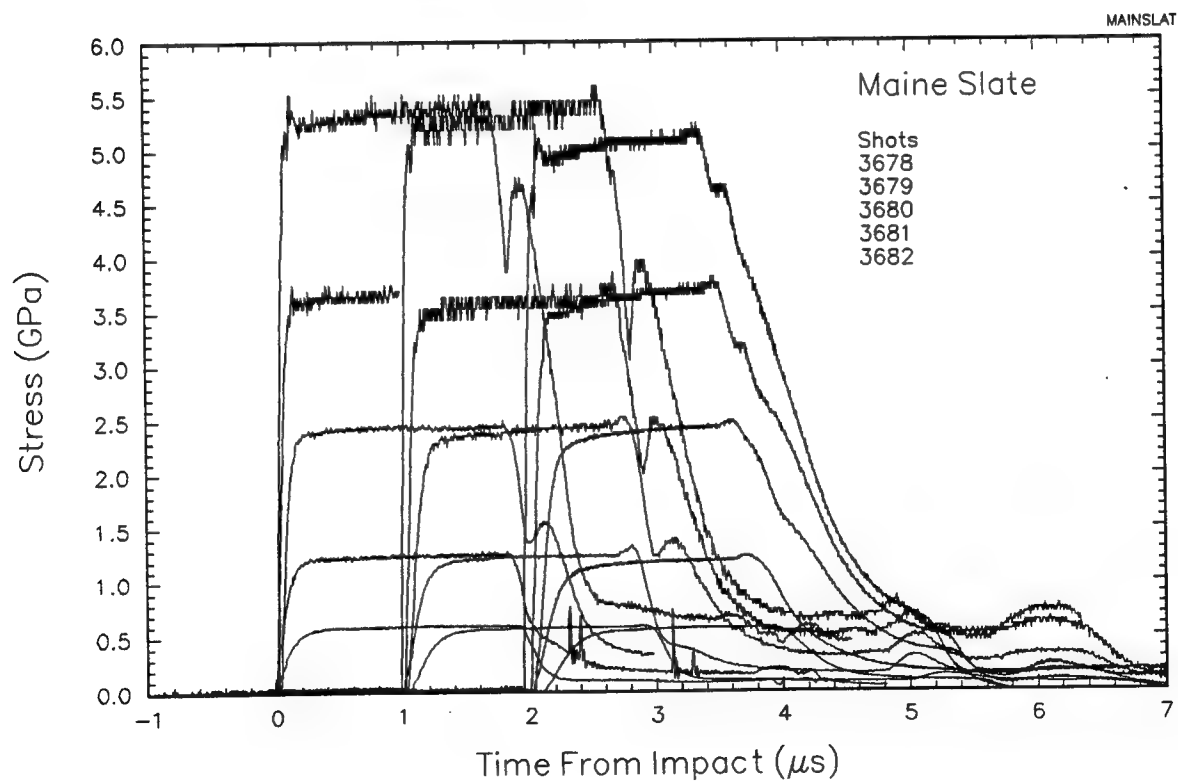


Figure 4-8. Measured stress profiles in Maine slate.

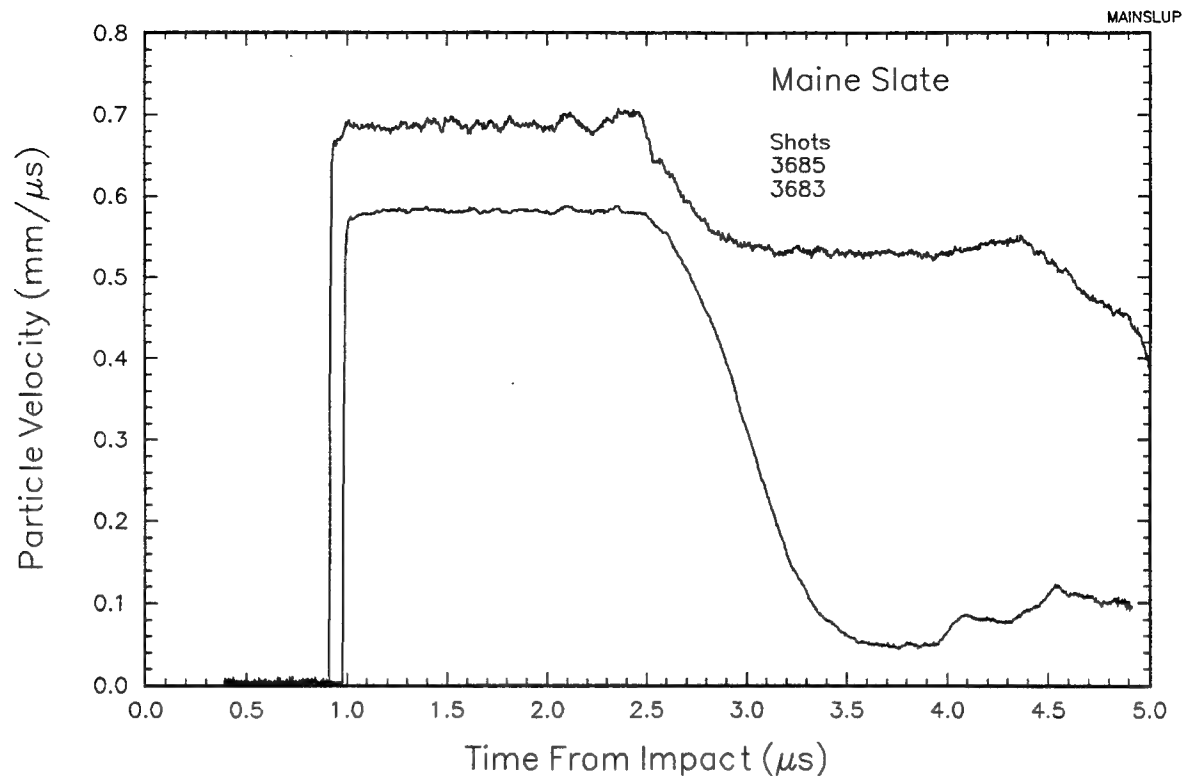


Figure 4-9. Measured particle velocity profiles in Maine slate.

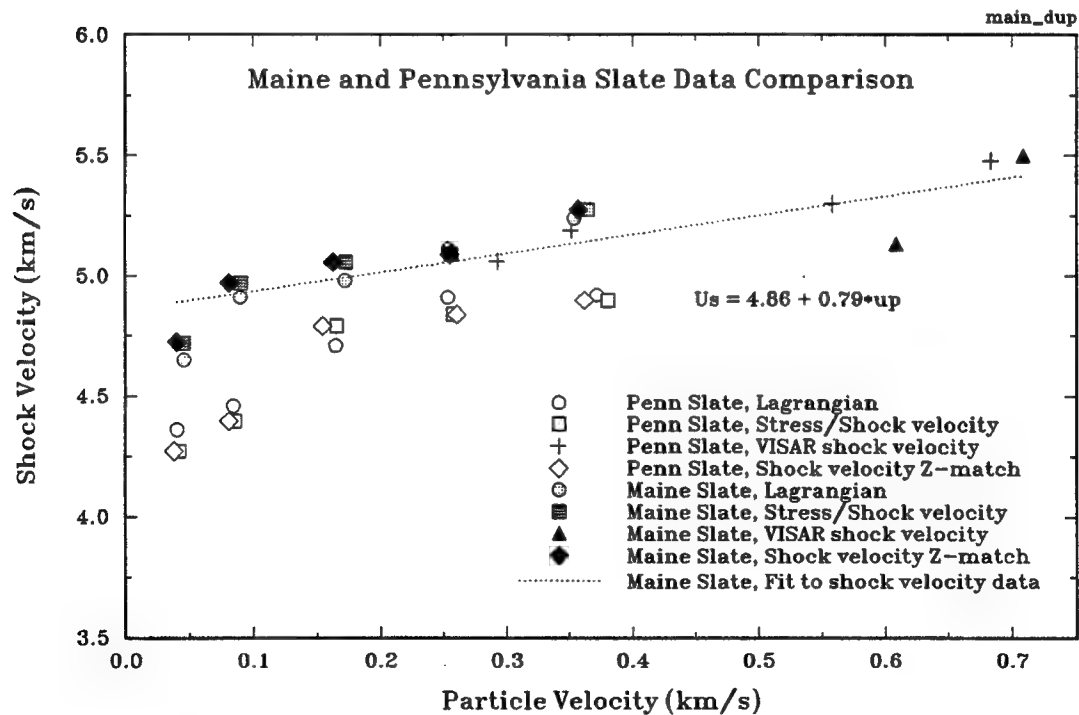


Figure 4-10. Comparison of Maine and Pennsylvania slate Hugoniots in the shock velocity-particle velocity plane.

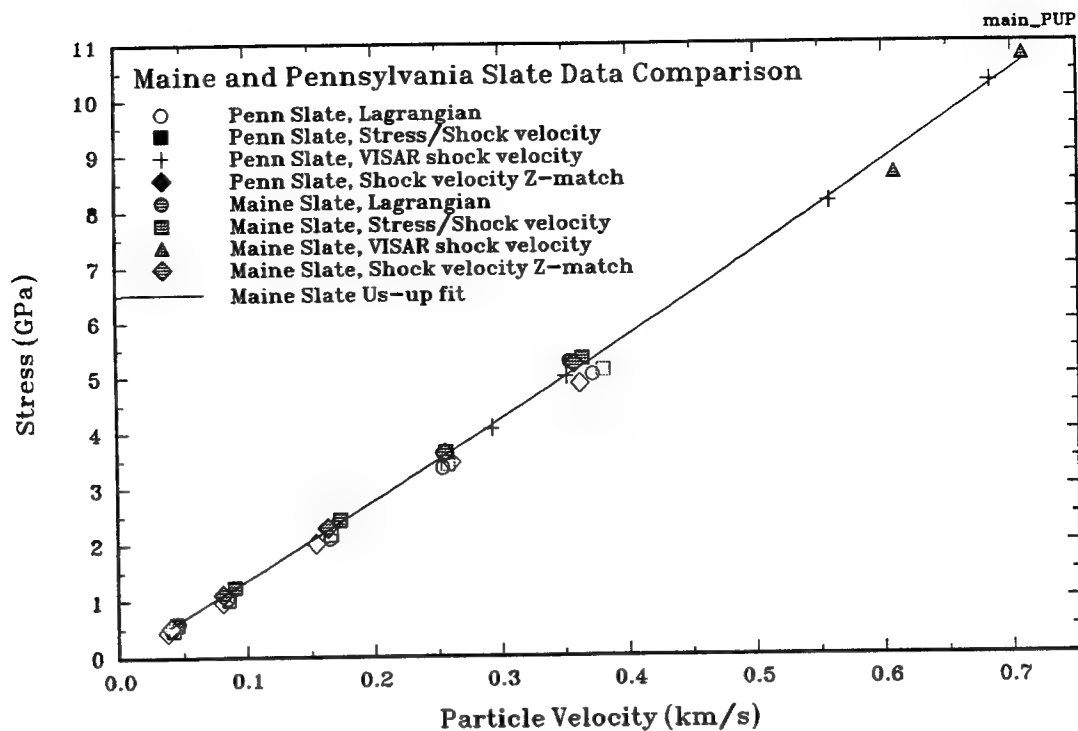


Figure 4-11. Comparison of Maine and Pennsylvania slate Hugoniots in the stress-particle velocity plane.

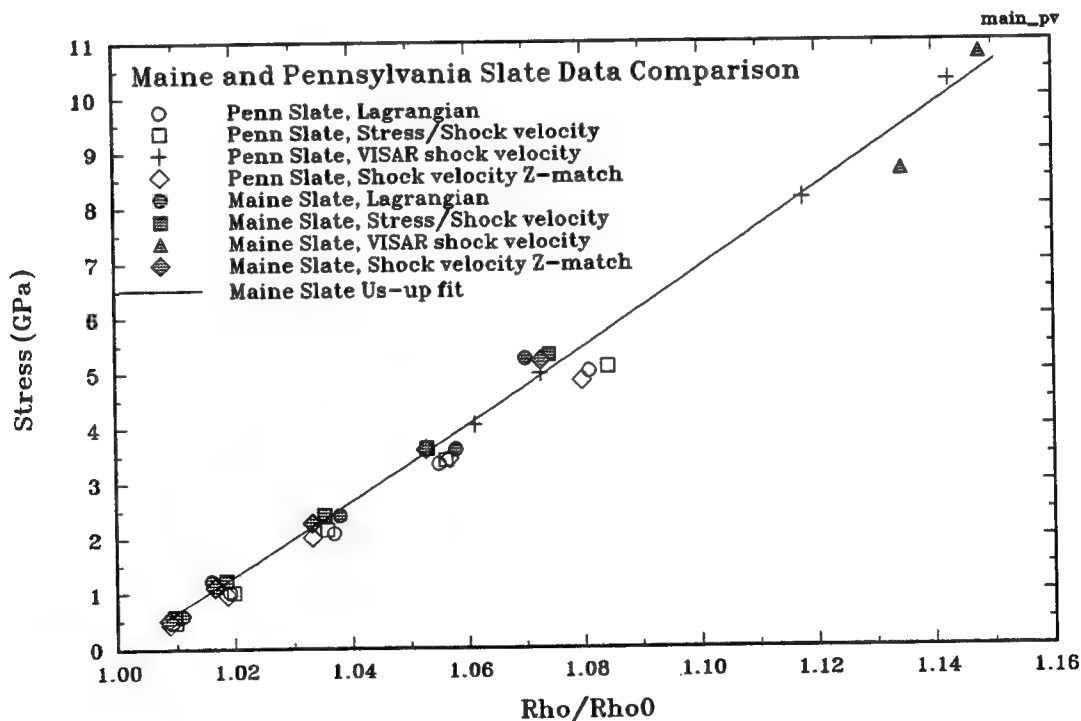


Figure 4-12. Comparison of Maine and Pennsylvania slate Hugoniots in the stress-relative density ( $\rho/\rho_0$ ) plane.

## SECTION 5

### PHYLLITE RESULTS

This section presents the results of two tests conducted on thawed, phyllite at stresses of 11 and 17 GPa. Hugoniot and wave propagation data for thawed, refrozen, and preserved frozen phyllite have been reported previously (Davies 1994). These two additional shots were performed to extend the measurement range to high stresses and to determine if a 6 to 7 GPa precursor exists. This precursor had been predicted from an examination of the low stress Hugoniot data. In this section, Hugoniot data and shot configuration tables showing details of impactor and buffer material thicknesses, and sample number, density, and thickness are presented. All recorded waveforms are illustrated in Appendix A.

#### 5.1 MATERIAL DESCRIPTION.

The phyllite was obtained from permafrost core drilled within the Lupin Gold Mine, Canada. The Lupin mine is located approximately 60 miles south of the Arctic Circle in the Northwest Territories Province of Canada, about 850 miles north-northeast of Edmonton, Alberta. The samples were prepared by Terra Tek from core obtained by DNA from core holes LU#2 and LU#2A. The thawed samples were obtained from core hole LU#2. A visual examination of the phyllite core was performed by DNA at the drill site. The results are presented in Table 5-1. Terra Tek performed physical material property tests, x-ray diffraction analysis, and thin section analysis on the phyllite obtained from core hole LU#2 and LU#2A. The mineralogy of the phyllite is given in Table 5-2. Based on the thin section analysis, the rock consists of silty and argillaceous layers in which the chief minerals are Muscovite, chlorite, quartz, and feldspar. Strong schistosity (foliation) was evident by the parallel arrangement of the Muscovite. The average grain size for the phyllite is approximately 0.04 mm.

The material properties data derived from the NDE measurements performed by Ktech for thawed phyllite are presented in Table 5-3. The accuracy of each measurement is indicated at the top of each column. The sample thicknesses listed in Table 5-3 are as-received sample thicknesses. The average density for the thawed phyllite was 2.790 (std. dev. = 0.012) g/cm<sup>3</sup>. The average longitudinal velocity for the thawed phyllite is 6.66 (std. dev. = 0.20) km/s. The as-received water content of the thawed samples was maintained at all times.

Table 5-1. Lithologic descriptions performed at the drill site by DNA.

ROCK TYPE	LITHOLOGIC DESCRIPTION	FORMATION AND AGE
Phyllite	Grayish-black to black with greenish black tint; very hard, dense; trace biotite; trace disseminated pyrite; foliation cuts core at 40 to 70° angle. Rare 1 to 4 mm wide calcite-filled fractures, usually with disseminated or intermittent pyrite fractures, typically tight with no visible porosity, and vary from single planar fractures parallel to foliation to branching and intersecting patterns crossing foliation. Several calcite and pyrite coated core partings show slickenside lineations. A calcite filled fracture in LU #2A, run #6, 1 cm wide with vuggy porosity along center of vein; calcite crystals up to 8 mm across; water ice fills void.	Contwoyto Fm. Archean Eon

Table 5-2. X-ray diffraction mineralogy of phyllite.

SAMPLE ID	DEPTH (m)	Mineralogy - Approximate Percent by Weight					
		Quartz	Plagioclase	Potassium Feldspar	Calcite	Muscovite	Chlorite
Unpreserved Phyllite LU #2	9.11-1.17	13	19	2?	5	37	24
Preserved Phyllite LU#2A	1.90-2.20	59	18	2?	1	14	6

Table 5-3. Material properties for phyllite.

Sample No.	Average* Thk (mm) ±1%	Density* (g/cm <sup>3</sup> ) ±1%	Longitudinal* Velocity (km/s) ±5%	Shear Velocity (km/s)	Sample No.	Average* Thk (mm) ±1%	Density* (g/cm <sup>3</sup> ) ±1%	Longitudi nalVelocit y* (km/s) ±5%	Shear Velocity *† (km/s)	
Thawed (Ktech measurements)										
TP-1-A	9.98	2.80	6.68	3.93	TP-3-B	5.03	2.79	6.65	4.10 4.45	
TP-2-A	9.93	2.78	6.81		TP-7-B	5.00	2.81	6.47		
TP-3-A	9.96	2.80	6.51	3.94	TP-8-B	5.02	2.80	6.43		
TP-4-A	9.95	2.78	6.65		TP-9-B	4.91	2.79	6.53		
TP-5-A	10.00	2.79	6.65		TP-10-B	4.54	2.79	6.67		
TP-6-A	10.04	2.79	6.70	4.47	TP-11-B	4.69	2.79	6.46	4.06 2.84‡	
TP-7-A**	9.95	2.77	7.11		TP-12-B	5.00	2.80	6.45		
TP-1-B	5.01	2.79	6.89		TP-13-B	4.95	2.80	6.46		
TP-2-B	4.96	2.81	6.25		TP-14-B**	4.97	2.76	7.02		
TP-3-B	4.90	2.78	6.68		TP-15-B	4.97	2.77	6.92		
TP-4-B	4.93	2.78	6.51		TP-16-B	4.97	2.77	6.83		
TP-5-B	5.04	2.79	6.79		TP-17-B	4.95	2.78	6.76		
Average Std Dev							2.79 0.012	6.66 0.21	4.17 0.24	
*Measurements have been rounded, however, the average and standard deviations were performed using nonrounded measurements. **These samples were from a 5.30 - 5.325 meter depth. All other thawed samples are from a 7.78 - 8.30 meter depth. †Perpendicular to foliation ‡Parallel to foliation										

## 5.2 TEST RESULTS.

Impact experiments were conducted at 11.0, and 17.0 GPa on the thawed samples. These two shots were VISAR shots with lithium fluoride windows which are an excellent impedance match to the phyllite.

The VISAR test configuration is described in Section 2.2. Table 5-4 contains shot configuration information for each of these experiments. The tungsten carbide (WC) impactor and aluminum buffer material thicknesses, and thicknesses and densities of the individual samples in each target are listed. Measured velocity-time profiles for each experiment are shown in Figures 5-1 and 5-2.

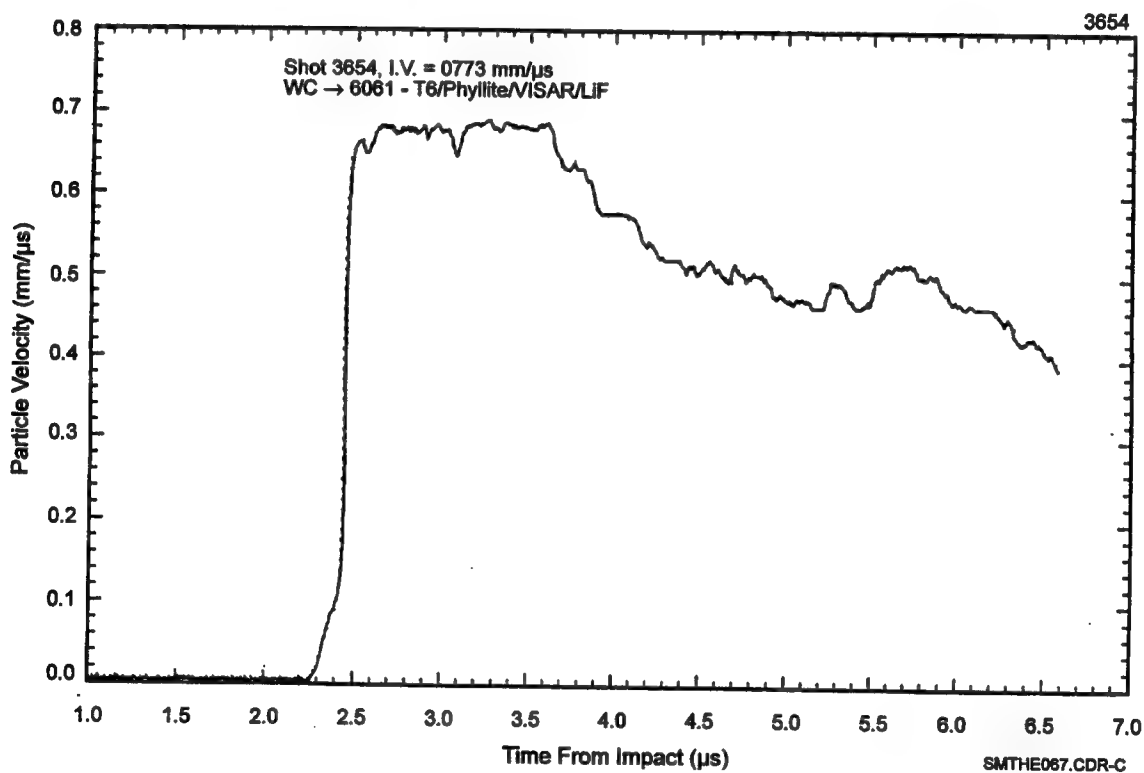


Figure 5-1. Shot 3654 measured particle velocity profile.

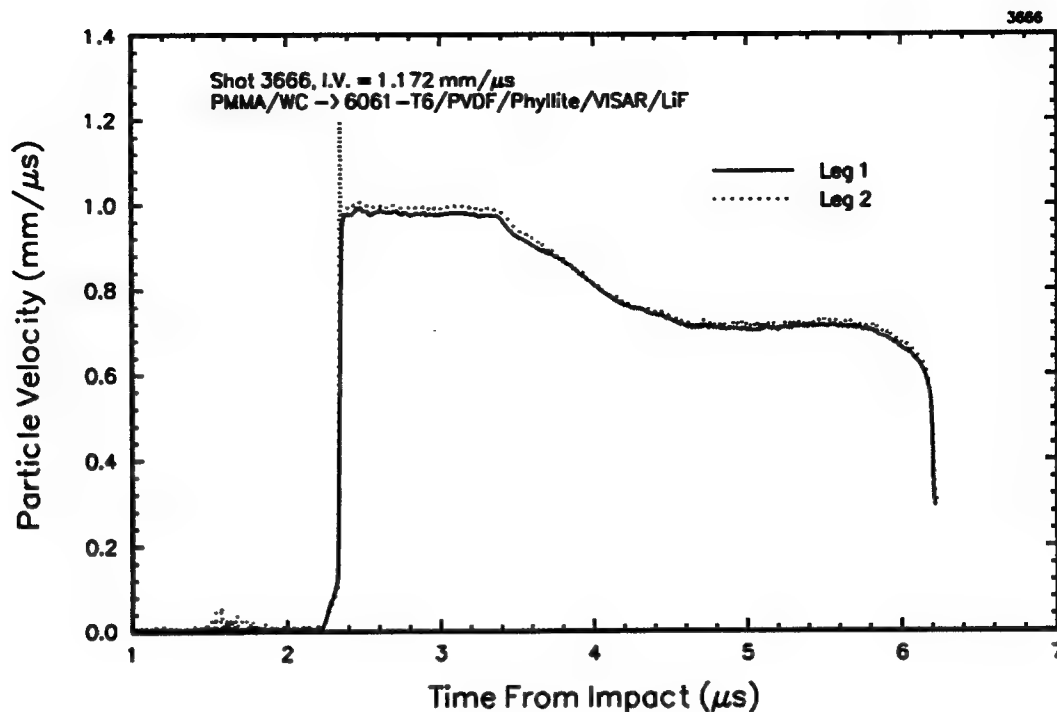


Figure 5-2. Shot 3666 measured particle velocity profile.

Hugoniot results obtained from the VISAR experiments are presented in Table 5-5, together with the previously reported VISAR data. These data were determined from measured shock velocity and material Hugoniots using standard impedance matching techniques as described in Section 2.2. The Hugoniot data are plotted in Figures 5-3, 5-4, and 5-5 in the stress-particle velocity, stress-relative density, and shock velocity-particle velocity planes, respectively. These plots included the low-stress data obtained by Davies (1994).

Table 5-4. Phyllite shot configuration data.

Shot No.	Thickness (mm) and Density (g/cm <sup>3</sup> ) at Ambient Temperature							
	WC Impact Thick	6061-T6 Buffer Thick	Sample 1			LiF Window		
			No.	Center Thick	ρ <sub>o</sub>	No.	Center Thick	ρ <sub>o</sub>
Thawed								
3654	6.35	9.52	TP-15-B	4.98	2.78	LiF	25.45	2.64
3666	6.35	9.51	TP-17-B	4.95	2.78	LiF	25.43	2.64



Table 5-5. Thawed phyllite Hugoniot data obtained from VISAR measurements.

Shot #	Impact Velocity (km/s)	Sample Initial Density (g/cm <sup>3</sup> )	Stress (GPa)	$u_p$ (km/s)	$U_s$ (km/s)	$\rho/\rho_0$
Thawed						
3595*	0.966	2.76	7.57	0.497	5.5	1.099
3654	0.773	2.78	10.49	0.688	5.49	1.143
3666	1.172	2.78	16.21	1.045	5.58	1.231
Configuration: 6061-T6 → 6061-T6/sample/lithium fluoride *Davies 1994 Note: Hugoniot data was determined from measured shock velocity using impedance matching techniques. A reflection of the 6061-T6 Hugoniot was used for unloading in calculation. The VISAR particle velocity profiles are shown in Figures 4-4 and 4-8.						

### 5.3 DISCUSSION.

The Hugoniot data for thawed phyllite including previously obtained data (Davies 1994 and Furnish 1993) are shown in Figure 5-6, in the shock velocity-particle velocity plane together with straight line fits to the data in various stress range. Davies (1994) showed that the data for thawed, refrozen, and preserved permafrost phyllite in the stress range to 5.6 GPa was well represented by:

$$U_s = 5.163 (0.153) + 0.287 (0.370) u_p$$

where  $U_s$  and  $u_p$  are in km/s and the numbers in parenthesis are the standard errors of the constants of the fit. This straight line is shown in Figure 5-6. A fit of only the thawed phyllite data in this stress range gives:

$$U_s = 5.084 (0.057) + 0.450 (0.172) u_p$$

If the stress range is extended to 16.21 GPa to include the VISAR data presented herein and the lower stress point derived by Furnish (1993) then:

$$U_s = 5.087 (0.078) + 0.540 (0.078) u_p$$

This fit, which is shown in Figure 5-6, is, within the accuracy of data, the same as the low stress thawed data fit. A linear fit of the data in the stress range of 10 to 50 GPa gives:

$$U_s = 4.939 (0.090) + 0.696 (0.054) u_p$$

This fit is also plotted in Figure 5-6. These data suggest that there is an inflection in the Hugoniot at

$$\begin{aligned}\sigma &= 14.8 \text{ GPa} \\ U_s &= 5.60 \text{ km/s} \\ u_p &= 0.95 \text{ km/s} \\ \rho/\rho_0 &= 1.204\end{aligned}$$

The Hugoniot in the stress-particle velocity and stress-relative density plots were calculated using:

$$\begin{aligned}U_s &= 5.087 + 0.540 u_p \text{ for } 0 < \sigma < 14.86 \text{ GPa} \\ \text{and } U_s &= 4.939 + 0.696 u_p \text{ for } 14.8 < \sigma < 50 \text{ GPa}\end{aligned}$$

These calculated Hugoniots are compared in Figures 5-7 and 5-8 to the experimental data in the stress-particle velocity and stress-relative density plane, respectively.

The Ktech measured particle velocity profiles (Figures 5-1 and 5-2) show no evidence of a precursor in the 10 to 15 GPa range (0.7 to 1.0 km/s particle velocity) however, since the upper Hugoniot is steeper than the lower Hugoniot, the shock velocities above the inflection are higher and the lower stress waves are over taken. (The small precursor, below 0.1 km/s, in Figures 5-1 and 5-2 was transmitted to the phyllite sample from the aluminum buffer.) The SNL data (Furnish 1993) was obtained using the reverse ballistic technique and consequentially a propagating precursor cannot be detected directly.

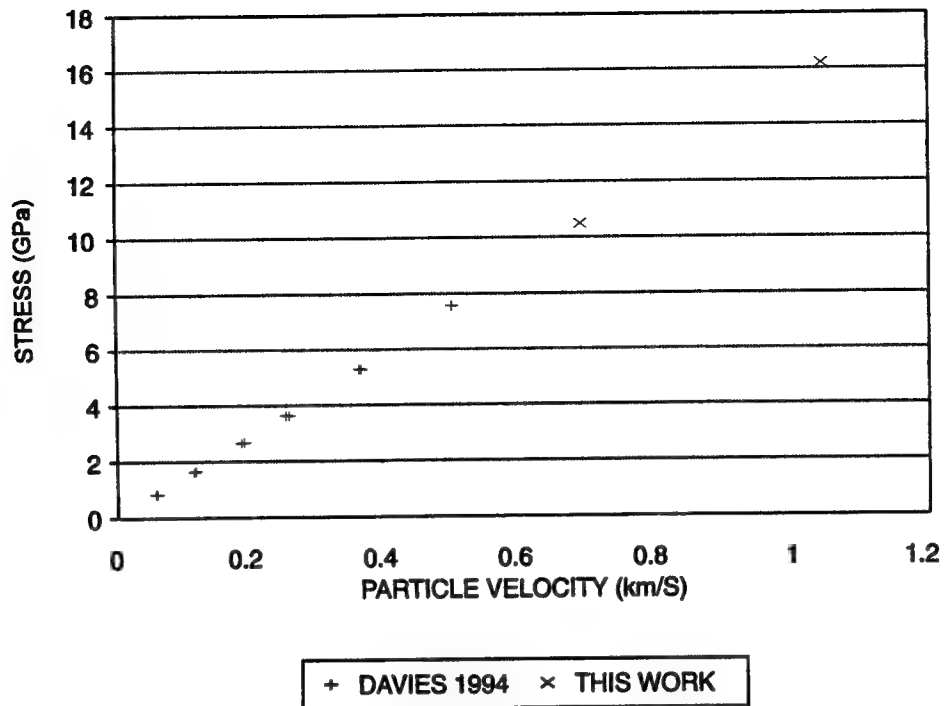


Figure 5-3. Thawed phyllite Hugoniot data in the stress-particle velocity plane.

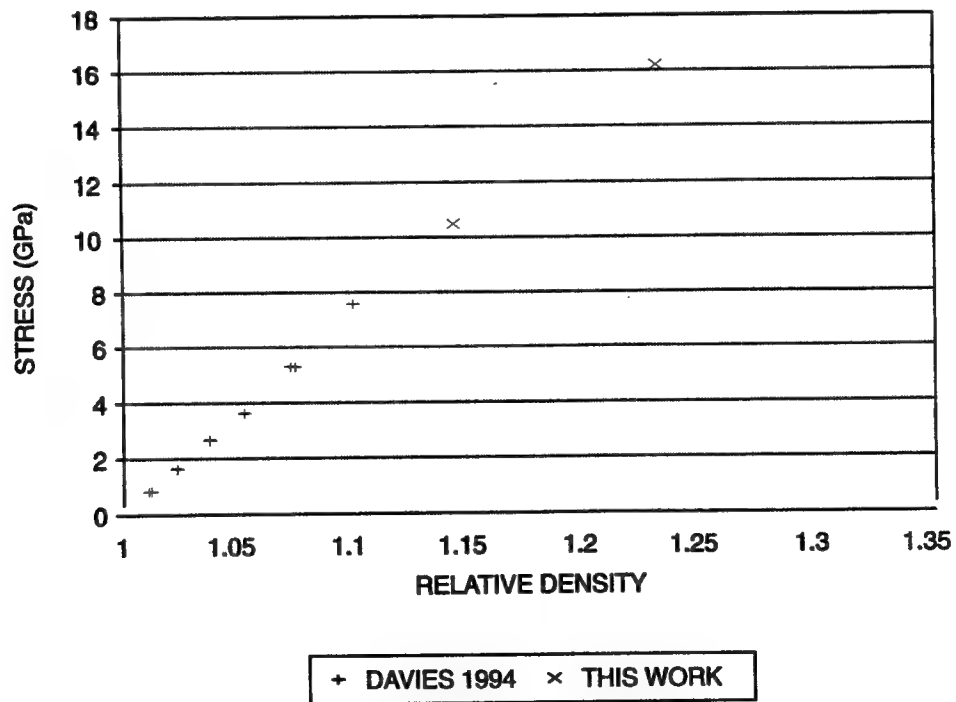


Figure 5-4. Thawed phyllite Hugoniot data in the stress-relative density ( $\rho/\rho_0$ ) plane.

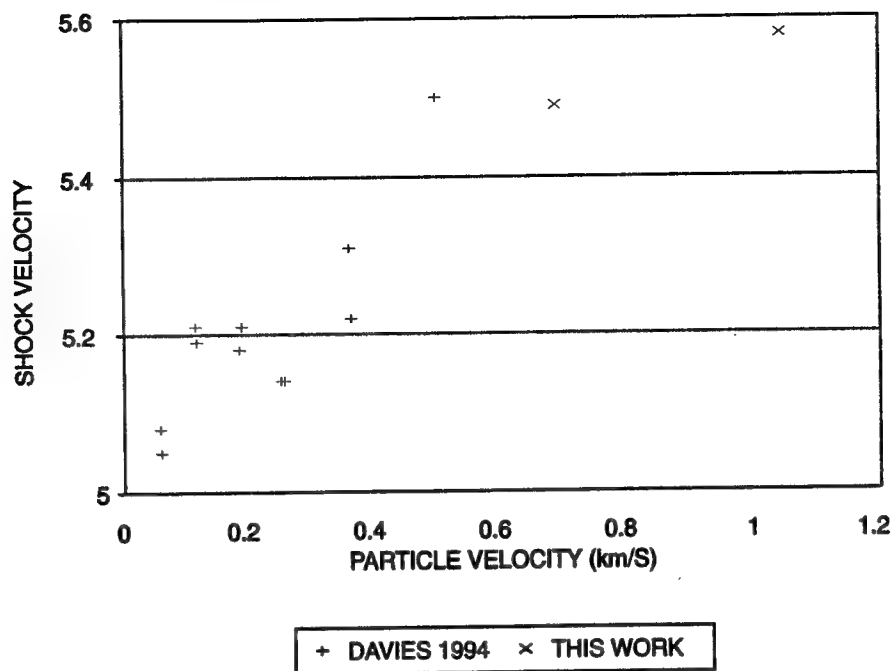


Figure 5-5. Thawed phyllite Hugoniot data in the shock velocity-particle velocity plane.

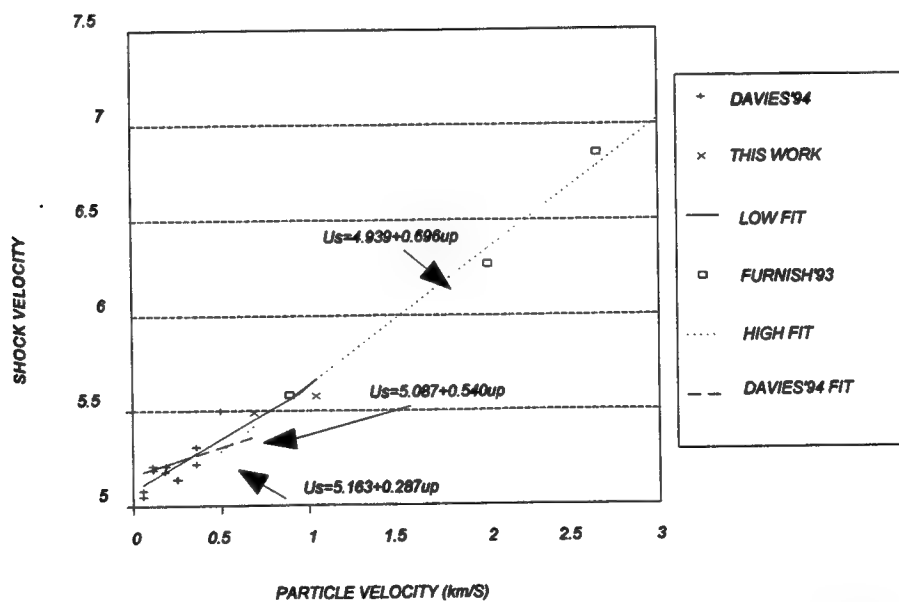


Figure 5-6. Comparison of linear fits to thawed phyllite data in the shock velocity-particle velocity plane.

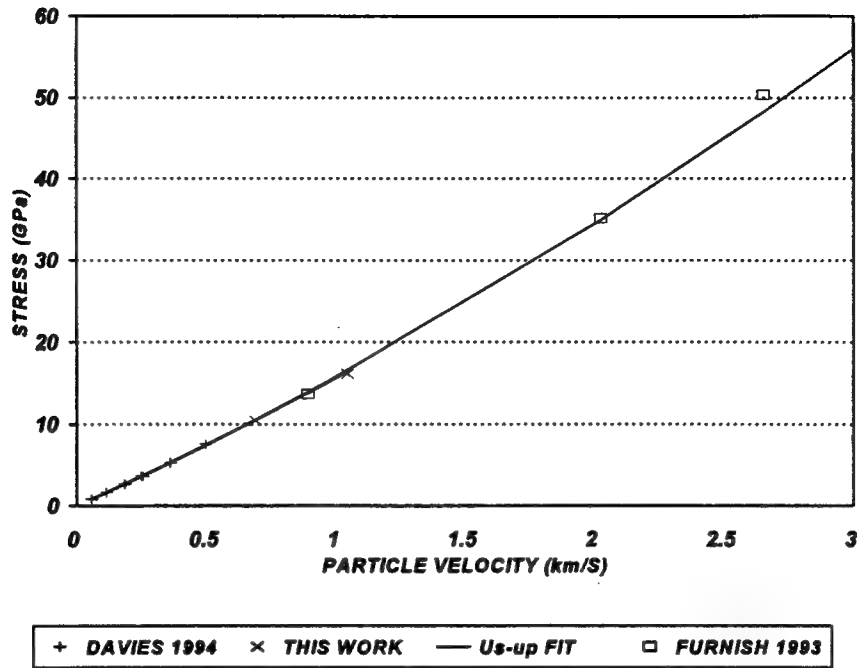


Figure 5-7. Comparison of experimental data in the stress-particle velocity plane to the  $U_s - u_p$  fits.

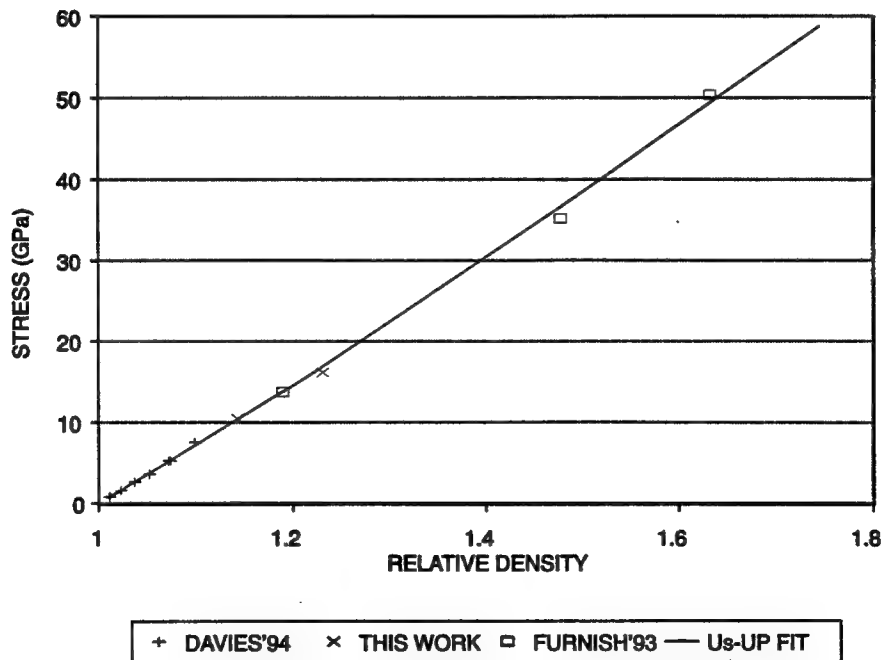


Figure 5-8. Comparison of experimental data in the stress relative density ( $\rho/\rho_0$ ) plane to the  $U_s - u_p$  fits.

## SECTION 6

### HSG-14 GROUT

This section presents material dynamic characterization data for HSG-14 Grout, a limestone matching grout. Five experiments were conducted using the Lagrangian-stress gauge configuration and three with the VISAR test configuration. Hugoniot data and shot configuration tables showing details of impactor and buffer material thicknesses, and sample number, density, and thickness are presented. All recorded waveforms are illustrated in Appendix A.

#### 6.1 MATERIAL DESCRIPTION.

The HSG-14 grout samples were machined from 4-inch diameter canisters poured by Waterways Experiment Station. The grout is a high density silicate grout (see Table 6-1) with particle diameters up to 4 mm as illustrated in Figure 6-1. The samples were stored in water to maintain saturation and tested at ambient temperature.

Table 6-1. Ingredients and mixture proportions for HSG-14 grout.

Ingredients	Weight in lbs to produce a 1-ft <sup>3</sup> batch
Portland Cement Type I (Capitol)	31.88
Fly Ash (NTS)	14.49
Silica Fume	4.83
Bauxite	82.12
Barite	17.10
PSP (Plasticizer)	0.96
Retarder	(2.03 fl.oz.)
Water	16.61
Theoretical Unit Weight	168.0 pcf (2.69 g/cm <sup>3</sup> )

Sample characterization data are presented in Table 6-2. The accuracy of each measurement is indicated at the top of each column. The sample thicknesses listed in Table 6-2 are as-received sample thicknesses. The average sample density was 2.63 g/cm<sup>3</sup> (std. dev. = 0.009) and the average ultrasonic longitudinal and shear velocities were 6.23 (std. dev. = 0.12) and 3.14 km/s, respectively.

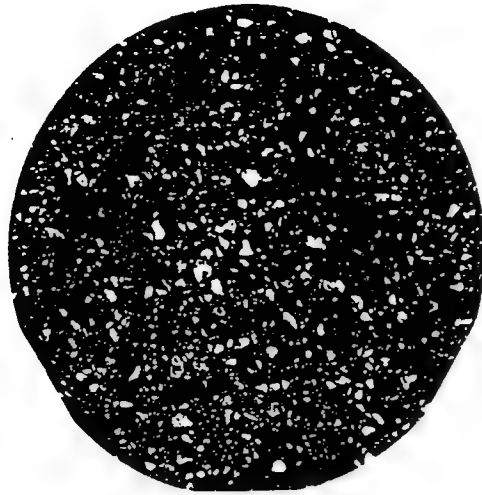


Figure 6-1. HSG-14 grout samples contained particles up to 4-mm diameter.

Table 6-2. Material properties for HSG-14 grout.

Sample No.	Avg. Thk (mm) $\pm 1\%$	Density* (gm/cc) $\pm 1\%$	Longitudinal Velocity* (km/s) $\pm 5\%$	Shear Velocity* (km/s) $\pm 5\%$
HSG14-1	5.02	2.64	6.32	3.13
HSG14-2	5.02	2.62	6.33	
HSG14-3	5.02	2.63	6.21	
HSG14-4	5.02	2.63	6.27	
HSG14-5	5.02	2.63	6.32	
HSG14-6	5.02	2.64	6.37	
HSG14-7	5.02	2.64	6.32	
HSG14-8	5.02	2.64	6.26	
HSG14-9	5.03	2.63	6.27	
HSG14-10	5.02	2.63	6.32	
HSG14-11	5.00	2.62	6.29	
HSG14-12	5.03	2.61	6.28	
HSG14-13	5.02	2.63	6.32	
HSG14-14	5.03	2.62	6.22	
HSG14-15	8.00	2.61	6.07	
HSG14-16	10.02	2.62	5.92	
HSG14-17	10.03	2.62	6.07	
HSG14-18	10.01	2.62	6.11	
HSG14-19	10.01	2.63	6.11	
Average		2.626	6.231	3.15
Std. Deviation		0.009	0.116	
*Measurements have been rounded, however, the average and standard deviations were performed using nonrounded measurements.				

## 6.2 TEST RESULTS.

Five Lagrangian stress gauge experiments were conducted at nominal stress levels of 0.8, 1.5, 3.0, 4.0, and 5.0 GPa and three VISAR experiments were conducted between 8 and 11 GPa. The experimental configuration for both the Lagrangian stress and VISAR measurements are detailed in Section 2.

Table 6-3 contains shot configuration information for each experiment. Impactor and buffer material thicknesses and thicknesses and densities of the individual samples in each target are listed. Sample thicknesses are as-built center thicknesses. Measured stress time and particle velocity-time profiles for each experiment are provided in Appendix A.

Table 6-3. HSG-14 grout.

Shot #	Thickness (mm) and Density (g/cm <sup>3</sup> )										
	6061-T6 Impact Thk	6061-T6 Buffer Thk	Sample 1			Sample 2			Sample 3		
			No	Ctr Thk	$\rho_o$	No	Ctr Thk	$\rho_o$	No	Ctr Thk	$\rho_o$
3628	6.32	9.55	HSG-14-6	5.02	2.64	HSG14-7	5.02	2.64	HSG14-16	10.02	2.62
3629	6.27	9.55	HSG14-11	4.99	2.62	HSG14-14	5.02	2.62	HSG14-19	10.01	2.63
3630	6.32	9.53	HSG14-10	5.02	2.63	HSG14-13	5.02	2.63	HSG14-17	10.02	2.62
3631	6.25	9.55	HSG14-5	5.02	2.63	HSG14-9	5.02	2.63	HSG14-18	10.01	2.62
3632	6.33	9.54	HSG14-2	5.02	2.62	HSG14-12	5.03	2.61	HSG14-15	10.02	2.61
3634	10.16	9.53	HSG14-1	5.02	2.64	PMMA	0.76	1.19	PMMA	24.82	1.19
3636	6.35*	9.52	HSG14-3	5.02	2.63	PMMA	0.77	1.19	PMMA	24.66	1.19
3638	7.52	9.53	HSG14-8	5.02	2.64	PMMA	0.77	1.19	PMMA	25.01	
*WC impactor											

The Hugoniot data were derived from the measured stress profiles using the Lagrangian analysis for each experiment. In addition, Hugoniot data were calculated from the measured half-amplitude shock velocity and the equilibrium stress level using the Rankine-Hugoniot relations. The steady state assumptions are discussed in Section 2. The Hugoniot data are given in Table 6-4. These data are presented in the stress-particle velocity, stress-relative density, and shock velocity-particle velocity planes in Figures 6-2, 6-3, and 6-4, respectively. The measured stress-time profiles for the shots with three Lagrangian (axial) stress gauges are shown in Figure 6-5. The measured particle velocity profiles are given in Figure 6-6.



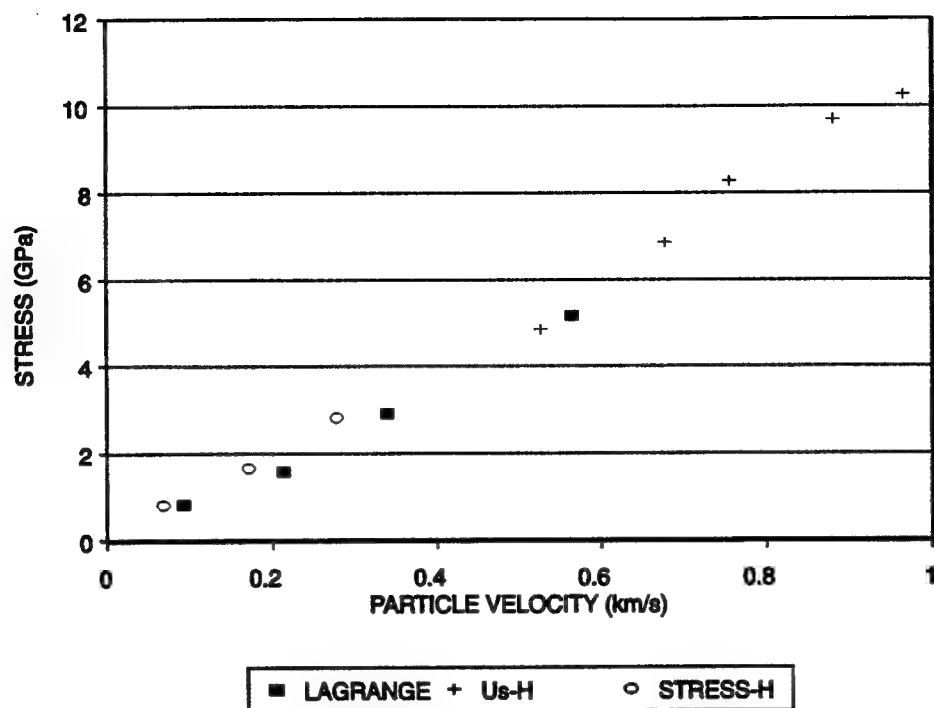


Figure 6-2. HSG14 Hugoniot data, stress-particle velocity plane.

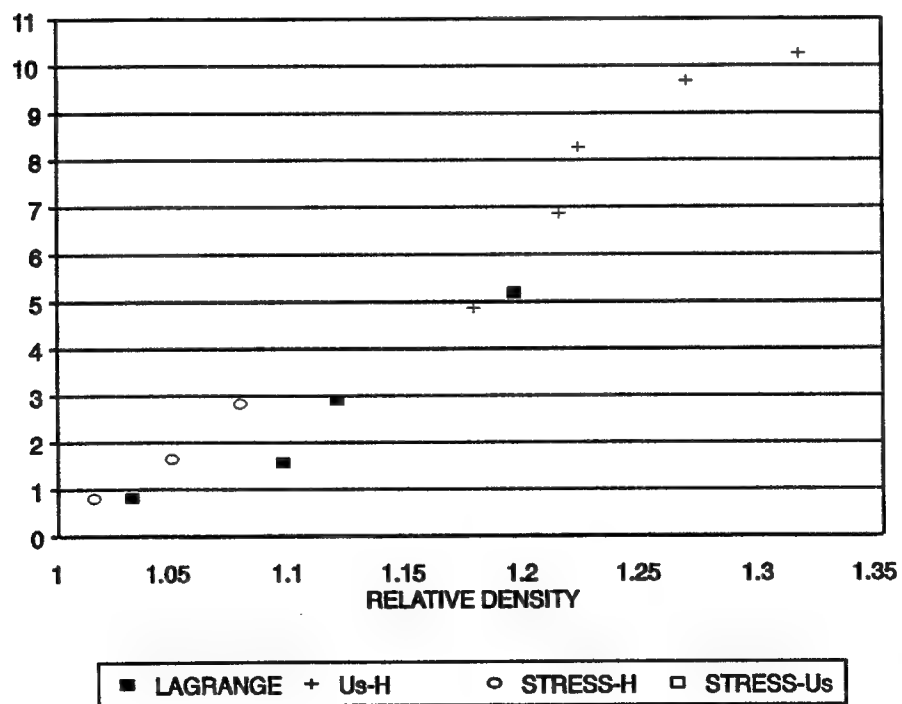


Figure 6-3. HSG14 grout Hugoniot data, stress-relative density ( $\rho/\rho_0$ ) plane.

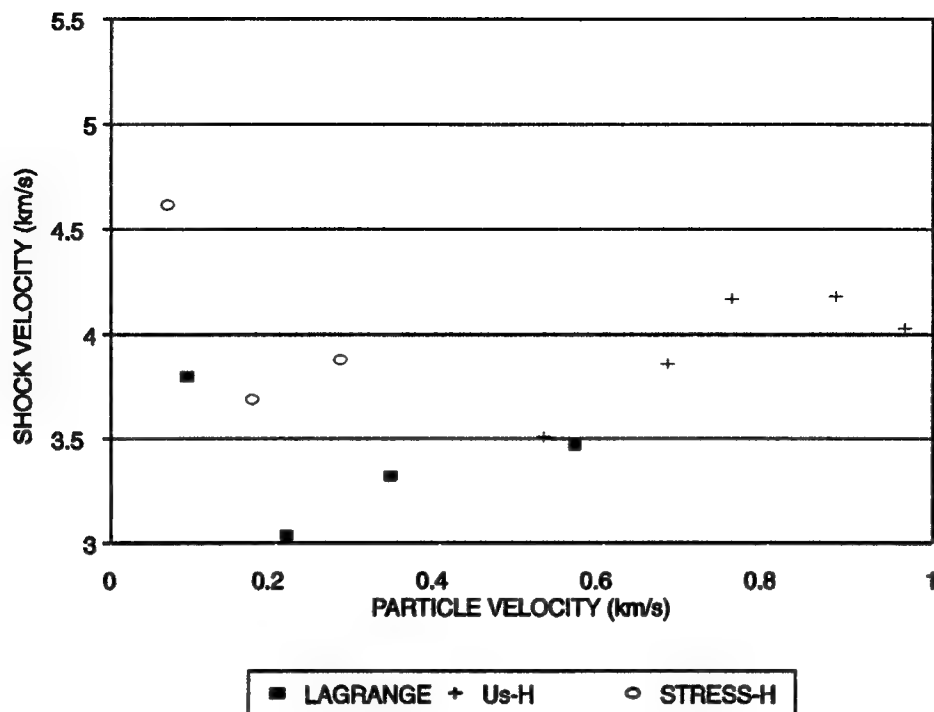


Figure 6-4. HSG14 grout Hugoniot data, shock velocity-particle velocity plane.

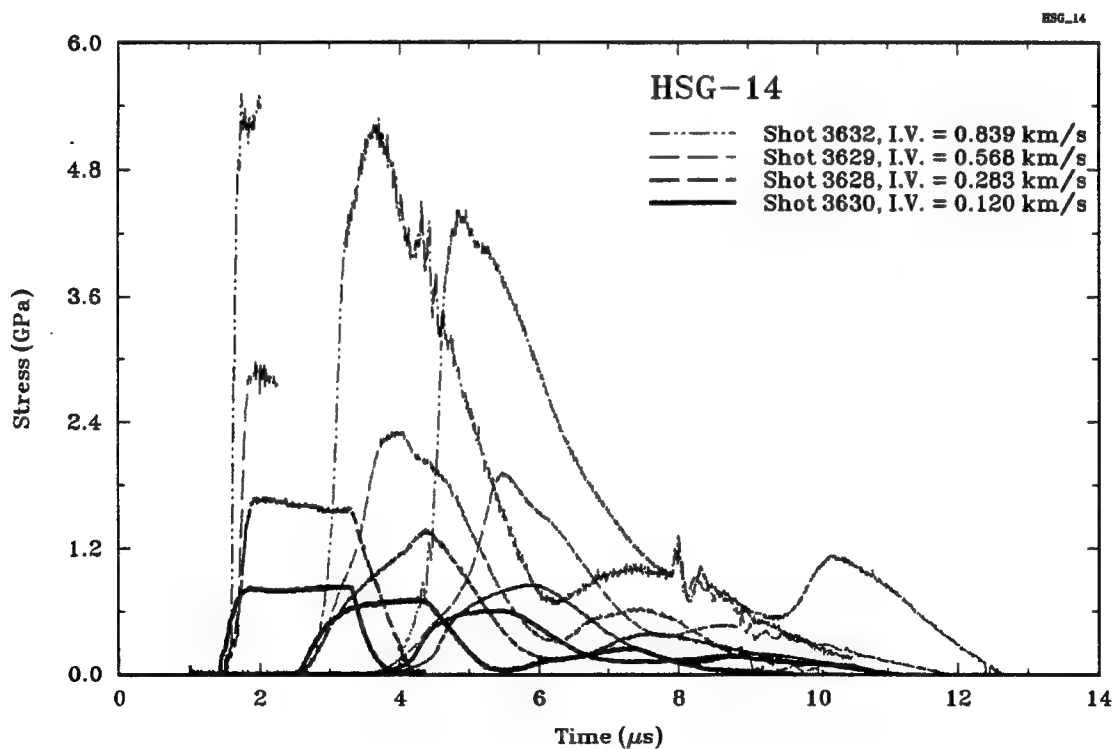


Figure 6-5. Measured stress profiles in HSG-14 grout.

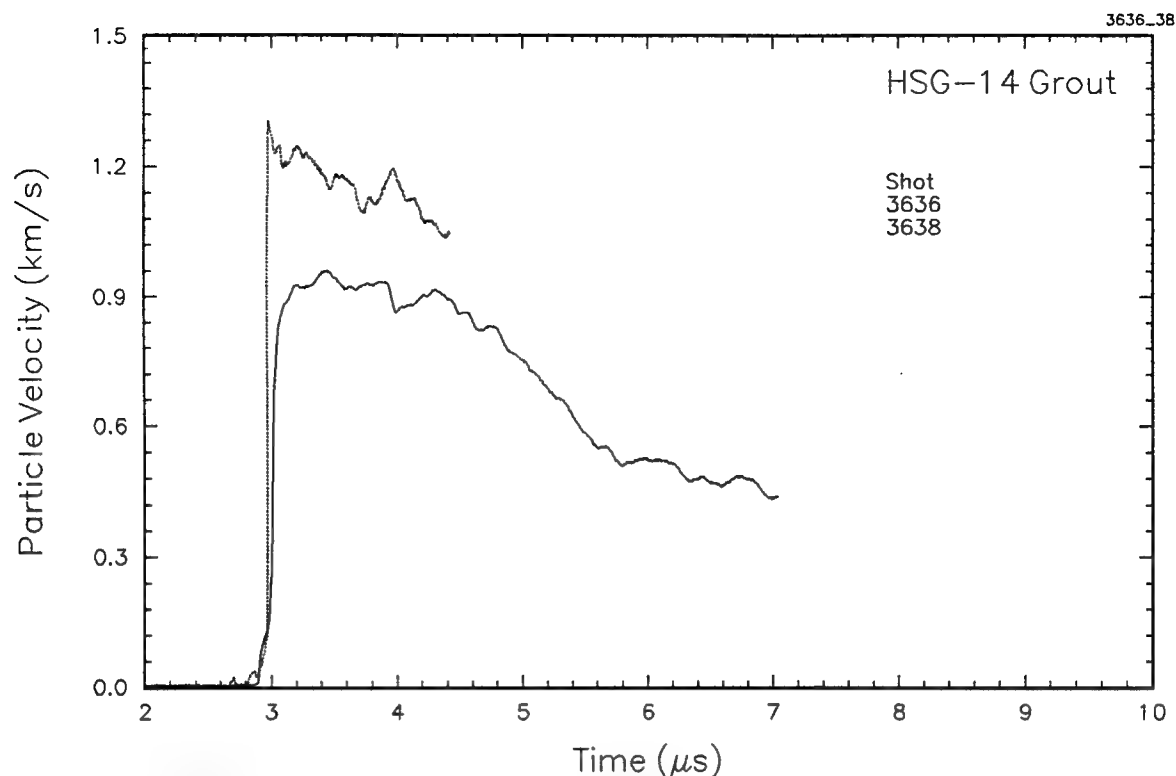


Figure 6-6. Measured particle velocity profiles in HSG-14 grout.

Table 6-4. HSG-14 grout hugoniot data.

Shot #	Impact Velocity (km/s)	Conf.	Initial Density (g/cm <sup>3</sup> )	Hugoniot			
				Stress (GPa)	U <sub>s</sub> , 1/2 amp (km/s)	u <sub>p</sub> (km/s)	ρ/ρ <sub>0</sub>
Lagrangian							
3628	0.283	a	2.63	1.58	3.04	0.213	1.095
3629	0.468	a	2.63	2.91	3.32	0.340	1.118
3630	0.120	a	2.63	0.83	3.80	0.092	1.031
3632	0.839	a	2.63	5.18	3.47	0.565	1.194
Shock Velocity, Known Al Hugoniot							
3631	1.122	a	2.63	6.87	3.86	0.678	1.213
3632	0.839	a	2.61	4.86	3.51	0.527	1.177
3634	1.472	b	2.64	9.69	4.18	0.882	1.267
3636	0.935	c	2.63	10.26	4.03	0.966	1.315
3638	1.268	b	2.64	8.28	4.17	0.756	1.221
Stress, Known Al Hugoniot							
3628	0.283	a	2.63	1.66	3.69	0.171	1.048
3629	0.468	a	2.62	2.83	3.88	0.278	1.077
3630	0.120	a	2.63	0.82	4.62	0.068	1.015
Stress, Shock Velocity							
3632	0.839	a	2.61	5.21	3.51	0.568	1.193
Configuration: (a) 6061-T6 → 6061-T6/CG/HSG14/CG/HSG14/CG/HSG14							

### 6.3 DISCUSSION

The measured stress profiles show that the peak stress of the propagating wave is attenuating and that the leading edge is dispersive (i.e., the rise time is increasing with propagating distance). The leading toe of the stress wave is propagating at a velocity equal to the ultrasonic bulk wavespeed (5.07 km/s). All of the in-depth stress profiles above 0.5 GPa show an inflection in the leading edge of the wave. At the higher impact stresses, the wave steepens above the inflection (i.e., the stress wave is shocking up). This suggests that the Hugoniot changes from downward concave (dispersive) to upward concave. The authors of this report have observed similar wave propagation characteristics (i.e., dispersive toe and shock-up at high impact stresses) in other heterogeneous, aggregate/matrix constituent tuff materials; namely, BEXGC-1 grout and Hunters Trophy Tuff (Davies 1993), Hunters Trophy Tuff (Gaffney 1994), HJC-7 concrete (Davies 1994) and granite grout (Section 7).

The Hugoniot data listed in Table 6-4 is plotted in Figure 6-7 in the shock velocity-particle velocity plane and the data is fitted with two straight lines.

$$U_s = 4.42 (0.37) - 2.96 (1.60) \text{ for } 0 < \sigma < 3.5 \text{ GPa}$$

$$\text{and } U_s = 2.75 (0.16) + 1.52 (0.30) \text{ for } 3.5 < \sigma < 11 \text{ GPa}$$

where the shock velocity,  $U_s$ , and the particle velocity,  $u_p$ , are given in km/s and the numbers in parenthesis are the standard errors of the constants. This fit is compared to the experimental data in the stress-particle velocity, stress-relative density ( $\rho/\rho_0$ ) plane in Figures 6-8 and 6-9, respectively.

The lowest shock velocity measurement (see Figure 6-10) was 3.04 km/s from shot 3628. It should be noted that this half amplitude velocity corresponds to a point on the stress profile which is a transition state between the dispersive toe and the beginning of stress wave shock-up.

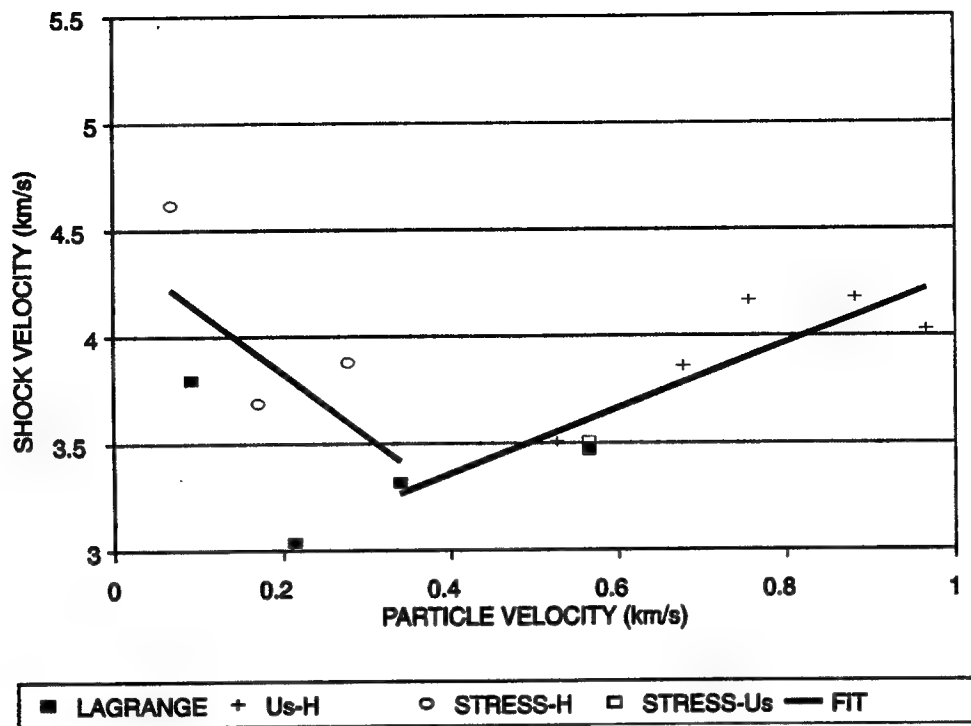


Figure 6-7. Comparison of fitted Hugoniot to experimental data in the shock velocity-particle velocity plane.

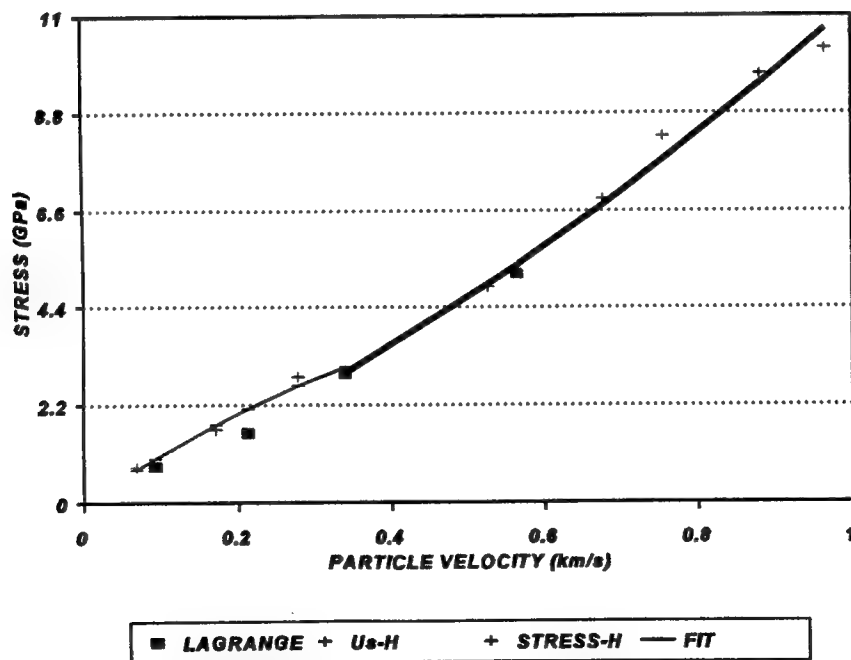


Figure 6-8. Comparison of measured HSG-14 grout data to fitted Hugoniot in the stress-particle velocity plane.

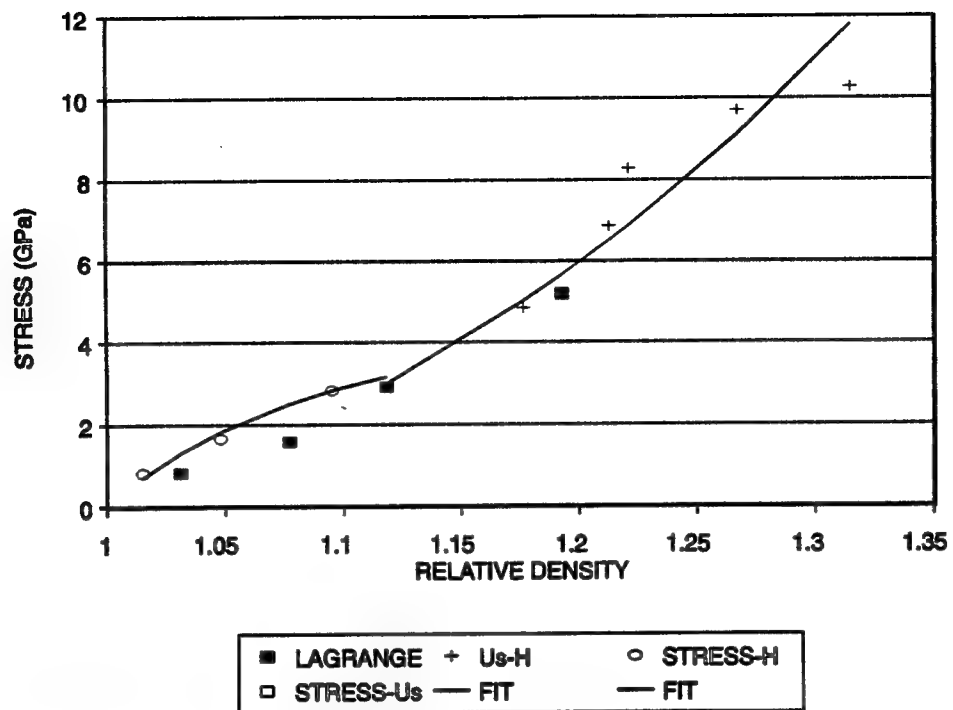


Figure 6-9. Comparison of fitted Hugoniot to experimental data in the stress-relative density plane.

## SECTION 7

### GRANITE GROUT

This section presents material dynamic characterization data for a Granite Grout, which was designed as a SHIST test satellite hole grout. Five experiments were conducted using the Lagrangian-stress gauge configuration and three with the VISAR test configuration.

Hugoniot data and shot configuration tables showing details of impactor and buffer material thicknesses, and sample number, density, and thickness are presented. All recorded waveforms are illustrated in Appendix A.

#### 7.1 MATERIAL DESCRIPTION.

The Granite grout samples were machined from 4-inch diameter cannisters (SHI mix #2) poured by Waterways Experiment Station (WES). The WES ingredients and mixture proportions of the Granite grout, a high-density grout, are listed in Table 7-1 (Martinez 1993). The samples were stored in ziplock bags to maintain water content and were tested in the as-received condition at ambient temperature.

Table 7-1. Ingredients and mixture proportions for granite grout SHI mix #2.

Ingredients	Weight in lbs to produce a 1-ft <sup>3</sup> batch
Portland Cement	25.81
Ilmenite Sand (Simi Valley, CA)	82.74
Silica Flour (NTS)	18.66
Silica Fume (NTS)	3.25
Gypsum (CALSEAL)	3.88
Aqua Gel Bentonite	1.68
PSP HRWR Powder	0.265
Retarding Densifer (Plastiment)	0.81 fl.oz.
DEAIR	0.065
Water	26.05
Total (air free)	162.07

Sample characterization data are presented in Table 7-2. The accuracy of each measurement is indicated at the top of each column.

Table 7-2. Material properties for granite grout.

Sample No.	Avg. Thk (mm) $\pm 1\%$	Density* (gm/cc) $\pm 1\%$	Longitudinal Velocity* (km/sec) $\pm 5\%$	Shear Velocity* (km/sec) $\pm 5\%$
GG-1	5.01	2.56	3.99	1.85
GG-2	5.02	2.59	4.06	1.93
GG-3	5.02	2.58	4.06	1.89
GG-4	5.00	2.59	4.05	
GG-5	5.01	2.56	4.05	
GG-6	5.01	2.57	4.01	
GG-7	5.00	2.58	4.00	
GG-8	5.02	2.59	3.97	
GG-9	5.01	2.55	4.07	
GG-10	5.00	2.57	4.09	
GG-11	5.01	2.56	4.08	
GG-12	5.02	2.56	4.02	
GG-13	5.01	2.57	4.05	
GG-14	5.01	2.56	4.01	
GG-15	5.01	2.55	4.01	
GG-16	5.01	2.57	3.99	
GG-17	10.02	2.58	3.77	
GG-18	10.02	2.57	3.78	1.86
GG-19	10.03	2.57	3.78	
GG-20	10.02	2.58	3.78	
GG-21	10.02	2.57	3.76	
GG-22	10.02	2.57	3.72	
Average		2.571	3.959	1.882
Std. Deviation		0.0116	0.1236	0.0282
*Measurements have been rounded, however, the average and standard deviations were performed using nonrounded measurements.				

The sample thicknesses listed in Table 7-2 are as-received sample thicknesses. The average sample density was  $2.571 \text{ g/cm}^3$  (std. dev. = 0.016) and the average ultrasonic longitudinal and shear velocities were 3.59 (std. dev. = 0.12) and 1.882 km/s (std. dev. = 0.03), respectively.

## 7.2 TEST RESULTS.

Five Lagrangian stress gauge experiments were conducted at nominal stress levels of 0.5, 1.0, 2.0, 3.5, and 5.0 GPa and three VISAR experiments were conducted at 5.5, 7.5 and 10.0 GPa. The experimental configuration for both the Lagrangian stress and VISAR measurements are detailed in Section 2.



Table 7-3 contains shot configuration information for each experiment. Impactor and buffer material thicknesses and thicknesses and densities of the individual samples in each target are listed. Sample thicknesses are as-built center thicknesses. Measured-stress time and particle velocity-time profiles for each experiment are provided in Appendix A.

Table 7-3. Shot configuration data.

Shot #	Thickness (mm) and Density (g/cm <sup>3</sup> )										
	6061-T6 Impact Thk	6061-T6 Buffer Thk	Sample 1			Sample 2			Sample 3		
			No	Ctr Thk	$\rho_0$	No	Ctr Thk	$\rho_0$	No	Ctr Thk	$\rho_0$
3708	9.88	-	GG-2	5.02	2.59	GG-3	5.01	2.58	GG-17	10.02	2.58
3709	9.45	-	GG-7	4.88	2.58	GG-10	5.00	2.57	GG-18	9.92	2.57
3716	6.42*	-	GG-15	5.01	2.57	PMMA	0.77	1.19	PMMA	24.71	1.19
3715	6.36*	-	GG-13	5.00	2.57	PMMA	0.56	1.19	PMMA	24.73	1.19
3717	9.54	-	GG-16	5.01	2.57	PMMA	0.77	1.19	PMMA	24.90	1.19
3721	9.51	9.53	GG-8	5.01	2.59	GG-9	5.00	2.55	GG-22	10.01	2.57
3722	9.50	9.57	GG-11	5.00	2.56	GG-14	5.00	2.56	GG-19	10.01	2.57
3723	9.50	9.54	GG-1	4.99	2.56	GG-14	4.98	2.59	GG-21	10.01	2.57
*Tungsten Carbide Impactor											

Hugoniot data were calculated from the measured half-amplitude shock velocity and the equilibrium stress level using the Rankine-Hugoniot relations. The steady state assumptions are discussed in Section 2. The Hugoniot data are given in Table 7-4. These data are presented in the stress-particle velocity, stress-relative density, and shock velocity-particle velocity planes in Figures 7-1, 7-2, and 7-3, respectively. The measured stress-time profiles for the shots with three Lagrangian stress gauges are shown in Figure 7-4. The measured particle velocity profiles are given in Figure 7-5.

Table 7-4. Granite grout hugoniot data.

Shot #	Impact Velocity (km/s)	Conf.	Initial Density (g/cm <sup>3</sup> )	Hugoniot			
				Stress (GPa)	U, 1/2 amp (km/s)	u <sub>p</sub> (km/s)	ρ/ρ <sub>o</sub>
Stress, Known Al Hugoniot							
3708	0.111	a	2.59	0.38	1.63	0.089	1.058
3709	0.271	a	2.58	0.9	1.63	0.215	1.152
3722	0.270	b	2.56	0.84	1.51	0.218	1.169
Shock Velocity, Known Al Hugoniot							
3709	0.271	a	2.58	0.85	1.502	0.219	1.170
3715	1.206	d	2.57	10.20	3.58	1.108	1.449
3716	1.029	d	2.57	8.40	3.45	0.948	1.379
3717	0.981	c	2.57	4.96	2.91	0.6630	1.295
3712	0.734	b	2.59	3.23	2.38	0.523	1.282
3723	0.476	b	2.56	1.49	1.53	0.379	1.328
Configuration: (a) 6061-T6 - CG/GG/CG/GG/CG/GG (b) 6061-T6 - 6061-T6/CG/GG/CG/GG/CG/GG (c) 6061-T6 - GG/PMMA/VISAR/PMMA (c) WC - GG/PMMA/VISAR/PMMA							

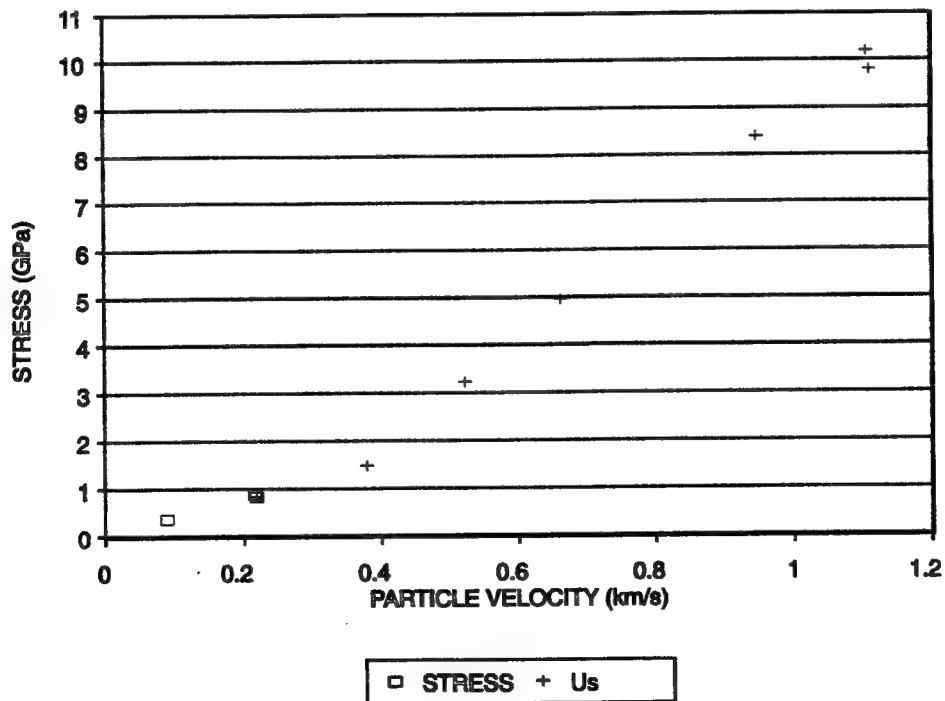


Figure 7-1. Granite grout Hugoniot data, stress-particle velocity plane.

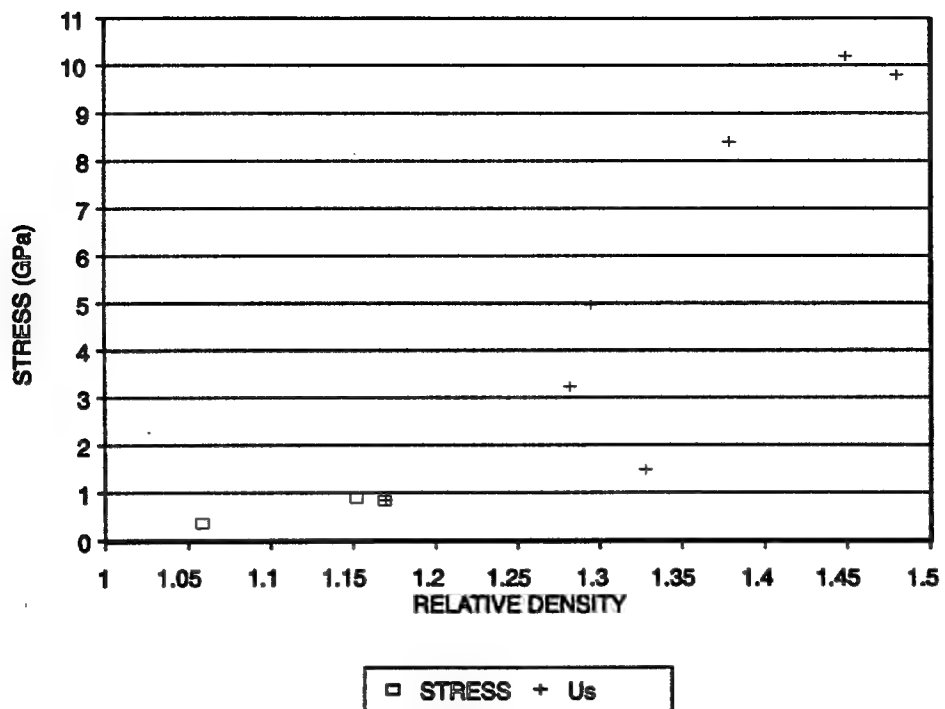


Figure 7-2. Granite grout Hugoniot data, stress-relative density ( $\rho/\rho_0$ ) plane.

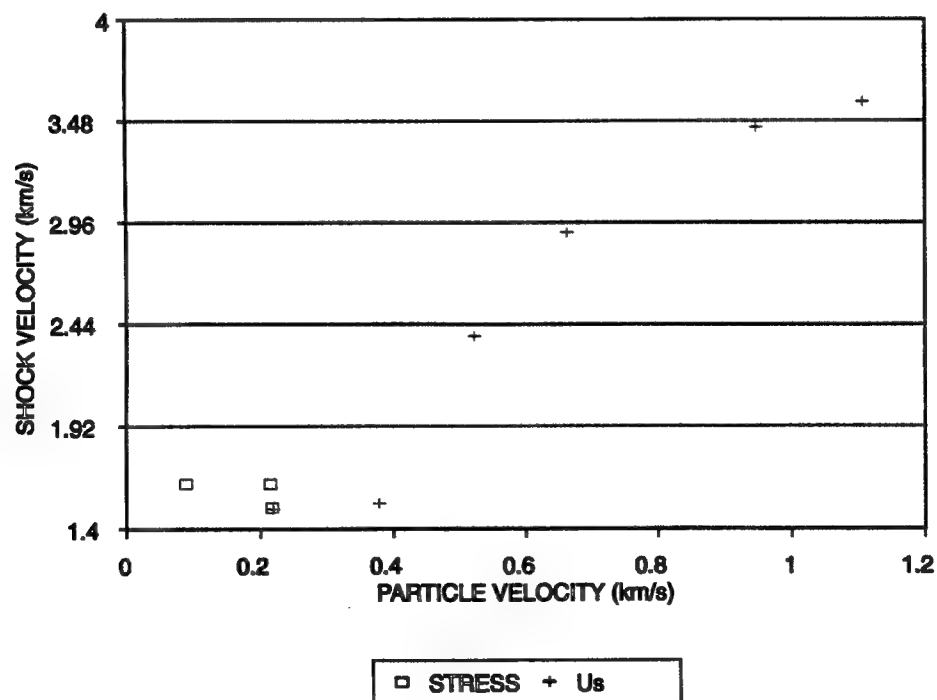
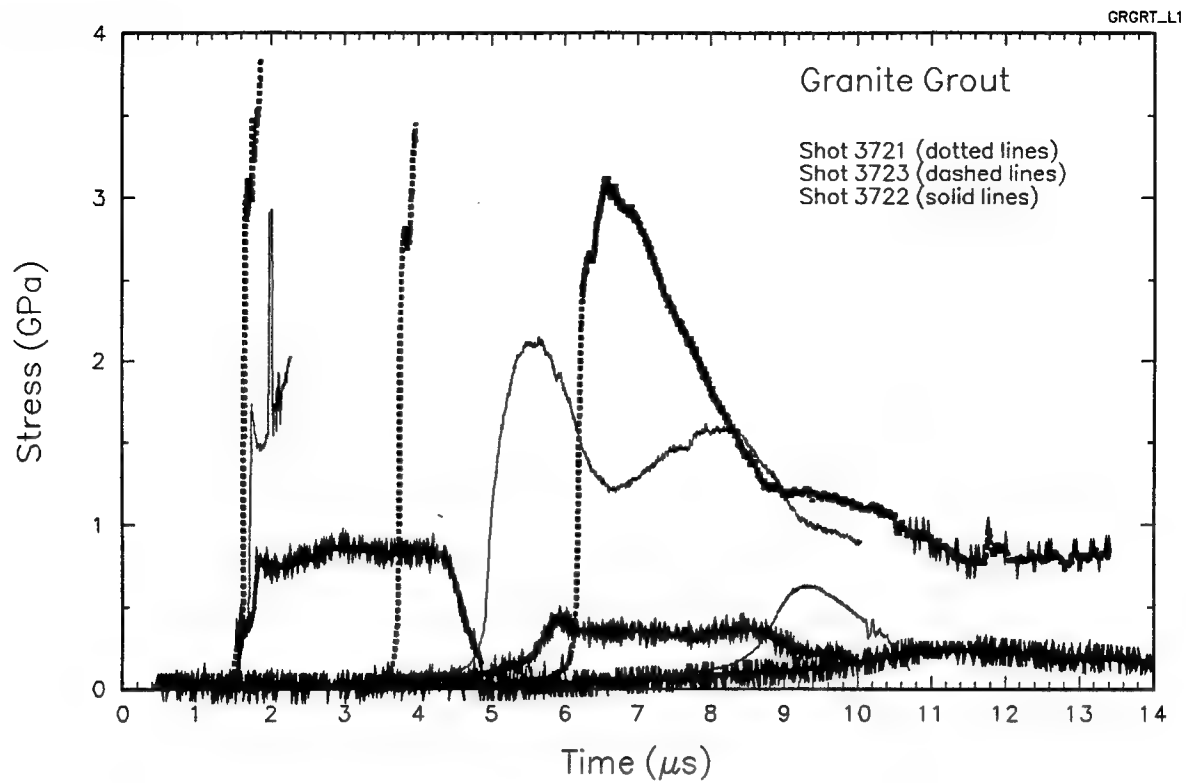
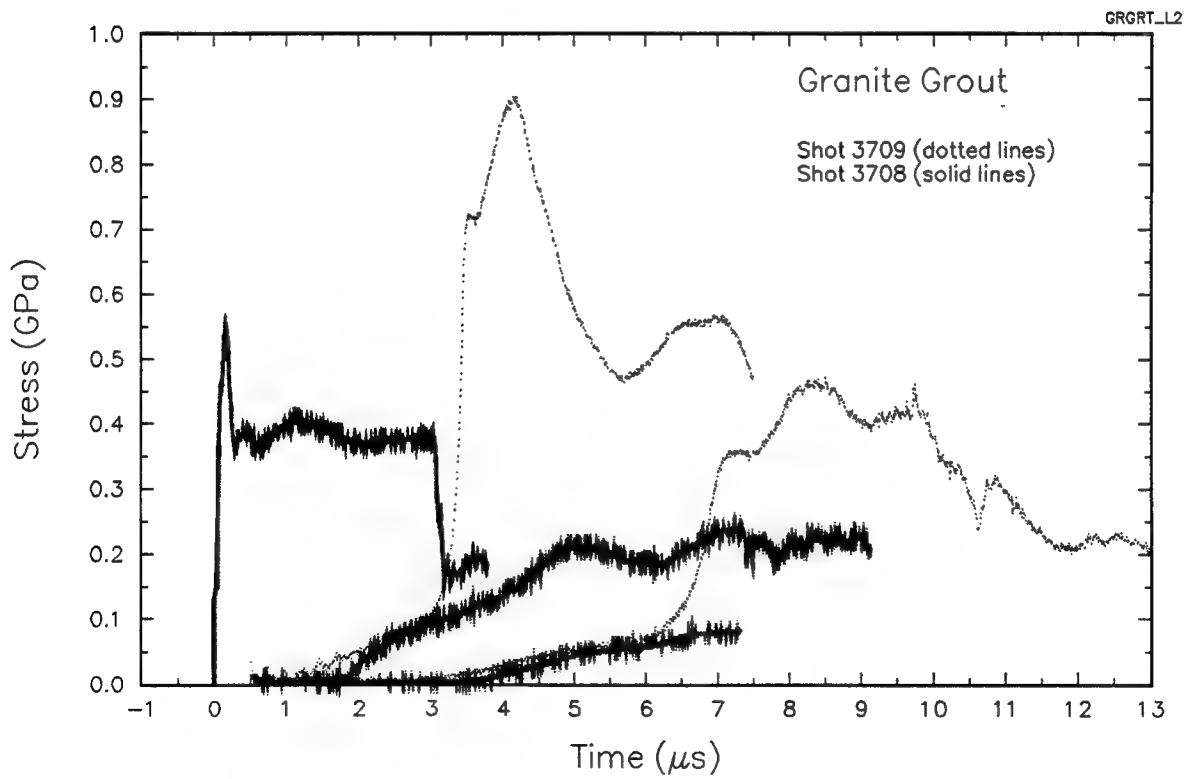


Figure 7-3. Granite grout Hugoniot data, shock velocity-particle velocity plane.



(a) with aluminum buffer.



(b) without aluminum buffer.

Figure 7-4. Lagrangian gauge stress-time profiles in granite grout.

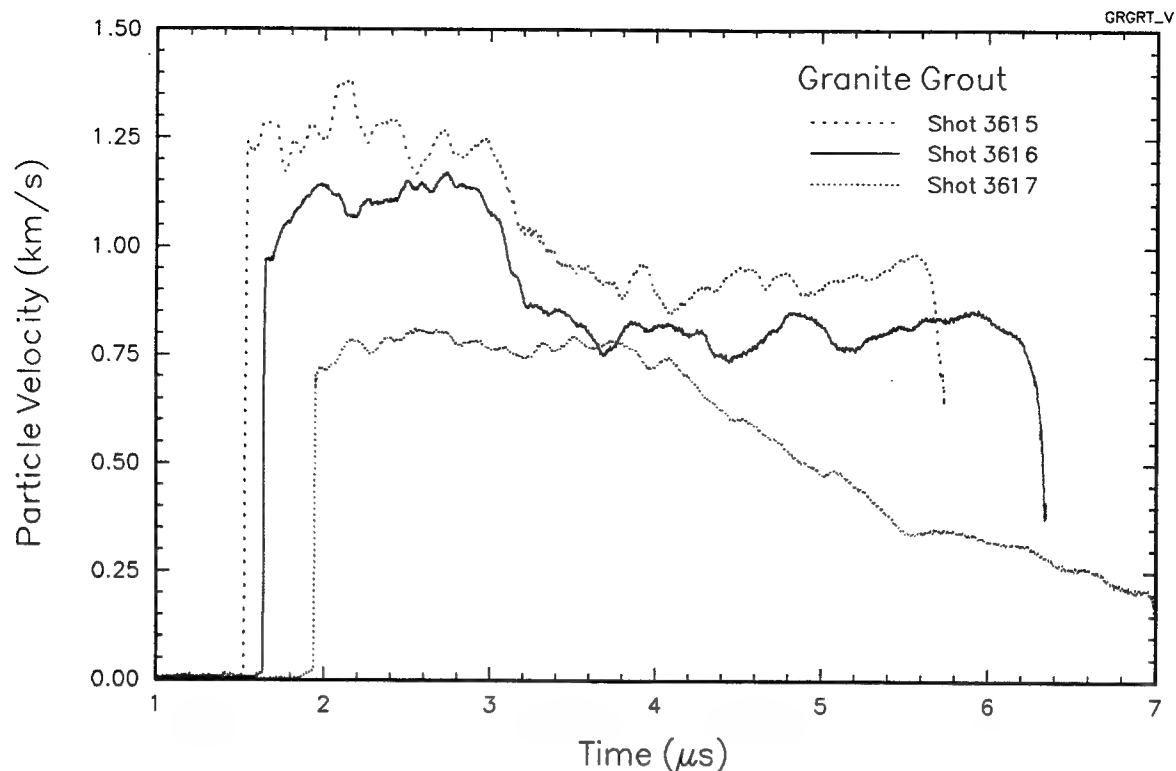


Figure 7-5. VISAR particle velocity-time profiles for granite grout.

### 7.3 DISCUSSION.

The Lagrangian stress-time profiles (Figure 7-4) show this Granite grout to be a highly attenuative and dispersive material. At an impact stress of 0.4 GPa (shot 3708) the propagating waveforms are slowly rising dispersive ramps with highly attenuated peak stresses. No shock (steep risetime) is propagated.

At 0.84 GPa impact stress (shot 3722), the waveforms are dominated by the dispersive precursor although the Lagrangian gauge at 5 mm shows steepening of a shock front about 2.5  $\mu$ s after the toe of the precursor arrives. The gauge at 10 mm recorded a ramp pulse. The attenuation of the stress pulse with distance is severe. The rise time of the waveform more than doubles during propagation from 5 to 10 mm into the test sample.

The shock is well defined at the 5 mm station for impact stresses above 0.9 GPa, while the waveform is starting to steepen at the 10 mm station. A highly dispersive precursor is still evident, however the shock is overtaking the precursor. At 3.2 GPa impact (shot 3721) the dispersive precursor is still

measurable, but the shock has nearly completely overtaken the dispersive ramp. The precursor was less than 0.2  $\mu$ s duration at an impact stress of 5 GPa (shot 3717) and no precursor was detected at the highest impact stresses (10 GPa, shot 3715) examined in this test series, as shown in Figure 7-5.

The precursor amplitude (the peak amplitude before the ramp starts to steepen into a shock) is 0.1 GPa and the leading toe propagates at 3.3 km/s. This compares to the measured ultrasonic longitudinal wave velocity of 3.96 km/s and the calculated bulk wavespeed of 3.0 km/s. Figure 7-6 shows attenuation of the peak stress as a function of impact stress after 5 and 10-mm propagation. The dispersive precursor is dominating the observed attenuation at the shorter distance at lower stresses. At the higher stresses after 5-mm propagation the main wave has not been attenuated by catchup and the attenuation is therefore low. The smoother attenuation curve after 10-mm propagation results from the main wave being attenuated by catchup of the relief wave at the higher impact stresses.

The Hugoniot data in the shock velocity-particle velocity plane can be fitted by two straight lines as shown in Figure 7-7. These fits are given by:

$$U_s = 1.69(0.070) - 0.667(0.63) \text{ for } 0 < \sigma < 0.85 \text{ GPa}$$

$$\text{and } U_s = 0.97(0.266) + 2.42(0.30) \text{ for } 0.85 < \sigma < 11 \text{ GPa}$$

where the shock velocity  $U_s$  and particle velocity  $u_p$  are in km/s and the numbers in parenthesis are the standard errors of the constants. The low stress data shows the shock velocity to be almost independent of particle velocity. In the precursor regime (below 0.1 GPa) the leading toe of the precursor is propagating at 3.3 km/s and the Hugoniot is expected to be concave downward to provide for the dispersive character of the propagating stress wave. The Hugoniot has an inflection changing to upward concave at 0.85 GPa. Comparison of the fitted Hugoniot to the experimental data in the stress-particle velocity and stress-relative density ( $\rho/\rho_0$ ) planes are shown in Figures 7-8 and 7-9, respectively.

Granite grout, HSG-14 grout and HJC-7 concrete (Davies, 1994) all show the same type of dynamic material behavior. Each has a dispersive precursor which is outrun by a steep front shock at higher stresses. All of these materials can be described as a high impedance aggregate in a low impedance matrix. The grouts could be considered to be a small scale concrete. Preliminary hydrocode

calculations have shown that the shape of the Hugoniot cannot account for all of the observed dispersion and attenuation. A geometric dispersion model is required to account for the observed character of the propagated stress waves. Additional low stress characterization of the grouts using a large bore gas gun combined with the development of a hydrocode geometric dispersion model could elucidate the modeling of large aggregate concrete materials.

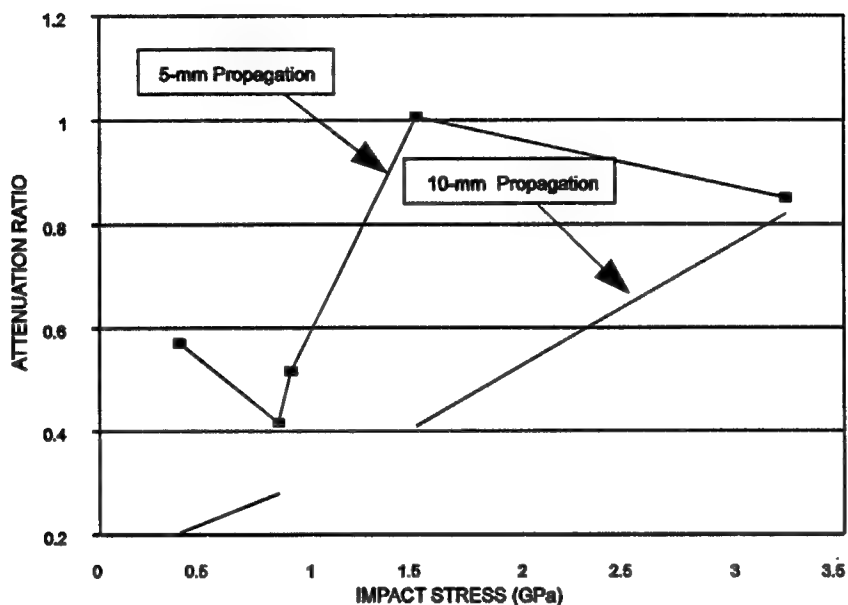


Figure 7-6. The attenuation of peak stress as a function of impact stress for propagation distances of 5 and 10 mm.

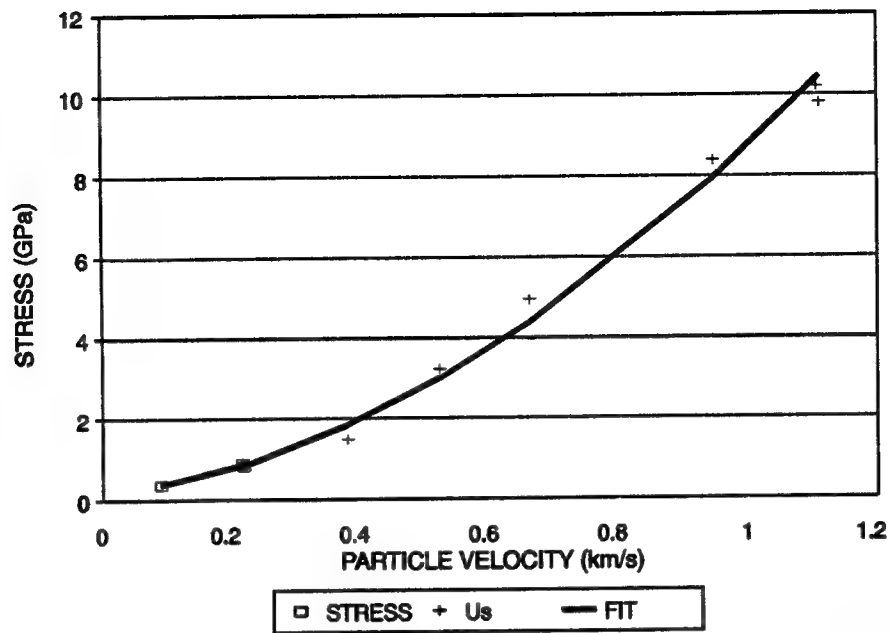


Figure 7-7. Comparison of the fitted Hugoniot to experimental data in the stress-particle velocity plane.

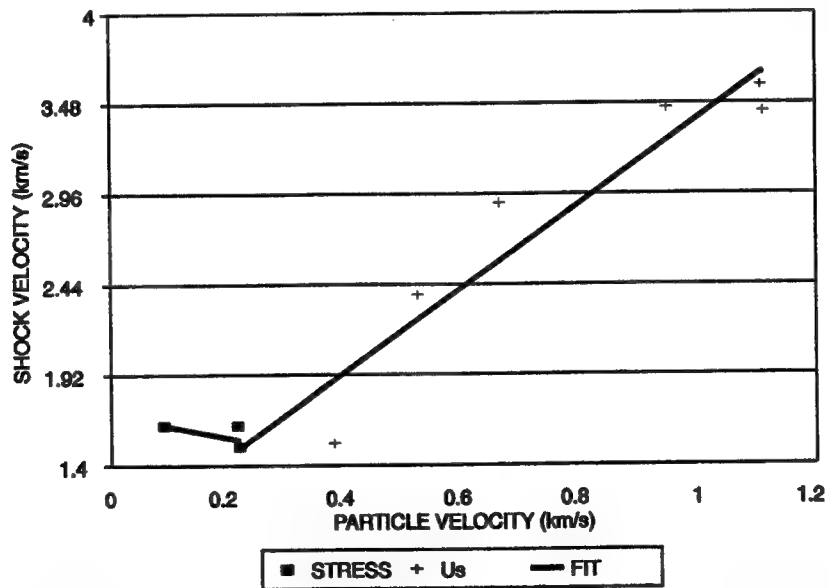


Figure 7-8. Comparison of fitted Hugoniot to experimental data in the shock velocity-particle velocity plane.



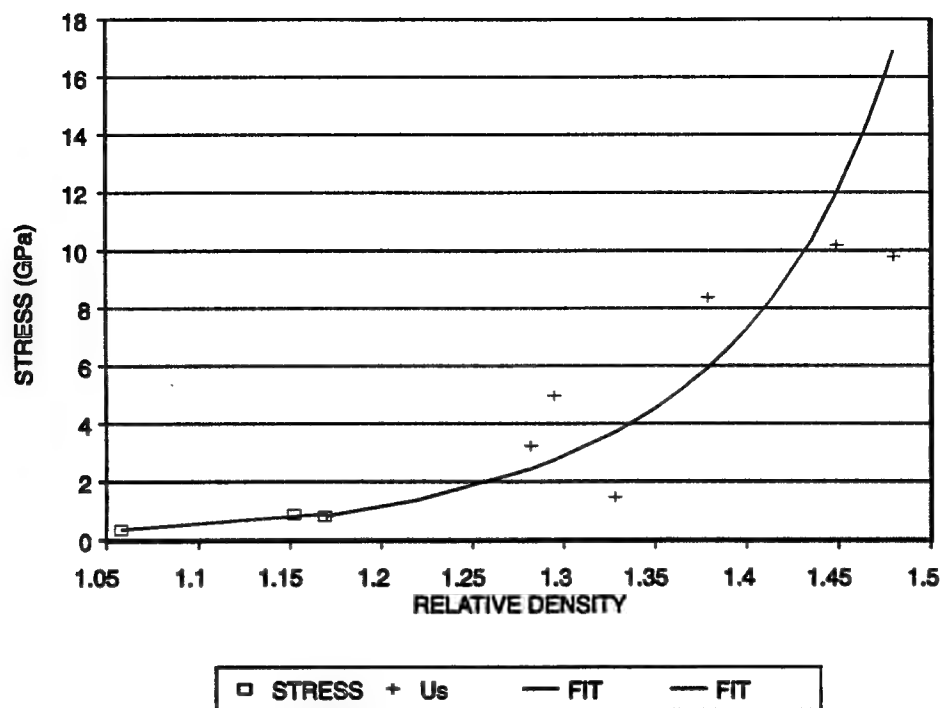


Figure 7-9. Comparison of the fitted Hugoniot to experimental data in the stress-relative density ( $\rho/\rho_0$ ) plane.

## SECTION 8

### SHIST GRANITE

This section presents material dynamic characterization data for SHIST Granite. Five experiments were conducted using the Lagrangian-stress gauge configuration and four with the VISAR test configuration.

Hugoniot data and shot configuration tables showing details of impactor and buffer material thicknesses and sample number, density, and thickness are presented. All recorded waveforms are illustrated in Appendix A.

#### 8.1 MATERIAL DESCRIPTION.

DNA planned to perform a HYDROPLUS experiment (SHIST) in granite geology. The material characterized in this test series was from a vertical drill hole, core hole #1, box 11 depth 156.4 to 170 ft, located on the SHIST site, WSMR. The core was received in an unpreserved dry slate and all measurements were made under these conditions. The material has a granite composition as shown by the x-ray diffraction mineralogy results presented in Table 8-1. Terra Tek manufactured the gas gun test samples from core hole #1. The axis of the test samples was parallel to the axis of the core. Terra Tek (Martin, 1993) also performed a series of physical properties measurements on plugs taken from the same core. Bulk density, dry, effective and true grain density, effective and total porosity, ultrasonic velocities and unconfirmed compression measurements were made. The Terra Tek test plugs were cut with orientations parallel to and normal to the axis of the core. Bulk density was determined by a mercury immersion technique. Effective grain density was determined using Boyle's Law helium porosimetry. The unconfined compression tests were conducted at an axial strain rate of  $10^{-5}$ /s until catastrophic failure occurred. Both axial and radial deformation were measured. Static material properties were calculated from the measured strains and axial stress. Following the unconfined tests, each plug was pulverized to less than  $100\mu\text{m}$  particles and the true grain density measured using the water pycnometry method. From the bulk density,  $\rho_d$ , and effective and true grain densities,  $\rho_s$ , the porosity,  $\alpha$ , was calculated using the relation:

$$\alpha = 1 - \frac{\rho_d}{\rho_s}$$

The results of these measurements are presented in Tables 8-2, 8-3, and 8-4.

Table 8-1. XRD semi-quantitative mineralogy of selected samples from the SHIST site.

Core Hole	Depth (ft)	Mineralogy, Approximate Weight Percent					
		Quartz	Plagioclase	K-Feldspar	Calcite	Chlorite	*Illite/Mica
#2	104.9-104.95	32	22	34	2	4	6
#1	163.2-163.25	28	26	36	3	3	4

\*Illite/mica is probably biotite (dark micaceous mineral) - verified from this section.

Table 8-2. Summary of physical properties for SHIST test plugs as measured by Terra Tek.

Sample ID (ft)	Core Hole	Length (in)	Dia. (in)	Weight (gm)	Bulk Density (gm/cc)	Effective Grain Density (gm/cc)	Effective Porosity (%)	True Grain Density (gm/cc)	Total Porosity (%)	Occluded Porosity (%)
163.2-163.3 (⊥)	#1	1.531	0.995	50.361	2.587	2.618	1.2	2.634	1.8	0.6
162.9-163.1 (  )	#1	1.996	0.994	66.116	2.603	2.613	0.4	2.634	1.2	0.8
166.2-166.3(⊥)	#1	1.526	0.996	50.123	2.596	2.618	0.9	2.639	1.6	0.7
1663-1665 (  )	#1	1.994	0.994	66.070	2.606	2.616	0.3	2.639	1.3	1.0

⊥ Designates perpendicular test plug - plug drilled perpendicular to the axis of the whole core.  
|| Designates parallel test plug - plug drilled parallel to the axis of the whole core.

Table 8-3. Summary of ultrasonic velocities and calculated dynamic properties for the SHIST test plugs as defined by Terra Tek.

Sample ID (ft)	Core Hole	Length (in)	Bulk Density (gm/cc)	Pwave Velocity (km/sec)	Swave Velocity (km/sec)	Dynamic Properties			
						Poisson's Ratio	Young's Modulus (GPa)	Bulk Modulus (GPa)	Shear Modulus (GPa)
163.2- 163.3 (⊥)	#1	1.532	2.587	5.147	3.297	0.15	64.8	30.8	28.2
162.9- 163.1 (  )	#1	1.994	2.603	5.326	3.343	0.17	68.3	34.5	29.2
166.2- 166.3(⊥)	#1	1.526	2.596	4.900	3.177	0.14	59.6	27.6	26.1
1663-1665 (  )	#1	1.995	2.606	5.356	3.290	0.20	67.5	37.5	28.1
⊥ Designates perpendicular test plug - plug drilled perpendicular to the axis of the whole core.    Designates parallel test plug - plug drilled parallel to the axis of the whole core.									

Table 8-4. Summary of static mechanical properties determined from unconfined compression tests for the SHIST test plugs by Terra Tek.

Sample ID (ft)	Core Hole	Compressive Strength (MPa)	Poisson's Ratio	Young's Modulus (GPa)	Bulk Modulus (GPa)	Shear Modulus (GPa)
163.2-163.3 (⊥)	#1	132.4	0.44 0.37*	50.9 48.6*	146.5 63.5*	17.7 17.7*
162.9-163.1 (  )	#1	116.9	0.22	43.7	25.8	18.0
166.2-166.3(⊥)	#1	114.2	0.43 0.34*	38.2 38.5*	93.5 39.4*	13.3 14.4*
1663-1665 (  )	#1	110.5	0.22	45.0	27.1	18.4
⊥ Designates perpendicular test plug - plug drilled perpendicular to the axis of the whole core.    Designates parallel test plug - plug drilled parallel to the axis of the whole core. * Static properties calculated between 10 and 40% of the maximum axial stress. All other static properties determined between 10 and 50% of the maximum axial stress.						

Sample characterization data performed by Ktech on the manufactured gas gun samples are presented in Table 8-5. The accuracy of each measurement is indicated at the top of each column. The sample thicknesses listed in Table 8-5 are as-received sample thicknesses. The average sample density was 2.591 g/cm<sup>3</sup> (std. dev. = 0.010) and the average ultrasonic longitudinal and shear velocities were 6.25 km/s (std. dev. = 0.176) and 3.29 km/s (std. dev. = 0.110), respectively. The density and ultrasonic shear velocity measurements are in good agreement with the Terra Tek measurements.

Figure 8-1 shows the measured longitudinal wavespeed as a function of sample thickness. Ktech measurements were performed with other 5- or 10-mm thick samples while the Terra Tek measurements used 50-mm thick samples. A near linear relationship between measured velocity and sample thickness is apparent in Figure 8-1. This decay is consistent with the dispersive character of the SHIST granite noted in the stress wave propagation data presented in the following sections.

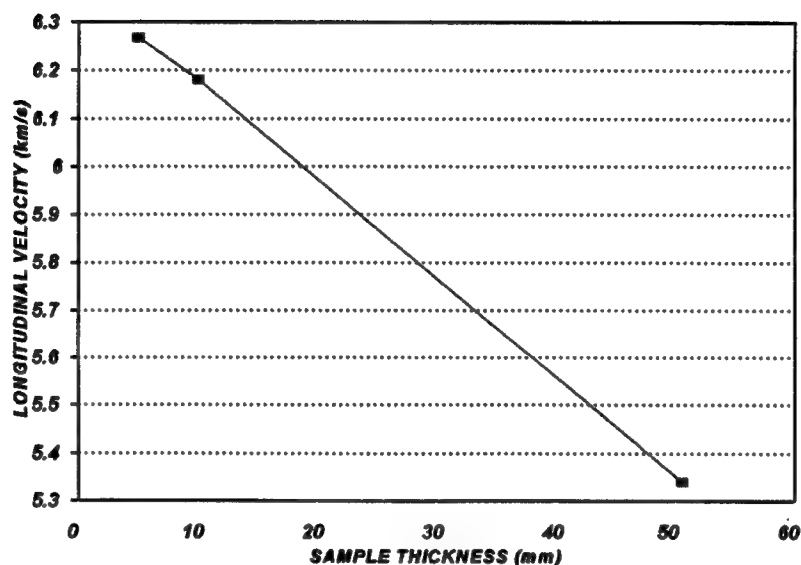


Figure 8-1. The dependence of longitudinal wavespeed upon SHIST granite sample thickness.

Table 8-5. Ktech measured SHIST granite material properties.

Sample No.	Avg. Thk* (mm) ±1%	Density* (gm/cc) ±1%	Longitudinal Velocity* (km/sec) ±5%	Shear Velocity* (km/sec) ±5%
GG-2	4.91	2.59	6.22	
GG-1	4.92	2.59	6.19	
GG-13	4.92	2.59	6.27	
GG-14	4.94	2.60	6.29	
GG-7	4.98	2.58	6.10	
GG-17	4.99	2.60	6.29	
GG-8	5.00	2.56	6.09	
GG-16	5.01	2.60	6.35	
GG-10	5.03	2.59	6.20	
GG-11	5.05	2.59	6.63	
GG-12	5.05	2.80	6.19	
GG-5	5.06	2.59	6.14	
GG-6	5.06	2.59	6.41	
GG-19	5.07	2.60	6.38	
GG-3	9.91	2.59	6.04	3.24
GG-9	9.96	2.60	6.38	3.44
GG-18	10.02	2.61	6.24	
GG-4	10.02	2.59	5.95	3.18
GG-15	10.04	2.60	6.31	
Average (all samples)		2.591	6.246	3.287
Std. Deviation		0.0097	0.1493	0.1097
Average (5 mm samples)		2.589	6.269	
Std. Deviation		0.0098	0.1371	
Average (10 mm samples)		2.598	6.182	3.287
Std. Deviation		0.0062	0.1630	0.10
*Measurements have been rounded, however, the average and standard deviations were performed using nonrounded measurements.				

## 8.2 TEST RESULTS

Five Lagrangian stress gauge experiments were conducted at nominal stress levels of 0.4, 0.8, 1.3, 1.9, and 3.3 GPa and four VISAR experiments were conducted at 5.9, 7.9, 9.4 and 13.4 GPa. The arrangement for both the Lagrangian stress and VISAR measurements are detailed in Section 2.

Table 8-6 contains shot configuration information for each experiment. Impactor and buffer material thicknesses and thicknesses and densities of the individual samples in each target are listed. Sample thicknesses are as-built center thicknesses. Measured stress-time and particle velocity-time profiles for each experiment are provided in Appendix A.

Table 8-6. SHIST granite shot configuration data.

Shot #	Thickness (mm) and Density (g/cm <sup>3</sup> )									
	Al Impactor Thk	Sample 1			Sample 2			Sample 3		
		No	Ctr Thk	$\rho_o$	No	Ctr Thk	$\rho_o$	No	Ctr Thk	$\rho_o$
3675	4.70	G-16	5.01	2.60	G-17	5.00	2.60	G-18	10.02	2.61
3674	4.79	G-13	4.92	2.60	G-14	4.91	2.60	G-15	10.03	2.60
3673	4.71	G-11	5.05	2.59	G-7	4.96	2.58	G-9	9.96	2.60
3672	4.65	G-5	5.06	2.59	G-6	5.06	2.59	G-4	10.02	2.59
3671	4.63	G-1	4.91	2.59	G-2	4.90	2.59	G-3	9.91	2.59
3669	6.31	G-12	5.05	2.58	LiF	25.36	2.64			
3670	6.32	G-10	4.98	2.59	LiF	25.49	2.64			
3676	6.35*	G-8	5.00	2.56	LiF	25.45	2.64			
3677	6.35*	G-19	5.07	2.60	LiF	25.44	2.64			
*Tungsten Carbide (WC) Impactor										

The Hugoniot data were derived from the measured stress profiles using the Lagrangian analysis for each experiment. In addition, Hugoniot data were calculated from the measured half amplitude shock velocity and the equilibrium stress level using the Rankine-Hugoniot relations. The analysis techniques and steady state assumptions used in these data reductions are discussed in detail in Section 2. The Hugoniot data are given in Table 8-7. These data are presented in the stress-particle velocity, stress-relative density and shock velocity-particle velocity planes in Figures 8-2, 8-3, and 8-4, respectively. SNL data (Furnish, 1993) on SHIST granite from hole #2 are also presented in these figures. The measured stress-time profiles for the shots with three Lagrangian stress gauges are shown in Figure 8-5. The measured particle velocity profiles are given in Figure 8-6. The SHIST granite data is compared to the Sierra White granite and other published granite data in Section 9.

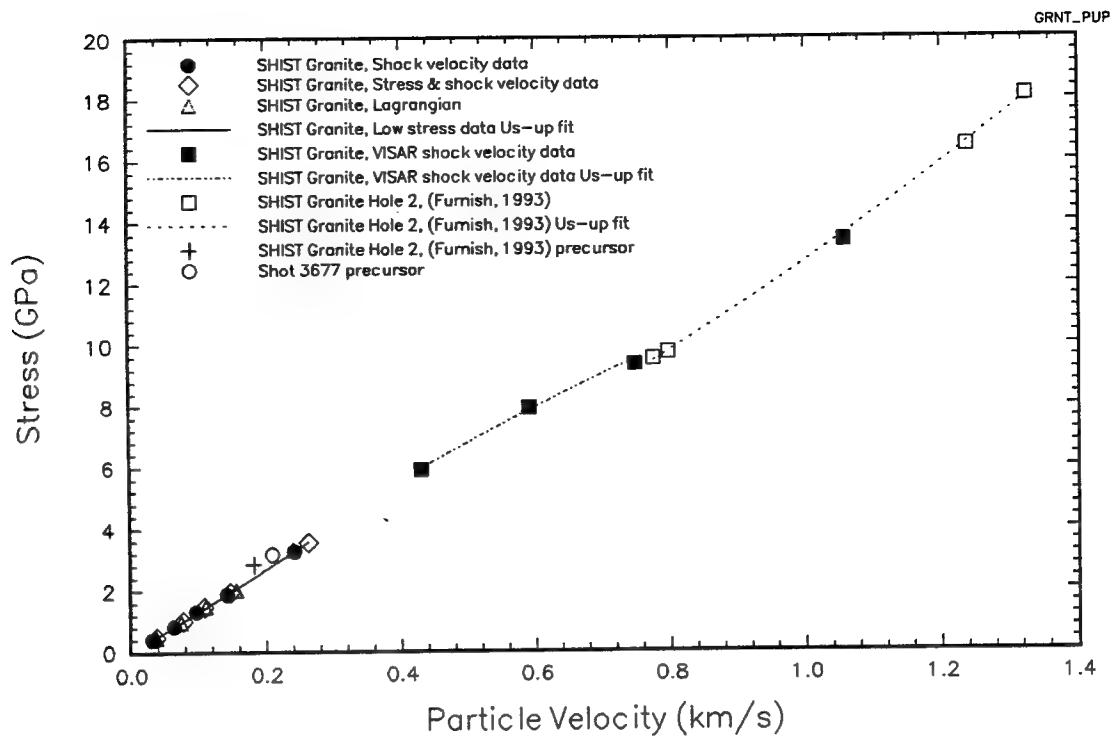


Figure 8-2. SHIST granite  $\sigma - u_p$  Hugoniot data.

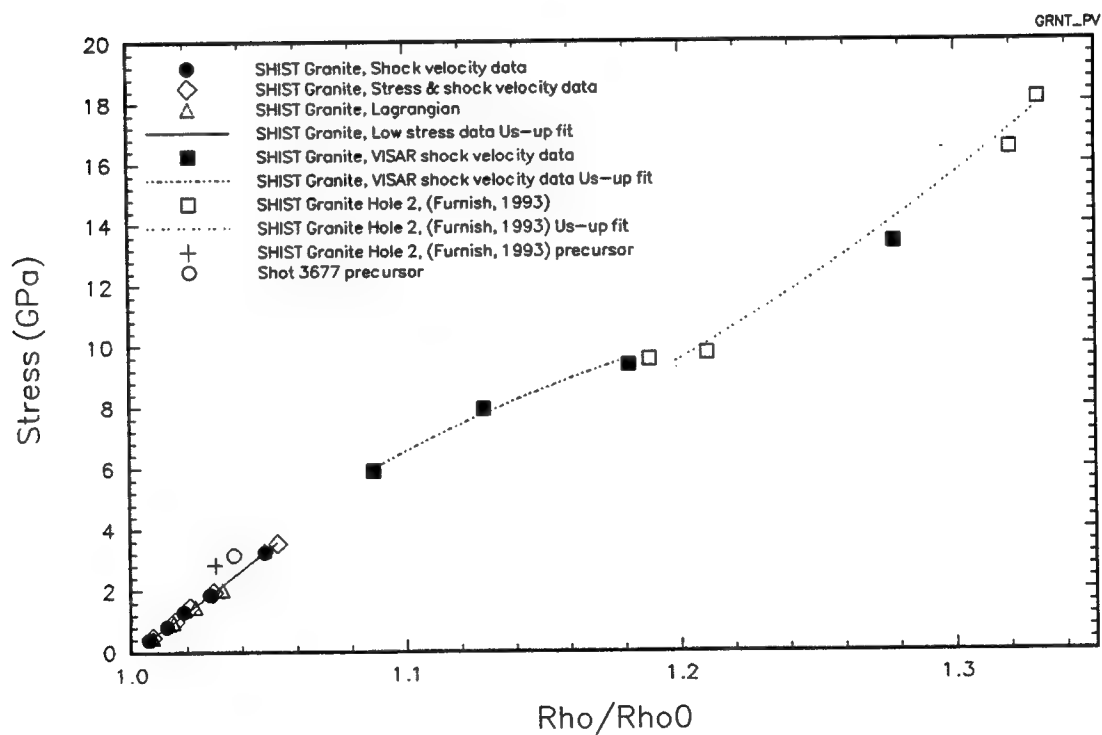


Figure 8-3. SHIST granite  $\sigma - \rho/\rho_0$  Hugoniot data.



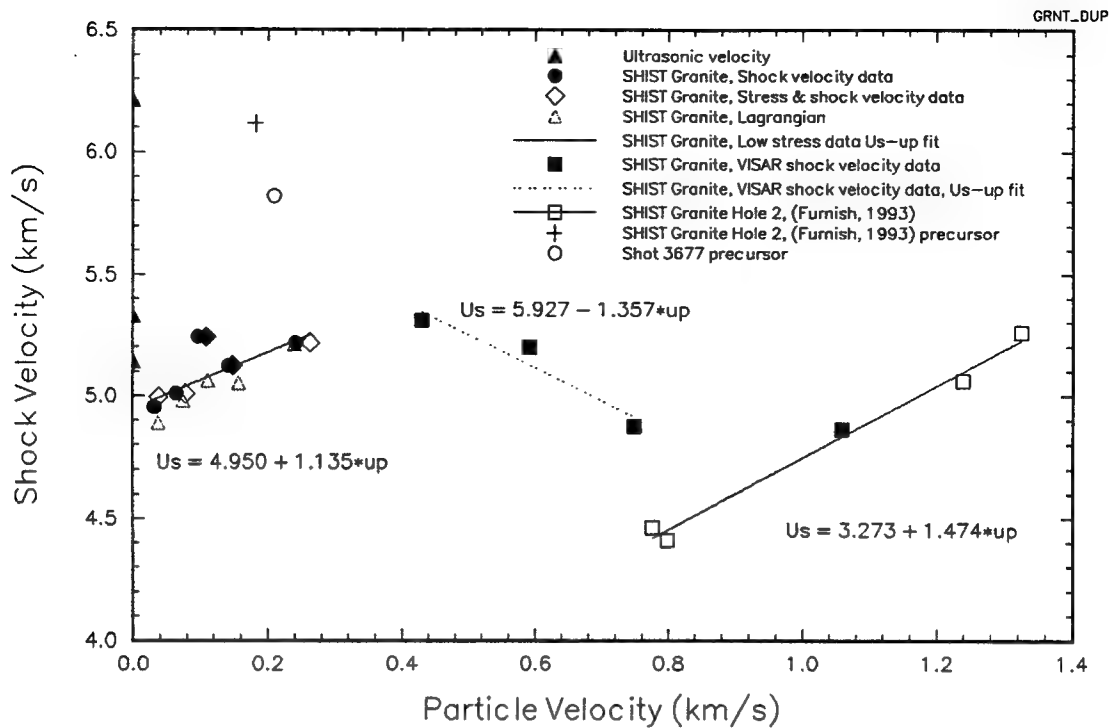


Figure 8-4. SHIST granite  $U_s$  -  $u_p$  Hugoniot data.

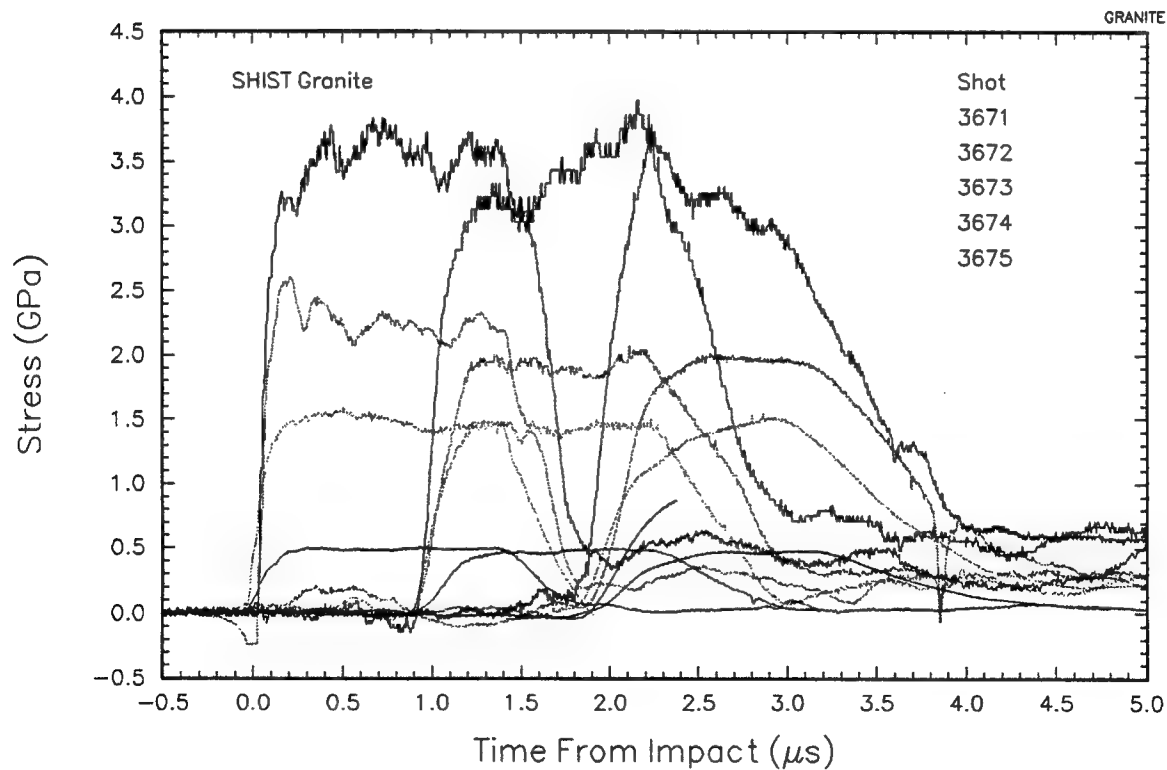


Figure 8-5. Lagrangian stress-time profiles for SHIST granite.

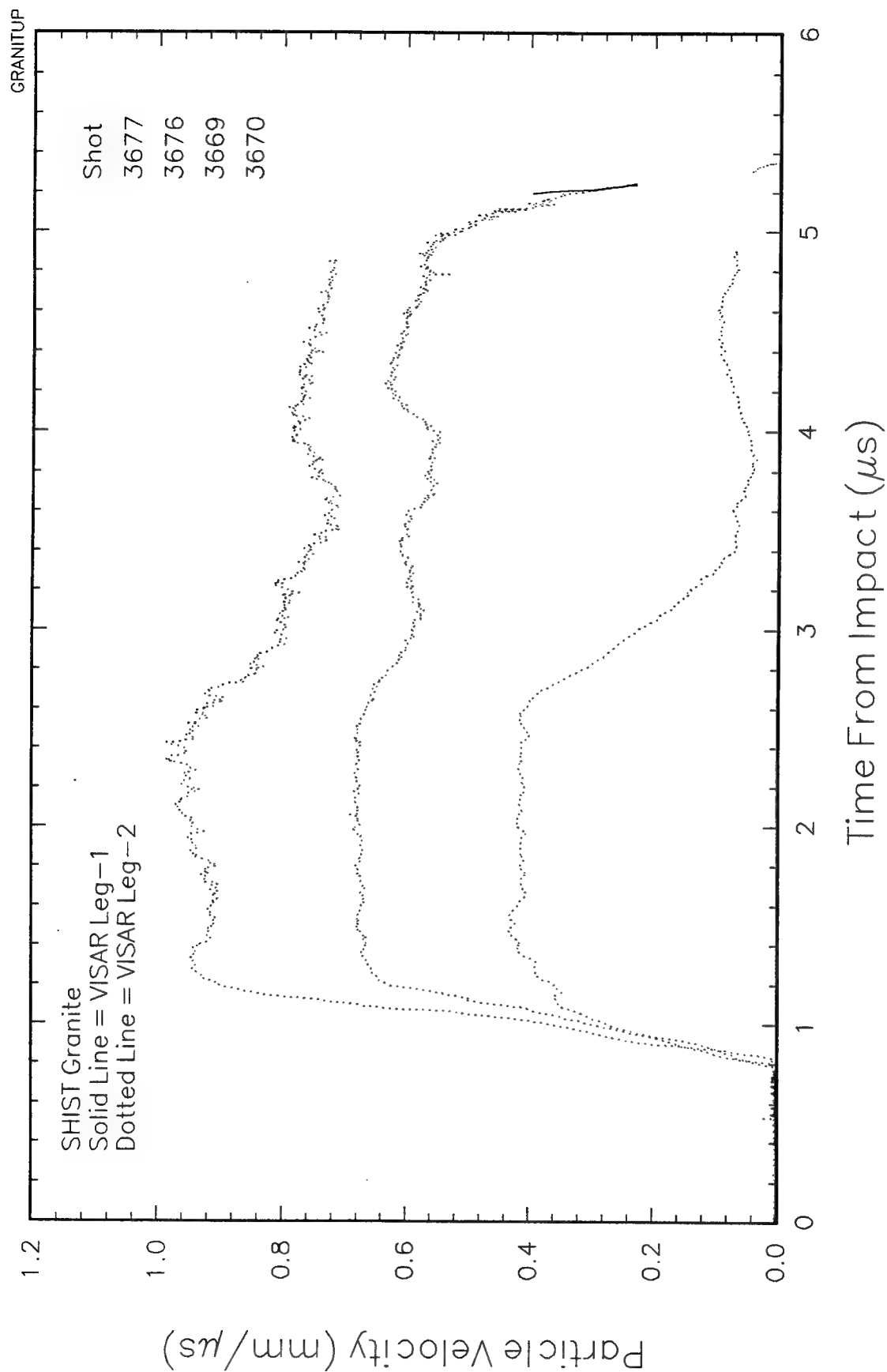


Figure 8-6. Particle velocity-time profiles for SHIST granite.

Table 8-7. SHIST granite Hugoniot data.

Shot #	Impact Velocity (km/s)	Conf.	Initial Density (g/cm <sup>3</sup> )	Hugoniot			
				Stress (Gpa)	U <sub>s</sub> 1/2 amp (km/s)	u <sub>p</sub> (km/s)	ρ/ρ <sub>o</sub>
Stress, Known Al Hugoniot							
3675	0.054	a	2.601	0.48	4.89	0.037	1.008
3674	0.114	a	2.595	0.96	4.98	0.074	1.015
3673	0.180	a	2.586	1.47	5.06	0.110	1.023
3672	0.264	a	2.588	2.02	5.05	0.156	1.033
3671	0.454	a	2.589	3.33	5.21	0.239	1.048
Shock Velocity, Known Al Hugoniot							
3675	0.054	a	2.601	0.40	4.95	0.031	1.006
3674	0.114	a	2.595	0.82	5.01	0.063	1.013
3673	0.180	a	2.586	1.30	5.24	0.096	1.019
3672	0.264	a	2.588	1.88	5.12	0.141	1.028
3671	0.454	a	2.589	3.26	5.22	0.241	1.048
3670	0.806	b	2.589	5.91	5.31	0.430	1.088
3669	1.083	b	2.580	7.92	5.20	0.591	1.128
3676	0.844	c	2.563	9.35	4.87	0.748	1.181
3677	1.199	c	2.601	13.39	4.86	1.058	1.278
Stress, Shock Velocity							
3675	0.054	a	2.601	0.489	4.99	0.038	1.008
3674	0.114	a	2.595	1.00 <sup>1</sup>	5.01	0.077	1.016
3673	0.180	a	2.586	1.47	5.24	0.108	1.021
3672	0.264	a	2.588	1.95	5.12	0.147	1.030
3671	0.454	a	2.589	3.55	5.22	0.263	1.053
Configuration:							
(a) 6061-T6 - CG/SG/CG/SG/CG/SG							
(b) 6061-T6 - SG/VISAR/LiF							
(c) WC - SG/VISAR/LiF							

### 8.3 DISCUSSION.

The Lagrangian gauge stress profiles in Figure 8-5 show no attenuation for the 5 and 10-mm travel distances. The profiles do show rise times increasing with distance due to the dispersion nature of the heterogenous material. Dispersion is greater at low stress than at high stresses due to the higher wave velocities associated with increased stresses. The top of the loading pulse was rounded off. The noise on the baseline and stress wave plateau, primarily above 1.5 GPa, is due to shock induced

charge generation of the piezoelectric quartz crystals in the granite. This noise was also observed by Jones (1969).

The VISAR particle velocity measurements are not sensitive to the quartz generated noise, and therefore, have a clean baseline (Figure 8-6). The ripple on the waveforms is due to the small, (1/2-mm diameter,) sensing area relative to the large sample heterogeneities (up to 5-mm diameter).

The transmitted wave on shot 3677 has separated into a two wave structure. The half amplitude velocity of this ramped precursor is travelling at 5.82 km/s. The toe of the precursor is travelling at 6.1 km/s. Impedance match analysis, based on the half amplitude precursor velocity, yielded a stress of 3.16 GPa and particle velocity of 0.21 km/s for a driving pressure of 13.4 GPa. The ramped rise of the precursor is similar to that observed in fused quartz below 0.6 km/s particle velocity (Wackerle 1961). The ramp toe velocity in fused quartz was about 6 km/s and the half amplitude ramp velocity was about 5.5 km/s.

The other three VISAR transmitted wave shots (3676, 3669, and 3670), which are at stresses in the precursor/transition region also have ramped waves the amplitudes of which are consistent with shot 3677. A precursor of 2.84 GPa( $\sigma$ ), 0.182 km/s ( $u_p$ ), and 6.114 km/s ( $U_s$ ) was measured by Furnish for SHIST granite, (hole #2), at a driving pressure of 9.53 GPa. Grine (Lombard 1961) reported precursors in granite of 2.9 and 3.6 GPa. Wackerle (1961) found that the elastic limit of crystalline quartz depended on driving pressure and sample thickness; therefore, a single value for the HEL of granite with its high quartz content may not be possible.

The precursor Hugoniot points in Figures 8-2 through 8-4 are higher than the Hugoniot results obtained from the lagrangian stress gauges. This is because dispersion is greater at low stresses in granite, and as a result, the half amplitude shock velocities are lower. Therefore, data obtained at precursor stress levels where dispersion dominates yielded lower Hugoniot values than precursor data obtained from tests with driving pressures three times greater than the precursor.

The SHIST granite Hugoniot data can be represented by linear fits in the  $U_s - u_p$  plane (Figure 8-2). The Hugoniot appears to be made up of three distinct regions; a concave upward region up to 0.4 km/s, a concave down region between 0.4 and 0.9 km/s and a concave up region above 0.9 km/s.

These three fits are:

$$U_s = 4.950 (0.0402) + 1.135 (0.2829) u_p \text{ for } 0 < \sigma < 4 \text{ GPa}$$

$$U_s = 5.927 (0.2396) - 1.357 (0.3967) u_p \text{ for } 6 < \sigma < 9.5 \text{ GPa}$$

$$U_s = 3.273 (.1178) + 1.474 (0.1107) u_p \text{ for } (9.5 < \sigma < 18 \text{ GPa})$$

where  $U_s$  and  $u_p$  are in km/s and number in parenthesis are standard errors for the constants.

These fits are also plotted against the data in  $\sigma - u_p$  and  $\sigma - \rho/\rho_0$  planes in Figures 8-3 and 8-4, respectively. The 0 - 4 GPa fit is nearly linear in  $\sigma - u_p$ . This fit will not predict the dispersive ramped loading wave. The addition of a dispersion model may be necessary to predict the transmitted stress profiles. At 6 GPa, a yielding or phase transition has begun resulting in an increase in compression until stiffening begins to occur at about 10 GPa. As a result of the dispersive ramp loading, the material may be loading up an adiabat and may not reach the Hugoniot state.

## SECTION 9

### SIERRA WHITE GRANITE

This section presents the dynamic characterization data for Sierra White Granite. This is a readily available granite which was being considered as a gauge packaging material for transducer assemblies that were to be installed in a granite medium for a HYDROPLUS experiment. Six experiments were conducted using the Lagrangian-stress gauge configuration and three with the VISAR test configuration.

Hugoniot data and shot configuration tables showing details of impactor and buffer material thicknesses, sample number, density, and thickness are presented. All recorded waveforms are illustrated in Appendix A.

#### 9.1 MATERIAL DESCRIPTION.

The Sierra White granite samples were machined from a large slab obtained from the Sierra White Quarry, Raymond, CA. This material which is also called "Granodionite of Knowles" is a light gray rock of even grain size. It is quite uniform in both texture and composition. Table 9-1 lists the typical composition of the Sierra White Granite (Bateman n.d.).

Table 9-1. Typical composition of Sierra White Granite.

Mineral	Percent Composition by Volume
Quartz	33 - 34
Potassium Feldspar	6 - 14
Plagioclase	53 - 44
Biotite	8

Sample characterization data are presented in Table 9-2. The accuracy of each measurement is indicated at the top of each column. The sample thickness listed in Table 9-2 are as-received sample thicknesses. The average sample density was  $2.64 \text{ g/cm}^3$  (std. dev. = 0.04) and the average ultrasonic longitudinal and shear velocities were 5.48 (std. dev. = 0.25) and 3.64 (std. dev. = 0.18) km/s, respectively. These ultrasonic measurements were made using 5- and 10-mm samples. The quoted velocities are averages of the propagation velocity through the sample. An additional ultrasonic measurement on a 19-mm sample yielded a longitudinal velocity of 3.96 km/s. The

variation of average longitudinal wavespeed with sample thickness is shown in Figure 9-1. The decrease in velocity with distance is consistent with the observed dispersive properties of this granite.

Table 9-2. Sierra White granite material properties.

Sample No.	Avg. Thk* (mm) ±1%	Density* (gm/cc) ±1%	Longitudinal Velocity* (km/sec) ±5%	Shear Velocity* (km/sec) ±5%
SWG-1	5.04	2.64	5.85	3.48
SWG-2	5.04	2.63	5.68	3.55
SWG-3	5.03	2.64	5.76	3.89
SWG-4	5.04	2.64	5.62	
SWG-5	5.04	2.64	5.65	
SWG-6	5.04	2.64	5.88	
SWG-7	5.04	2.64	5.67	
SWG-8	5.03	2.63	5.58	
SWG-9	5.04	2.64	5.62	
SWG-10	5.04	2.64	5.60	
SWG-11	5.04	2.64	5.41	
SWG-12	5.04	2.64	5.48	
SWG-13	5.04	2.65	5.59	
SWG-14	5.04	2.65	5.59	
SWG-15	5.04	2.64	5.39	
SWG-16	5.04	2.64	5.43	
SWG-17	10.03	2.64	5.13	
SWG-18	10.04	2.64	5.28	
SWG-19	10.04	2.63	4.85	
SWG-20	10.02	2.65	5.27	
SWG-21	10.03	2.65	5.38	
SWG-22	10.04	2.63	4.96	
SWG-23	10.05	2.64	5.52	
SWG-24	10.05	2.63	5.34	
Average		2.640	5.481	3.642
Std. Deviation		0.0045	0.2495	0.1777
Average 5 mm			5.613	
Std. Deviation			0.1378	
Average 10 mm			5.216	
Std. Deviation			0.2095	
*Measurements have been rounded; however, the average and standard deviations were performed using nonrounded measurements.				

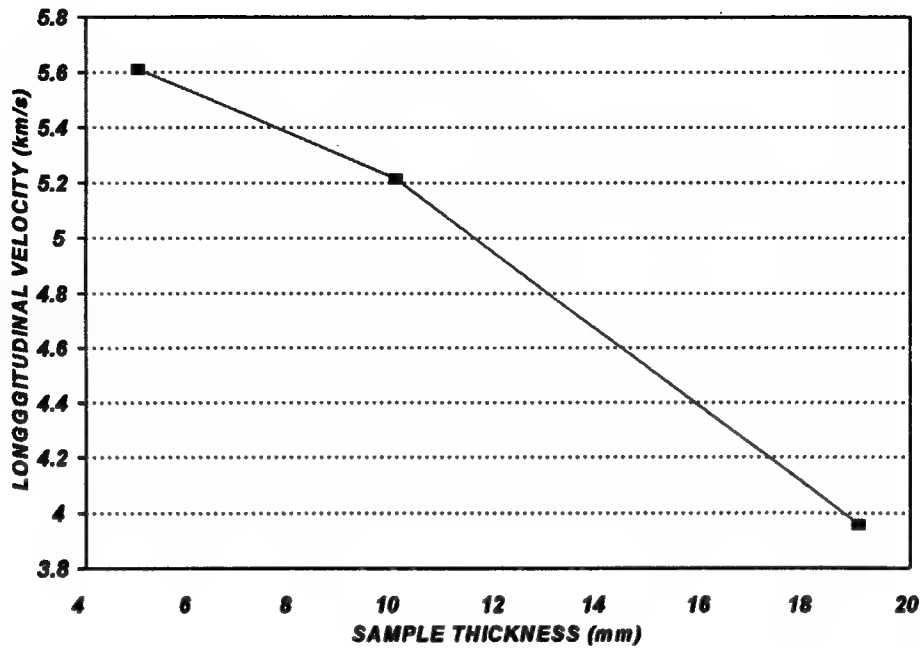


Figure 9-1. The variation of longitudinal wavespeed with sample thickness.

## 9.2 TEST RESULTS.

Five Lagrangian stress gauge experiments were conducted at nominal stress levels of 0.5, 1.0, 2.0, and 3.0 GPa and three VISAR experiments were conducted at 6 and 10 GPa. The experimental configuration for both the Lagrangian stress and VISAR measurements are detailed in Section 2. Table 9-3 contains shot configuration information for each experiment. Impactor and buffer material thicknesses and thicknesses and densities of the individual samples in each target are listed. Sample thicknesses are as-built center thicknesses. Measured stress-time and particle velocity-time profiles for each experiment are provided in Appendix A.

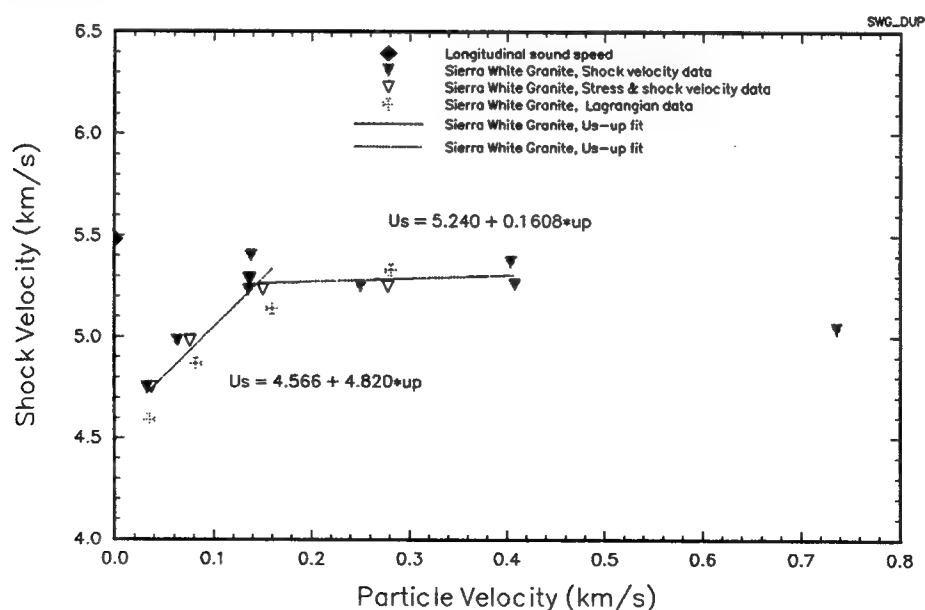


Table 9-3. SHIST granite shot configuration data.

Shot #	Thickness (mm) and Density (g/cm <sup>3</sup> )									
	Al Impactor Thk	Sample 1			Sample 2			Sample 3		
		No	Ctr Thk	$\rho_0$	No	Ctr Thk	$\rho_0$	No	Ctr Thk	$\rho_0$
3690	4.73	SWG-1	5.04	2.64	SWG-9	5.03	2.64	SWG-18	10.04	2.64
3691	4.69	SWG-24	10.05	2.63	SWG-23	10.05	2.64	SWG-20	10.02	2.64
3700	4.67	SWG-22	10.02	2.63	SWG-12	5.04	2.64	SWG-15	5.04	2.64
3705	4.75	SWG-4	5.04	2.64	SWG-13	5.03	2.65	SWG-17	10.03	2.65
3706	4.76	SWG-6	5.04	2.64	SWG-7	5.03	2.64	SWG-21	10.05	2.64
3707	4.78	SWG-2	5.04	2.63	SWG-8	5.02	2.63	SWG-19	10.03	2.64
3710	6.34	SWG-16	5.04	2.64	LiF	25.47	2.64			
3711	6.35*	SWG-14	5.04	2.65	LiF	25.36	2.64			
3712	6.24	SWG-11	5.04	2.64	LiF	25.46	2.64			

\*Tungsten Carbide Impactor

Hugoniot data were derived from the measured stress profiles using the Lagrangian analysis for each experiment. In addition, Hugoniot data were calculated from the measured half-amplitude shock velocity and the equilibrium stress level using the Rankine-Hugoniot relations. The steady state assumptions are discussed in Section 2. The Hugoniot data are given in Table 9-4. These data are presented in the stress-particle velocity, stress-relative density and shock velocity-particle velocity planes in Figures 9-2, 9-3, and 9-4, respectively. The measured stress-time profiles for the shots with three Lagrangian (axial) stress gauges are shown in Figure 9-5. Particle velocity-time profiles from the VISAR shots are shown in Figure 9-6.

Figure 9-2. Sierra white granite  $\sigma - u_p$  Hugoniot data.

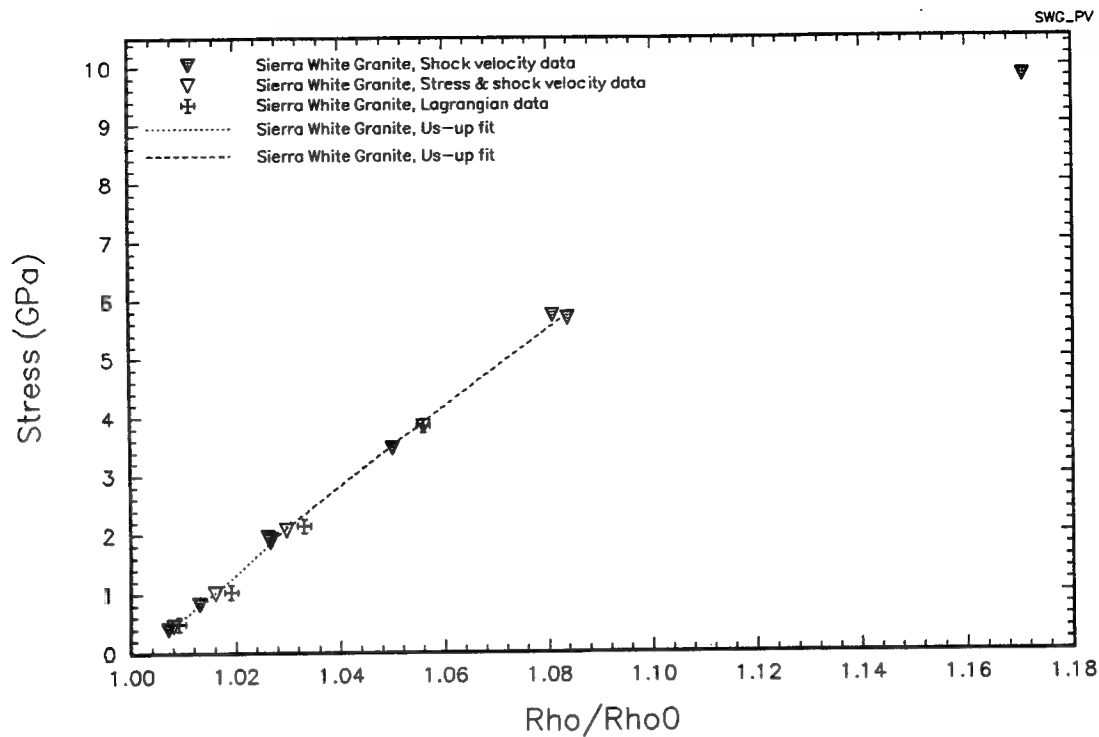


Figure 9-3. Sierra white granite  $\sigma - \rho/\rho_0$  Hugoniot data.

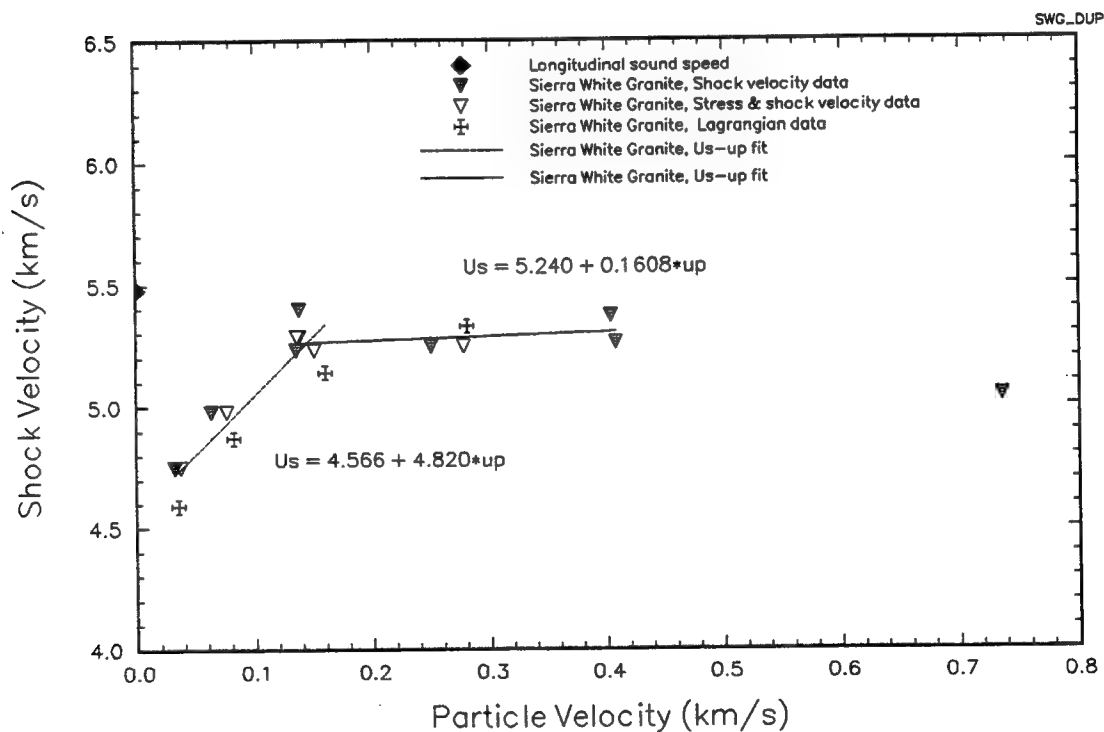


Figure 9-4. Sierra white granite  $U_s - u_p$  Hugoniot data.

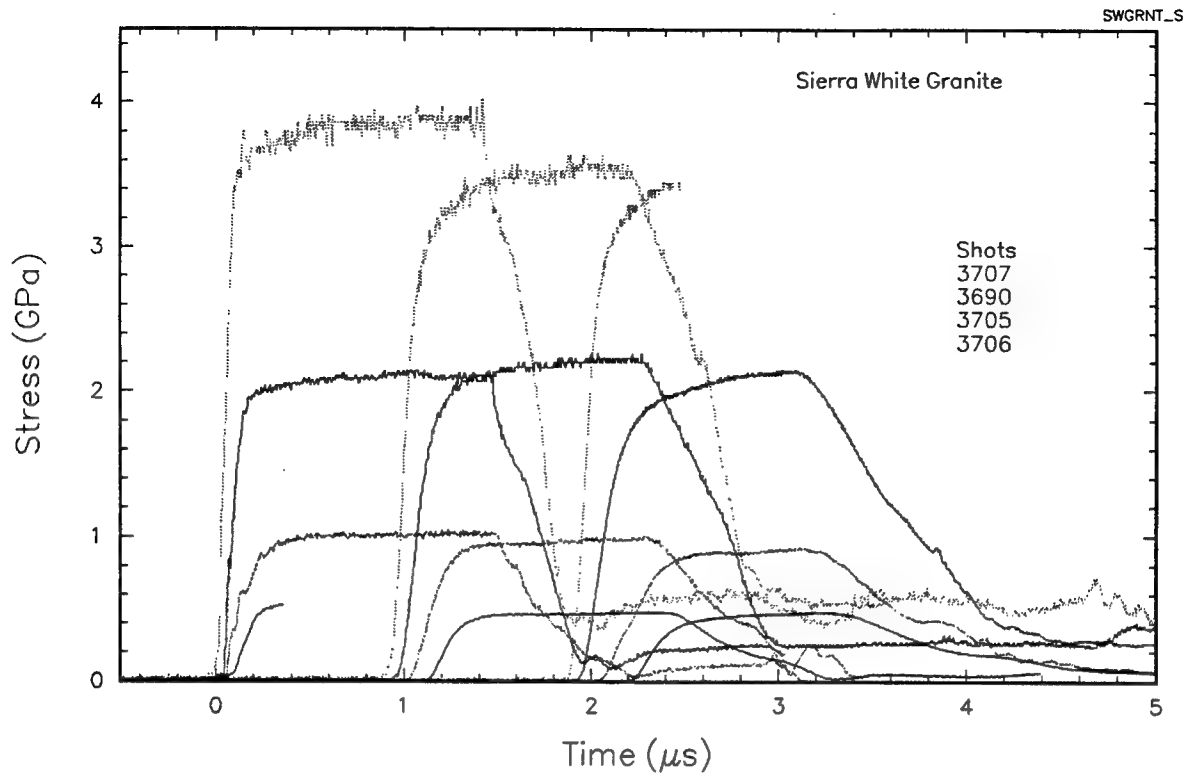


Figure 9-5. Comparison of measured stress profiles in sierra white granite.

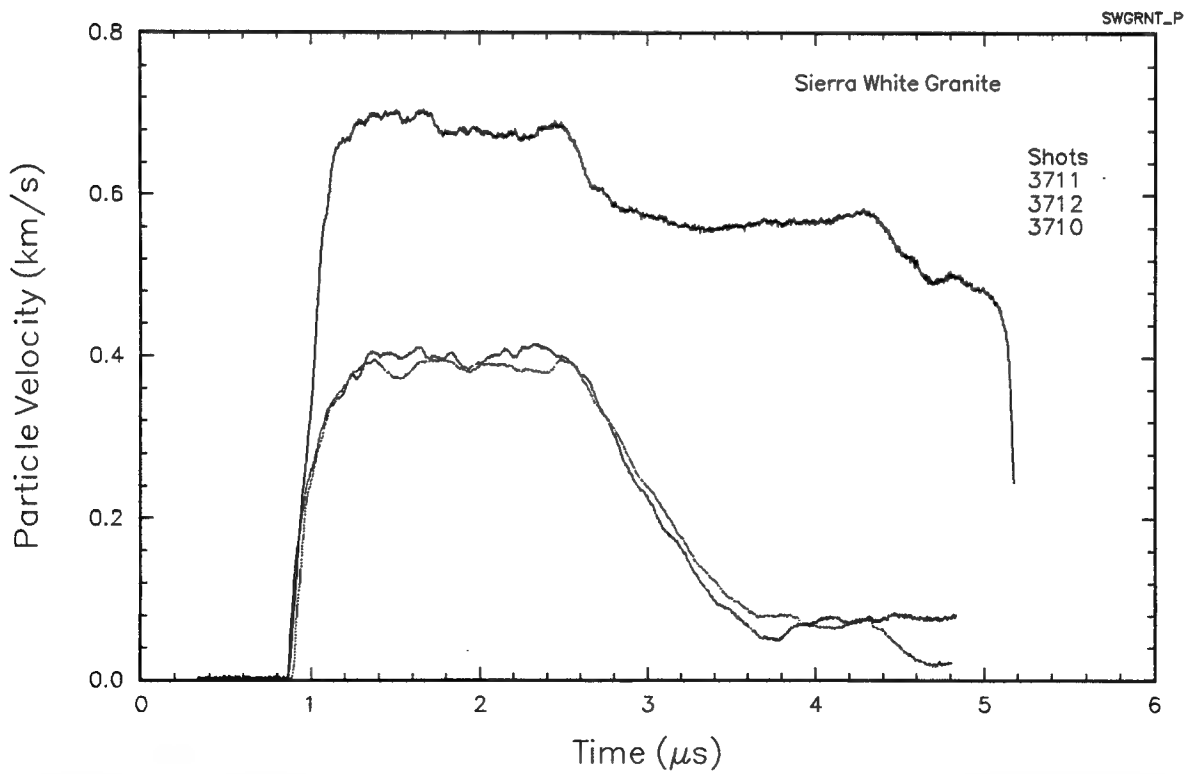


Figure 9-6. Comparison of measured particle velocity profiles in sierra white granite.

Table 9-4. Sierra white granite Hugoniot data.

Shot #	Impact Velocity (km/s)	Conf.	Initial Density (g/cm <sup>3</sup> )	Hugoniot			
				Stress (Gpa)	U <sub>s</sub> 1/2 amp (km/s)	u <sub>p</sub> (km/s)	ρ/ρ <sub>o</sub>
Lagrangian Analysis							
3706	0.053	a	2.64	0.46	4.59	0.035	1.009
3705	0.114	a	2.64	1.03	4.87	0.082	1.019
3690	0.258	a	2.64	2.14	5.14	0.160	1.033
3707	0.476	a	2.63	3.85	5.33	0.281	1.056
Shock Velocity, Known Impactor Hugoniot							
3706	0.053	a	2.64	0.04	4.75	0.032	1.007
3705	0.114	a	2.64	0.83	4.98	0.063	1.013
3690	0.258	a	2.64	1.87	5.23	0.136	1.027
3641	0.263	a	2.63	1.92	5.29	0.138	1.027
3700	0.265	a	2.63	1.96	5.40	0.138	1.026
3707	0.476	a	2.63	3.46	5.25	0.250	1.050
3710	0.770	b	2.64	5.68	5.26	0.408	1.084
3711	0.769	c	2.64	5.73	5.04	0.404	1.081
3712	0.837	b	2.64	9.81	5.37	0.736	1.171
Stress, Shock Velocity							
3706	0.053	a	2.64	0.46	4.75	0.037	1.008
3705	0.114	a	2.64	1.01	4.98	0.076	1.016
3691	0.263	a	2.64	1.89	5.29	0.136	1.026
3690	0.258	a	2.64	2.08	5.23	0.151	1.030
3707	0.476	a	2.63	3.84	5.25	0.278	1.056
Configuration: (a) 6061-T6 ~ CG/SWG/CG/SWG/CG/SWG (b) 6061-T6 ~ SWG/VISAR/LiF (c) WC ~ SWG/VISAR/LiF							

### 9.3 DISCUSSION.

The stress wave profiles measured by the Lagrangian gauges and the particle velocity profiles show no evidence of a precursor in this stress range. The peak stress amplitude does not attenuate with distance, however the risetime of the leading edge of the stress wave increases with increasing propagation distance and the top of the pulses round off. The toe of the leading edge is propagating close to the longitudinal sound speed. The Hugoniot data can be represented by two linear fits in the shock velocity (U<sub>s</sub>) particle velocity (u<sub>p</sub>) plane:

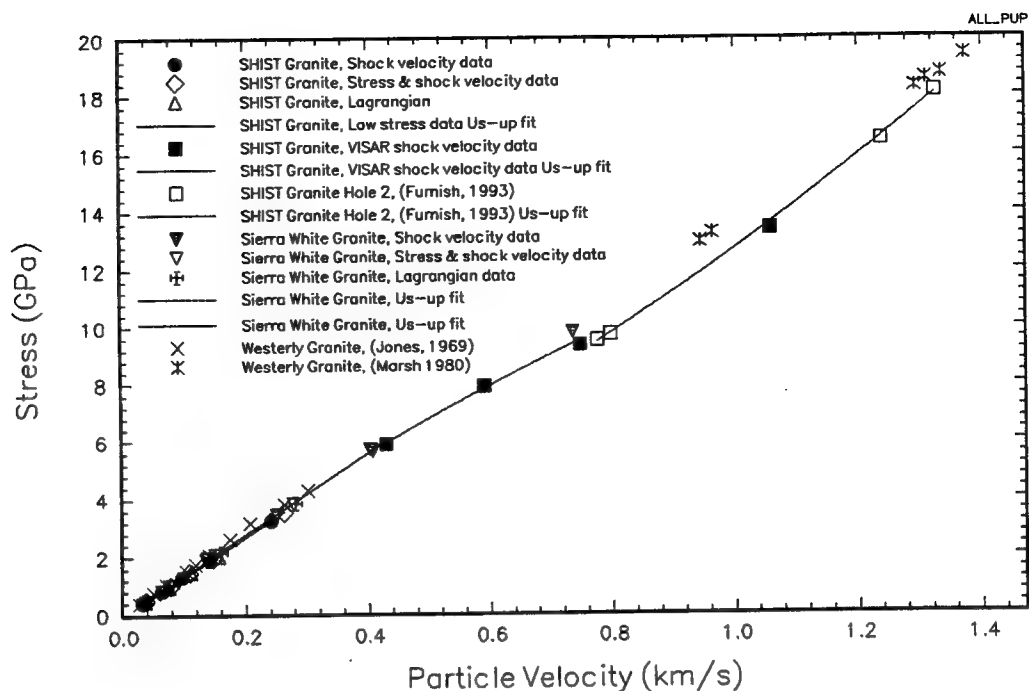
$$U_s = 4.566 (0.074) + 4.820 (0.680) u_p \text{ for } 0 < \sigma < 2 \text{ GPa}$$

$$U_s = 5.240 (0.054) + 0.161 (0.218) u_p \text{ for } 2 < \sigma < 6 \text{ GPa}$$

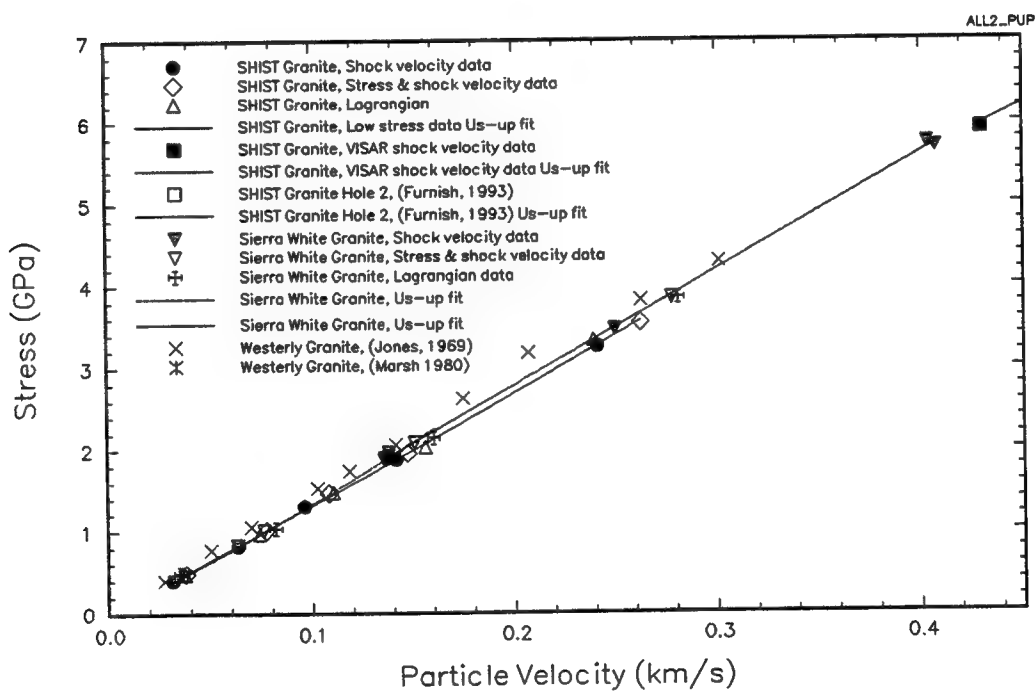
where  $U_s$  and  $u_p$  are in km/s and the numbers in parenthesis are standard errors of the constant.

The comparison of the Hugoniot defined by these equations and the experimental data is shown in Figures 9-2, 9-3 and 9-4 in the stress-particle velocity, stress-relative density ( $\rho/\rho_0$ ) and shock velocity-particle velocity planes, respectively. The highest stress data point (10 GPa) lies below the derived Hugoniot. Additional high stress data points are required to define if the Hugoniot suffers an inflection in this region. Grine (Lombard 1961) has reported precursors of 2.9 and 3.6 GPa in granite. The inflection in the derived Hugoniot probably represents the elastic limit of the quartzite.

The Sierra White granite data is compared to the SHIST granite data obtained on this program (Section 8) and published data on Westerly granite ( $\rho_0 = 2.63$ ) by Jones (1969) and Marsh (1980) in Figures 9-7, 9-8, and 9-9. The Sierra White granite high stress point is consistent with the SHIST measurements and is considered to be evidence of an inflection in the Hugoniot at about 10.0 GPa. This inflection may represent a polymorphic transition in the granite. Comparison of the Hugoniot data shows the Westerly granite has a slightly higher impedance than the SHIST and Sierra White granites. The SHIST and Sierra White responses are similar.

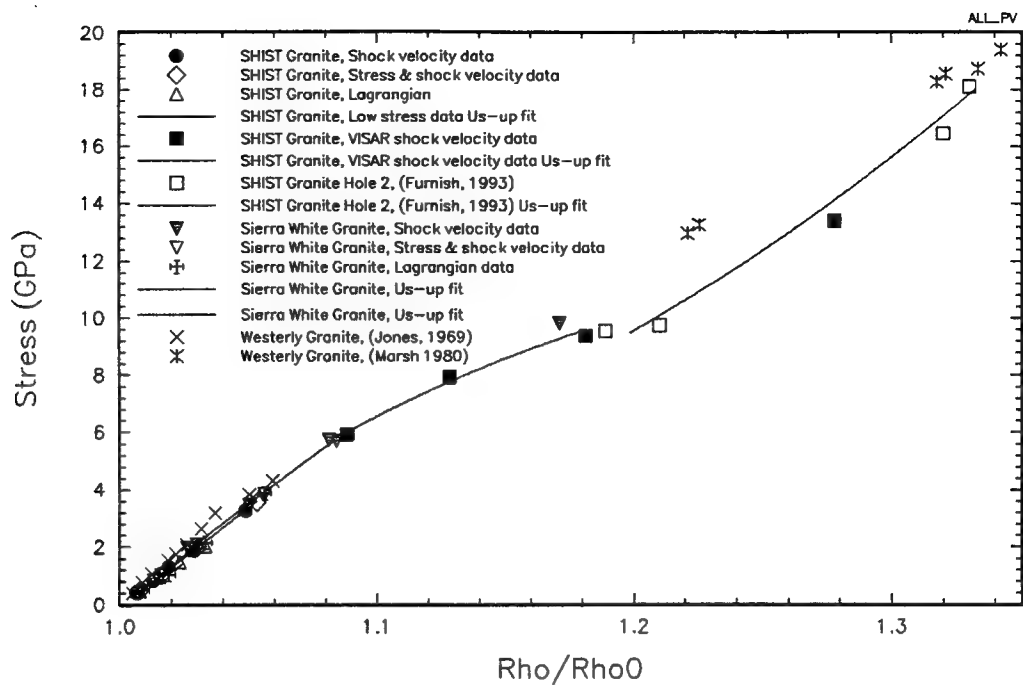


(a)

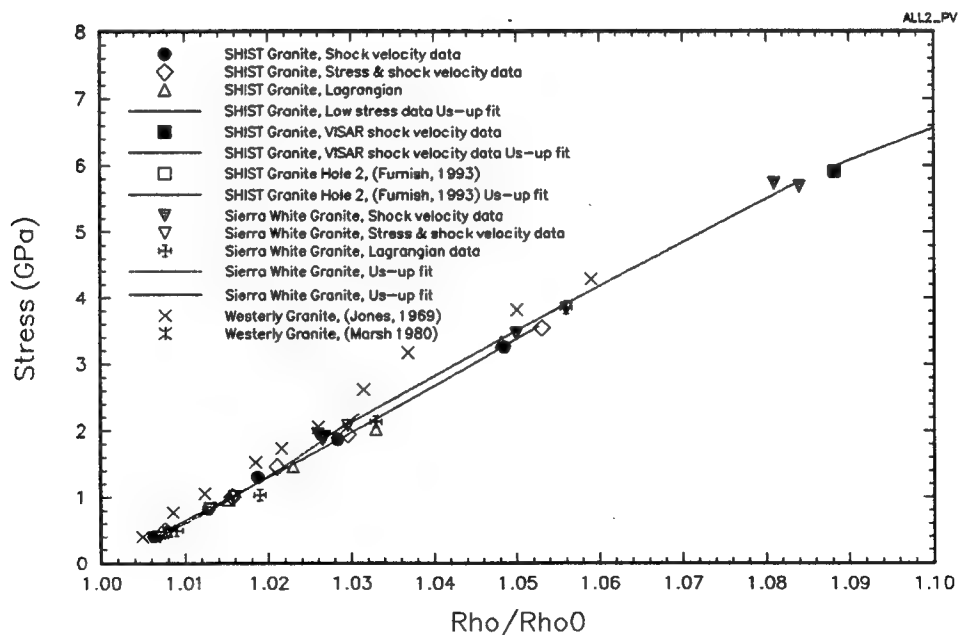


(b)

Figure 9-7. Comparison of SHIST granite, sierra white granite and westerly granite  $\sigma - u_p$  Hugoniot data.



(a)



(b)

Figure 9-8. Comparison of SHIST granite, sierra white granite, and westerly granite  $\sigma - \rho/\rho_0$  Hugoniot data.

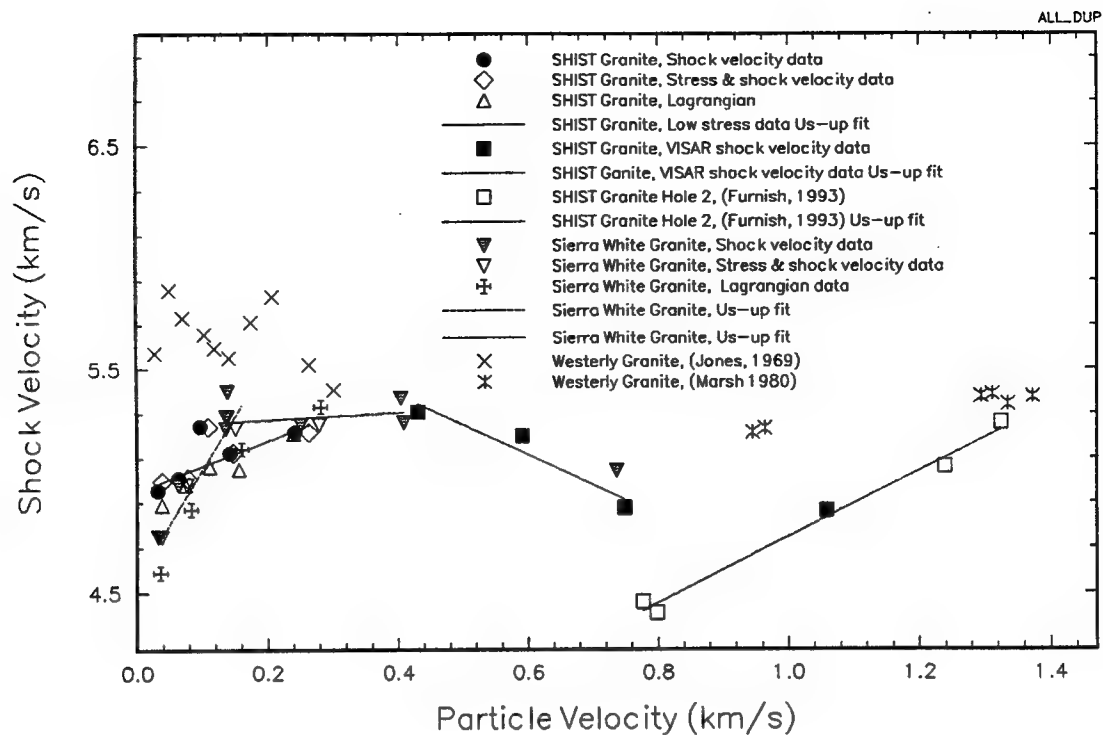


Figure 9-9. Comparison of SHIST granite, sierra white granite, and westerly granite  $U_s - u_p$  Hugoniot data.



## SECTION 10

### REFERENCES

- Ahrens, T. J. and Gregson, V. G.. "Shock Compression of Crustal Rocks: Data for Quartz, Calcite, and Plagioclase Rocks." J. of Geophys. Res. 69 22 (1964) : 4839-4874.
- Baker, L. M. and Hollenbach, R. E. "Shock-Wave Studies of PMMA, Fused Silica, and Sapphire." J. Appl. Phys. 42 10 (1970): 4208-4226.
- Barker, L. M. and Hollenbach, R. E. "Laser Interferometer for Measuring High Velocities of Any Reflecting Surface." J. Appl. Phys. 43 11 (1972).
- Bateman, P.C. and Sawka, W.N. Raymond Quadrangle Madera and Mariposa Counties, CA, Analytical Data (n.d.).
- Butcher, B. M. and Cannon, J. R. "Influence of Work Hardening on the Dynamic Stress-Strain Curves of 4340 Steel." AIAA Journal 2 12 (1964).
- Carter, W. J. "Hugoniot Equation of State of Some Alkali Halides." High Temp. High Press. 5:313 (1973).
- Christman, D. R., et al. Measurements of Dynamic Properties of Materials. Vol. III, 6061-T6 Aluminum, Final Report, Materials and Structures Laboratory, Warren, MI, Nov. 1971.
- Davies, F.W. and Smith, E.A. High Pressure Equation of State Investigation of Rocks. Defense Nuclear Agency Report No. DNA-TR-94-1. Ktech Corporation, Albuquerque, NM: 1994.
- Dremin, A. N. and Adadurov, G. A. "Shock Adiabatic for Marble." Fluid Mechanics (1959): 970-973.
- Dynasen, Inc., 20 Arnold Place, Goleta, CA.
- Fowles, R. and Williams, R. C. "Plane Stress Wave Propagation in Solids." J. Appl. Phys. 41 (1970): 360-362.
- Furnish, M. D. Measuring the Dynamic Compression and Release Behavior of Rocks and Grouts Associated with Hydro-Plus. Sandia National Laboratories Report No. SAND92-0984 (in publication). Albuquerque, NM: 1993.
- Furnish, M. D. "Dynamic Properties of Indiana Limestone, Danby Marble, and Jeffersonville and Louisville Limestones Over the Range 0-20 GPa." Private communication to be published as SAND92-0983.
- Furnish, M. D. Private communication, letter to A. Martinez, 20 April 1993.
- Furst, B. Private communication, 1993.

Gaffney, E. S. "Hugoniot of water ice." Ices in the Solar System edited by Reidel Publishers (1985): 119-148.

Gaffney, E. S. and Smith, E. A. Hydroplus Experimental Study of Dry, Saturated, and Frozen Geological Materials. Defense Nuclear Agency Report No. TR-93-74. Ktech Corporation, Albuquerque, NM: 1993.

Gagnon, R. E., H. Kiefte, M. J. Clouter, and E. Whalley. "Acoustic Velocities in Ice Ih, II, III, V, and VI, By Brillouin Spectroscopy." J. de Physique 48 (C1-1987): pp. 29-34.

Grady, D. E. "Experimental Analysis of Spherical Wave Propagation." J. Geophys. Res. 78 8 (1973): 1299.

Grady, D. E. Compression Wave Studies in Oakhall Limestone. Sandia National Laboratories Report No. SAND83-0370. Albuquerque, NM: 1983.

Grady, D. E., Hollenbach, R. E., and Schuler, K. W. "Compression Wave Studies on Calcite Rock." J. of Geophys. Res. 83 B6 (1978): 2839-2849.

Greb, A. and Smith, E.A. Cryogenic Gas Gun Spall Testing. Ktech Corporation Report No. TR90-16. Albuquerque, NM: 1990.

Hysol Division of Dexter, Inc., Andover, MA.

Jones, A. H. and Froula, N. H. "Uniaxial Strain Behavior of Four Geological Materials to 50 Kilobar." DASA-2209, March 1969.

Karnes, C. K., Private communications, Sandia National Laboratories, Albuquerque, NM 87185.

LeCroy Research Corporation, Chestnut Ridge, NY.

Lee, L. M., Scotten, E. M., and Smith, T. W. Weapons Laboratory Material Response Impact Facility Test Programs (June 1984 through June 1989). Air Force Weapons Laboratory Report No. AFWL-TR-85-31 Vol. 2. Kirtland AFB, NM: 1989.

Lee, L. M., Jenrette, B. D., and Newcomb, C. G. Carbon Stress Gauge Characterization Air Force Weapons Laboratory Report No. AFWL-TR-81-68. Kirtland AFB, NM: 1981.

Lombard, D.B. The Hugoniot Equation of State of Rocks. University of California, Radiation Laboratory Report No. UCRL-6311. Livermore, CA: 1961.

Marsh, S. P. LASL Shock Hugoniot Data University of California Press, Berkeley, CA, 1979.

Martin, J. W. Private communication to A. Martinez, 1993.

Martin, J.W. SHIST Granite Laboratory Material Properties Tests. Ktech Corporation Letter Report No. TR94-16 to Terra Tek. Albuquerque, NM: 1993.

Martin, J. W., C. W. Felice, and J. Marquardt. "Material Property Measurements on Permafrost From the Lupin Mine, Canada." Terra Tek: TR93-31 Dec. 1992.

Martinez, A. Private communication, December 1993.

Meyers, S. Private communication to A. Martinez 1992.

Pronto CA5 Instant Adhesive, 3M, St. Paul, MN.

Rohm & Haas Type II UVA Polymethyl Methacrylate (PMMA) obtained in sheet stock.

Seaman, L. "Analysis of Dynamic In-Site Backfill Property Tests: Report 2 an Improved Lagrangian Analysis for Stress and Particle Velocity Gauge Arrays" SL-87-11 Waterways Experiment Station Vicksburg, MS, 1987.

Seaman, L. "An Improved Lagrangian Analysis for Stress and Particle Velocity Gage Arrays" U.S. Army Corps of Engineers Waterways Experiment Station Technical Report SL-87-11 (Report 2) Vicksburg, MS, 1987.

Smith, Eric A. WL Impact Facility Double-Delay-Leg, Push-Pull VISAR. Ktech Corporation Report No. TR89-11. Albuquerque, NM: 1989.

Tektronix, Inc., P.O. Box 500, Beaverton, OR.

Tyburczy, J. A. and Ahrens, T. J. "Dynamic Compression and Volatile Release of Carbonates." J. of Geophy. Res. 91 B5 (1986): 4730-4744.

Wise, J. L. and Chhabildas, L. C. "Laser Interferometer Measurements of Refractive Index In Shock-Compressed Materials." Shock Waves in Condensed Matter, 1986.

## APPENDIX

### STRESS AND PARTICLE VELOCITY WAVEFORMS

The figures in this appendix contain stress-time and stress-particle velocity profiles for each experiment. The table below summarizes the contents of this Appendix and lists the order in which the profiles are presented along with page numbers.

Table A-1.

Material	Experiment Type	Shot No.	Page No.
Pennsylvania Slate	Lagrangian	3668	106
	Lagrangian	3647	106
	VISAR	3646	107
Maine Slate	Lagrangian	3682	108
	Lagrangian	3681	108
	Lagrangian	3680	109
	Lagrangian	3679	109
	Lagrangian	3678	110
	VISAR	3683	110
	VISAR	3685	111
Phyllite	Lagrangian	3654	112
	Lagrangian	3666	112
HSG-14 Grout	Lagrangian	3630	113
	Lagrangian	3628	113
	Lagrangian	3629	114
	Lagrangian	3632	114
	Lagrangian	3631	115
	VISAR	3638	115
	VISAR	3634	116
	VISAR	3636	116
Granite Grout	Lagrangian	3708	117
	Lagrangian	3722	117
	Lagrangian	3709	118
	Lagrangian	3723	118
	Lagrangian	3721	119
	VISAR	3717	119
	VISAR	3716	120
	VISAR	3715	120

Table A-1. (Continued).

Material	Experiment Type	Shot No.	Page No.
SHIST Grout	Lagrangian	3675	121
	Lagrangian	3674	121
	Lagrangian	3673	122
	Lagrangian	3672	122
	Lagrangian	3671	123
	VISAR	3670	123
	VISAR	3669	124
	VISAR	3676	124
	VISAR	3677	125
Sierra White Granite	Lagrangian	3706	126
	Lagrangian	3705	126
	Lagrangian	3690	127
	Lagrangian	3707	127
	Lagrangian	3691	128
	Lagrangian	3700	128
	VISAR	3710	129
	VISAR	3712	129
	VISAR	3711	130

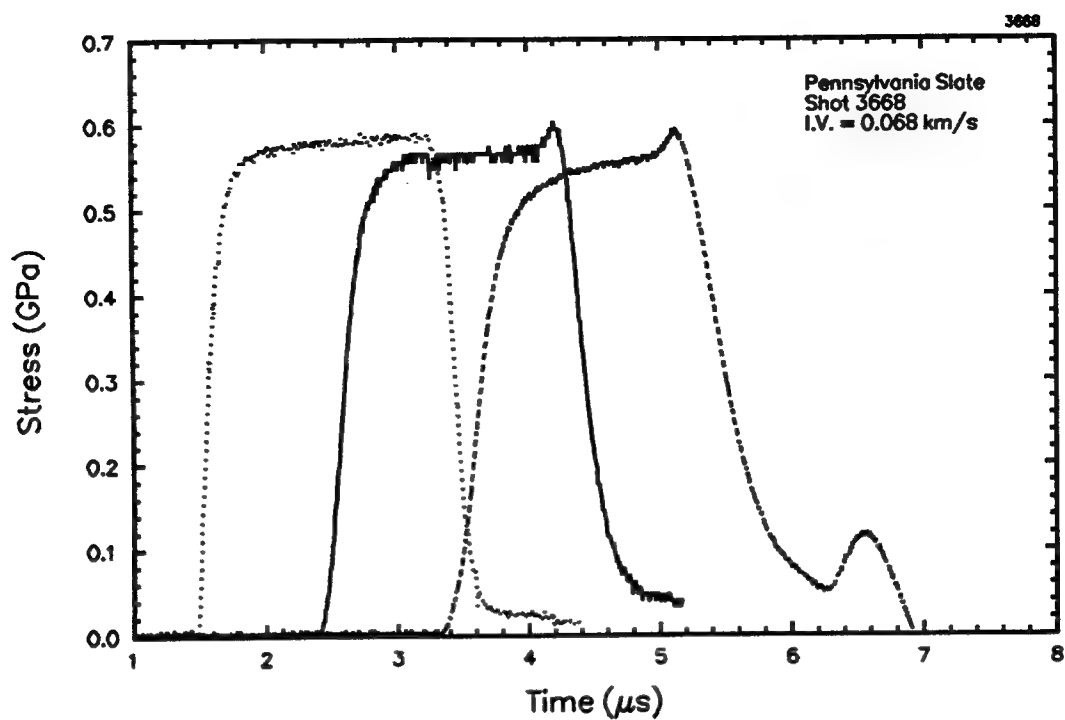


Figure A-1. Shot 3668.

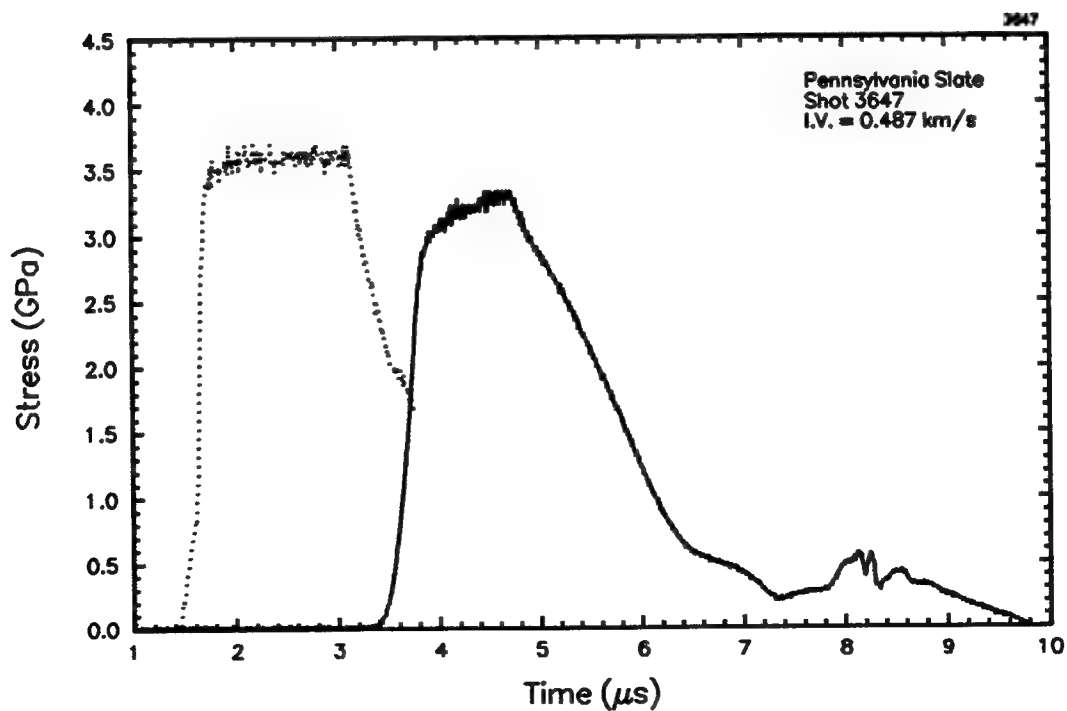


Figure A-2. Shot 3647.

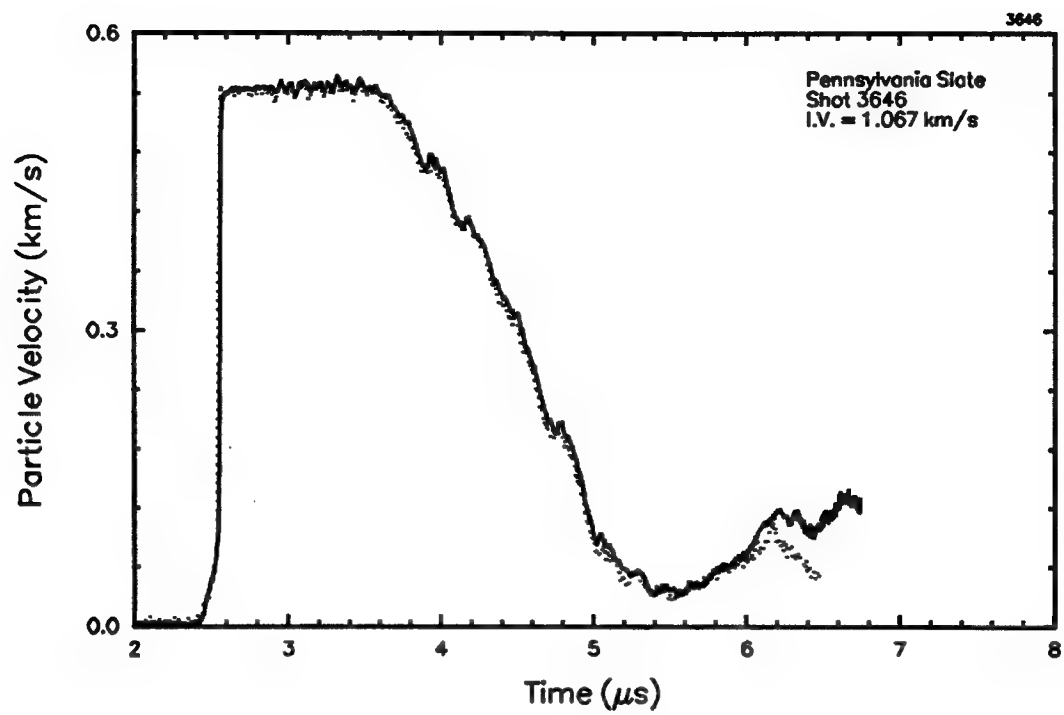


Figure A-3. Shot 3646.

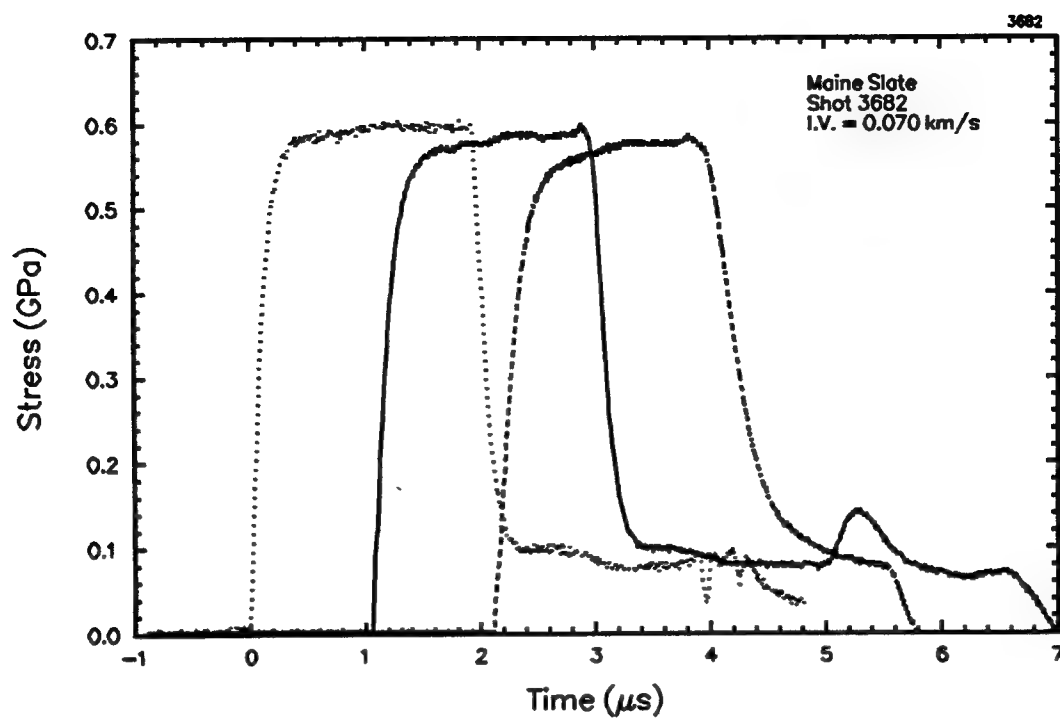


Figure A-4. Shot 3682.

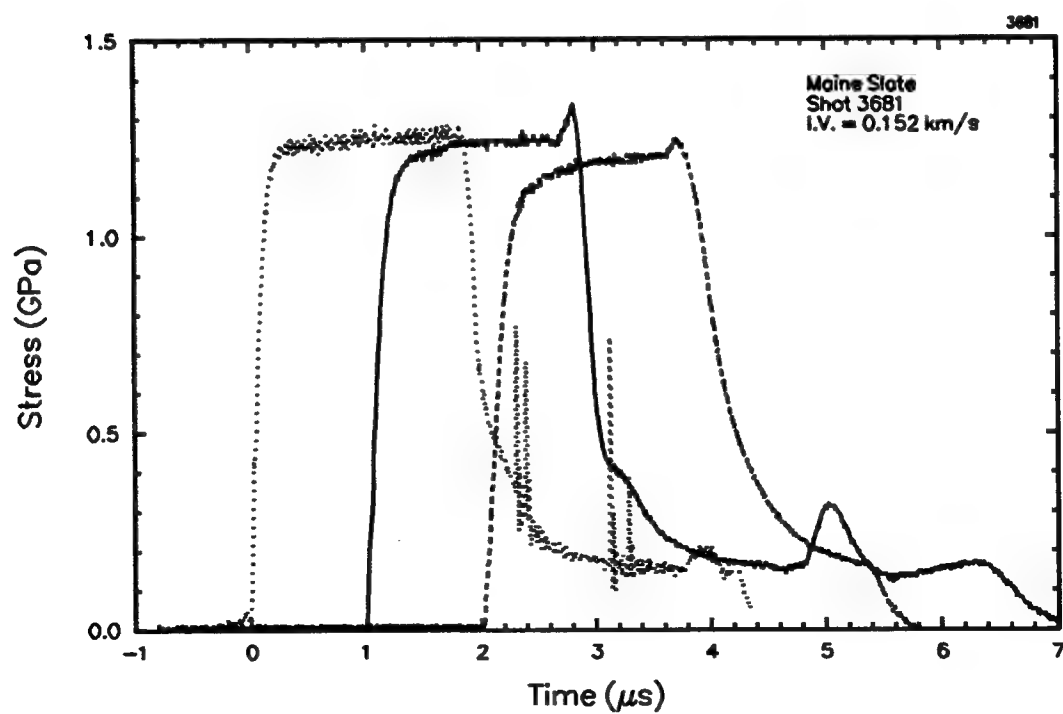


Figure A-5. Shot 3681.



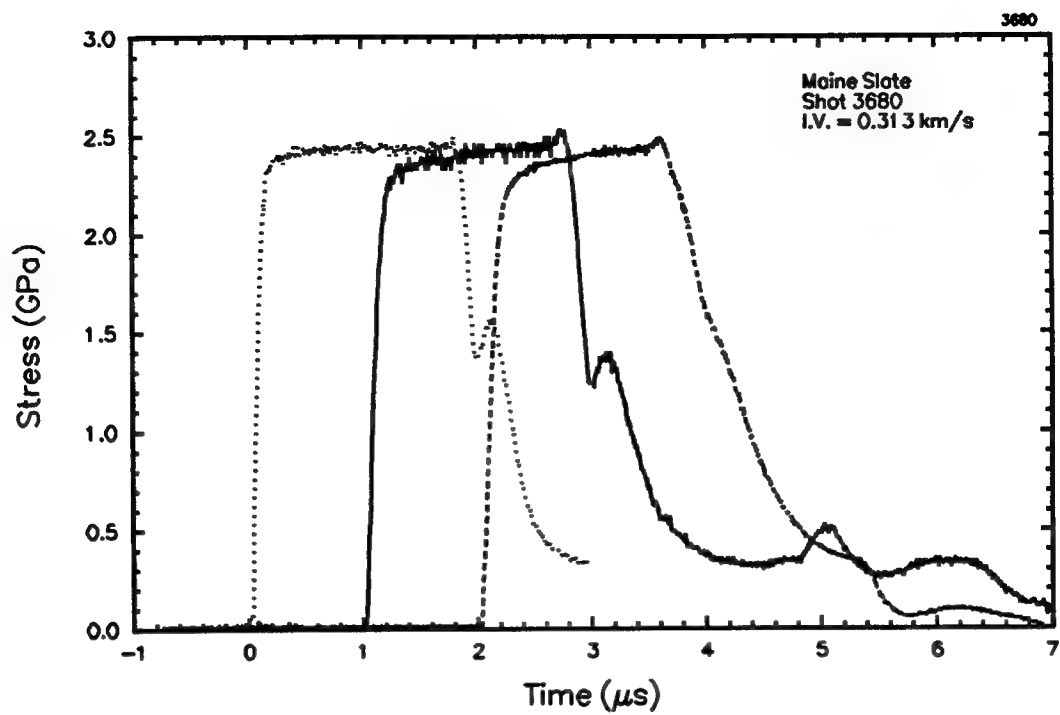


Figure A-6. Shot 3680.

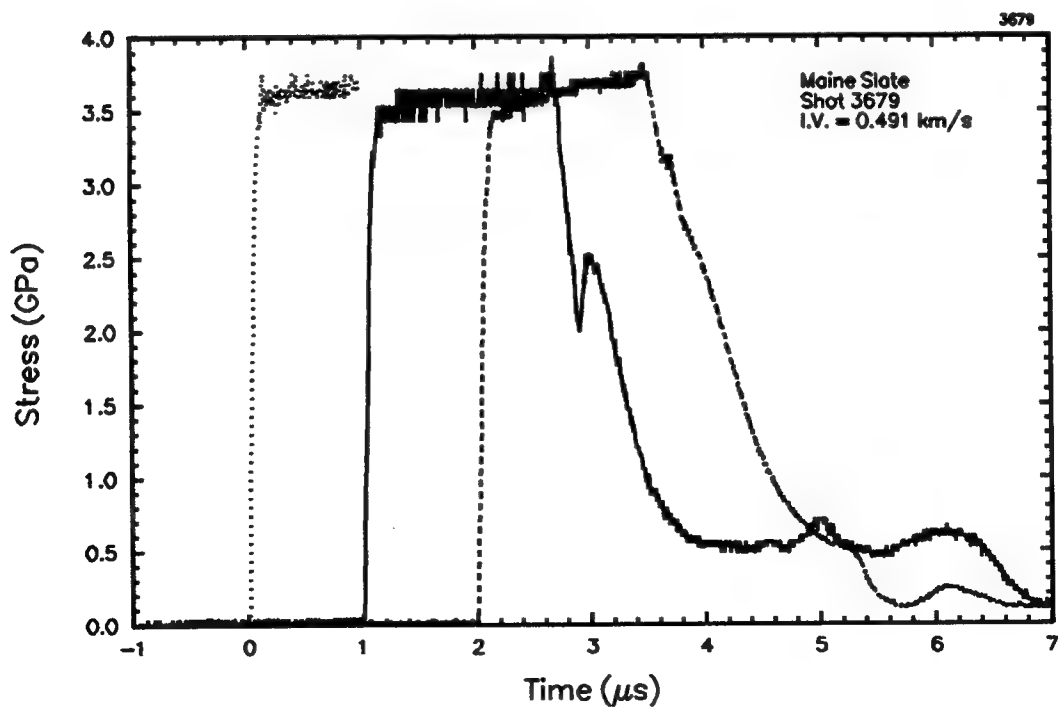


Figure A-7. Shot 3679.

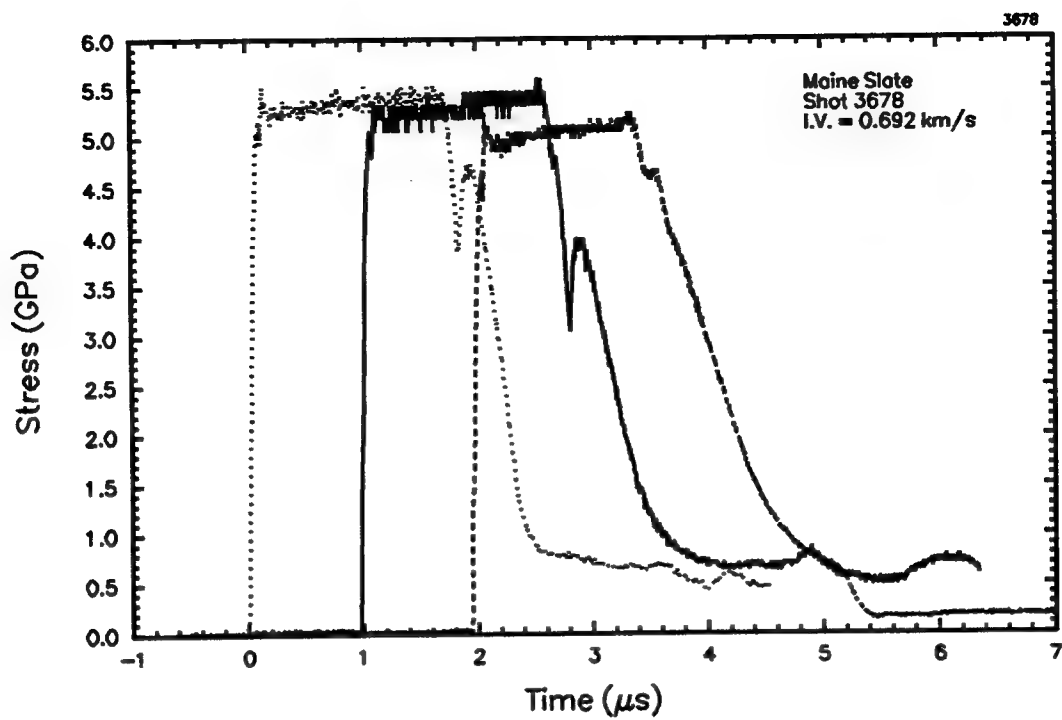


Figure A-8. Shot 3678.

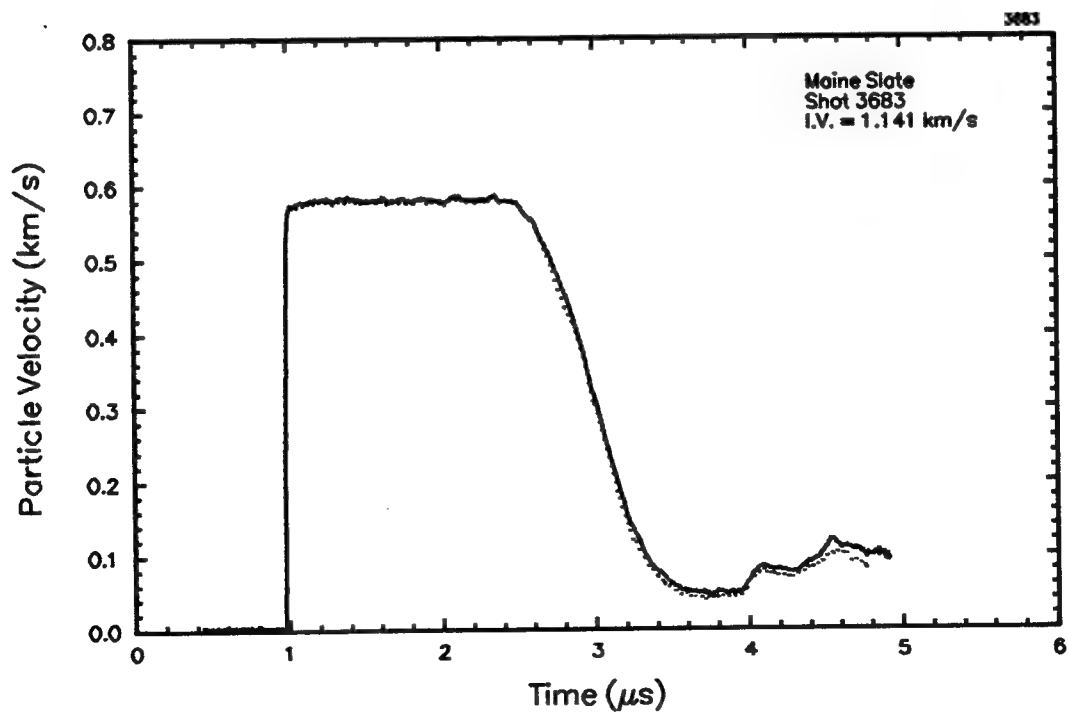


Figure A-9. Shot 3683.

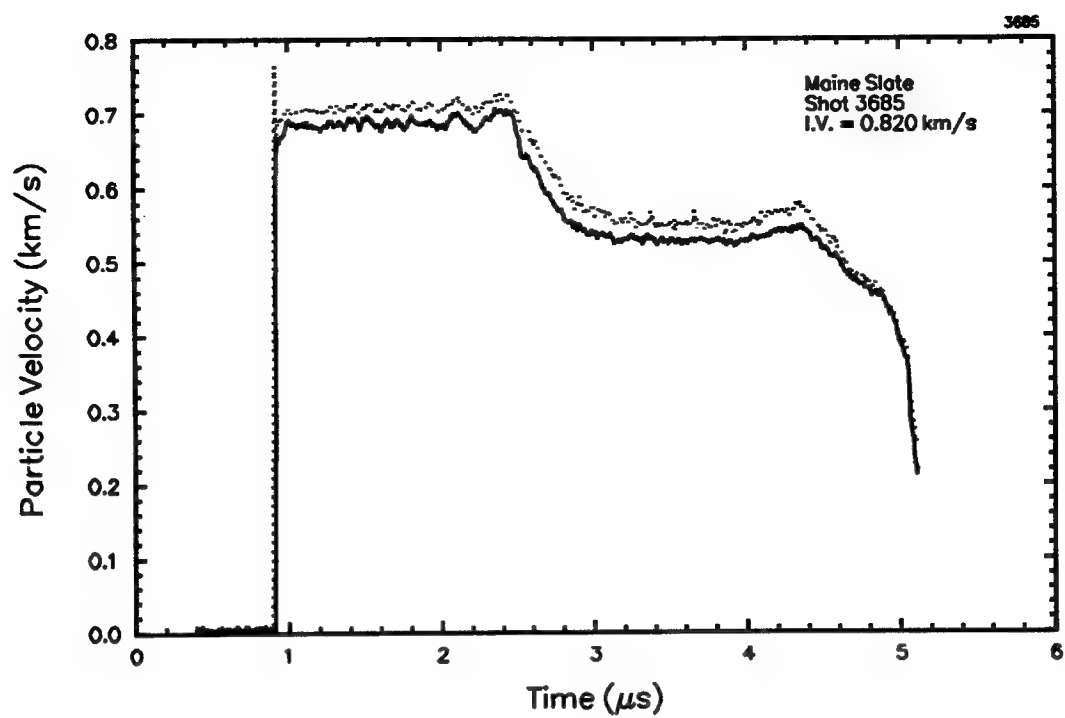


Figure A-10. Shot 3685.

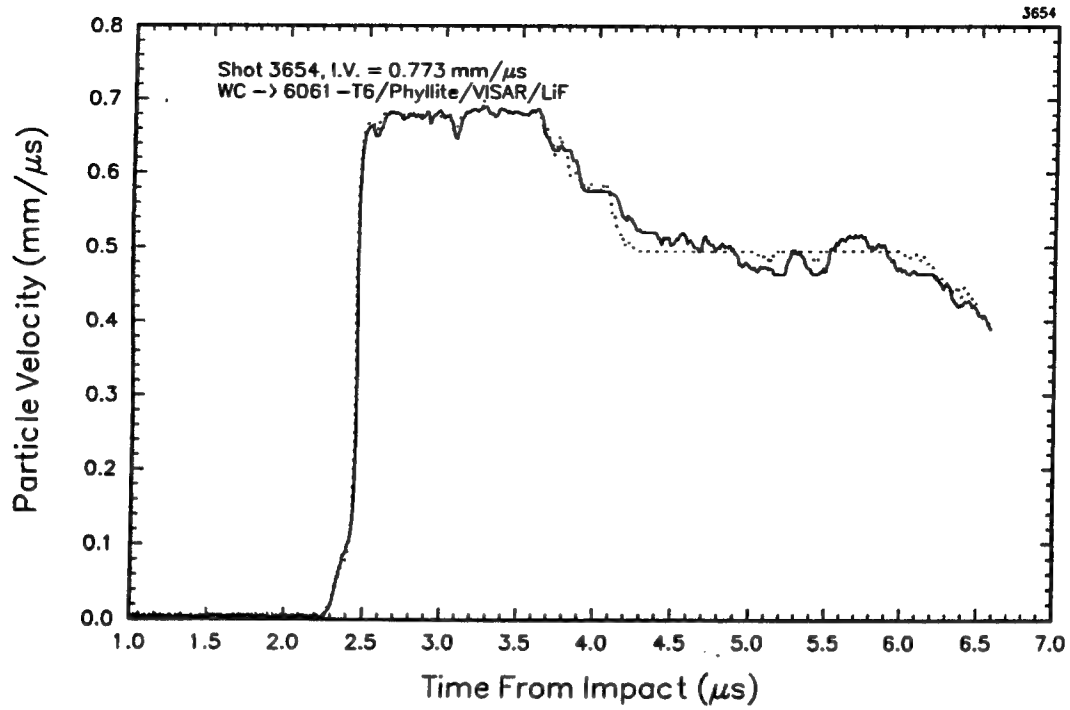


Figure A-11. Shot 3654.

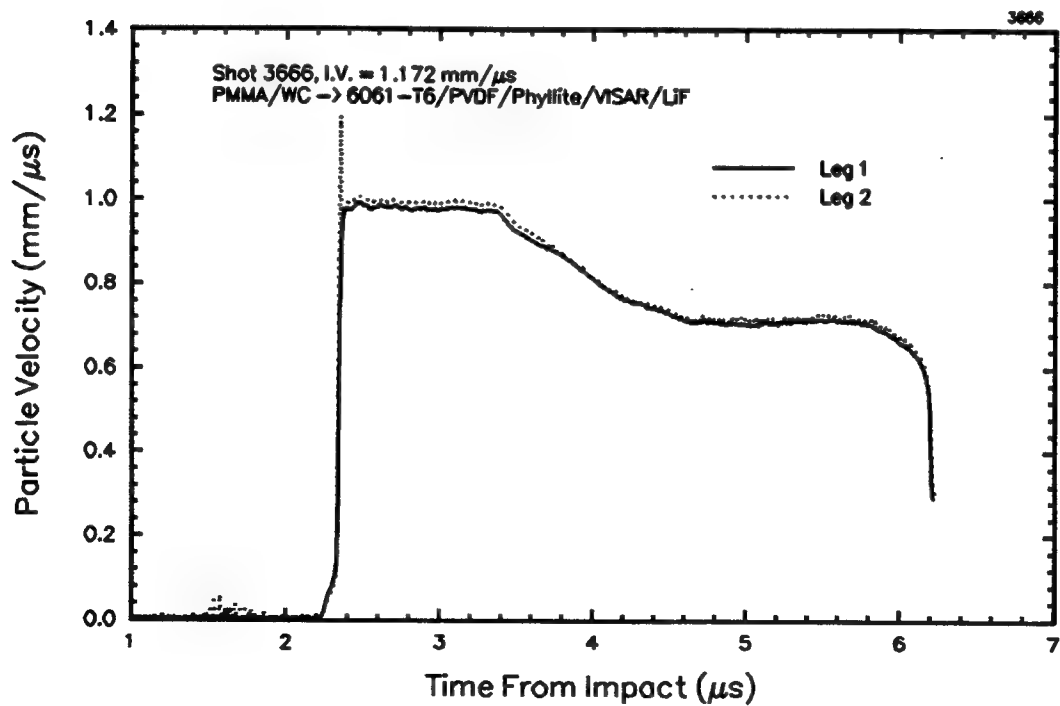


Figure A-12. Shot 3666.

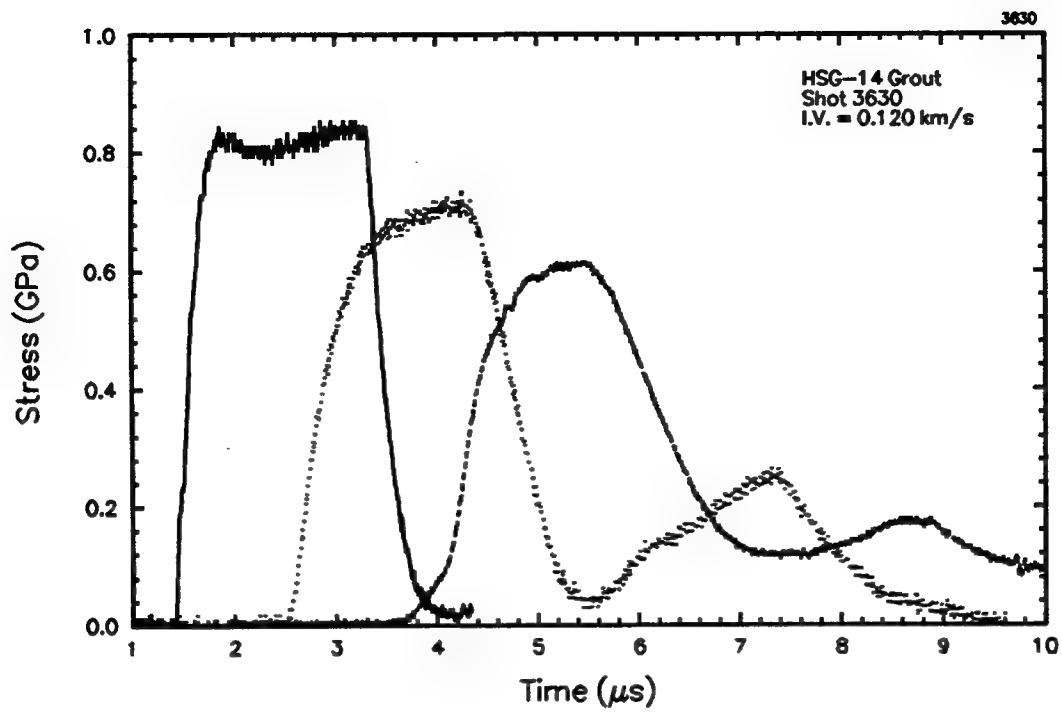


Figure A-13. Shot 3630.

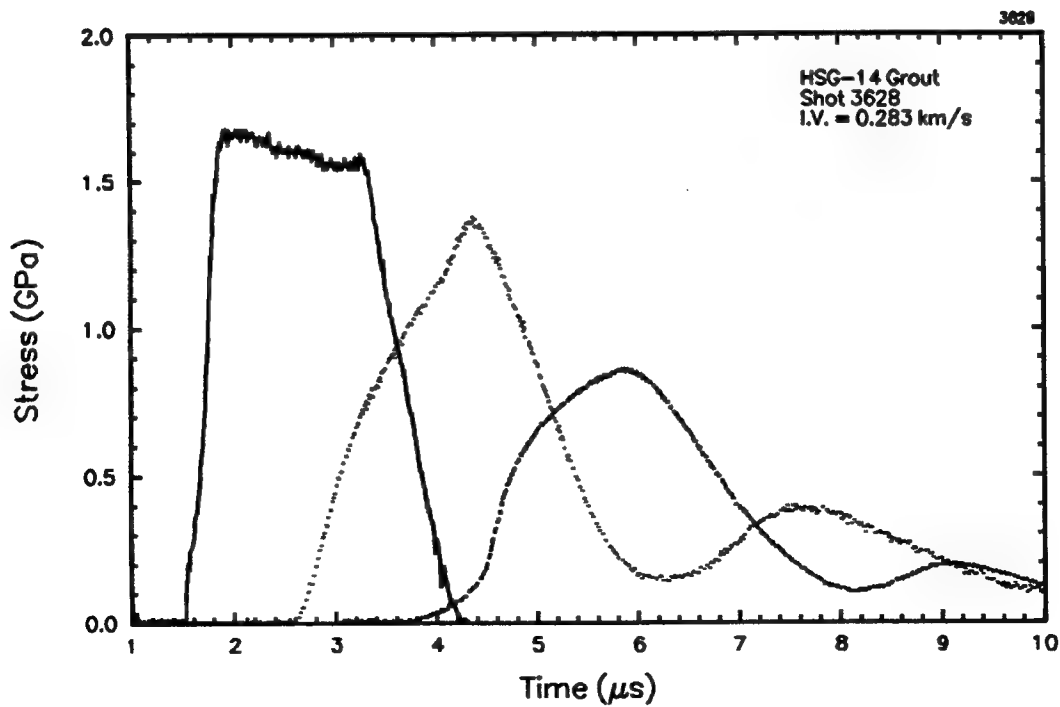


Figure A-14. Shot 3628.

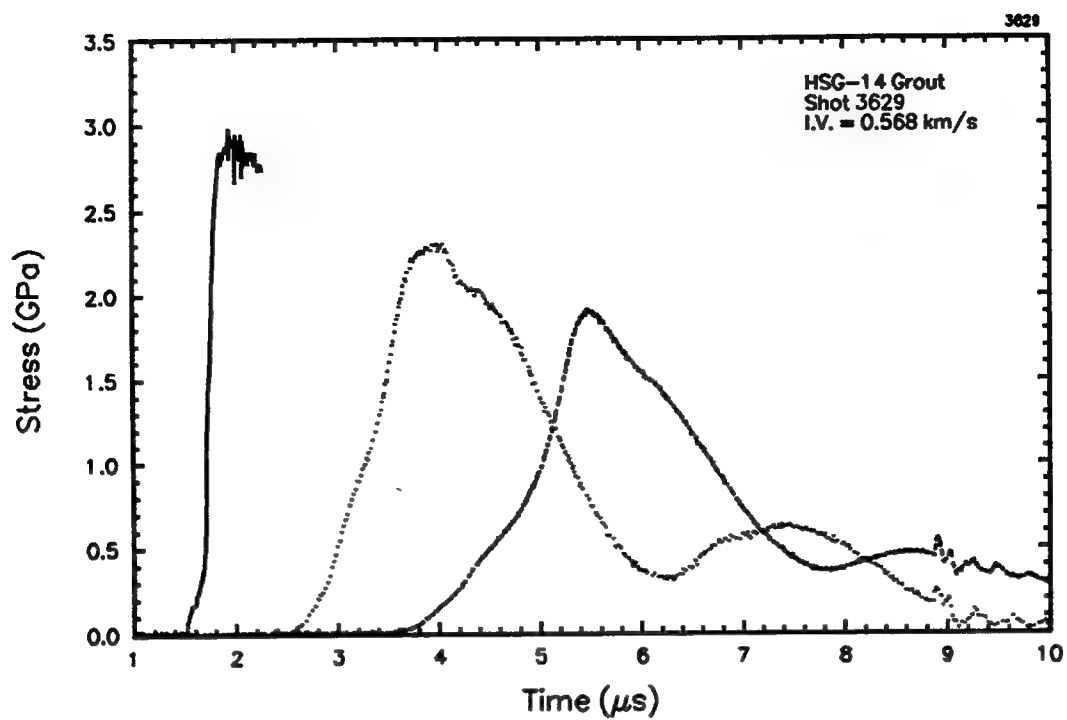


Figure A-15. Shot 3629.

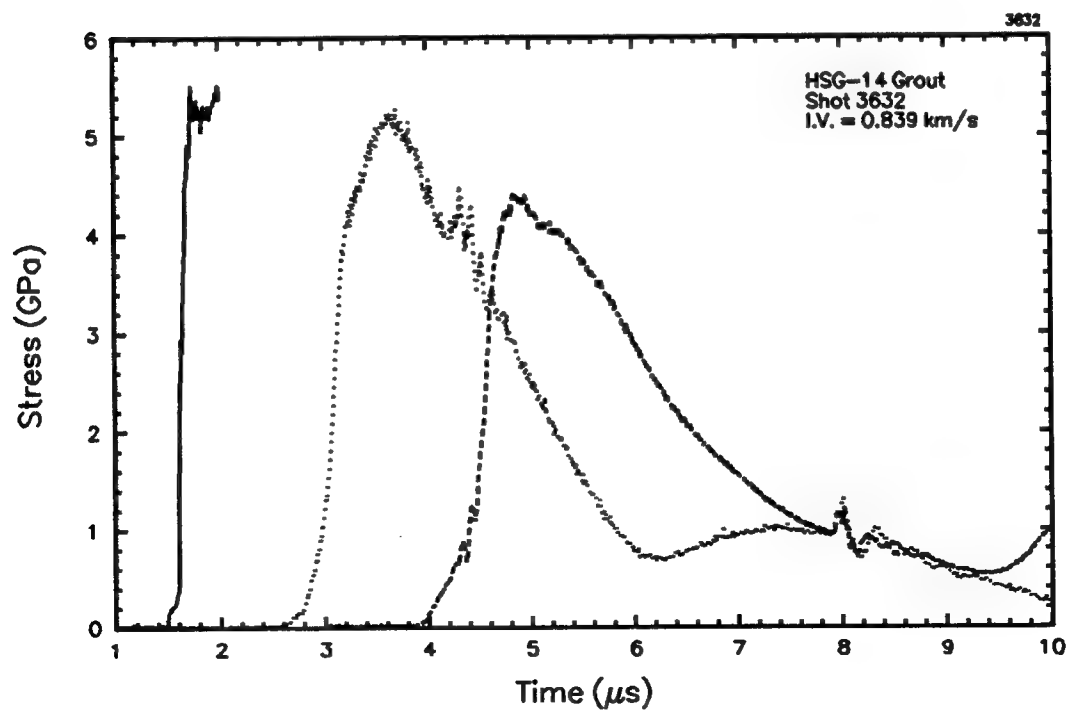


Figure A-16. Shot 3632.

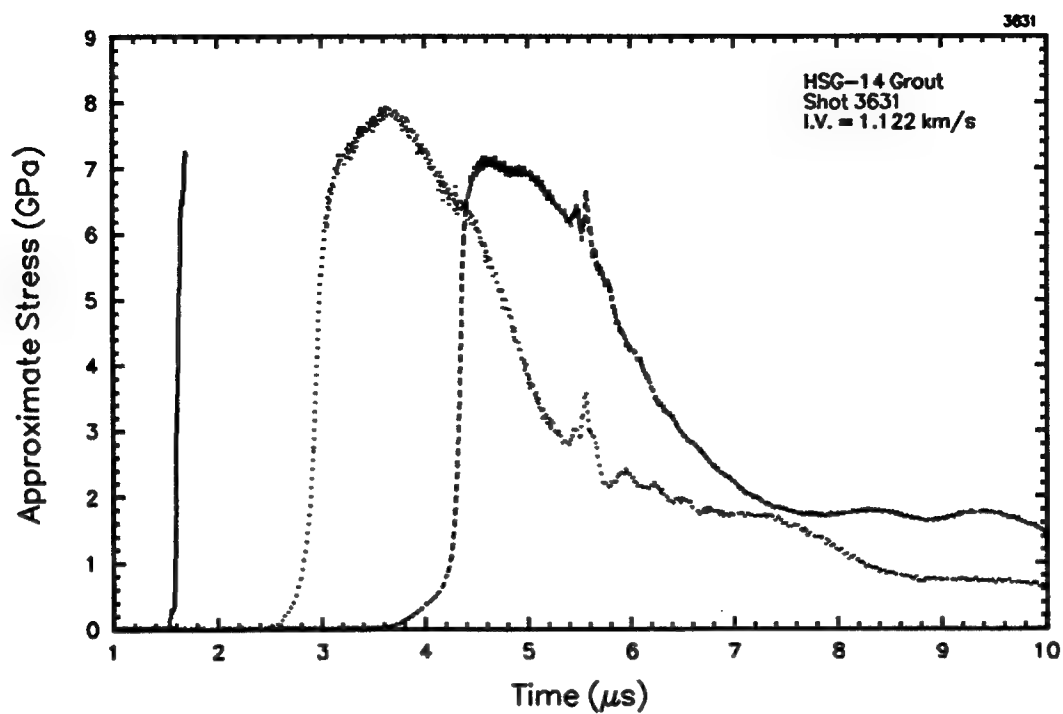


Figure A-17. Shot 3631.

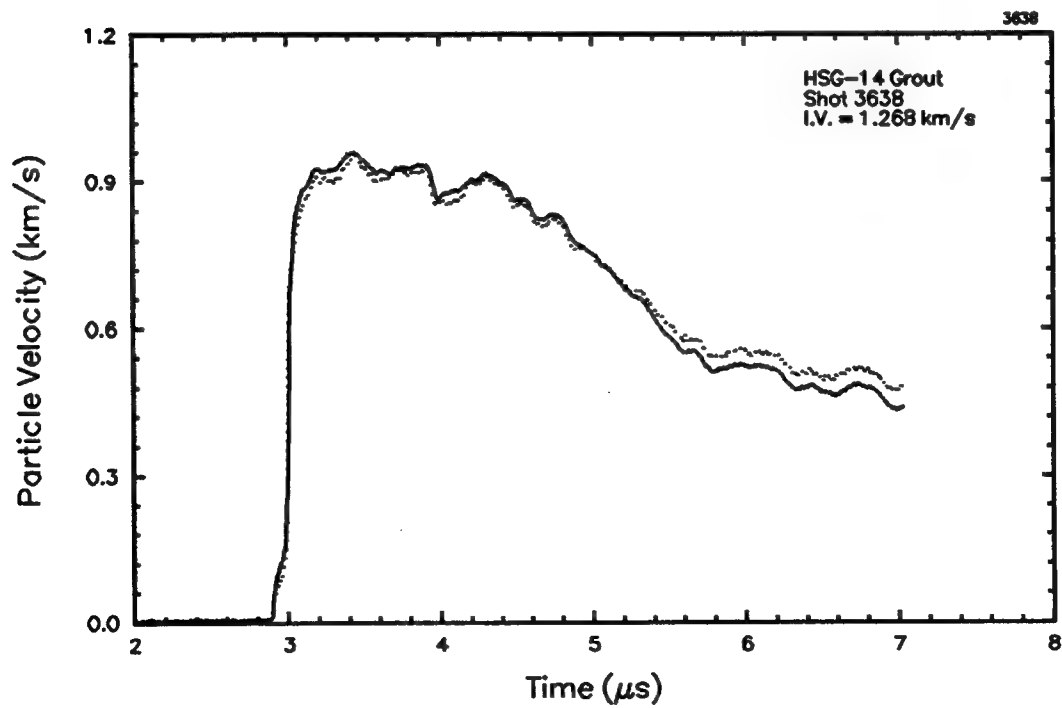


Figure A-18. Shot 3638.

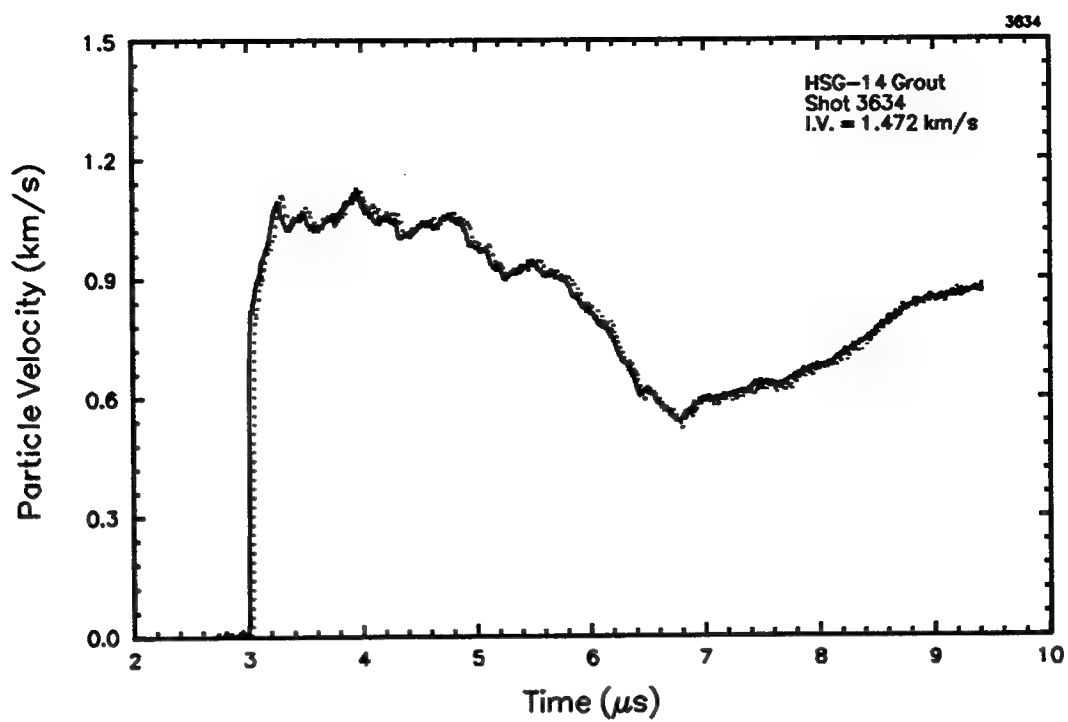


Figure A-19. Shot 3634.

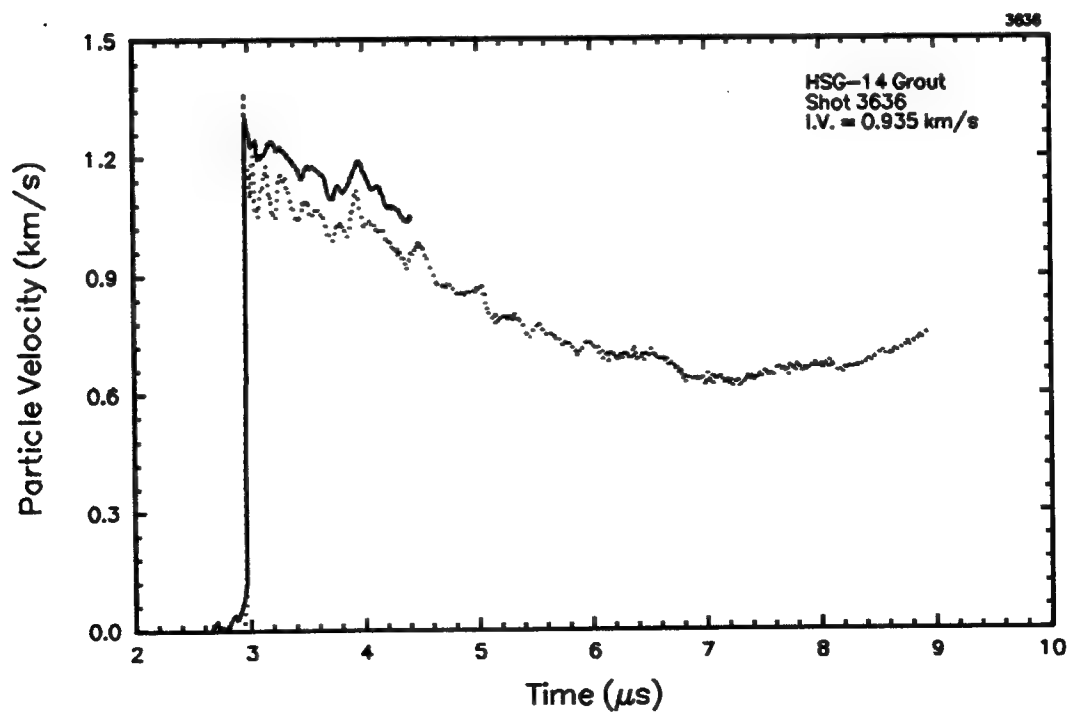


Figure A-20. Shot 3636.



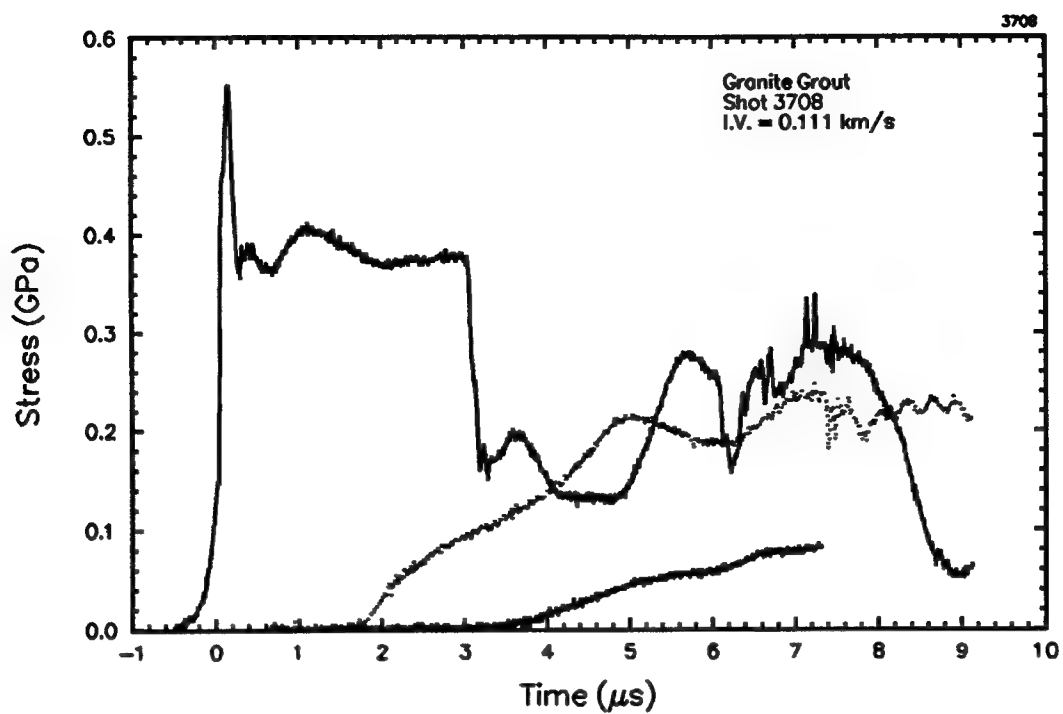


Figure A-21. Shot 3708.

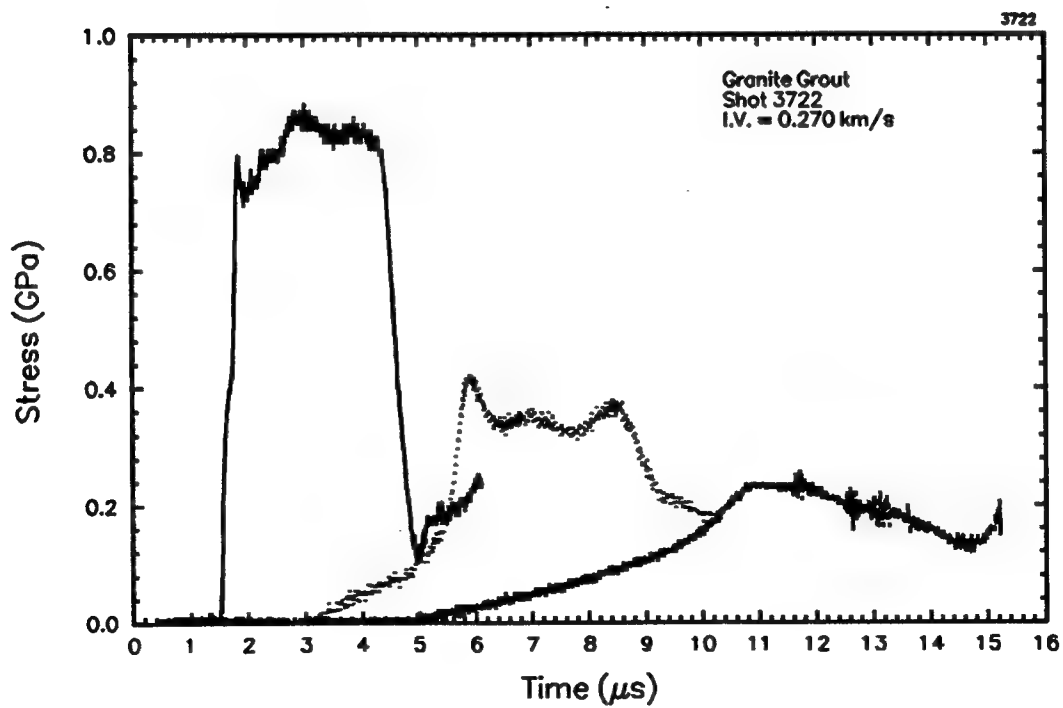


Figure A-22. Shot 3722.

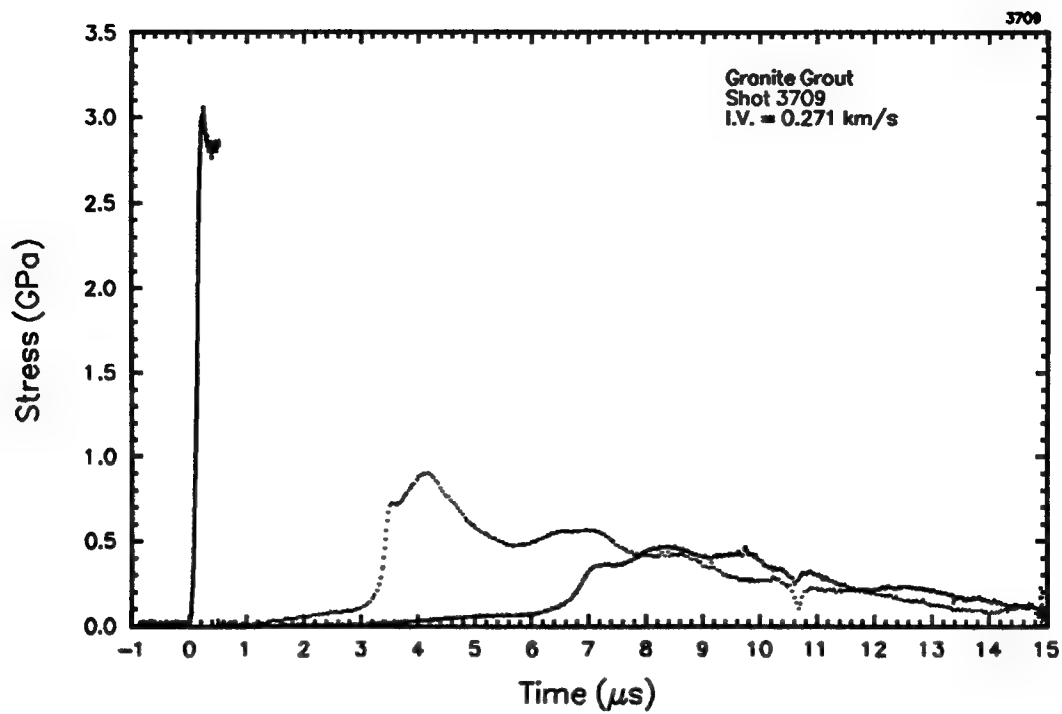


Figure A-23. Shot 3709.

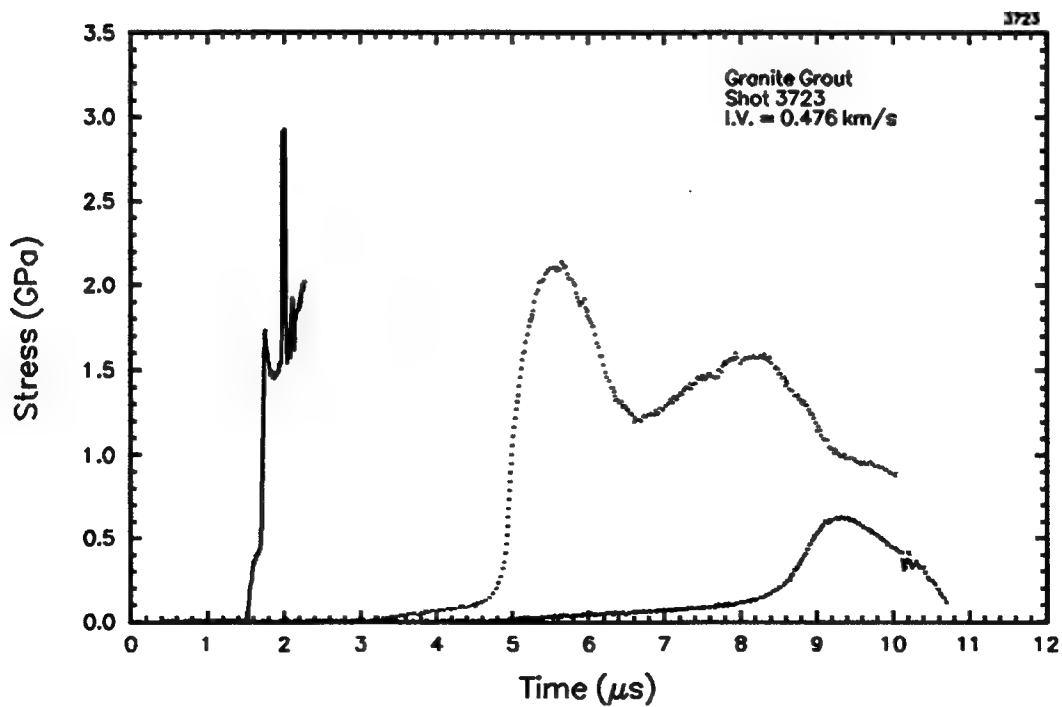


Figure A-24. Shot 3723.

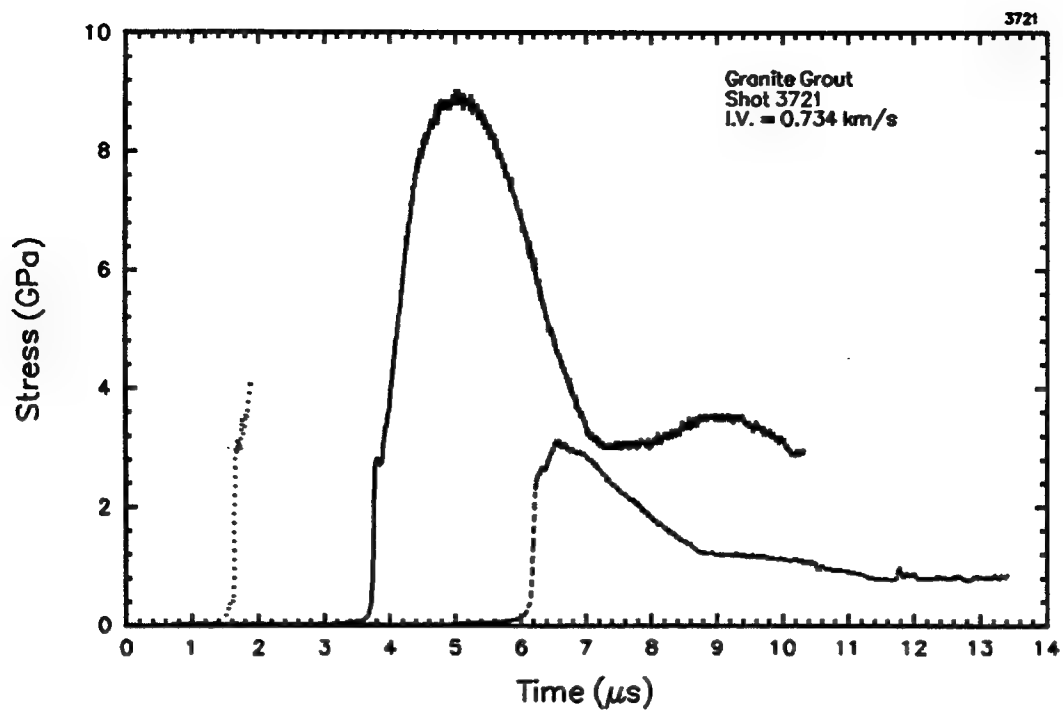


Figure A-25. Shot 3721.

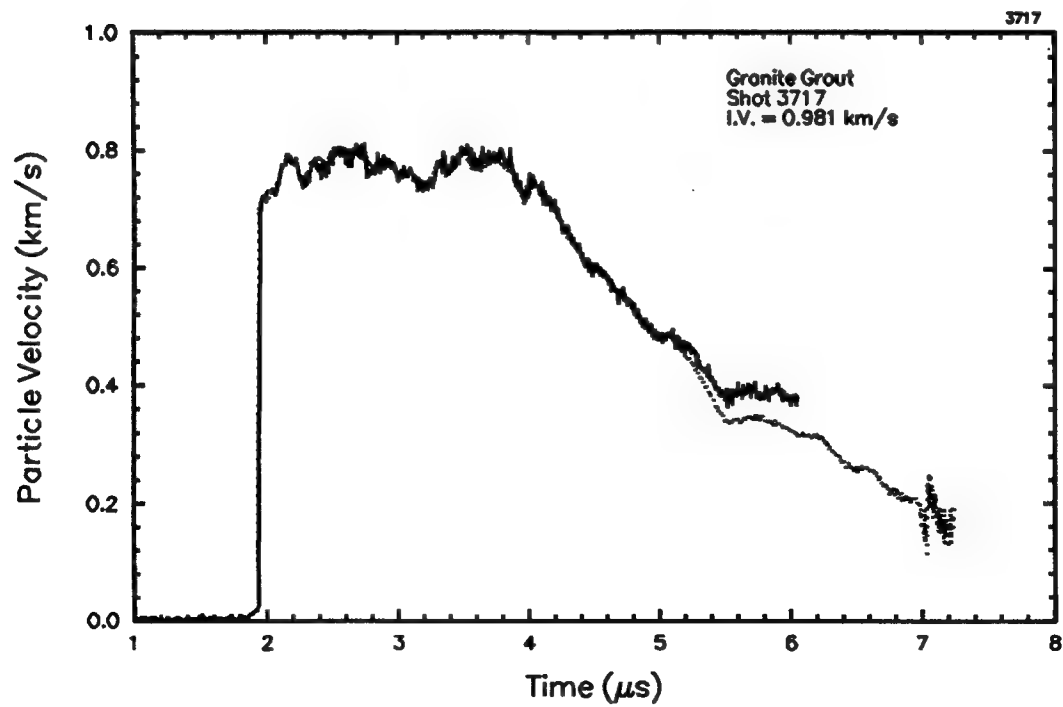


Figure A-26. Shot 3717.

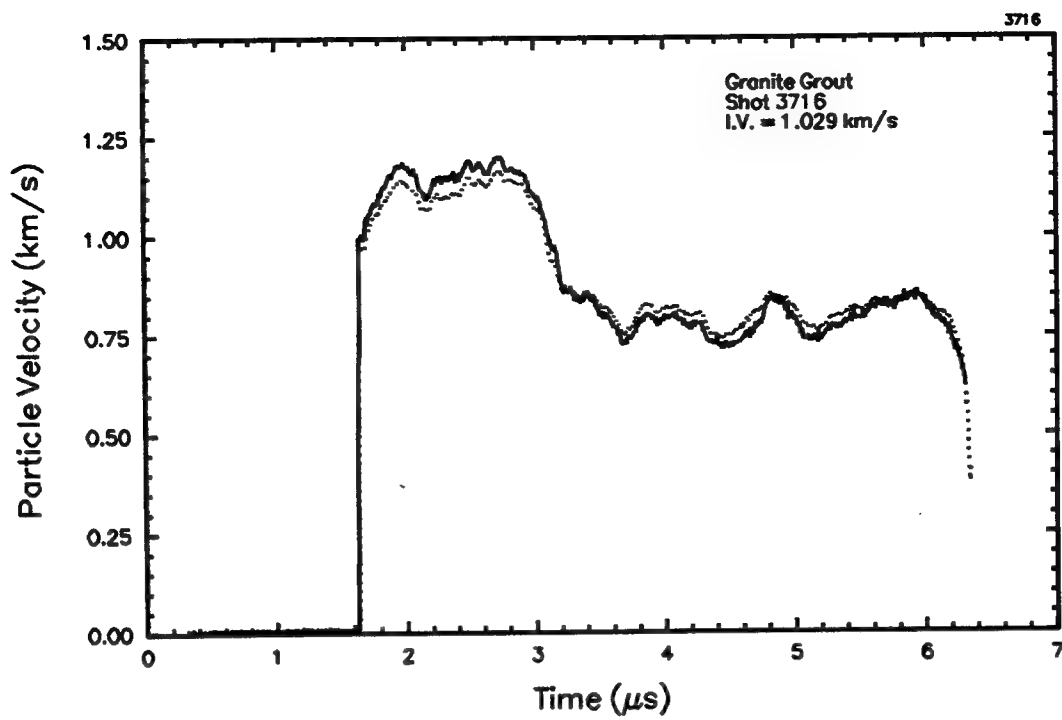


Figure A-27. Shot 3716.

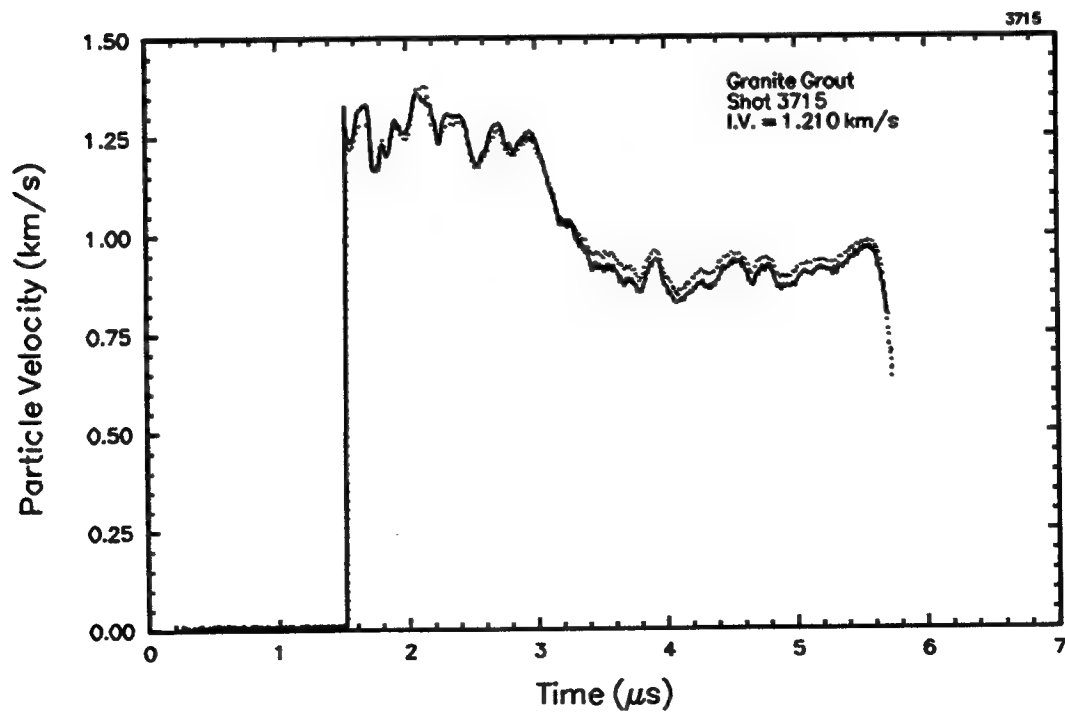


Figure A-28. Shot 3715.

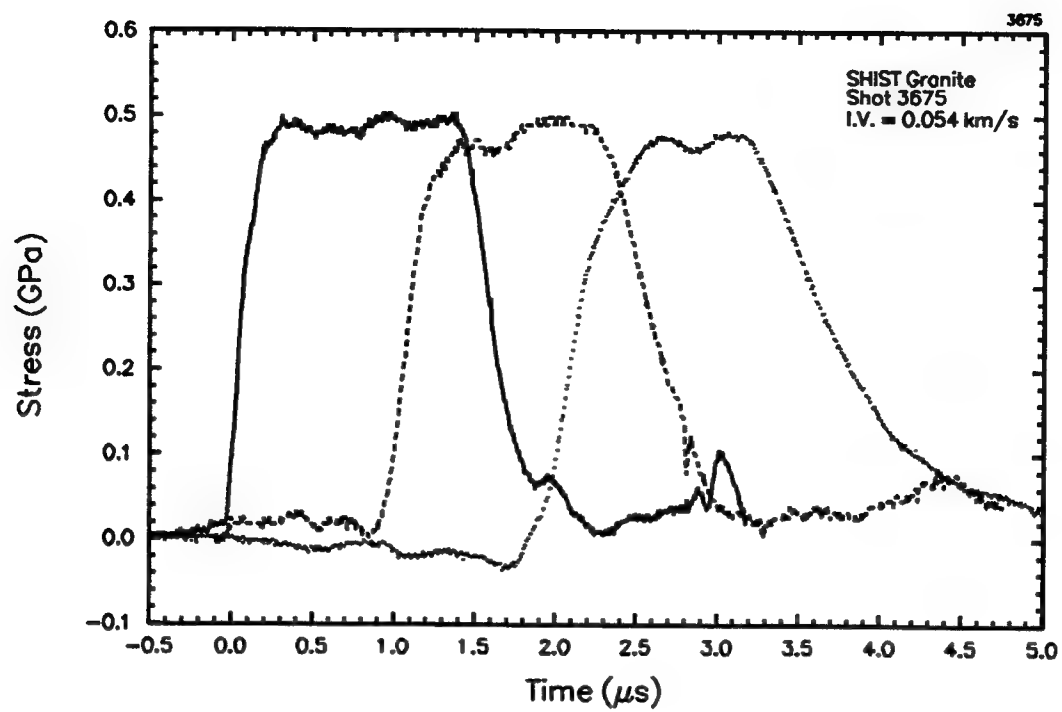


Figure A-29. Shot 3675.

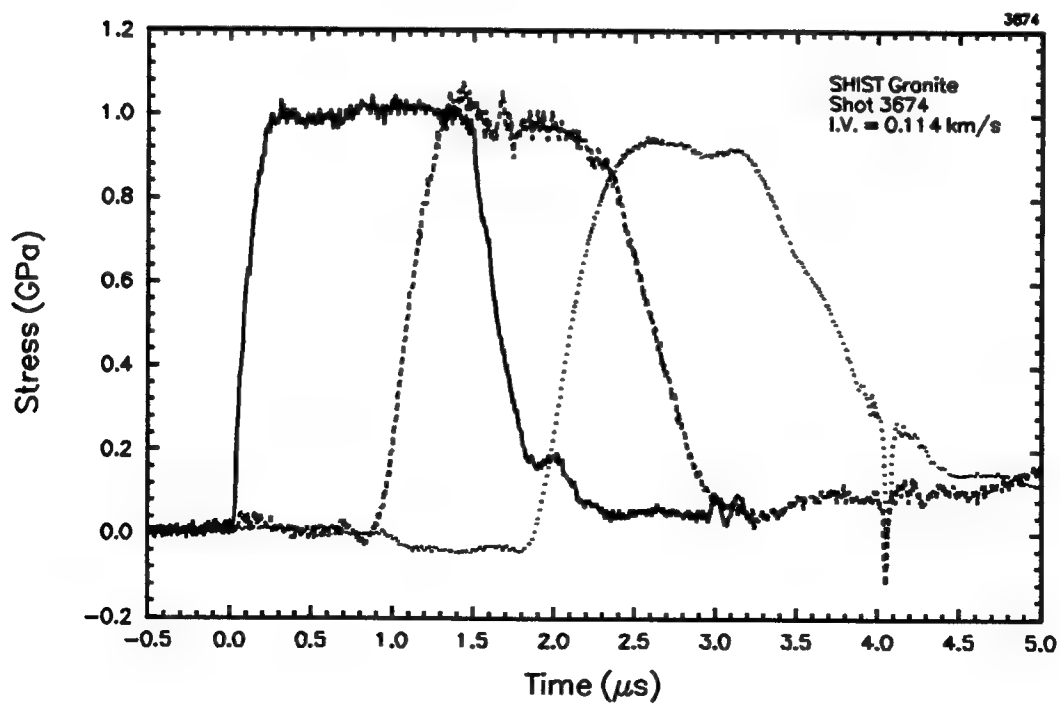


Figure A-30. Shot 3674.

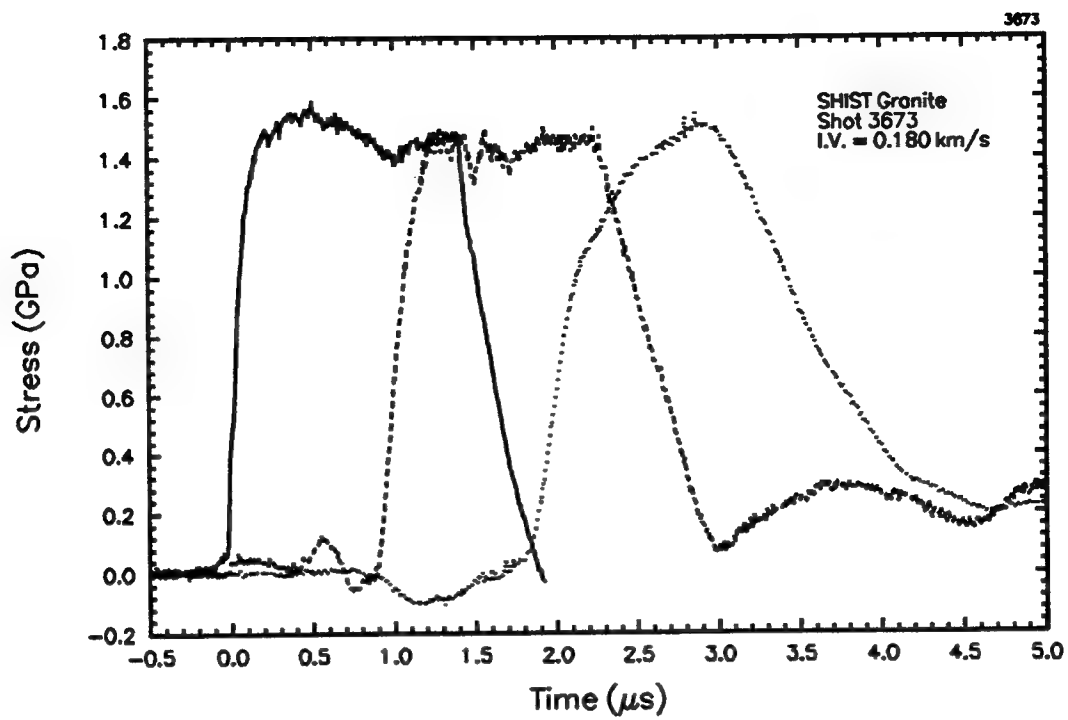


Figure A-31. Shot 3673.

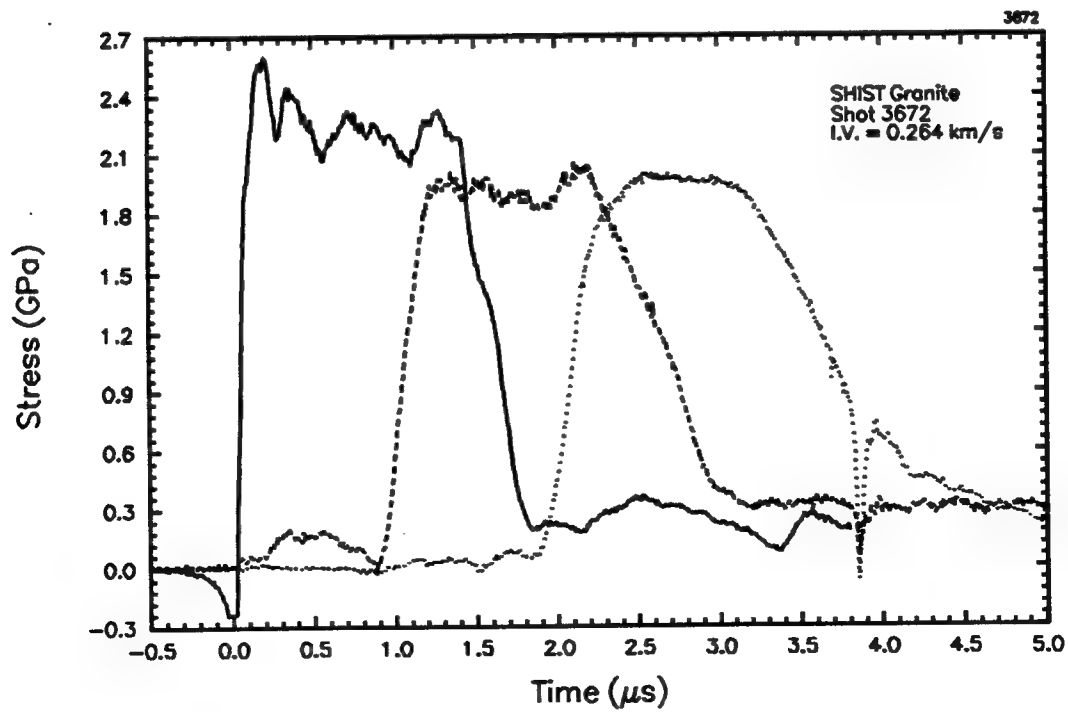


Figure A-32. Shot 3672.

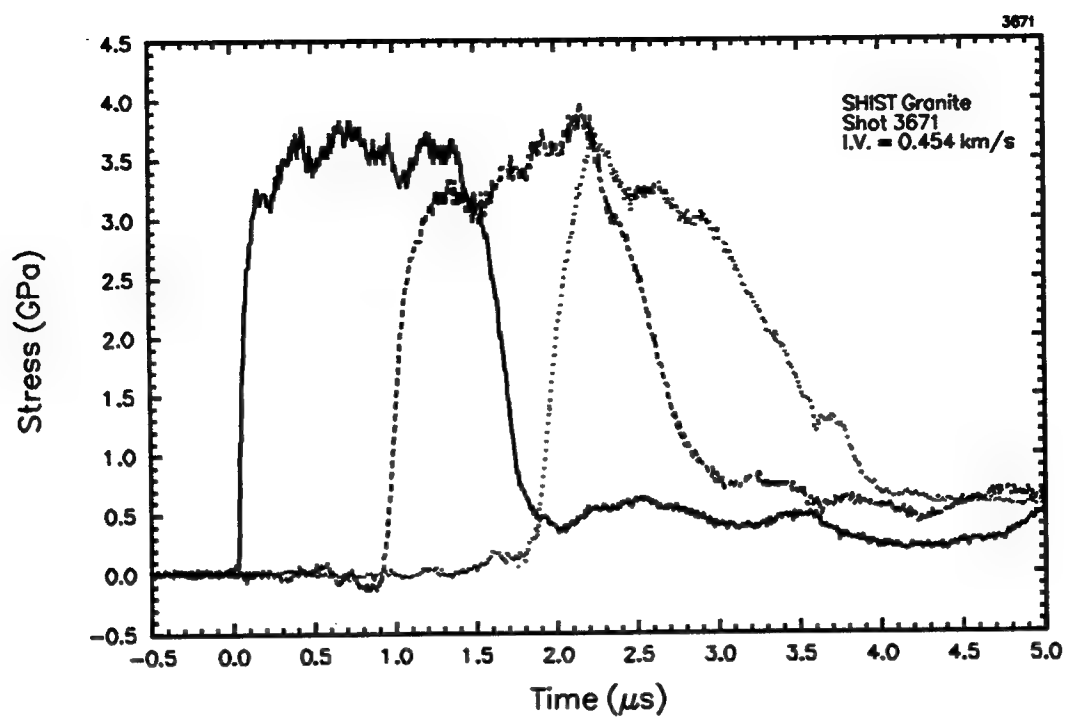


Figure A-33. Shot 3671.

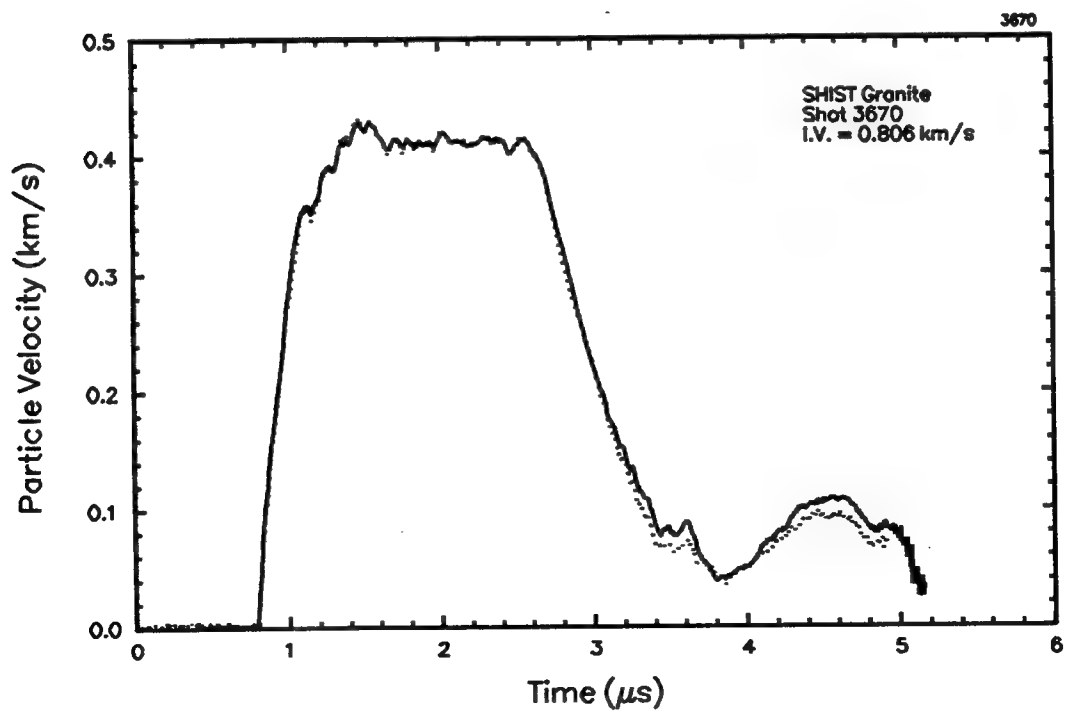


Figure A-34. Shot 3670.

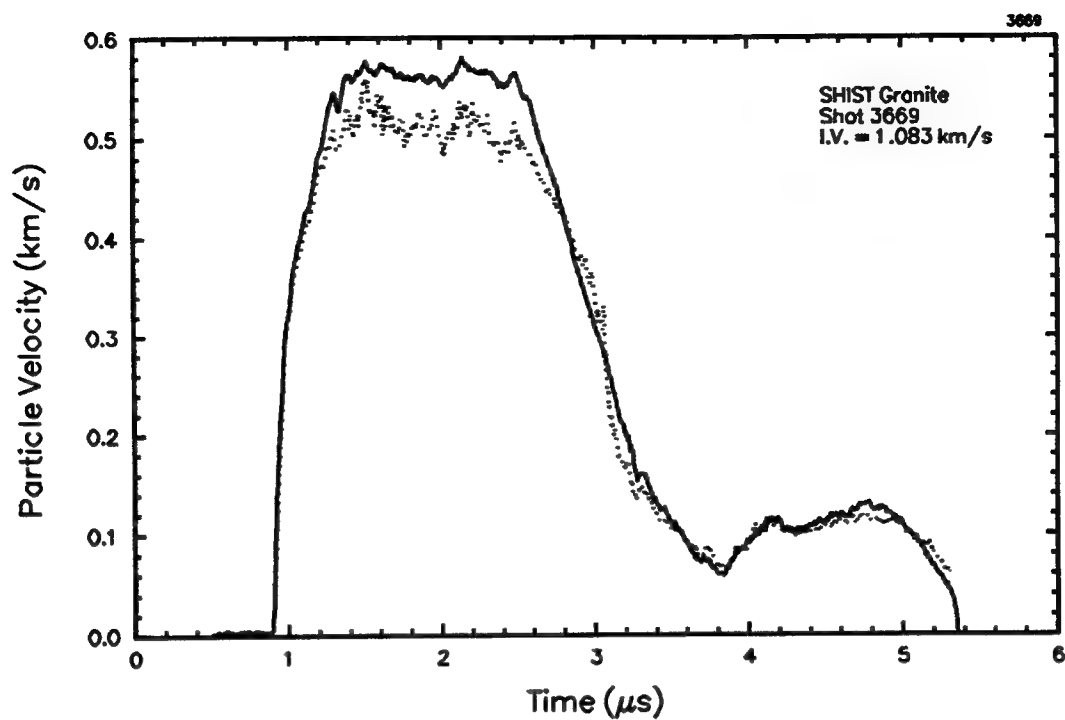


Figure A-35. Shot 3669.

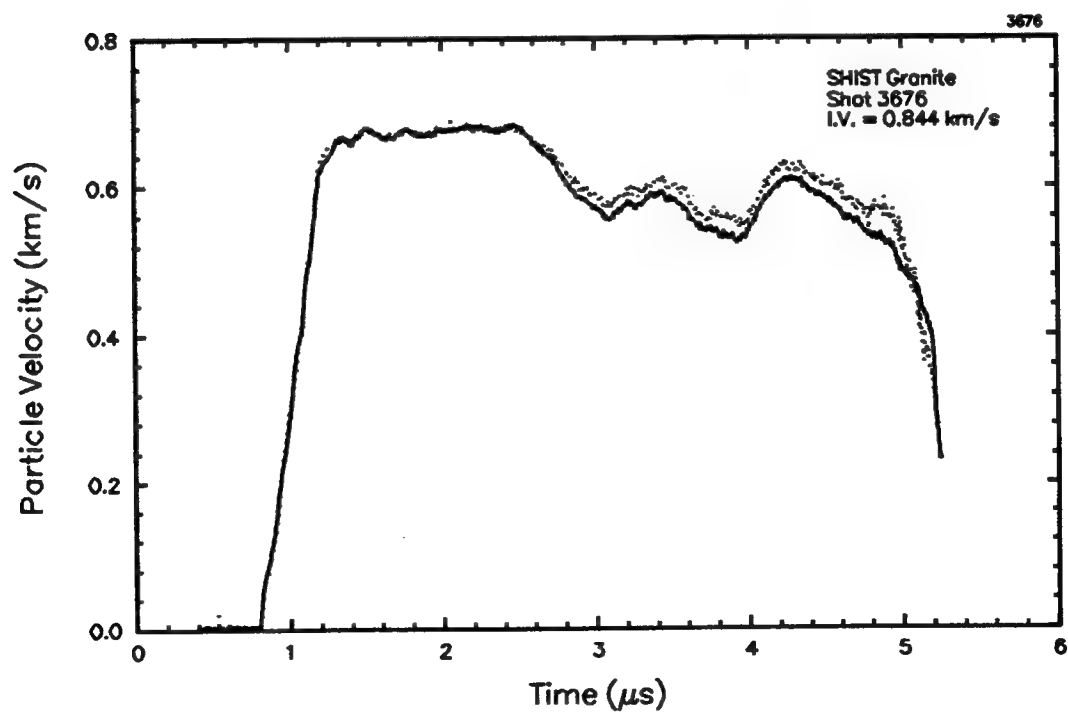


Figure A-36. Shot 3676.



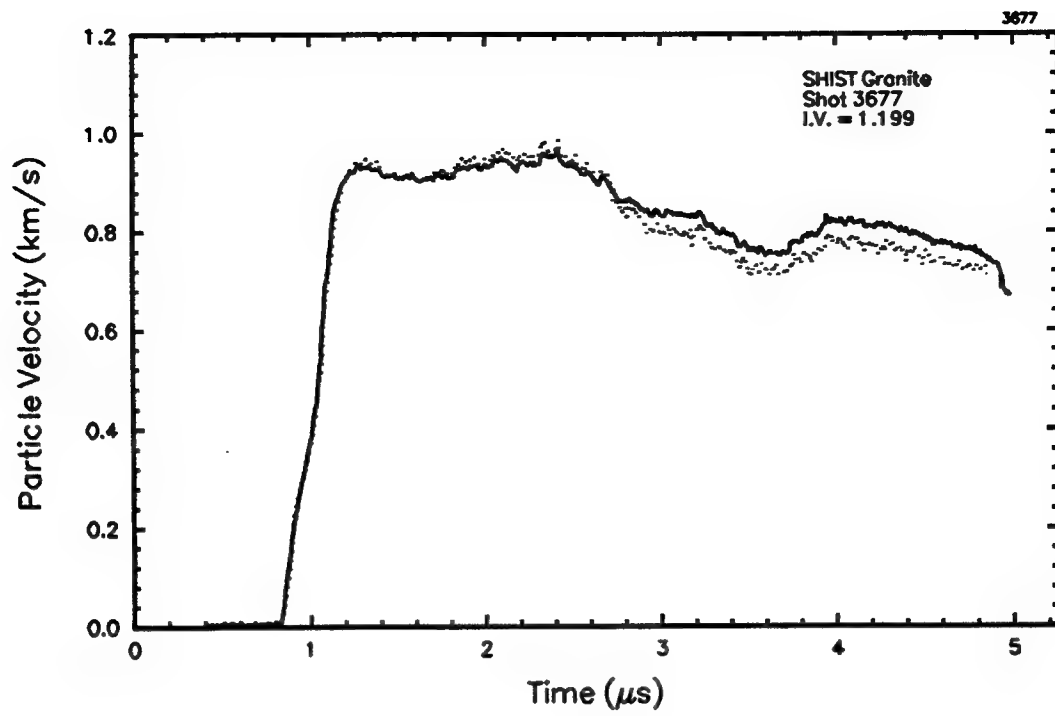


Figure A-37. Shot 3677.

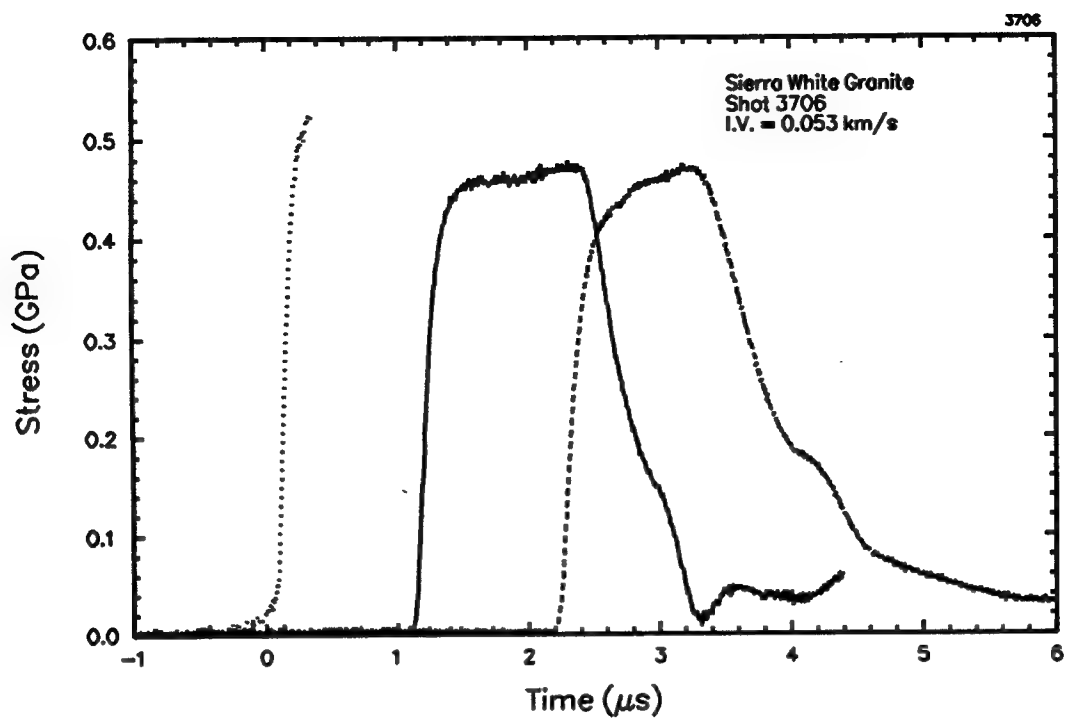


Figure A-38. Shot 3706.

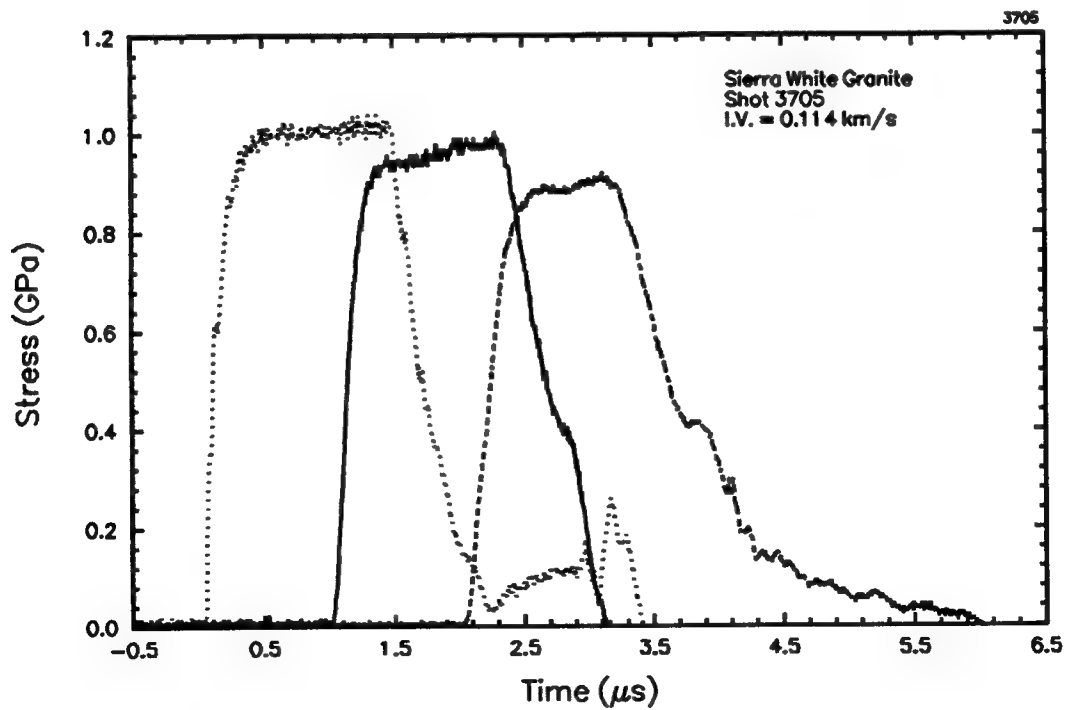


Figure A-39. Shot 3705.

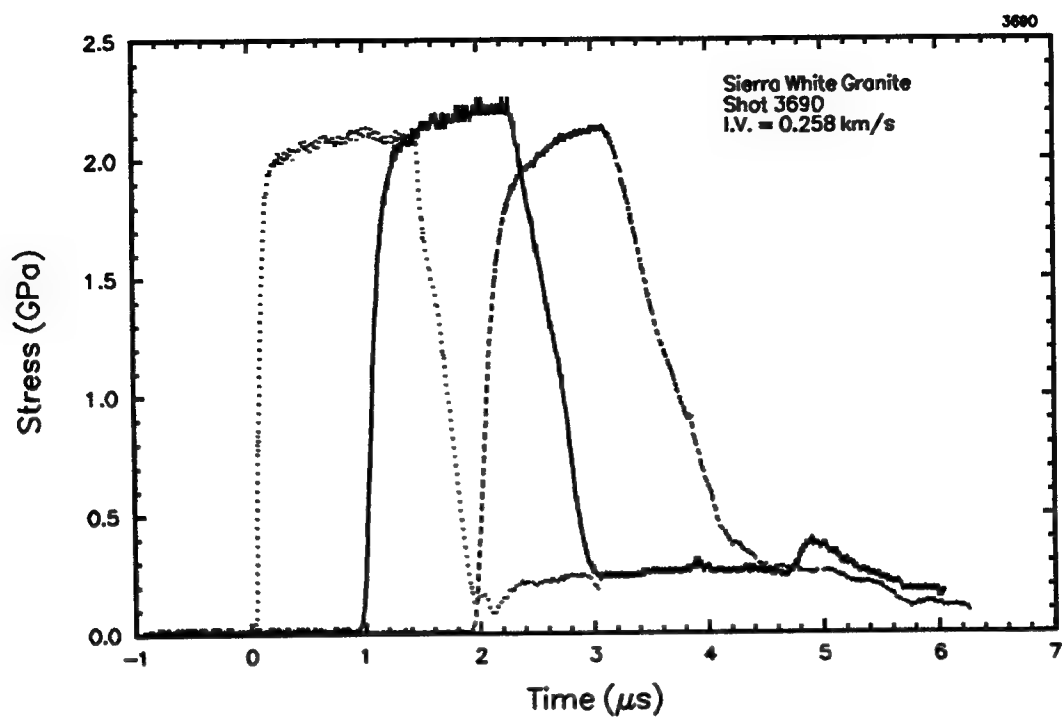


Figure A-40. Shot 3690.

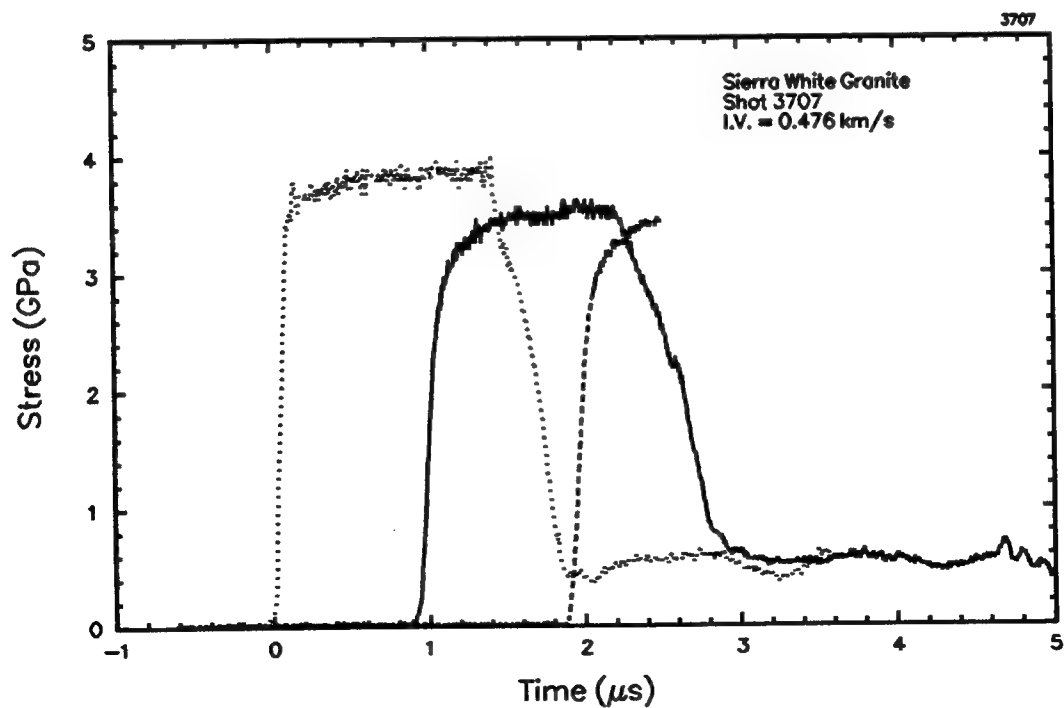


Figure A-41. Shot 3707.

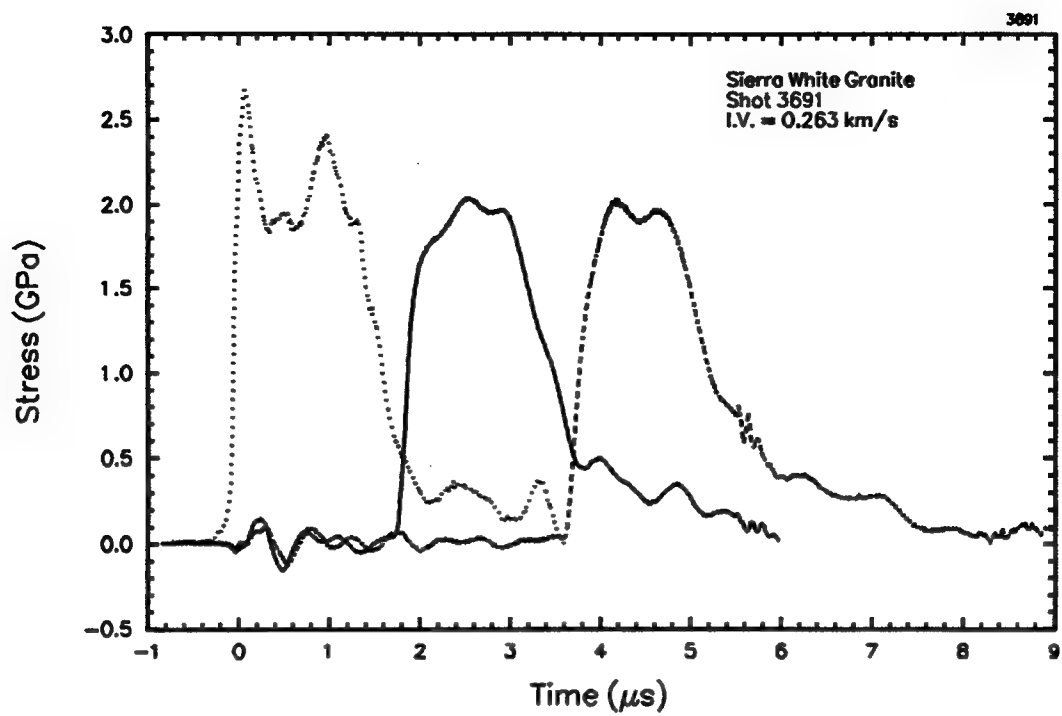


Figure A-42. Shot 3691.

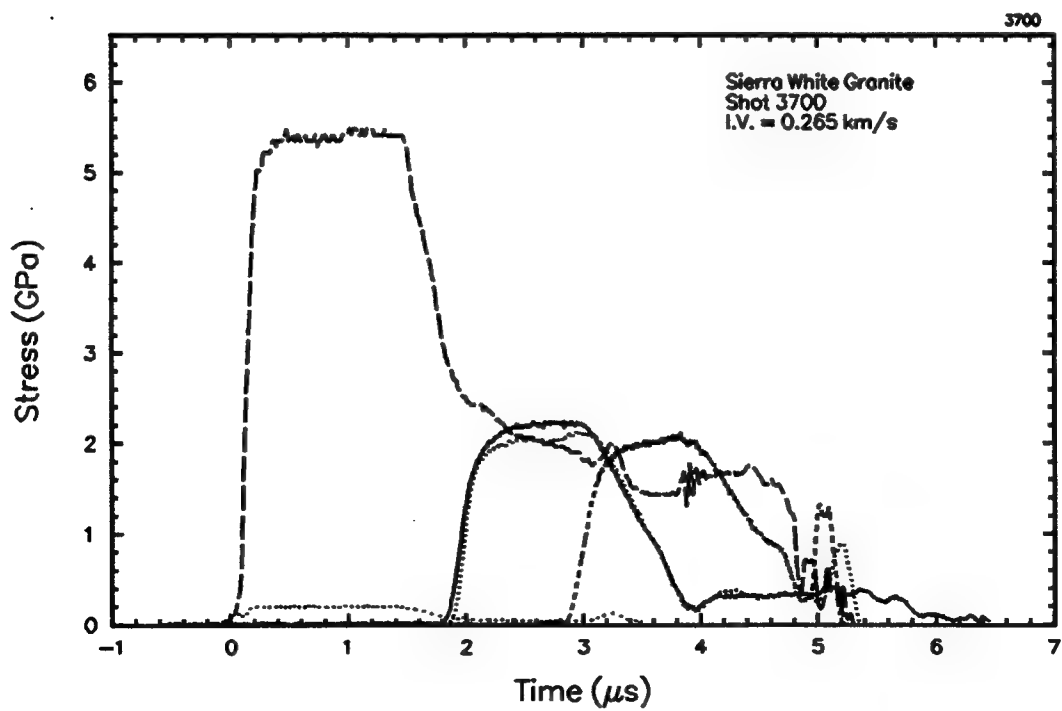


Figure A-43. Shot 3700.

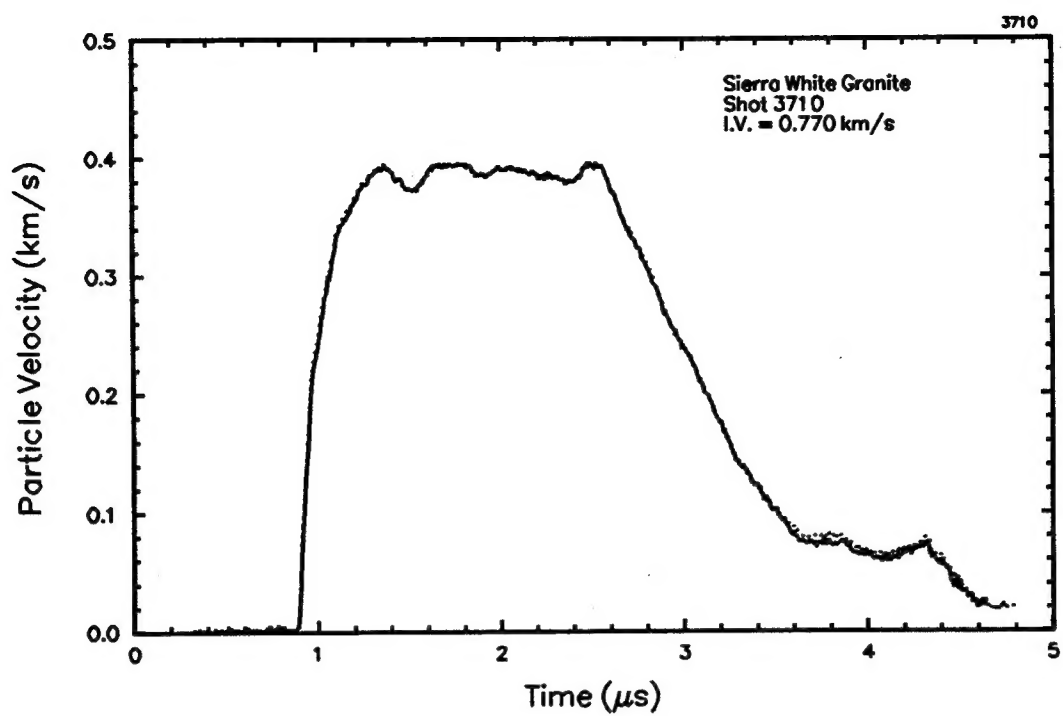


Figure A-44. Shot 3710.

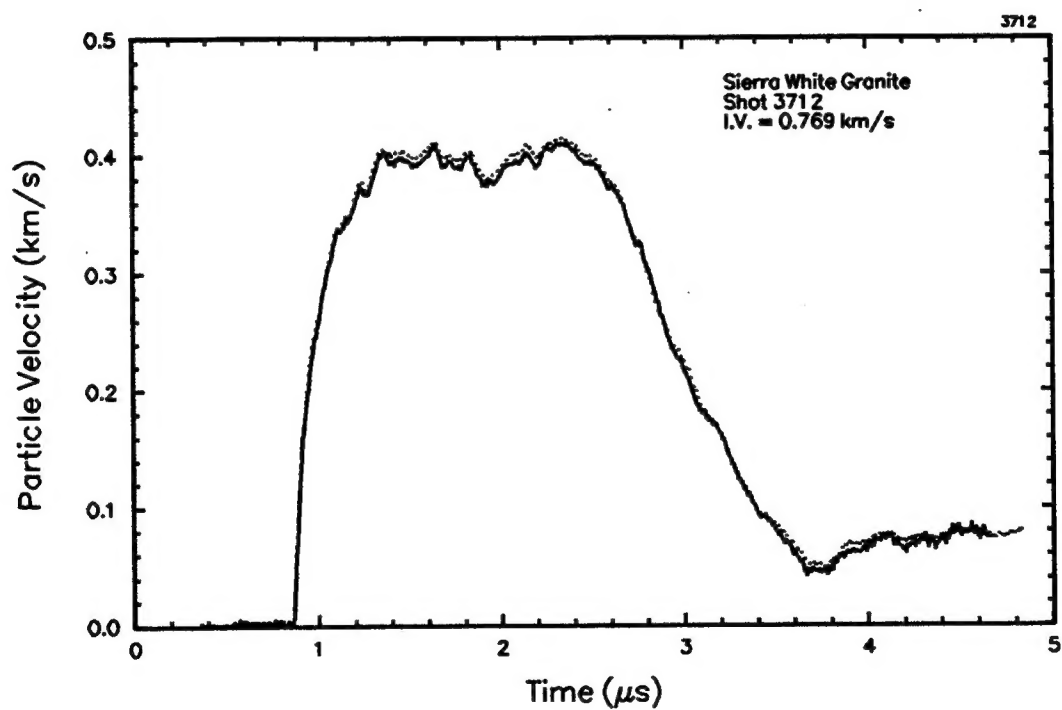


Figure A-45. Shot 3712.

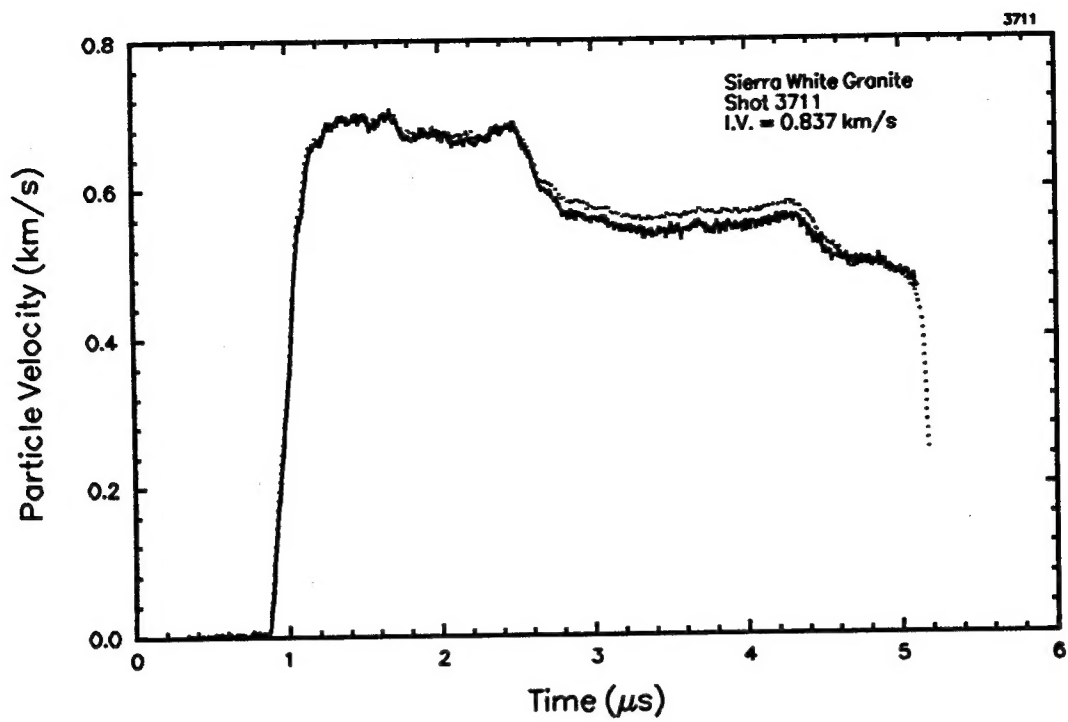


Figure A-46. Shot 3711.

## DISTRIBUTION LIST

DNA-TR-94-133

### DEPARTMENT OF DEFENSE

DEFENSE INTELLIGENCE AGENCY  
ATTN: DT-1

DEFENSE NUCLEAR AGENCY  
ATTN: DFSP  
ATTN: DFTD D LINGER  
ATTN: SPWE  
2 CY ATTN: SSTL  
ATTN: TDTV F RENSOLD

DEFENSE TECHNICAL INFORMATION CENTER  
ATTN: DTIC/OCP

FIELD COMMAND DEFENSE NUCLEAR AGENCY  
ATTN: FCTN B HARRIS-WEST  
ATTN: NVTV

FIELD COMMAND DEFENSE NUCLEAR AGENCY  
ATTN: FCTO M OBRIEN  
ATTN: FCTT-T E RINEHART  
ATTN: FCTT DR BALADI  
ATTN: FCTTS  
ATTN: FCTTS A MARTINEZ  
ATTN: FCTTS D SEEMANN  
ATTN: FCTTS J LEVERETTE  
ATTN: FCTTS LT COL LEONARD  
ATTN: FCTTS P RANGLES

### DEPARTMENT OF THE ARMY

U S ARMY ENGR WATERWAYS EXPR STATION  
ATTN: E JACKSON CEWES-SD-R  
ATTN: J ZELASKO CEWES-SD-R

### DEPARTMENT OF THE AIR FORCE

PHILLIPS LABORATORY  
ATTN: PL/SUL

### DEPARTMENT OF ENERGY

EG&G, INC  
ATTN: D EILERS

LAWRENCE LIVERMORE NATIONAL LAB  
ATTN: DONALD LARSON  
ATTN: F HEUZE L-200  
ATTN: L-13 B DUNLAP  
ATTN: L-200 LEWIS GLENN  
ATTN: L-200 J RAMBO  
ATTN: L-200 J WHITE  
ATTN: L-200 W C MOSS  
ATTN: L-58 R WARD  
ATTN: TECH LIBRARY

### LOS ALAMOS NATIONAL LABORATORY

ATTN: DAVID KING  
ATTN: FRED APP  
ATTN: T KUNKLE  
ATTN: T MCKOWN  
ATTN: J FRITZ  
ATTN: C MORRIS  
2 CY ATTN: REPORT LIBRARY  
ATTN: J N JOHNSON  
ATTN: THOMAS DEY  
ATTN: TOM WEAVER

### SANDIA NATIONAL LABORATORIES

ATTN: DIV 9321 W BOYER  
ATTN: MIKE FURNISH  
2 CY ATTN: TECH LIB 3141

### DEPARTMENT OF DEFENSE CONTRACTORS

DEFENSE GROUP, INC  
ATTN: ROBERT POLL

ENSCO INC  
ATTN: P FISHER

JAYCOR  
ATTN: CYRUS P KNOWLES

KAMAN SCIENCES CORP  
ATTN: DASIAAC

KAMAN SCIENCES CORPORATION  
2 CY ATTN: DASIAAC

KTECH CORP  
2 CY ATTN: E SMITH  
2 CY ATTN: FRANK DAVIES  
ATTN: L LEE

LOGICON R & D ASSOCIATES  
ATTN: J RENICK  
ATTN: L GERMAIN

MAXWELL LABORATORIES INC  
ATTN: DR E PETERSON  
ATTN: J BAKER  
ATTN: J MORRIS  
ATTN: P COLEMAN  
ATTN: S PEYTON

SCIENCE APPLICATIONS INTL CORP  
ATTN: DAN PATCH  
ATTN: DR M MCKAY  
ATTN: JACK KLUMP  
ATTN: L SCOTT  
ATTN: MARTIN FOGEL

**DNA-TR-94-133 (DL CONTINUED)**

**SRI INTERNATIONAL**  
ATTN: DR JIM GRAN  
ATTN: MARK GROETHE  
ATTN: P DE CARLI

**TECH REPS, INC**  
ATTN: F MCMULLAN  
ATTN: R NAEGELI

**TERRA TEK, INC**  
ATTN: W MARTIN

**TITAN CORPORATION (THE)**  
ATTN: ANNE COOPER  
ATTN: S SCHUSTER

**DIRECTORY OF OTHER**

**MARYLAND UNIVERSITY OF**  
ATTN: RICHARD DICK